Università degli Studi di Ferrara

DOCTORAL COURSE IN
ENGINEERING SCIENCE

CYCLE XXXIII

COORDINATOR Prof. STEFANO TRILLO

”ON THE CORROSION BEHAVIOUR OF CoCrMo BIOMATERIALS FABRICATED BY SELECTIVE LASER MELTING (SLM) AND CONVENTIONAL TECHNIQUES IN SYNTHETIC BODY FLUIDS, SIMULATING PHYSIOLOGICAL AND INFLAMMATORY CONDITIONS”

Scientific Disciplinary Sector ING-IND/22

Candidate
Dott. ssa Mahla Seyedi

_____
(signature)

Supervisor
Prof. ssa Cecilia Monticelli

_____
(signature)

Co-supervisor
Prof. Andrea Balbo

_____
(signature)

Years 2017/2021

With all my love;

To my irreplaceable mother, ***Zahra***, who gave me the greatest gift anyone could give another person; she believed in me,
To my inimitable father, ***Mehdi***, who taught me that we are all works in progress and made me realize my true potential,
To my beloved sister, ***Maryam***, who has always been the most supportive and encouraging one in my very life,
and to my adored sister, ***Mahdis***, whose ideas and actions make the world a better place, and for all her endeavor and loves, with which made my living so charming.

Preface

The present work, carried out at the Corrosion and Metallurgy Study Centre "Aldo Daccò", Department of Engineering of University of Ferrara (UNIFE), is submitted in partial fulfillment of the requirement for achieving the Doctor of Philosophy (Ph.D.) degree. This work has been performed under the supervision of Professor Cecilia Monticelli and, Associate Professor Andrea Balbo, from November 2017 to March 2021.

Mahla Seyedi

Ferrara, April 30th, 2021

Abstract

Traditional endoprostheses are widely used to replace bone and articular surfaces in case of degenerative joint disease; however, the mechanical, biological and structural mismatches between bone and the implants may cause significant problems like failure or patient pain. Considering the increasing patients' population with orthopedic implants, the clinical implication caused by corrosion of the biomedical implants must be considered very relevant for its serious consequences. Although the studies of corrosion and electrochemical behavior of CoCrMo alloys have reached a wide understanding of the phenomena involved, many aspects related both to the manufacturing processes and the biological environments to which they are exposed, are still unknown and need to be clarified to minimize the problems created by endoprosthetic implants.

Moreover, it is crucially important to design an implant, fully customizable and scalable, with an optimum combination of properties and geometries. In fact, the worse clinical outcomes are observed in post-traumatic patients, where the limited availability of prosthesis size and shape and the difference between the bone and implant stiffness further reduces osteointegration due to the stress concentration and shielding. The introduction of selective laser melting (SLM) technique offers a great potential in the fabrication customized implants through the consolidation of layer-by-layer metal powders. Although selective laser melted bioimplants may provide structures closer to the host bone, the rapid melting/cooling process, resulting in non-equilibrium microstructures, may change the corrosion and mechanical properties and affect structural integrity.

Several aspects concerning the effect of different SLM process parameters and different simulated body fluids (SBF) on the behavior of SLM CoCrMo samples are studied within this Ph.D. work, including:

- Microstructural characterization of CoCrMo alloys fabricated with different SLM process parameters
- Corrosion and electrochemical behaviour of the SLM CoCrMo alloys exposed to the different SBF also reproducing inflammatory conditions.
- Comparison of the conventional CoCrMo alloys properties with those of SLM fabricated ones.

- Effect of SLM process parameters on the mechanical behaviour of these materials compared to those of wrought CoCrMo alloys.
- Effect of the post-processing heat treatment on the microstructure and corrosion behaviour in SBF of SLM fabricated CoCrMo alloys.

Within this thesis, 4 different types of samples were fabricated by SLM technique using different set of laser parameters. To address the above-mentioned points, the bulk and surface microstructural changes, induced by selective laser melting process, are investigated using X-ray diffraction (XRD) and a combination of different (post) microscopical characterization techniques: optical microscopy (OM), scanning electron microscopy (SEM) coupled with energy dispersive X-Ray spectroscopy (EDX) and Focused Ion Beam (FIB) technique. Moreover, to provide an in-depth investigation on the surface film nature and characteristics of the studied CoCrMo alloys, also Transmission Electron Microscopy (TEM), and Atomic Force Microscopy (AFM) are used. The corrosion and electrochemical behaviour are studied by polarization curves (PC), electrochemical impedance spectroscopy (EIS) and cyclic voltammetry (CV) techniques during the exposure to SBF both in the presence and in the absence of simulated inflammatory conditions.

In order to understand the effect of SLM process on mechanical behaviour and for exploring the mutual effect of electrochemical and mechanical processes on the alloy behavior, mechanical methods such as Vickers microhardness (VH), tensile and slow strain rate tests (SSRT) were utilized.

The main results of this Ph.D. work are classified into four types of experimental studies, each discussing the microstructural changes and the corresponding corrosion mechanisms comprehensively. The first study aimed at exploring the microstructure evolution and characteristics of CoCrMo alloys manufactured by selective laser melting. Both SLM alloys and their wrought (WRO) counterparts were examined using different characterization techniques. The results of this work demonstrate that the rapid melting and cooling induced non-equilibrium microstructure in the SLM built samples, consisting of cellular dendritic structures. The samples showed a fine microstructure, characterized by Mo enrichment at the cell boundaries. On the contrary, wrought CoCrMo alloy showed a typical fine-grained monophasic FCC structure. The second study addressed the corrosion and electrochemical behaviour of the SLM alloys in controlled Phosphate-

buffered saline (PBS) solutions in the presence and in the absence of inflammatory conditions. The results of this work lead to the better understanding of the effect of SLM process parameters on the corrosion properties of the alloys. The materials fabricated with SLM technology seem to be quite promising in terms of corrosion resistance, even in the presence of inflammatory condition, simulated with the addition of H_2O_2, but the corrosion behavior was found to depend appreciably on the alloy microstructure. Samples with finer microstructure showed a better corrosion behaviour, due to the uniform distribution of alloying elements and less Mo micro-segregations.

The alloys studied showed excellent corrosion resistance connected to the barrier properties of the passive film, mainly attributed to the protective capacity of Cr_2O_3. In the presence of inflammatory conditions, a lower corrosion resistance was observed in all the materials studied compared to that measured at pH= 7.4 and at pH= 4.

The studied alloys showed quite similar behaviour at pH= 7.4 and pH= 4 suggesting comparable barrier properties of the passive film, mainly ascribed to the protective capability of Cr_2O_3, reinforced by the presence of MoO_2. In the presence of inflammation conditions, the lower corrosion resistance was observed in all studied materials.

Following this, the third study focuses on the determination of the effect of the SLM process parameters on the mechanical properties of the studied alloys. The results reveal that the SLM process can build parts with mechanical properties comparable with traditional wrought CoCrMo alloy.

Eventually, the fourth study investigated the correlation between the SLM process parameters and heat treatments on the microstructural characteristics and corrosion behaviour of the fabricated CoCrMo alloys. Finer cellular structure was found in sample fabricated with lower laser power. Heat treatment at 850°C for 180 min induced a progressive modification of the cellular structure, that broke down into fine and homogeneously dispersed globular particles. Electrochemical tests showed an overall good corrosion resistance of the as-built SLM alloys, comparable or higher than those of conventional wrought alloy. Heat treatment processes remarkably increase the corrosion resistance of sample fabricated with lower laser power. This result is probably connected to the formation of finer precipitates and more uniform distribution of particles.

Sommario

Le endoprotesi tradizionali sono ampiamente utilizzate per sostituire le superfici ossee e articolari in caso di malattia degenerativa delle articolazioni; tuttavia, i disallineamenti meccanici, biologici e strutturali tra l'osso e le endoprotesi possono causare problemi significativi come rotture dell'impianto o dolore e malessere nel paziente. Considerando il numero crescente di persone con impianti ortopedici, le implicazioni cliniche causate dalla corrosione degli impianti biomedicali devono essere considerate rilevanti per le loro gravi conseguenze.

Sebbene gli studi sul comportamento a corrosione ed elettrochimico delle leghe CoCrMo abbiano raggiunto un'ampia comprensione dei fenomeni coinvolti, molti aspetti legati ai processi di fabbricazione ed agli ambienti biologici a cui sono esposti sono ancora sconosciuti e devono essere chiariti al fine di minimizzare i problemi creati dagli impianti endoprostesici.

Pertanto, è di fondamentale importanza progettare impianti, completamente personalizzabili e scalabili, con una combinazione ottimale di proprietà e geometrie. Infatti, gli esiti clinici peggiori si osservano nei pazienti post-traumatici, dove la limitata disponibilità di dimensioni e forme delle protesi e la differenza di rigidità tra l'osso e l'impianto riducono ulteriormente l'osteointegrazione a causa della concentrazione di stress e di effetti di shielding.

Lo sviluppo della tecnica Selective Laser Melting (SLM) offre un grande potenziale nella fabbricazione di impianti personalizzati attraverso il consolidamento di polveri metalliche strato per strato. Sebbene le protesi SLM possano fornire strutture più simili all'osso ospite, il rapido processo di fusione/raffreddamento, che porta a microstrutture non in equilibrio, può modificare il comportamento a corrosione e le proprietà meccaniche ed influire sull'integrità strutturale.

Nell’ambito di questo dottorato sono stati studiati gli effetti di differenti parametri del processo SLM sul comportamento di campioni di CoCrMo esposti a differenti fluidi corporei sintetici (SBF). In particolare, è stata eseguita:

- Caratterizzazione microstrutturale di leghe CoCrMo fabbricate con diversi parametri di processo SLM
- Studio del comportamento a corrosione ed elettrochimico delle leghe SLM CoCrMo esposte a differenti SBF sia in presenza che in assenza di condizioni infiammatorie.
- Confronto delle proprietà delle leghe CoCrMo convenzionali con quelle di quelle fabbricate con tecnica SLM.
- Studio dell’effetto dei parametri di processo SLM sul comportamento meccanico di questi materiali rispetto a quelli delle leghe CoCrMo tradizionali.
- Studio dell’effetto dei trattamenti termici sulla microstruttura e sul comportamento corrosione di leghe CoCrMo SLM in SBF.

Nel corso di questo dottorato sono stati fabbricati, con tecnica SLM, 4 diversi tipi di campioni utilizzando differenti parametri del processo di fabbricazione.

Per affrontare i punti sopra menzionati, i cambiamenti microstrutturali di massa e di superficie, indotti dal processo SLM, sono studiati utilizzando la tecnica di diffrazione dei raggi X (XRD) e una combinazione di diverse tecniche di caratterizzazione microscopica come microscopia ottica (OM) e microscopia elettronica a scansione (SEM) accoppiata alla spettroscopia a dispersione di energia (EDX) ed alla tecnica di fascio di ioni focalizzati (FIB).

Inoltre, per fornire un'indagine approfondita sulla natura del film superficiale e sulle caratteristiche delle leghe CoCrMo SLM, sono state utilizzate anche la microscopia elettronica a trasmissione (TEM) e la microscopia a forza atomica (AFM).

Il comportamento corrosione ed elettrochimico è stato studiato mediante la registrazione curve di polarizzazione (PC), spettroscopia di impedenza elettrochimica (EIS) e tecniche di voltammetria ciclica (CV) durante l'esposizione a SBF sia in presenza che in assenza di condizioni di infiammazione.

Per comprendere l'effetto del processo SLM sul comportamento meccanico e per esplorare l'effetto reciproco dei processi elettrochimici e meccanici sul comportamento della lega, sono stati utilizzati metodi meccanici come prove di microdurezza Vickers (VH), prove di trazione e prove di trazione a bassa velocità di deformazione (SSRT).

I principali risultati di questo lavoro di tesi sono raggruppati in quattro studi sperimentali, ciascuno dei quali descrive e discute i cambiamenti microstrutturali e i meccanismi di corrosione in modo completo.

Il primo studio ha avuto come obbiettivo quello di esplorare l'evoluzione della microstruttura e le caratteristiche delle leghe CoCrMo prodotte mediante tecnica SLM. Le leghe SLM e le loro controparti tradizionali (WRO) sono state esaminate utilizzando diverse tecniche di caratterizzazione. I risultati di questo lavoro hanno mostrato che la rapida fusione e raffreddamento inducono, nei campioni fabbricati con tecnica SLM, una microstruttura di non equilibrio caratterizzata da una struttura cellulare e dendritica.

I campioni SLM hanno evidenziato una microstruttura fine, caratterizzata da un arricchimento di Mo al bordo delle microcelle. Al contrario, la lega CoCrMo tradizionale ha mostrato una tipica struttura FCC monofasica a grana fine.

Il secondo studio ha affrontato analizzato il comportamento a corrosione ed elettrochimico delle leghe SLM in soluzioni PBS sia in presenza che in assenza dei processi di infiammazione. I risultati di questo lavoro hanno portato ad una migliore comprensione dell'effetto dei parametri di processo SLM sulle proprietà di corrosione delle leghe.

I materiali fabbricati con tecnologia SLM si sono mostrati molto promettenti in termini di resistenza alla corrosione, anche in presenza di condizioni infiammatorie, simulate con l'aggiunta di H_2O_2, ma si è riscontrato che il comportamento alla corrosione dipende in modo apprezzabile dalla microstruttura della lega: il campione con microstruttura più fine ha evidenziato un migliore comportamento alla corrosione, grazie alla distribuzione uniforme degli elementi alliganti e alle minori micro-segregazioni di Mo.

Le leghe studiate hanno mostrato un'ottima resistenza a corrosione legate proprietà di barriera del film passivo, principalmente attribuite alla capacità protettiva di Cr_2O_3. In presenza di condizioni di infiammazione, è stata osservata una minore resistenza alla corrosione in tutti i materiali studiati rispetto a quella misurata a pH=7.4 e a pH=4.

Successivamente, il terzo studio si è concentrato sullo studio dell'effetto dei parametri di processo SLM sulle proprietà meccaniche delle leghe studiate. I risultati hanno mostrato che attraverso la tecnica SLM si possono realizzare parti con proprietà meccaniche paragonabili a quelle delle leghe tradizionali.

In fine, il quarto studio ha analizzato l'effetto di diversi parametri di processo SLM e trattamenti termici sulle caratteristiche microstrutturali e sul comportamento alla

corrosione delle leghe SLM CoCrMo. Il campione fabbricato con una potenza del laser inferiore ha evidenziato una microstruttura cellulare più fine. Il trattamento termico a 850°C per 180 min ha indotto una progressiva modificazione della struttura cellulare, che si è scomposta in particelle globulari fini ed omogeneamente disperse. I test elettrochimici hanno evidenziato una buona resistenza alla corrosione complessiva delle leghe SLM as-built, paragonabili o superiori a quelle delle leghe convenzionali. Il trattamento termico ha aumentato notevolmente la resistenza alla corrosione del campione fabbricato con una potenza laser inferiore. È probabile che questo risultato sia da attribuire alla formazione, in questo campione, di precipitati più fini e più uniformemente distribuiti.

Acknowledgments

”سر ارادت ما و آستان حضرت دوست که هرچه بر سر ما می رود ارادت اوست “

I still clearly remember the first painting exhibition that I held. It was very challenging and asked a lot of persistence and hard work, especially for a 14 years old teenager. At the moment, I felt very thrilled and proud, but it takes many years after holding more exhibitions that I discovered, holding a successful exhibition is not all about you. A trustful leader (s) and companionable team members are essential for a successful and memorable experience. Four years ago, when I moved to Italy, I expected that there would be no room for holding an exhibition in a fully colourful and artistic country! But this was a wrong assumption, as obtaining a Ph.D. degree was the most challenging and wonderful exhibition ever that I achieved. And of course, it was not possible without great leaders and nice team members, whom I would like to express my deep gratitude here.

First and foremost, I would like to express my sincere appreciation to my principal supervisor, *Professor Cecilia Monticelli*, for her valuable help and support, continuous guidance, and precious advice throughout this research. Dear Cecilia, you were definitely one of the most reliable leaders that I could imagine during this long and challenging journey. Your attitude towards others was quite unique as you treated them more as a colleague, but at the same time feel very much responsible for them. I greatly appreciate the professional guidance, time, patience, and encouragement you devoted to me in these years. How fascinating it was that you manage all limitless duties and simultaneously stay positive, focused, and optimistic. Your deep knowledge in materials and corrosion science and being such a responsible and patient leader was certainly the major reason behind my success to achieve this point, and I have no words to express my sincere gratitude to you.

Secondly, I would like to express my deep appreciation to my co-supervisor, *Associate Professor Andrea Balbo* for his valuable discussion, mentorship, and insight. I am grateful to him for helping me formulate the project and his guidance during this work. Dear Andrea, I cannot surely count the number of times that I knocked your door to ask question and guidance. And how wonderful was that you were always willing to help no matter how busy you were. Perhaps, without your insights, I was still sitting in front of canvas and wondering which colour I should choose. I have definitely said thanks each

and every time after our discussions, but of course here is the place to repeat it, equals to the number of times that I knocked your door.
I also extend my sincere thanks to *Dr. Erica Liverani* and *Prof. Alessandro Fortunato* for arranging the fabrication of SLM components.
I would like to thank my colleagues as friend in Aldo Daccò Center. Dear *Prof. Fabrizio Zucchi* and *Prof. Alessandro Frignani*, you were retired before I joined the center. It was my honour to get know you. However, we had no collaborative research. It was of course very pity for me, as you were knowledgeable people in the field of corrosion and materials engineering who are also very modest and mindful for others. I would like to thank you for all your inputs and positive energy. Dear *Dr. Federica Zanotto* and *Dr. Vincenzo Grassi*, you helped me always enthusiastically and willingly with the experimental testing as well as personal activities. Sometimes, I was amazed by your smart solutions. I also would like to thank my office mates; Dear *Dr. Chiara Soffritti* and *Dr. Sebastiano Merchiori*, many thanks for being so helpful and friendly in every way and making the office such a great working place. I also thank all the former and present member of Materials Engineering section: Dear *Prof. Gian Luca Garagnani*, you were involved in my selection committee and among the first people that I get to know at UNIFe. It was a fortune to have you as the director of the materials laboratory, a person who always help others. Dear *Dr. Annalisa Fortini*, *Dr. Lucia Lattanzi* and *Dr. Maverick Giovagnoli*, thank you for being friends in need. You were always there when I need help. It is difficult to imagine that colleagues can be like friends, but having you proved me that fantastic colleagues can be the same as friends. I wish you best of luck for your next career, my FEmily.
I would like to extend my sincerest thanks and appreciation to *Prof. Matteo Ferroni* and staffs of the microscopic center of "CNR Bologna" for sharing their knowledge, experiences, and technical supports for conducting FIB and TEM measurements. Thank you, Matteo, for your interesting and useful inputs to make the characterization part of the current thesis possible.
I also wish to thank *Prof. Jinshan Pan* for hosting me as a visiting Ph.D. student at the division of surface and corrosion of the KTH Royal Institute of Technology, Sweden. I also would like to knowledge *Fan Zhang* and other wonderful people at the division for their technical support and discussions during my stay at KTH, even at the uncertain condition caused by Covid-19. But this did not mean that I can forget how much I learned

at your division. Dear *Prof. Mark Rutland*, I would like to express my deepest gratitude to you for all your supports and kindness during my stay in Stockholm. I find myself very proud and lucky to have you as my friend. I learned a lot form you through your course and social activities we have had together. Thanks for being so great friend and make me feel at home in any way during that tough and challenging time in Stockholm.

Fantastic friends and family members also accompany me during this amazing journey whom I shared great moments with, and I would like to extend my sincerest gratitude for their friendship and support. Thank you for all good memories and your help whenever I asked for.

Last but not least, I would like to express my sincere thank from bottom of my heart to *my beloved family*. My gratitude for all their supports, helps and sacrifices cannot be expressed by words. Dear *Mommy and Daddy*, my beloved sisters; *Maryam and Mahdis*, I truly love you, and I would not have made it this far without you. You were always so patient and supportive, and your love was so strong that returned me back to track, even when you are miles and miles apart. You have always been and will be the reason for me to stand up and overcome all the challenges that I meet in my life.

" مقام امن و می بی غش و رفیق شفیق گرت مدام میسر شود زهی توفیق"

مادر مهربان من، در تمامی این سالها توجه و پشتیبانی بی انتهایت در هموار کردن این راه دشوار، یاری رسان من بوده است. تشکر و سپاس که درد دوری را به جان خریدی و اکنون شاهد به ثمر نشستن نتیجه همه دوریها و دلتنگی ها هستی. بی هیچ تردیدی بخش مهمی از این موفقیت مدیون بودنت است ، نمیدانم با چه زبانی از همه لحظاتی که برای من نگران بودی و با کلام آرام و مهربانت تمام سختی ها و دلتنگی های مرا هموار کردی، تشکر کنم.

پدر یکتای من، بدون شک بدون آموزش وحمایتت من در فراز این قله نبودم. تو نه تنها راهنمای من برای انتخاب مسیر زندگی ام بودی، بلکه در تمامی این سالها درس استقامت و پشتکار را از تو فرا گرفتم. درود بی پایان برای همه لحظاتی که به من آموختی چگونه مستقل و بدون واهمه از خطرات و سختیها، قدم در مسیرهای چالش برانگیز بردارم و از تجربیاتم نهایت لذت را ببرم.

با تمام قبلم افتخار میکنم پدر و مادر دلسوز وفداکاری چون شما دارم. سایه تان همیشه بر سرما مستدام و تنتان سلامت.

مریم و مهدیس عزیزتر از جانم، خودم را خوشبخت میدانم از داشتن دوخواهر منحصر بفرد و دوست داشتنی. در تمام لحظات خستگی و آشفتگی، لحظه کوتاهی شنیدن صدای شما کافی بود تا انرژی ام را به من و مرا به مسیرم بازگرداند. دوری شما تنها سختی غیرقابل تحمل این مسیر بود و تشکر من بی پایان است برای این همه گذشت و دوست داشتن بی دریغ، هرچه دارم از وجود و حمایت شماست. امیدوارم روزی فرا رسد که بتوانم تمام حمایت هایتان را جبران کنم.

دلتان سبز، لبخندتان به راه و روزگارتان به کیف و آرامش باشد، تا به ابد.

مهلا سیدی – فروردین یکهزار و چهارصد هجری شمسی – فرارا- ایتالیا

Mahla Seyedi – April 2021 – Ferrara - Italia

Table of Contents

“Imagination is more important than knowledge. For knowledge is limited to all we now know and understand, while imagination embraces the entire world, and all there ever will be to know and understand.”

— Albert Einstein


1

CHAPTER ONE

Introduction

This thesis is the result of a research project entitled “Study of the electrochemical behavior of CoCrMo biomaterials fabricated through SLM: The effect of process parameters and inflammation conditions,” carried out at the “Aldo Daccò” Corrosion and Metallurgy Center, Department of Engineering, University of Ferrara (UNIFE).
The framework and hypothesis of the research are given in section 1.1. Then the motivation and research objectives are presented in section 1.2. Section 1.3 gives the experimental approaches used for the design of the project map. Finally, the structure of the thesis comes in section 1.4.

1.1. Statement of intent and hypothesis

One of the most recurrent problems faced in the healthcare system is the loss of damaged bone joins due to age-related and degenerative diseases like osteoarthritis, rheumatoid arthritis, and arthritis secondary to other causes such as osteoporosis and accidents. As a consequence, the mobility is significantly restricted, and the damaged structure induces further pain, limping, and associated disabilities. Therefore, the development of an operative treatment that both relieves pain and restores motion is of paramount importance to many patients [1–3]. Artificial joint replacement is a widely used treatment and has been extensively applied when severe pain or dysfunction is not alleviated by less-invasive therapies [4–6]. At the same time, the past several decades has seen a rapid demand for artificial body parts as older people want to remain active and younger patients do not want to lose their mobility at such an early age. From the report ‘Broken bones, broken lives: a roadmap to solve the fragility fracture crisis in Europe’ [7], it is estimated that more than 4 million Italian older than 50 years are suffering from osteoporosis. Moreover, the estimated lifetime risk for hip fracture for men and women in Italy is 7.97% and 16.7%, respectively. Besides, according to this report, the fragility fracture incidence is expected to increase by about 22.4% within 2030 [7]. On the other hand, sport-related injuries, as well as road accidents are fueling the number of breakdown and failure cases [8].
The first attempts to find artificial joint substitutes go back to a century ago when scientists and surgeons started to identify possible biomaterials capable of replacing or repair damaged joints to restore biological function. Bioimplants have considerable importance in improving the longevity and quality of human life [9–11].

Due to their intended use in a very complex environment, adequate and efficient biomaterials need to fulfill mechanical, durability in terms of corrosion resistance, and biological requirements [12–14]. In particular:

1. *Biocompatibility*: biomaterials must be non-toxic and must induce a low inflammatory response in the surrounding tissues;
2. *Sterilization*[1]: biomaterials need to be able to withstand sterilization without losing their function;
3. *Functionality*: biomaterials are designed for a specific application. Consequently, their behavior must be optimized in terms of corrosion resistance, integration with the surrounding host tissue, and mechanical properties;
4. *Manufacturing*: the rising demand for biomaterials forces them to be manufactured with cost-effective and high-speed methods.

Metallic biomaterials exhibit many of the features required from ideal biomaterials, such as good mechanical properties, good corrosion and wear resistance, and suitable biocompatibility [11,15]. Metallic implants are used for two primary purposes: one of them is replacing a portion of the body such as joints, long bones, skull plates, and the other is fixation and stabilization of broken bones [14]. In the past decades, the expansion of metallic biomaterials for medical applications brought to the attention of research scientists the excellent properties of CoCrMo alloys [15–17]. CoCrMo alloys represent excellent biocompatibility, which is closely related to their satisfactory resistance to corrosion [15,18]. Simultaneously, the crystallographic nature of their major element, cobalt, ensures the alloy possesses superior mechanical properties [15,19]. Consequently, they were satisfactorily applied in this field during the last five decades.

[1] Sterilization is defined as a condition of complete destruction or removal of all forms of life on an instrument to be used or on a device to be implanted. In practice, however, the acceptable level of microbial contamination of a sterilized object is 10^6 cfu/g or cfu/ml or less. Noted that CFU stands for colony-forming units of the sample.

As the demand for joint replacements has escalated, patients' expectations for the effectual long-lasting joints with the possible full restoration of function, including sporting activity and minimizing the need for revision surgery, remain mostly unmet due to early loosing of the implanted prostheses. Improper implant sizing or flawed design, inferior osteointegration, difference in mechanical properties between bone and implant materials, and foreign body reaction induced by inflammatory cells were ascribed to imperfect production of materials and implants, leading to early failures and patients' dissatisfaction [20–22].

Accordingly, methods to eliminate or decrease these deficiencies were actively looked for in order to optimize the performances of CoCrMo prostheses. Additive manufacturing (AM) has recently emerged as a fabrication method in which three-dimensional (3D) objects are built by depositing the constituent materials precisely in a layer-by-layer fashion using CAD data [23–26]. Selective laser melting (SLM) is a laser-based additive manufacturing process, and according to its name, it is a layer-wise material addition method that allows fabricating 3D parts by selectively melting successive layers of metal powder on top of each other, using the thermal energy supplied by a focused and computer-controlled laser beam [23,27]. Because of the exploitation of the layer-by-layer process and a very precise laser beam (≈ 30μm), SLM is not only capable of producing geometrically complex parts but can also be used for achieving fully customizable and scalable prostheses. It is thus best suited for manufacturing dense components, porous graded or fully customized architectures, improving osseointegration and bone adaptation [23,28,29].

The idea to produce CoCrMo bioimplants by selective laser melting technique is relatively new, and recently researchers have investigated a variety of approaches to study their potential for medical applications [28,30–34]. The materials fabricated with SLM technology seem to be promising in terms of corrosion resistance, but their behaviour in biological environments needs to be studied in much detail, considering different parameters. Since the biocompatibility is directly related to the corrosion resistance of the alloy and is an essential complementary requirement for a biomaterial, the effect of process parameters on the corrosion properties of these alloys is crucial.

1.2. Motivation and research objectives

The present Ph.D. project aims at exploring the electrochemical and corrosion behavior of Selective Laser Melted (SLM) Cobalt-Chromium-Molybdenum (CoCrMo) bio-implants in order to optimize the properties of the next generation of implants and, consequently, to improve the implanted patients' life. This activity was carried out in collaboration with ALMA MATER STUDIORUM - Università di Bologna, Italia, CNR Area della Ricerca di Bologna, Italia and Division of Surface and Corrosion, Royal Institute of Technology (KTH), Sweden.

The main objectives of the current research are as follows:

- Deriving the proper SLM process parameters for fabrication of reliable CoCrMo bioimplants in order to achieve a proper combination of mechanical and corrosion properties. The latter properties were assessed in phosphate-buffered saline (PBS) solution.
- Understanding the correlation between SLM process parameters, post-heat treatments microstructure, mechanical and corrosion properties of SLM CoCrMo alloy.
- Studying the influence of inflammatory conditions around the implant induced by properly modifying the PBS solution composition.
- Improving the knowledge about the nature and characteristics of the passive surface layers formed during immersion in PBS solution.

1.3. Experimental approach

In order to achieve the objectives stated above, CoCrMo alloys fabricated with the SLM technique by the Technologies and Processing Systems group of the Industrial Engineering Department of the University of Bologna were used.

After applying some initial characterization on selected SLM alloys and traditional counterparts with X-ray diffraction, different tests were planned. The corrosion resistance behavior of the alloy is related to the stability of the oxide film formed on the CoCrMo alloy surface. Thus, an electrochemical characterization of the alloy was carried out in order to find the correlation between different physico-chemical properties of the body fluids and the stability of this oxide film. In particular, CoCrMo

alloy samples were subjected to immersions in simulated body fluids (phosphate-buffered saline (PBS) solution, characterized by a pH value of 7.4), during which corrosion potential (E_{corr}) measurements, Cyclic Voltammetries (CV), polarization curves (PC) and Electrochemical Impedance Spectroscopy (EIS) tests were carried out. These tests were also performed in solutions simulating inflammatory conditions, reproduced by using acidic pH values (PBS solution adjusted at pH=4) and by adding 30 mM hydrogen peroxide (H_2O_2). The effect of SLM process parameters on the microstructure and passive film properties was further studied by different characterization methods, including light optical microscope (LOM) and electron microscopy techniques (such as scanning electron microscopy (SEM) coupled with energy dispersive X-Ray spectroscopy (EDX), Focused Ion Beam (FIB), Transmission Electron Microscopy (TEM), and Atomic Force Microscopy (AFM)). The samples were further subjected to hardness, tensile, and slow strain rate testing in order to evaluate their mechanical properties and the influence of an aggressive environment on these properties.

Besides, the effect of post-processing heat treatment on the microstructure and corrosion behavior of SLM built alloys were studied.

1.4. Structure of the thesis

The thesis is composed of eleven individual chapters (Figure 1.1) with the following content:

Chapter 1: Introduction

- This chapter comprises research motivation and objectives of the thesis followed by an outline of the experimental approach of the present doctoral work.

Chapter 2: Background

- Chapter 2 comprises the relevant literature review on the biomaterials and their properties. Firstly, the fundamental topics associated with biomaterials, especially CoCrMo alloys, are reviewed. Then, additive manufacturing (AM) technique is introduced, where the advantages of utilizing selective laser melting (SLM) for

orthopedic applications are presented. Corrosion in biomaterials, human body fluid compositions as well as the effect of alloying elements, are also presented. Finally, research studies related to the microstructure and electrochemical and corrosion behavior of CoCrMo alloys have been critically evaluated within the context of the objectives of this work.

Chapter 3: Materials and Experimental methods

- This chapter focuses on the materials and experimental procedures utilized in this research. A brief overview of the various techniques (electrochemical, mechanical and characterization methods) employed is also given.

Chapter 4 – 8: Results and Discussion chapters

- The detailed description and comprehensive discussion of the experimental results of the thesis are presented in these chapters in the manuscript-form style.

Chapter 9: Conclusion Remarks

- The main findings of the thesis are summarized in this chapter.

Chapter 10: Recommendations for future works

- This chapter discusses the outlook and perspectives for further studies.

Chapter 11: Abbreviations and appendix

- This chapter represents the abbreviations and appendix of the present work.

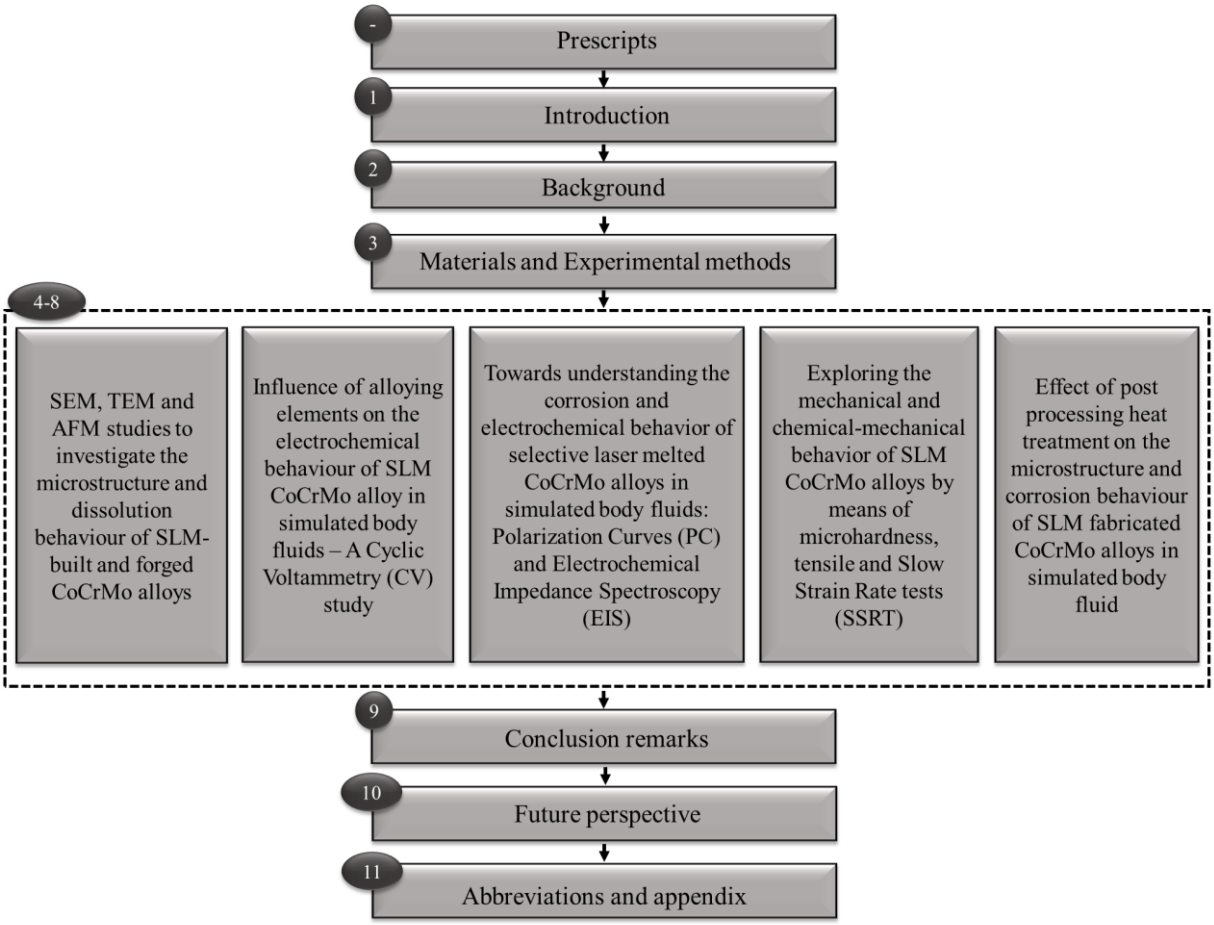

Figure 1.1. Flowchart on the structure of the present Ph.D. dissertation.

References

[1] J.A. Kanis, O. Johnell, C. De Laet, H. Johansson, A. Oden, P. Delmas, J. Eisman, S. Fujiwara, P. Garnero, H. Kroger, E. V McCloskey, D. Mellstrom, L.J. Melton, H. Pols, J. Reeve, A. Silman, A. Tenenhouse, A meta-analysis of previous fracture and subsequent fracture risk, Bone. 35 (2004) 375–382.

[2] S.L. Hughes, D. Dunlop, P. Edelman, R.W. Chang, R.H. Singer, Impact of joint impairment on longitudinal disability in elderly persons, J. Gerontol. 49 (1994) S291–S300.

[3] J. Cushnaghan, J. Bennett, I. Reading, P. Croft, P. Byng, K. Cox, P. Dieppe, D. Coggon, C. Cooper, Long-term outcome following total knee arthroplasty: a controlled longitudinal study, Ann. Rheum. Dis. 68 (2009) 642–647.

[4] S.C. Humphreys, S.D. Hodges, E.C. Lange, D. Braddock Jr, H.H. Trieu, Total joint replacement, (2012).

[5] S.G. Ghalme, A. Mankar, Y. Bhalerao, Biomaterials in hip joint replacement, Int. J. Mater. Sci. Eng. 4 (2016) 113–125.

[6] Y.T. Konttinen, I. Milošev, R. Trebše, R. Van Der Linden, J. Pieper, T. Sillat, S. Virtanen, V.M. Tiainen, Metals for joint replacement, in: Jt. Replace. Technol., Elsevier, 2014: pp. 81–151.

[7] BROKEN BONES , BROKEN LIVES :, (n.d.).

[8] N. Maffulli, U.G. Longo, N. Gougoulias, D. Caine, V. Denaro, Sport injuries: a review of outcomes, Br. Med. Bull. 97 (2011) 47–80.

[9] S.B. Goodman, E. Gómez Barrena, M. Takagi, Y.T. Konttinen, Biocompatibility of total joint replacements: A review, J. Biomed. Mater. Res. Part A. 90A (2009) 603–618.

[10] M. Niinomi, M. Nakai, J. Hieda, Acta Biomaterialia Development of new metallic alloys for biomedical applications, Acta Biomater. 8 (2012) 3888–3903.

[11] M.J. Yaszemski, D.J. Trantolo, K. Lewandrowski, V. Hasirci, D.E. Altobelli, D.L. Wise, Biomaterials in Orthopedic s, 2004.

[12] J. Bronzino, J. Park, Biomaterials: principles and applications, (2002).

[13] B.D. Ratner, A.S. Hoffman, F.J. Schoen, J.E. Lemons, Biomaterials Science: An Introduction to Materials in Medicine, Elsevier Science, 2012.

[14] V. Hasirci, N. Hasirci, Fundamentals of biomaterials, Springer, 2018.

[15] Q. Chen, G.A. Thouas, Metallic implant biomaterials, Mater. Sci. Eng. R Reports. 87 (2015) 1–57.

[16] T. Corrigendum, Implants for surgery — Metallic materials — Part 12 : Wrought cobalt-chromium-molybdenum alloy, 2008 (2008) 5832.

[17] I. Milošev, CoCrMo Alloy for Biomedical Applications, 2012.

[18] E.J. Evans, I.T. Thomas, The in vitro toxicity of cobalt-chrome-molybdenum alloy and its constituent metals, Biomaterials. 7 (1986) 25–29.

[19] J. Alvarado, R. Maldonado, J. Marxuach, R. Otero, Biomechanics of hip and knee prostheses, Appl. Eng. Mech. Med. GED–University Puerto Rico Mayaguez. (2003) 1–20.

[20] N. Gougoulias, A. Khanna, N. Maffulli, How successful are current ankle replacements?: A systematic review of the literature, Clin. Orthop. Relat. Res. 468 (2010) 199–208.

[21] S. Sivan, Y. Liu, S.B. Kocagöz, C.M. Arnholt, J.L. Gilbert, S.M. Kurtz, Direct in vivo inflammatory cell-induced corrosion of CoCrMo alloy orthopedic implant surfaces , J. Biomed. Mater. Res. Part A. 103 (2014) 211–223.

[22] J.M. Anderson, A. Rodriguez, D.T. Chang, Foreign body reaction to biomaterials, Semin. Immunol. 20 (2008) 86–100.

[23] B. AlMangour, Additive manufacturing of emerging materials, Springer, 2019.

[24] I. Gibson, D.W. Rosen, B. Stucker, Design for additive manufacturing, in: Addit. Manuf. Technol., Springer, 2010: pp. 299–332.

[25] T. Wohlers, 3D printing and additive manufacturing state of the industry, Annu. Worldw. Prog. Report. Wohlers Assoc. (2014).

[26] E.C. Santos, M. Shiomi, K. Osakada, T. Laoui, Rapid manufacturing of metal components by laser forming, Int. J. Mach. Tools Manuf. 46 (2006) 1459–1468.

[27] B. Vandenbroucke, J. Kruth, Selective laser melting of biocompatible metals for rapid manufacturing of medical parts, Rapid Prototyp. J. (2007).

[28] X. zhen Xin, J. Chen, N. Xiang, B. Wei, Surface Properties and Corrosion Behavior of Co-Cr Alloy Fabricated with Selective Laser Melting Technique, Cell Biochem. Biophys. 67 (2013) 983–990.

[29] Y.S. Hedberg, B. Qian, Z. Shen, S. Virtanen, I. Odnevall Wallinder, In vitro biocompatibility of CoCrMo dental alloys fabricated by selective laser melting, Dent. Mater. 30 (2014) 525–534.

[30] Y.S. Hedberg, B. Qian, Z. Shen, S. Virtanen, I. Odnevall Wallinder, In vitro biocompatibility of CoCrMo dental alloys fabricated by selective laser melting, Dent. Mater. 30 (2014) 525–534.

[31] M. Seyedi, F. Zanotto, C. Monticelli, A. Balbo, E. Liverani, A. Fortunato, Microstructural characterization and corrosion behaviour of SLM CoCrMo alloy in simulated body fluid, Metall. Ital. (2018).

[32] Y. Lu, S. Wu, Y. Gan, T. Huang, C. Yang, L. Junjie, J. Lin, Study on the microstructure, mechanical property and residual stress of SLM Inconel-718 alloy manufactured by differing island scanning strategy, Opt. Laser Technol. 75 (2015) 197–206.

[33] L. Zeng, N. Xiang, B. Wei, A comparison of corrosion resistance of cobalt-chromium-molybdenum metal ceramic alloy fabricated with selective laser melting and traditional processing, J. Prosthet. Dent. 112 (2014) 1217–1224.

[34] Y. Lu, S. Wu, Y. Gan, J. Li, C. Zhao, D. Zhuo, J. Lin, Investigation on the microstructure, mechanical property and corrosion behavior of the selective laser melted CoCrW alloy for dental application, Mater. Sci. Eng. C. 49 (2015) 517–525.


2

CHAPTER TWO

Background

This chapter comprises an introduction to metallic biomaterials, with a particular focus on CoCrMo biomedical alloys. The successive sections deal with the role of alloying elements on these alloys, describe the alloy microstructure, the more common thermal treatment, and the effect of various parameters on the electrochemical and corrosion behavior of CoCrMo metallic bioimplants alloys in human body fluids. The manufacturing techniques for the production of artifacts in CoCrMo alloys and particularly additive manufacturing techniques are finally reported.

2.1. Biomaterials

The term" Biomaterial" refers to any substrate (such as a system or part of a system) which can be successfully implanted in the human body for a period of time to improve the longevity and quality of human life. The most accepted definition of "biomaterial" is the one proposed by the American National Institute of Health [1]:

"*Any substance or combination of substances, other than drugs, synthetic or natural in origin, which can be used for any period of time, which augments or replaces partially or totally any tissue, organ or function of the body, in order to maintain or improve the quality of life of the individual*."

The use of biomaterials for the replacement of damaged tissues or organs is not new and was introduced for the first time as early as four millennia ago by Egyptians. They utilized wooden toe replacement, iron, and gold for dental use and linen for suture application with no scientific knowledge about the properties of these materials [2]. However, the advancements in the knowledge of these practices were systematized in the science of implantology in the late 18th century [3].

An appropriate selection of biomaterials is critically essential for the long-term reliability and durability of implants housed in the human body. Exposure to the aggressive body environment is a severe concern because it accelerates wear, corrosion, and degradation of implanted materials over the service time. Accordingly, understanding the properties of materials as well as the effects of environmental conditions and applying this knowledge to the materials selection and bioimplant design is crucial for reducing the chance of implant failure, controlling maintenance time, and increasing the patient's satisfaction. Figure 2.1 illustrates the major applications of biomaterials in the human body.

There are several requirements for biomaterials to be accepted in the human body, affecting the reliability and lifetime of bioimplants:

i. ***Biocompatibility –*** Biocompatibility is the first and foremost requirement for the selection of biomaterials representing the ability of a material to perform its intended functions for a specific application with an appropriate host response [4]. A standard definition of biocompatibility is:

"The *ability of a biomaterial to perform its desired function with respect to a medical therapy, without eliciting any undesirable local or systemic effects in the recipient or beneficiary of that therapy, but generating the most appropriate beneficial cellular or tissue response in that specific situation, and optimizing the clinically relevant performance of that therapy*" [5].

Since the living organism identifies the embedded material as a foreign matter, biomaterials require the characteristics of biocompatibility. Given this, a proper biomaterial should not trigger rejection reactions, and the amounts of eluted substances from these materials should be scarce and harmless. Biocompatibility is a fundamental factor for selecting biomaterial alloys, and the corrosion resistance of metal implants in the body fluids is closely related to this property.

ii. ***Corrosion and wear resistance –*** Since the bio-fluid is a quite corrosive environment, where proteins, inflammatory agents, and loading conditions increase the environment aggressiveness, excellent corrosion and wear properties of biomaterials are of great importance. Actually, corrosion and wear cause several problems during implant service lives, such as adverse reactions [6], malfunctions of the corroded or worn implants [7], and in some cases, even local tumors generated by the accumulation of corrosion and wear products [8]. Given this, the corrosion rate and amount of debris generated at the contact region between embedded materials and corrosive body fluid should be small.

iii. ***Mechanical strength –*** Bioimplants, especially hip, and knee joints, have to bear the patient's body weight and are often subjected to periodical stress and cyclic loading. Therefore, proper mechanical properties and, in particular, high fatigue strength are important factors to be considered in biomaterial selection [9]. As far as practical applications are concerned, the mechanical properties of biomaterials, such as strength, elongation to fracture, fracture toughness, Young's modulus,

wear properties, fatigue and fretting fatigue properties and the corrosion behavior under static stress are all critical factors [10].

Consequently, considering all the above-mentioned criteria, the total number of appropriate materials for medical device applications is quite limited. Metallic materials as biomaterials are getting more and more promising for biomedical applications, mostly when high biocompatibility and corrosion, wear and fatigue resistance are required [4,11]. Despite the availability of many types of metallic materials, only a few of them are biologically compatible with the human body and can be used for long-term applications. At present, the most important 'biometals' include stainless steels, cobalt-based alloys, and titanium alloys. Stainless steel was firstly introduced in biological orthopedics in the 1930s, when Wiles [12,13] attained the total hip replacement. However, stainless steel is now mainly being used in short-term implant devices due to low corrosion resistance and fatigue strength [14–17].

As an alternative, Titanium alloys were admitted for long-term metallic bioimplants due to their remarkable characteristics like good corrosion resistance, high strength, toughness, and lightweight. They attracted great demand since the 1970s, and the upward trend of employing them as bioimplant materials is likely to continue, even if their low wear resistance is recognized as a major clinical issue [2,18].

Since the toxicity of nickel ions in metallic materials such as stainless steels and Ni-Ti alloys is still an unresolved issue, CoCr alloys have been intentionally investigated as biomaterials. CoCr alloys meet the demands of different applications in the field of bioimplants due to their good biocompatibility, suitable wear and corrosion resistance, and proper mechanical strength [18–20].

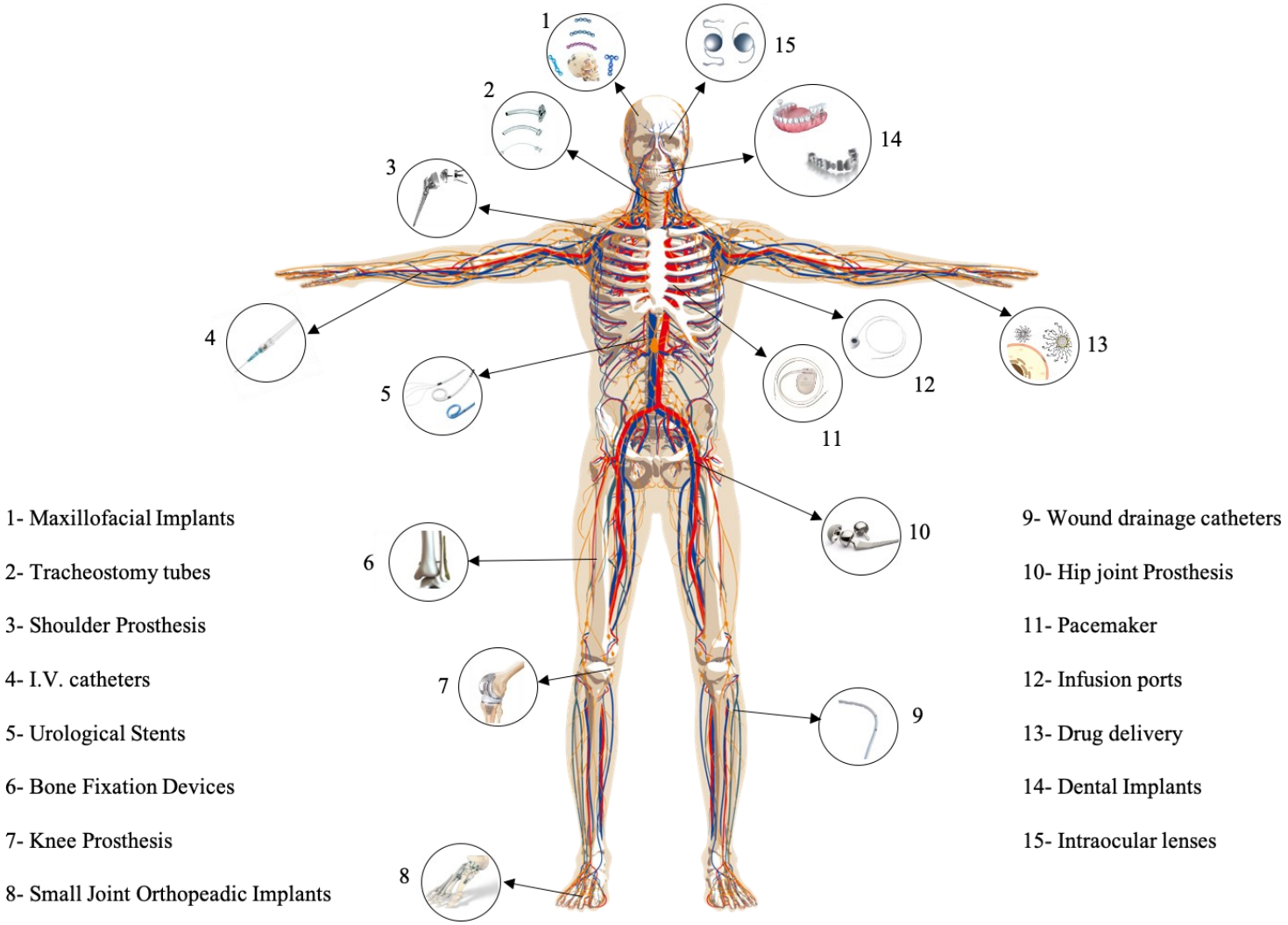

Figure 2.1. Major applications of biomaterials in the human body. Reprinted and modified from [21].

2.1.1. Stainless steel alloys

The earliest metal implant, introduced in the early 1900s, was made of vanadium steel [22]. Vanadium steel surgical implants suffer from premature loss of implant function, patient dissatisfaction, and require revision surgery because of mechanical and corrosion failure; thus, the medical use of vanadium steel has been discontinued. As a consequence, stainless steel alloys with better mechanical and corrosion behavior were introduced. 302 stainless steel alloy was initially developed as an alternative to vanadium steel. This was subsequently replaced by two other stainless steel alloys, 316 and 316 L (L; designates low carbon content), containing molybdenum [23]. Molybdenum-containing stainless steel alloys were developed to improve their corrosion resistance. These alloys contain at least 16-18 % chromium. Therefore, the formation of a protective Cr-based oxide film on the alloy surface occurs spontaneously in the body environment, so conferring corrosion and wear resistance to the fabricated implant [22,24]. The presence of 8-10 % nickel helps to stabilize the austenitic phase at room temperature and increases the alloy corrosion resistance [25].

Nevertheless, the existence of these large amounts of Ni can provoke an allergic reaction in patients, which require revision surgery for the implant retrieval and substitution [11]. These alloys are also susceptible to pitting corrosion and stress corrosion cracking, because they tend to form deep pits on the metal surface from which crack propagation may start [26]. Thus, in summary, the primary limiting factors in the clinical use of stainless steels are the reported Ni toxicity to the host organism and the vulnerability of the alloy to pit and crevice corrosion and to stress-corrosion cracking [27–29]. It is not surprising then that the modern application of stainless steels is now mainly limited to temporary and short-term biomedical devices that are not subjected to large loads for a long time, like plates and screws [14–17]. However, it was found that surface modifications such as plasma-assisted low-temperature nitriding, carburizing, and carbonitriding can potentially enhance the corrosion resistance of stainless steel-based devices to ensure good long-term performances [29].

2.1.2. Titanium and its alloys

The first attempts to implant Ti-based biomaterials go back to the 1930s, when it was observed that similarly to stainless steel and CoCrMo, Ti was sufficiently accepted by the femoral bone tissues in felines. Titanium alloys are now considered suitable for biomedical applications due to desirable characteristics, such as lightweight, high strength, good corrosion resistance, and biocompatibility [30,31]. A further important factor contributing to determine this favourable behaviour is represented by their Young's modulus (110 GPa), much lower than that of stainless steels (around 190 GPa). An even lower Young's modulus would be desirable for orthopedic implants because materials with Young's moduli exceeding those of natural bone (10-30 GPa) cause stress-shielding and subsequently bone resorption, which finally results in implant loosening [32–34]. Another advantage of titanium alloy consists in their relatively low density, about 4.5 gr/cm^3, that is only slightly higher than one half of those of stainless steels and CoCr alloys [35]. There are other beneficial aspects of titanium alloys. In fact, titanium alloys are resistant to in vivo corrosion, pitting attack, and crevice corrosion [36,37]. Since titanium does not enter the body chemistry as readily as other implant materials, healing is relatively unimpeded, and the life span of the implant is significantly extended. However, problems still exist in titanium and titanium alloy application as biomaterials because the strength of pure titanium is low, whereas Ti-6Al-4V characterized by good mechanical strength contains vanadium and aluminum that are harmful to the human body [31,34,37].

Overall, commercially pure titanium (CP-Ti) and Ti-6Al-4V are the preferred materials for manufacturing orthopedic implants, but titanium alloys with lower Young's moduli, composed of non-toxic and allergy-free elements, have been recently introduced such as Ti-12Mo-6Zr-2Fe, Ti-15Mo-5Zr-3Al, Ti-15Mo, To-13Nb-13Zr and etc. [10].

The excellent corrosion resistance of titanium alloys is strictly related to the formation and persistence of a thin, stable surface oxide film [36–38], which is easily abraded under tribological contact conditions, due to the low alloy wear resistance. For this reason, these alloys cannot be used without proper surface treatments and coatings [39,40].

2.1.3. Cobalt Chromium Molybdenum (CoCrMo) alloys

Cobalt-based alloys like Cobalt Chromium Molybdenum (CoCrMo) are worldwide among the most widely used biomaterials due to their excellent corrosion and wear resistance, good mechanical properties, and satisfactory biocompatibility. They particularly offer excellent wear properties compared to other metallic biomaterials like stainless steel and Ti alloys [41–45]. It is reported that the first application of Co-based alloys in the biomedical field was in 1936 for hip arthroplasty [46].

The good biocompatibility of Co-based alloys is closely linked to their outstanding corrosion resistance, which is in turn connected to their excellent passivation ability [11,47]. Numerous researchers have revealed that the oxide layer is mostly composed of Cr-oxide, Cr-oxyhydroxide, and minor amounts of Co- and Mo-oxides [48–51].

Moreover, it is empirically proven that the presence of microstructural heterogeneities such as precipitated carbides, secondary phases, and grain boundaries may have a significant effect on the corrosion behavior by initiation and propagation of localized corrosion/dissolution in corrosive environments [52].

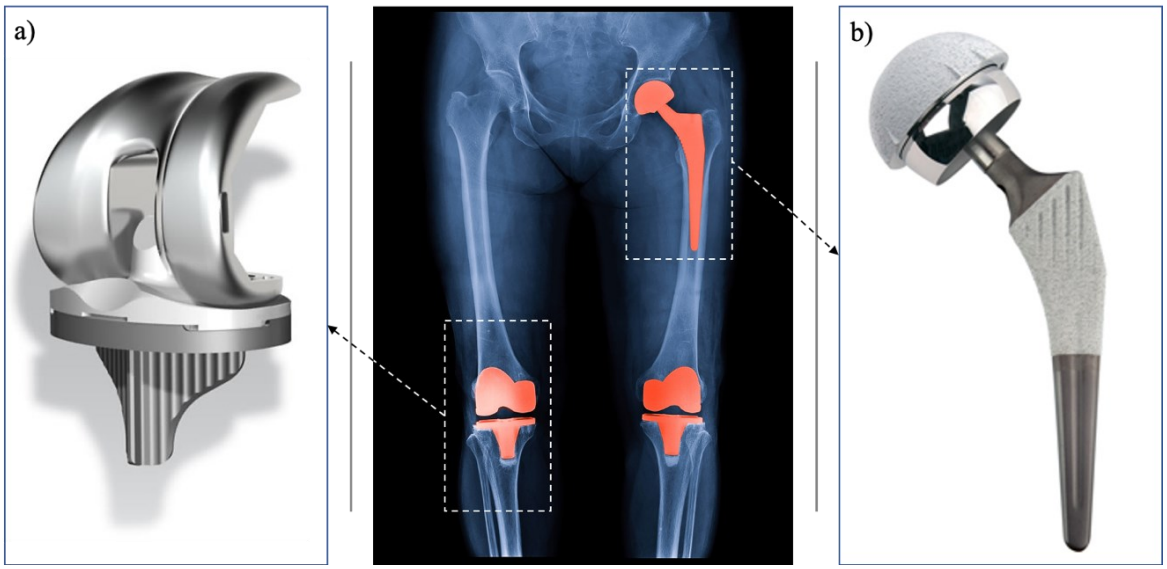

Figure 2.2. Examples of total joint replacements made in CoCrMo alloys: a) Knee prosthesis; b) Hip joint prosthesis [53]**.**

Figure 2.2 shows hip and knee artificial joints made of CrCrMo alloys.

Cobalt has two crystallographic structures: Face-Centered Cubic (FCC) and Hexagonal Closed-Packed (HCP), presented in Figure 2.3. Upon cooling from high temperatures, pure cobalt undergoes an allotropic transformation from unstable FCC structure (known

as γ-phase) to the thermodynamically stable HCP structure (known as ε-phase) in the vicinity of 690 K (~417 ℃) [54,55]. Actually, most cobalt-based alloys exhibit a metastable FCC matrix structure at room temperature, because the kinetics of metastable FCC to stable HCP structure transformation is quite sluggish and does not occur at a significant extent under normal cooling rates [56].

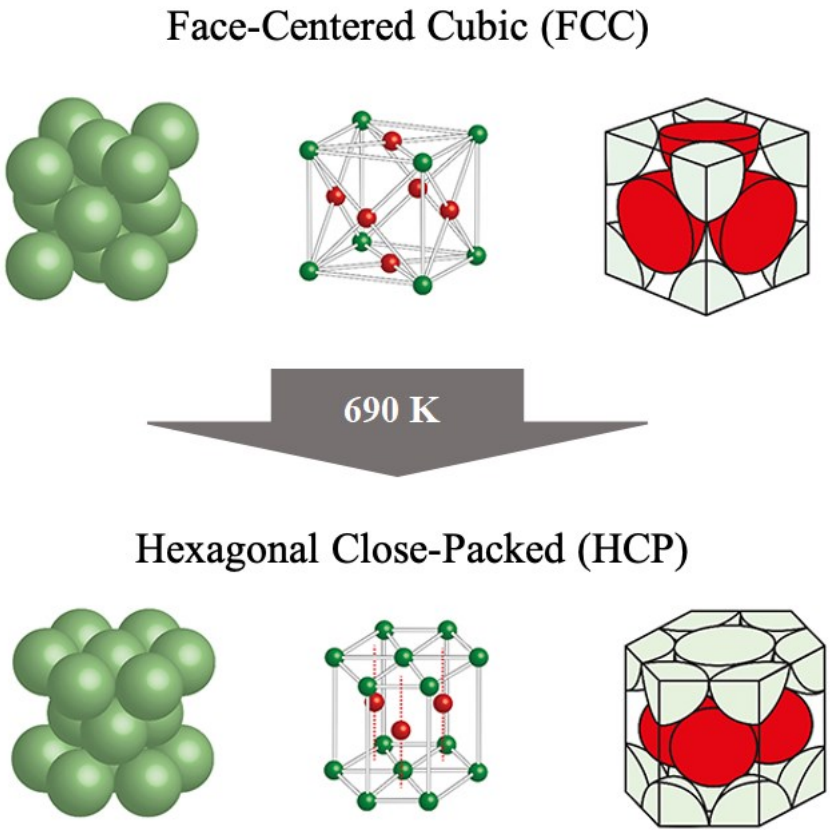

Figure 2.3. Crystal Structure representation of HCP and FCC [54,55].

The extent of transformation into the stable HCP phase depends on several factors, like the nature and amount of alloying elements and the type of thermal treatments during material production. Accordingly, the addition of alloying elements to pure cobalt changes this transformation temperature. Considering the CoCr binary phase diagram shown in Figure 2.4 [57], there is a clear trend of increasing the transformation temperature by chromium addition. For instance, the transformation temperatures for two different CoCr alloys containing 20 and 30 wt% Cr are around 110 K (827°C) and 1200 K (927°C), respectively.

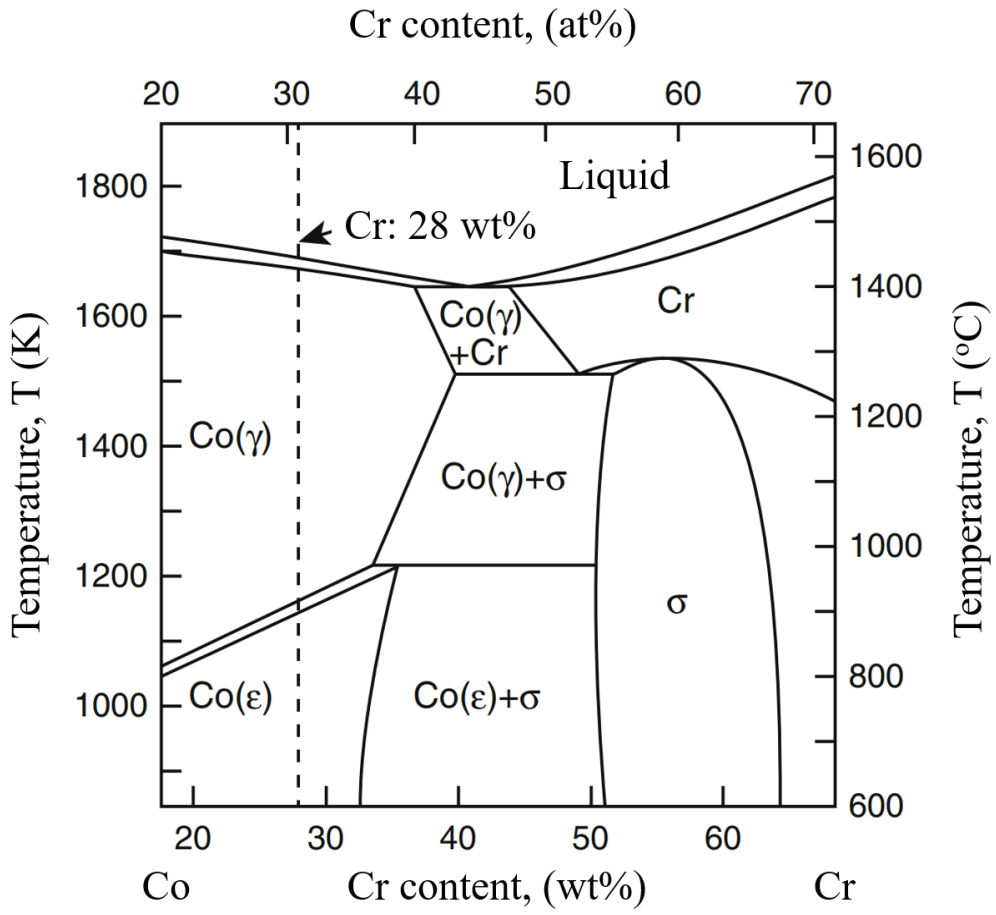

Figure 2.4. The binary phase diagram of CoCr system [57].

The effect of different alloying elements on the transformation temperature of HCP phase to FCC phase of Co alloys is summarized in Figure 2.5. The change in the transformation temperature of HCP to FCC phase from that for pure Co per 1 at% of the alloying element is given on the horizontal axis, and the alloying element's solubility in FCC-Co is drawn in the vertical axis. Alloying elements like nickel, iron, and carbon (within the soluble range) are known as FCC stabilizers and reduce the HCP-to-FCC transformation temperature. In parallel, chromium, tungsten, silicon, and molybdenum are recognized as HCP stabilizers and have the opposite effect on the transformation temperature [55].

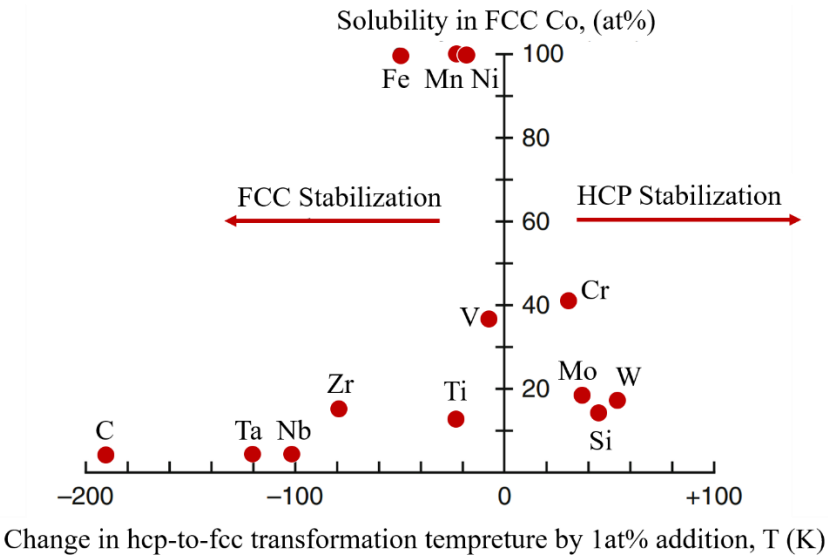

Figure 2.5. Effects of alloying elements (by addition of 1 at%) on the transformation temperature of the HCP-Co to FCC-Co as a function of element's solubility in FCC-Co [55].

2.2. CoCrMo alloys for biomedical application

The chemical composition of different types of CoCrMo alloys used for biomedical applications is shown in the Table 2.1. The ASTM F75 standard refers to casting alloys, while other codes indicate wrought alloys [58]. The physico-chemical properties of the cast and wrought CoCr alloys differ significantly. The process of casting can result in larger grain sizes, pronounced boundary segregation, holes, and shrinkage cavities within the bulk material. Wrought alloys are characterized by higher fracture toughness and fatigue strength, essential for their large load-bearing applications. Although both cast and wrought alloys display corrosion stability, the former type is preferred when hardness and resistance to wear is required [59].

Processability of cast alloys is enhanced by the presence of Ni; however, the element level is closely monitored due to its reported toxicity [60,61]. Introduction of some amounts of C (~0.25 wt%) notably improves castability by decreasing the melting point of the alloy by approximately 100 °C [62].

Table 2.1. Chemical compositions (wt%) of biomedical CoCr alloys, based on American Society for Testing and Materials (ASTM) standards [63,64]**.**

ASTM	Type		Chemical composition (wt%)															
			Cr	**Mo**	**Ni**	**Fe**	**c**	**Si**	**Mn**	**W**	**P**	**S**	**N**	**Al**	**Ti**	**B**	**La**	**Be**	**Co**
F75-12	**Casting**		27.0-30.0	5.0-7.0	<0.50	<0.75	<0.35	<1.0	<1.0	<0.20	<0.020	<0.010	<0.25	<0.10	<0.10	<0.010	-	-	Bal.
F799-11	**Forging**	**Low carbon**	26.0-30.0	5.0-7.0	<1.0	<0.75	<0.14	<1.0	<1.0	-	-	-	<0.25	-	-	-	-	-	Bal.
F1537-11	**Wrought**	**High carbon**	26.0-30.0	5.0-7.0	<1.0	<0.75	0.15 - 0.35	<1.0	<1.0	-	-	-	<0.25	-	-	-	-	-	Bal.
		Dispersion strengthened	26.0-30.0	5.0-7.0	<1.0	<0.75	<0.14	<1.0	<1.0	-	-	-	<0.25	0.30-1.0	-	-	0.03-0.20	-	Bal.
F90-09	**Wrought**		19.0-21.0	-	9.0 - 11.0	<3.0	0.50 - 0.10	<0.40	1.0 - 2.0	14.0-16.0	<0.040	<0.030	-	-	-	-	-	-	Bal.
F1091-12	**Wrought (wire)**																		Bal.
F56-13	**Wrought**		19.0-21.0	9.0-10.5	33.0-37.0	<1.0	<0.025	<0.15	<0.15	-	<0.015	<0.010	-	-	<1.0	<0.015	-	-	Bal.
F68-10	**Wrought (plate, sheet, and foil)**																		
F96-08	**Forgings**																		
F1058-08	**Wrought (wire and strip)**	**Grade 1**	19.0-21.0	6.0-8.0	14.0-16.0	Bal.	<0.15	<1.20	1.5 - 2.5	-	<0.015	<0.015	-	-	-	-	-	< 0.10	39.0-41.0
		Grade 2	18.5-21.5	6.5-7.5	15.0-18.0	Bal.	<0.15	<1.20	1.0 - 2.0	-	<0.015	<0.015	-	-	-	-	-	< 0.001	39.0-42.0

2.2.1. Role of alloying elements

Cobalt, chromium, and molybdenum are the fundamental elements of Co-based prosthetic alloys. Traditionally, Elwood Haynes figured out the stainless nature and excellent mechanical properties of the binary cobalt-chromium alloy (patented by Elwood Haynes in 1907). Later, tungsten and molybdenum were identified as powerful strengthening agents within the cobalt-chromium system. These alloys were also widely used in high-temperature industries where wear and corrosion resistance at high temperatures were required. Of the corrosion resistant alloys, a CoCrMo alloy with a moderately low carbon content was developed to satisfy the need for a suitable investment-cast dental material. This biocompatible material is still in use today predominantly as an alloy for surgical implants.

Cobalt (Co) **–** The alloy is mainly composed of cobalt (~ 60 wt%), which conveys a room temperature unstable FCC crystalline structure with very low stacking fault energy. As mentioned before, this FCC structure may transform to HCP on cooling at about 417 °C if very slow cooling rates are applied. Under normal cooling rates, the FCC structure in cobalt alloys is retained down to room temperature and HCP formation is only triggered by mechanical stress or time persistence at elevated temperatures. The FCC structure and its associated low stacking fault energy are believed to induce some properties to these alloys like high yield strengths, high work hardening rates, limited fatigue damage under cyclic stresses and ability to absorb stresses. These characteristics are of importance if an improvement of wear and erosion-corrosion properties are needed [54].

Chromium (Cr) **–** Chromium is the second main element of CoCrMo alloys (27-30 wt%), with a dual function in the alloys. First, it is the element that mostly contributes to induce passivity in the alloy by the formation of a highly protective chromium-rich passive layer (mainly constituted by Cr_2O_3). This passive layer acts as a barrier between the metal and the aggressive environment and provides

high corrosion resistance in a wide range of potentials [65]. Furthermore, chromium is the most effective carbide former and, consequently, a grain-refining element, increasing the material hardness, and the mechanical strength [54]. The most common carbide in the CoCr alloys is a chromium-rich M_7C_3 type, although also chromium-rich $M_{23}C_6$ carbides are abundant in low-carbon alloys.

Molybdenum (Mo) **–** Typically, 5-7wt% Mo is added to Co-based alloys to increase the biodegradation resistance and to improve the mechanical properties by solid-solution strengthening and by grain growth refining. These latter properties are ensured by Mo solute atoms that due to their large atomic radius hinder the dislocation sliding [54] and by the precipitation of M_6C carbides (at Mo concentrations higher than ca. 5 wt%) that hamper the grain boundary motion [66].

Carbon (C) **–** Depending on the carbon content, CoCrMo alloys can be named "low carbon" and "high carbon", containing 0.06 wt% and 0.15-0.25 wt% of carbon, respectively. Carbon additions to Co-based alloys have been shown to favor the formation of carbides, which enhance wear resistance. As already reported, an increase in carbon content led to a significantly higher volume fraction of carbides, mostly in the form of M_7C_3 and $M_{23}C_6$, whereas M_6C is observed in alloys containing Mo in the range of 5-7 wt%. Generally, carbides in CoCrMo alloys have the ability to increase hardness and strength [67].

2.2.2. Application of CoCrMo alloys in biomedical fields

Based on the previously described fundamental characteristics of CoCrMo alloys, some of their current applications are summarized in table 2.2. The ASTM F75 alloy (Cast Co-28Cr-6Mo) has been used to fabricate the stem, ball, and cup of artificial hip joints as well as sliding components for knee joint implants. Wrought alloys such as ASTM F799 and F1537 have been qualified to be used in joint replacements for the hip, knee, shoulders, etc. The other wrought CoCr systems like ASTM F90/F1091 (CoCrWNi), ASTM F 562 (CoNiCrMo), and ASTM F 1058 (CoCrFeNiMo), which exhibit excellent hot and cold workability, have been used in fixation wires, vascular stents, springs, catheters, surgical clips, and orthodontic dental archwires.

Table 2.2. Applications of Co-Cr alloys in biomedical fields [1,11,23,68]**.**

ASTM standard	Alloy composition (wt%)	Trade name	Application
F 75-12	Co-28Cr-6Mo	Vitallium (Howmedica, Inc); Haynes-Stellite 21(HS21) (Cabot Corp.); Protasul-2 (Sulzer AG); Zimaloy (Zimmer Inc.).	Stem, ball, and cup of artificial joints; Fixation screws; Bone plates.
F 799-11 F 1537-11	Co-28Cr-6Mo	BioDur CCM Plus Alloy (Carpenter Technology Corp.)	Joint replacements (hip, knee, shoulder); Fixation devices.
F 90-09 F 1091-12	Co-20Cr-15W-10Ni	Haynes-Stellite 25 (HS25) (Cabot Corp.) L-605 (Carpenter Technology Corp.)	Fixation wires; Vascular stents; Heart valves.
F 562-13 F 688-10 F 961-08	Co-5Ni-20Cr-10Mo	MP35N (SPS Technologies, Inc.) Biophase (Richards Medical Co.) Protasul-10 (Sulzer AG)	Lead conductor wires; Springs; Stylets; Catheters; Orthopedic cables; Cardiovascular stents..
F 1058-08	40Co-20Cr-16Fe-15Ni-7Mo	Elgiloy (Elgiloy Ltd.) Phynox (Arcelor Mittal Stainless & Nickel Alloys) Conichrome (Carpenter Technology Corp.)	Arch wires; Springs; Lead conductor wires; Surgical clips; Balloon-expanable stents (annealed); Self-expanding stents (aged).

2.2.3. Microstructure and processing of CoCrMo alloys

2.2.3.1. Precipitates

Precipitates in CoCr alloys are known to have a direct effect on the mechanical properties [69,70], and on corrosion [71–73], and wear [74–78] resistances of both cast and wrought parts. Considering this, the final microstructure of these alloys (as-cast and after heat treatment) is of great importance for establishing reasonable production processes for biomedical CoCr alloy devices. The precipitates in CoCr alloys are generally classified into two types: intermetallic compounds and carbides/carbonitrides [79]. Therefore, the phase and morphology of the precipitates are significantly affected by the carbon and nitrogen contents.

Figure 2.6 provides the typical morphology of the precipitates found in CoCrMo alloys [79], which are listed as follows and described thereafter:

i. Blocky-dense features such as σ-phase [80] and χ-phase [79,81] (which are Cr- and Mo-rich intermetallics), $M_{23}X_6$ and, η-phase (M_6X-$M_{12}X$-type compounds, [82]), where M = metallic elements; X = C and/or N
ii. Star-like-dense morphologies such as π-phase [83] (a carbon-rich carbonitride)
iii. Star-like morphologies with striped patterns, containing $M_{23}X_6$-type compounds
iv. Star-like morphologies with complicated microstructures, including M_7X_3-type compounds
v. Lamellar cellular colony morphologies, for instance, M_2X-type compounds.

The σ-phase is a CrCo type intermetallic compound with a topologically closed-packed structure, found in low carbon alloys [84,85]. The χ-phase phase is an intermetallic component and has an α-Mn structure with 58 metallic atoms in the unit cell [86,87].

The $M_{23}X_6$-type phase has a complex cubic structure with 96 M and 24 X atoms in its unit cell [88]. The M_6X-type and $M_{12}X$-type phases have similar crystallographic structures and both types are classified as η-phase which is a carbon-rich carbonitride [89,90]. Both $M_{23}X_6$-type ($Cr_{23}C_6$-type) and M_2X-type phases are markedly Cr-enriched, while the η-phase precipitates are Mo-enriched. The π-phase is a carbon-rich carbonitride which exhibits a β-Mn structure, and its chemical composition can be ideally represented

as M_2T_3X, where M and T are metallic elements with a low and high affinity for X (carbon and/or nitrogen), respectively.

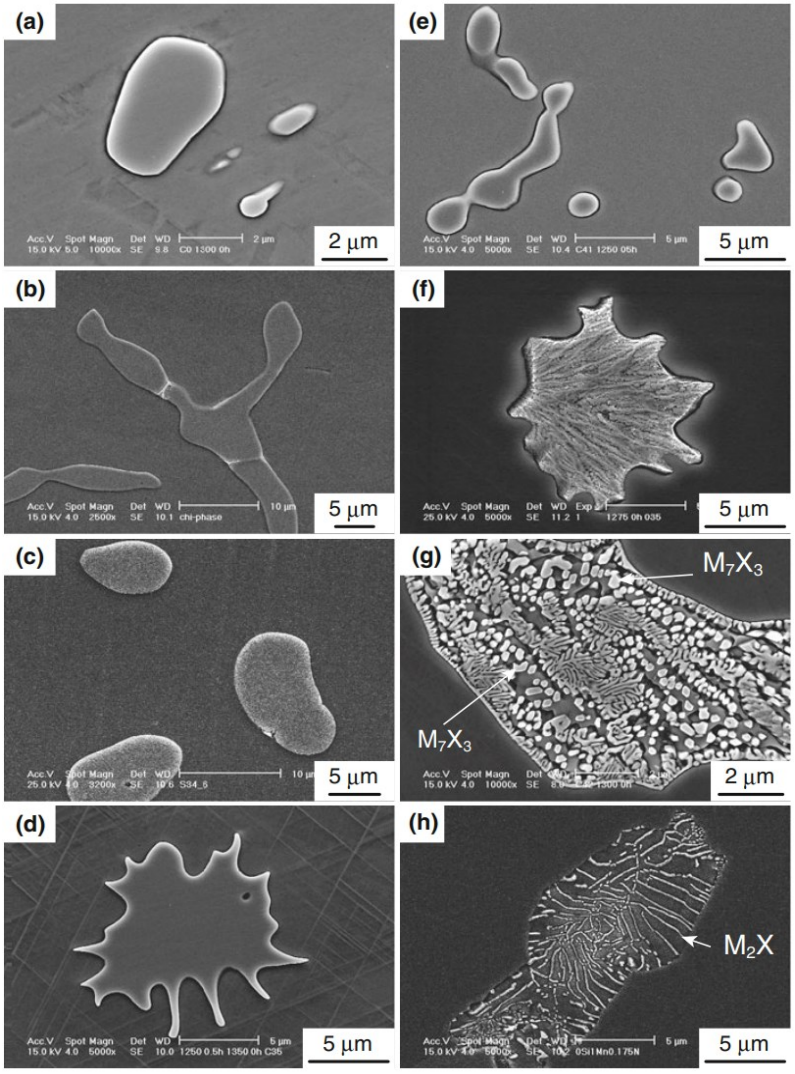

Figure 2.6. Morphologies and phases of precipitates observed in biomedical Co-Cr-Mo alloys: (a) σ-phase (blocky dense), (b) χ-phase (blocky dense), (c) η-phase (blocky dense), (d) π-phase (star-like dense), (e) $M_{23}X_6$ type (blocky dense), (f) $M_{23}X_6$ type, (g) M_7X_3 type (starlike with complicated microstructures), and (h) M_2X type (lamellar cellular colony) [79]**.**

It is reported by Clemow and Daniell [91] that the formation of the star-like features is due to the initial melting around the edge of the carbide particles. It is also stated that the $M_{23}X_6$- type precipitates include little nitrogen and are mostly carbides [79]. The M_2X type precipitates are categorized as nitrogen-rich carbonitrides that occur in nitrogen-containing CoCrMo alloys.

Kilner et al. [92] were the first researchers to suggest the formation of M_7X_3-type precipitates in the Co-Cr-Mo alloys, which was then confirmed by the other groups [83]. However, their chemical composition has not yet been clarified because they are too small for analysis (Figure 2.6g).

The stabilization of these precipitates is affected by alloying elements, by way of example: carbon stabilizes the $M_{23}X_6$-type, and M_7X_3-type precipitates [83], the M_2X-type and η-phase precipitates are stabilized by nitrogen, while Si stabilizes the η-phase [93] and χ-phase [79] precipitates. Giacchi et al. [94] confirmed that the microstructure of CoCrMo alloys in as-cast condition (ASTM F75) was mainly constituted by dendritic fcc-Co matrix and carbides precipitated at the grain boundaries and interdendritic spaces. The primary precipitates in as-cast alloys showed a pearlitic structure formed by thin interlayed plates of σ-phase and $M_{23}C_6$ carbides in accordance with Kilner [92]. They suggested that the initial "pearlitic" colonies dissolved in the first 15 minutes of solution treatment. Given this, after long-term solution treatments these structures were no more observed. Moreover, during these heat treatments, the $M_{23}C_6$ carbide suffered a spheroidization and transformed according to the $M_{23}C_6 \rightarrow M_6C$ reaction. These results are consistent with Clemow and Daniell [91], Lane [95], and Mancha et al. [96], who established that carbide decomposition occurred through a solid-state reaction. Besides, after prolonged solution-treatments, the alloy exhibited recrystallization and carbide decomposition with a decrease in the carbide size [94].

Besides, it is confirmed that the formation of the π-phase is connected to the partial melting taking place at temperatures of 1275–1350 °C. The formation of the π-phase after heat treatment of the Co-28Cr-6Mo alloys was observed at all carbon levels allowed by ASTM F 75 standard ($C \leq 0.35$ wt%), but more frequently with C around 0.15 wt%. The presence of a π-phase precipitate in the alloys at room temperature is dependent on the cooling rate from high temperature. Rapid cooling from high temperatures allows the π-phase retention in the alloys, while lower cooling rates seem to cause the π-phase transformation into other phases such as the $M_{23}X_6$-type + metallic fcc γ-phase [83–85,99]. Table 2.3 summarized the chemical compositions of precipitates in biomedical CoCrMo Alloys reported thus far [60,73,75,76,82,83,91,92,96–110].

Table 2.3. Chemical compositions of precipitates in biomedical Co-Cr-Mo alloys, reprinted from [79].

Phase	Alloy (mass pct) (Heat-Treatment Conditions)	Co (at. pct)	Cr (at. pct)	Mo (at. pct)	C (at. pct)	N (at. pct)	Si (at. pct)	Mn (at. pct)
σ-phase	Co-27.5Cr-5.32Mo (1448 K, 0 ks)		Co:Cr:Mo = 47.6:41.1:11.2 (atomic ratio) (C content: not measured)					
	Co-28Cr-6Mo-0.25C (Hot isostatic pressing after casting)		Co:Cr:Mo = 44:44:12 (atomic ratio) (C content: not measured)					
$M_{23}X_6$ type	Co-27.96Cr-6.09Mo-0.26C-0.98Si-1.02Mn (1448 K, 1.8 ks)	12.6	58.6	6.0	22.1	–	0.2	0.6
	Co-28Cr-6.3Mo-0.2C-0.5Mn-0.2Fe-0.2Ni (casting + high isostatic pressing + heat treatment)		Co:Cr:Mo = 15:76:9 (atomic ratio) (C content: not measured)					
	Co-27.67Cr-6.01Mo-0.24C-0.17N-1.19Si-1.15Mn (1448 K, 0 ks)	12.7	60.3	5.2	21.7	N.D.	N.D.	0.1
	Co-29.7Cr-6.64Mo-0.27C-0.15N (1473 K, 43.2 ks)	14.6	61.6	5.5	17.5	0.8	–	–
η-phase	Co-28Cr-6.3Mo-0.2C-0.5Mn-0.2Fe-0.2Ni (casting + high isostatic pressing + heat treatment)		Co:Cr:Mo:Si = 33:30:29:8 (atomic ratio) (C content: not measured)					
	Co-27.90Cr-6.17Mo-0.25C-0.15N-1.21Si (1523 K, 1.8 ks)	31.1	23.4	22.7	10.8	4.0	8.0	–
	Co-28.05Cr-6.01Mo-0.22C-2.6Si (1498 K, 43.2 ks)	29.4	23.5	22.6	13.1	–	11.4	–
M_2X type	Co-28.5Cr-6.40Mo-0.27C-0.24N (1473 K, 43.2 ks)	3.7	62.9	5.5	12.7	15.2	–	–
π-phase	Co-27.96Cr-6.09Mo-0.26C-0.98Si-1.02Mn (1548 K, 1.8 ks)	33.4	40.2	11.1	12.1	–	2.3	0.9
	Co-27.67Cr-6.01Mo-0.24C-0.17N-1.19Si-1.15Mn (1548 K, 0 ks)	31.0	38.9	12.0	11.9	2.7	2.5	1.1
	Co-28.4Cr-5.93Mo-0.33C Intragranular (1623 K, 43.2 ks)	30.8	43.7	11.2	14.3	–	–	–
	Co-28.4Cr-5.93Mo-0.33C Grain boundary (1623 K, 43.2 ks)	38.0	41.0	9.6	11.4	–	–	–
	Co-27.6Cr-6.23Mo-0.34C-0.21N (1573 K, 0 ks)	35.8	42.4	10.1	8.5	3.3	–	–
χ-phase	Co-27.06Cr-5.61Mo-0.13C-1.33Si (1523 K, 0 ks)	48.5	34.6	12.7	N.D.	–	4.3	–
M_7X_3 type	Co-28.4Cr-6.00Mo-0.41C (as cast)		Co:Cr:Mo = 26.0:65.8:8.2 (atomic ratio) (C content: not measured)					

N.D.: not detected

2.2.3.2. Grain refinement

Grain refinement has been used to strengthen metallic materials while maintaining their ductility. It is well known that ultrafine grains smaller than 1 μm have been achieved by severe plastic deformation. However, the dual-phase microstructure of CoCrMo alloys and the strain-induced γ→ε martensitic transformation during plastic deformation restricted the application of severe plastic deformation techniques for these alloys [111]. It is reported that the conventional hot-compression deformation [111] and reverse transformation [111,112] techniques are the main methods used for grain refinement of CoCrMo alloys. An ultrafine-grained microstructure with a grain size of around 0.6 μm was obtained by Yamanaka et al. [113], who applied the conventional hot-compression deformation on the Co-29Cr-6Mo alloy with low carbon and low nitrogen contents. This microstructure was produced from an initial average grain size of 40 μm under dynamic recrystallization at 1323 K using a strain rate of 0.1 s^{-1}. It was recommended that the formation of this fine microstructure is attributed to the inhomogeneity in the local strain distribution induced by planar slips and deformation twins due to the lower stacking fault energy (SFE) of this alloy at elevated temperatures [113]. It was found that Co-29Cr-6Mo alloy with an average grain size of 0.8 μm produced by hot-compression deformation showed a significantly high 0.2% yield strength of 1330 MPa [114]. In another study, Kurosu et al. [112] developed a grain refinement process for the Co-27Cr-5Mo-0.16N alloy on the basis of reverse transformation from a lamellar (hcp ε-phase + Cr_2N) phase to an fcc γ-phase. They used a two-step heat treatment without a hot or cold plastic transformation: applying isothermal aging at 1073 K for 90 s to the solution-treated alloy to form a lamellar structure composed of the hcp ε-phase + Cr_2N; followed by reverse-treatment at a temperature of 1273–1473 K. The ε-phase and γ-phase are stable at a temperature of 1073 K and 1273–1473 K, respectively. They reported that the initial grains with an average size of 200 μm transformed into the grains with a finer size of 20–25 μm. The stress-strain curves of the Co-27Cr-5Mo-0.16N alloys after solution treatment (ST), aging treatment (AT), and reverse treatment (RT) at 1273 K for 300 s are shown in Figure 2.7. As can be seen from the graphs, the reverse transformation improved the tensile strength, while the ductility remained almost the same.

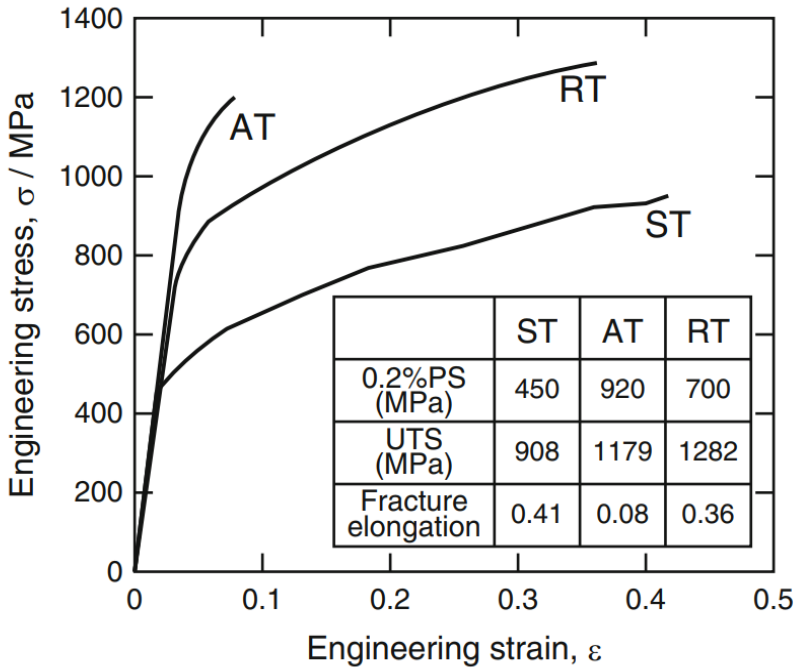

Figure 2.7. Typical stress-strain curves of the Co-27Cr-5Mo-0.16N alloys after solution treatment (ST), aging treatment (AT), and reverse transformation (RT) at 1273 K for 300 s. Mechanical properties for each specimen are reported in an inset table in the figure [112]**.**

2.2.3.3. Heat Treatment (HT)

For the manufacturing of CoCrMo orthopedic implants, thermal treatments of the base materials are needed in order to improve their physico-chemical and mechanical properties. These treatments modify the alloy microstructure and change the amount of defects (porosity and lack of homogeneity) and consequently the material properties may alter. Main metallurgical modifications produced by high temperatures sintering cycles consist of dissolution of interdendritic carbides, massive precipitation of lamellar carbide eutectic phases at grain boundaries, localized porosity formation from incipient melting (not entirely eliminated by following hot isostatic pressing treatments) and grain boundaries in fine-grained materials [50]. It is well known that the microstructure of CoCrMo alloys and the resulting properties strongly depend on the fabrication process (e.g., casting or forging), degree of cold-working, and heat treatments [115–118].

Cawley et al. [115] showed that the as-cast microstructural condition with the highest carbide volume has the lowest wear, and they also found a correlation between carbide volume fraction and wear-rate, with the highest carbide volume fraction giving the lowest wear-rate. Clemow and Daniell [91] examined the influence of time and temperature of solution treatment on the metallurgical behavior of CoCrMo alloy and proposed a

reduction in the carbon content of the alloy in order to improve this solution treatment behavior.

Vander Sande [119] studied the strengthening mechanism of cast CoCrMo alloys after heat treatment at 1230℃ and aging at 650℃, and that of low carbon wrought CoCrMo alloys heat-treated at 650℃ and 750℃, through TEM observation. They demonstrated that aging promoted the fcc stacking fault formation and induced an initial fcc-to-hcp martensitic transformation. Precipitates were found in hcp regions of cast-CoCrMo alloys after 20 h at 650 ℃ and in hcp areas of the wrought alloy after 20 h at 750 ℃. Aging at 750 ℃ for a prolonged time resulted in the transformation into hcp structure, with a relatively fault-free structure in the wrought alloy. They suggested that the principal strengthening mechanism activated by aging was the interruption of fcc slip by formation of both fcc stacking faults and bands of hcp phase. Precipitate's formation in the hcp phase was found to play a primary role at increasing aging times.

In an analysis of the influence of compaction and sinterization conditions on the properties of the powder metallurgy CoCrMo alloy, Oksiuta and Dabrowski [120] found that a heat treatment at 1240 ℃ improves the structure and mechanical properties of the material. Better mechanical properties, i.e., higher ultimate compressive strength (UCS) and plastic deformation, and lower Young's modulus and shear modulus were reported for CoCrMo alloy after re-pressing and heat treatment compared with that of the cast alloy.

2.2.3.4. Hot isostatic pressing

Hot isostatic pressing (HIP) offers an effective way of upgrading castings, densifying pre-sintered components, and consolidating powders. It consists of the application of a high temperature treatment under isostatic compression achieved by pumping an inert gas, such as argon or nitrogen at a pressure of a few hundred MPa, in a specially constructed vessel. It causes the entrapped gases in the pores to overcome the surface-energy driving force for pore closure, resulting in their dissolution in the matrix. Under these conditions of temperature and pressure, internal pores or defects collapse leading the encapsulated powder or sintered components to densification and improved less scattered mechanical properties [121].

HIP (figure 2.8) provides various advantages in comparison to the conventional sintering processes [122,123], many of which are contributed by the isostatic nature of the applied pressure:

- achievement of higher densities at lower temperatures and consequent possibility to develop finer microstructures.
- production of highly complex shapes;
- homogeneous porosity distribution;
- rapid heating, due to quick heat transfer under high gas density conditions, and consequently shorter cycle time;
- possibility to process brittle materials due to the more uniform heating;
- production of near-net-shape parts.

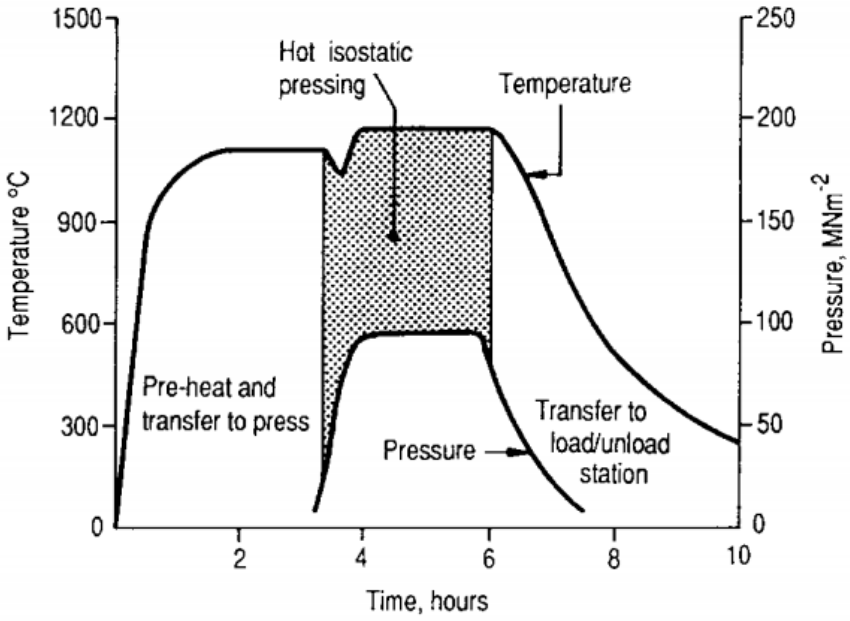

Figure 2.8. Typical HIP cycle conditions [124]**.**

Yamada H [125] was among the first scientists to study the strength of biomaterials and reported that the majority of metallic alloys, and in particular HIP CoCr alloys, have fatigue strengths over 500 MPa in air, which is compatible with orthopedic implant applications.

Georgette et al. [126] investigated how the HIP process influences the corrosion and mechanical behavior of components made of a cast porous-coated CoCrMo alloy. Their findings showed that the application of a porous coating thermal cycle during sintering

resulted in the formation of grain boundary precipitates and porosity, accompanied by a reduction in elemental segregation in comparison to as cast condition. The effect of a subsequent HIP processing enhanced both mechanical properties and corrosion resistance. It was suggested that the improvement in corrosion resistance was due to a further reduction in elemental segregation, as compared to the as-sintered condition.

It is well known that cast CoCr alloys exhibit an inhomogeneous, large-grained, cored microstructure, in which the dendritic regions are Co-rich, whereas the interdendritic regions can be a mixture of various Co-rich, Cr-rich, and Cr- and Mo-rich phases. With HIP processing, the grain size can be reduced [127]. The reported fatigue strength for cast CoCrMo is below 310 MPa, but forging with subsequent heat treatment and casting with subsequent HIP-process enable fatigue strength values above 600 MPa [128,129].

Vidal et al. studied the passive behavior of CoCrMo alloys combining the synergic effect of carbon content with the thermal treatments. The alloys were processed as T1 (solution annealing, SA), T2 (solution annealing, hot isostatic pressing and final solution annealing, SA + HIP + SA) and T3 (solution annealing, porous coating, hot isostatic pressing, and final solution annealing, SA + PC + HIP + SA). The authors found that alloy with T1 appeared to be more susceptible to corrosion than alloy with T2 and T3, owing to the formation of an oxide film with faster passive dissolution. It was suggested that the increase in thermal treatment steps (T3) leads to the formation of a more corrosion resistant oxide film due to carbide dissolution during thermal treatments. This increases the Cr level in the alloy, available for the formation of protective surface oxide film [50].

2.2.4. Mechanical properties of CoCrMo Alloys

The minimum requirements for the ultimate tensile strength and elongation of CoCr alloys for medical applications, based on the ASTM standards, are summarized in Figure 2.9.

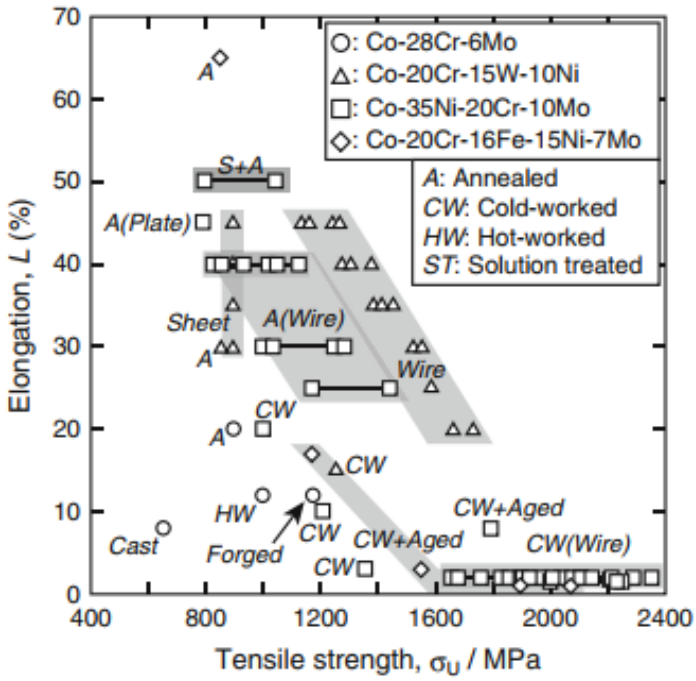

Figure 2.9. Tensile strength and elongation required for biomedical Co-Cr alloys in ASTM standards.

Such as for other metallic materials, the mechanical strength and ductility of CoCr alloys can be modified by controlling their microstructure, using alloying and thermomechanical treatments.

The addition of Zr to the as-cast ASTM F75 affords a fine microstructure, increasing the alloy mechanical resistance and ductility [129]. The addition of nitrogen is an effective way to improve the workability of wrought Co-28Cr-6Mo alloys [130] by suppressing the formation of σ-phase and γ-to-ε martensitic transformation. It was found that nitrogen acts as a γ-phase stabilizer in Co-29Cr-6Mo alloy by increasing the energy barrier for the γ-to-ε transformation. In particular, it slows down the transformation kinetics by forming Cr-N short-range order [131] or nanoscale Cr_2N precipitates in the γ-matrix [132–134]. For this reason, the addition of nitrogen improves the hot-working properties of Co-28Cr-6Mo-0.16N alloy in the temperature range of 1273-1473 K [135]. Better elongation and workability were achieved in the alloy with a nitrogen content of 0.10 wt%, sufficient to suppress the γ-to-ε martensitic transformation entirely. Further addition of nitrogen resulted in a slight decrease in the elongation to failure due to enhanced formation of annealing twins [133].

2.2.5. Wear properties of CoCrMo Alloys

Wear resistance is another excellent characteristic of CoCr alloy. Such a good wear resistance is particularly required when CoCrMo alloys are used in sliding parts of artificial joints. Under these conditions, the formation of wear debris [136] and ion leaching [137] are the main concerns regarding the application of metal-on-metal (MOM)-type joint replacements such as hip replacement. The formation of wear debris seems to be linked to the microstructure of the CoCrMo alloys, which is in turn affected by the γ-to-ε transformation and intermetallic and carbonitrides compounds in the matrix. Several studies have investigated the effect of precipitation on the metal-on-metal wear properties of CoCrMo alloys [76,78,138,139]. Chiba et al. identified σ-phase precipitates as the major causes of the abrasive wear in CoCrMo alloys. They also reported that in CoCrMo alloys where ε-phase formed by strain-induced martensitic transformation during wear tests excellent wear resistance was observed due to increased hardness [78,139].

Moreover, some researchers highlighted that the higher amounts of carbon could improve the wear properties of the CoCrMo alloys [76,138]. In another study performed by Ueda et al, the pin-on-disk wear behavior of as-cast and solution-treated (ST) Co-28Cr-6Mo-0.3N, Co-28Cr-6Mo-1Si-1Mn-0.3N, Co-28Cr-6Mo-1Si-1Mn, and Co-28Cr-6Mo-1Si-1Mn-3Ni alloys, used as materials for the pins, was investigated in contact with either 1% lactic acid (pH = 2.3) or the Kokubo solution (pH = 7.4) [77]. They referred that in as-cast alloys the π-phaseand $M_{23}X_6$-, and M_2X-type precipitates formed, while the ST alloys showed no precipitates. Their results evidenced that the mass loss of ST pins showing continuous wear grooves was lower than that of as-cast pins, exhibiting discontinuous deep wear grooves [77]. An investigation on the worn surfaces showed that during wear tests some of the precipitates in the as-cast pins first detached from the metallic matrix making cavities, then caused discontinuous deep grooves. The elemental analysis of the solutions after wear tests indicated the presence of small amounts of Ni ions from Ni impurities in Co-28Cr-6Mo-0.3N, Co-28Cr-6Mo-1Si- 1Mn-0.3N, and Co-28Cr- 6Mo-1Si-1Mn-3Ni alloy pins. They concluded that in order to decrease Ni ion elution and thereby to improve the safety of CoCrMo alloys, it is necessary to decrease the alloy Ni content [77].

2.3. Corrosion properties of CoCrMo Alloys

The central question in the field of artificial bioimplants is: “what is the principal property of a metallic biomaterial?”. Definitely, the answer is biocompatibility, and this property is strictly related to the material corrosion resistance in contact with human fluids [140–142].

Implementation of artificial biomaterials in biological environments may induce several reactions due to the interaction with salts, proteins, enzymes, and various cells, which may prompt toxicity, allergy, and eventually implant failure. Several factors influence the corrosion behavior of the metallic biomaterials, such as [143,144]:

- *Material characteristics,* like chemical composition (type and quantity of alloying elements, segregations, impurities), microstructure (grain size and orientation), and surface properties (coated or uncoated status, surface oxide layer stability).
- *Medium properties,* like type and concentration of chemical species (pH, chloride content, etc.), temperature, and pressure.
- *Other factors,* like operating conditions of the implant (static and dynamics loads), implant production method (casting, forging, additive manufacturing, etc.), and thermomechanical history of the alloy (dislocation density, amounts of thermal or residual stress, point defects, and deformation ratio).

2.3.1. Human body fluids

Table 2.4. represents the general composition of biological body solution (Plasma/serum as well as synovial fluid). Several factors affect the properties and compositions of body fluids like disease, aging, and drug ingestion [145]. Thus, understanding the effects of biological conditions during the exposure of biomaterials to this aggressive biological environment is crucial to understand the corrosion behavior of these materials and reducing the chance of failure, and controlling maintenance criteria.

Table 2.4. General chemical composition of human body fluids [145]**.**

Compound	Synovial Fluid	Plasma or Serum
Bicarbonate	-	25 – 30 mM
Calcium	1.2 – 2.4 mM	2.12 – 2.72 mM
Chloride	87 – 138 mM	100 – 108 mM
Phosphorous (total)	-	2.87 – 4.81 mM
Potassium	3.5 – 4.5 mM	3.5 – 4.7 mM
Sodium	133 – 139 mM	134 – 143 mM
Amino acids	-	20 – 51 mg mL^{-1}
Glucosa	-	650 – 966 mg mL^{-1}
Uric acid	39 mg mL^{-1}	30.5 – 70.7 mg mL^{-1}
Water	960 – 988 mg mL^{-1}	930 – 955 mg mL^{-1}
Albumin	6 – 10 mg mL^{-1}	37.6 – 54.9 mg mL^{-1}
IgG	1.47 – 4.62 mg mL^{-1}	6.4 – 13.5 mg mL^{-1}
Fibrinogen	-	2 – 4 mg mL^{-1}

Table 2.5 collects the compositions of artificial body fluids used to simulate the real ones under normal physiological conditions [145].

Table 2.5. Chemical composition of various media used to investigate the behavior of CoCrMo alloys [146]**.**

Solution (pH)[i]	Composition	Reference
0.9% NaCl at pH=7.4 **(adjusted by conc. HCl and conc. NaOH)**	9.08 gr/l NaCl	[[126]
0.14 M NaCl at pH=7.4 **(adjusted by conc. HCl and conc. NaOH)**	8.2 gr/l NaCl	[127]
0.14 M NaCl at pH=7.4 **(adjusted by conc. HCl and buffered by use of Tris[ii])**	8.2 gr/l NaCl	[128]
Hank's simulated physiological solution (SPS) at pH=7.4 **(adjusted by 1 M NaOH, nonbuffered)**	8 gr/l NaCl 0.4 gr/l KCl 0.35 gr/l $NaHCO_3.H_2O$ 0.25 gr/l $NaH_2PO_4.H_2O$ 0.19 gr/l $CaCl_2.H_2O$ 0.19 gr/l $MgCl_2$ 0.06 gr/l $MgSO_4.7H_2O$ 1 gr/l glucose	[38,126,129,131]
Simulated physiological fluid (SPF) at pH=7.4 **(adjusted by conc. HCl and buffered by use of Tris)**	0.14 M NaCl 1 mM KH_2PO_4 3 mM KCl 4.2 mM $NaHCO_3$ 2.5 mM $CaCl_2$ 1.5 mM $MgSO_4$ 0.5 mM Na_2SO_4	[128]
Saline phosphate buffer solution (SPBS) at pH=7.4	0.14 M NaCl 1 mM KH_2PO_4 3 mM KCl 10 mM Na_2HPO_4	[47,127,132,133]
Saline phosphate buffer solution (SPBS) at pH=7.4	8 gr/l NaCl 0.2 gr/l KCl 1.15 gr/l Na_2HPO_4 0.2 gr/l KH_2PO_4	[134,135]
Phosphate buffer solution (PBS) at pH=7.4	0.1 M $Na_2HPO_4.H_2O$ 0.1 M K_2HPO_4	[126,136]

[i] Not additionally buffered.

[ii] Tris, tris (hydroxymethyl) aminomethane.

2.3.2. Effect of the solution composition on CoCrMo corrosion behaviour

Test solution ranges from pure water to complex electrolytes containing more than 40 species including absorbable organic molecules and antibiotics [43]. The choice of complex body fluids which approaches the fluid to more realistic body conditions limit the mechanistic interpretation of the components on the corrosion behaviour of the alloy. A study with XPS and auger electron spectroscopy found that the oxide was thinner for all samples immersed in synovial fluid, followed by water, while PBS produced the thickest oxide passive film. According to this study, the influence of a prepassivation process reduced the ion release in synovial fluid and should be always applied in the manufacture of orthopedic implants using CoCrMo alloy [147].

Temperature is a key parameter due to the fact that some electrochemical reactions can be accelerated and changing the corrosion mechanism at body temperature (37ºC) from that occurring at room temperature [143]. The pH of the electrolytes is also playing an important role on controlling the conformation of organic molecules and thus their surface reactivity. In general, the selected electrolytes are buffered solutions which maintain constant the neutral pH of the media approaching in-vivo conditions.

2.3.2.1. Effect of pH and specific chemical species

The pH of the body solution is one important factor, which can affect the corrosion resistance of the implanted alloy. The solution pH tends to increase on surface regions mainly cathodic in nature, while it decreases on localized anodic regions due to cation hydrolysis. Under these latter conditions, the oxide layer becomes more susceptible to dissolution, so triggering an autocatalytic dissolution process [148,149]. The solution acidity was found to play an essential role on the nature of the surface oxide layer on CoCrMo alloys [150–152].

Inductively coupled plasma mass spectrometry (ICP-MS) was utilized to perform a chemical analysis of metal ion concentrations in Hank's solution at pH 2.0 and 6.8, after 30 days of immersion of CoCrMo alloy and pure Co, Cr and Mo [150]. It was found that by decreasing the pH of solution, the quantities of all metal ions released from the alloy increase. The same trend was observed for pure metals, except Mo, whose stability increases by decreasing the solution pH. Moreover, the results of quantitative analysis of dissolved metal ions showed that the quantities of Co and Mo released from pure metals

are much higher (by a factor of 10^3) than those from CoCrMo alloy, while the quantities of Cr released from the alloy are slightly higher than those from pure Cr [150].

Phosphate ions can play a vital role on the properties of the passive film and consequently affect the electrochemical behavior of bioimplants in body solution [147,153,154].

Milosev et al. [146] recorded cyclic voltammetry curves for CoCrMo alloy in NaCl solution, Hank's simulated physiological solution (SPS), and phosphate buffer solution (PBS). Their findings showed that the alloy behaves more similarly to chromium, and to some extent also to molybdenum. The most distinct differences in the CVs of the alloy in the mentioned solutions were observed in the transpassive region. An increase in current density and a shift of the onset of transpassivity to more negative potentials were induced by phosphates in phosphate-containing solutions in comparison to those in NaCl. A pronounced peak at 0.8 V vs SCE was observed in the voltagramms of the alloy exposed to PBS, while a shoulder, rather than a peak, appeared in SPS at 0.88 V. The findings of CV curves in NaCl are consistent with those in PBS and SPS, in which the increase in current proceeds steadily in transpassive range without a peak or shoulder. The observed feature (peak or shoulder) in the transpassive region are evidently attributed to the composition of the studies solution, i.e., presence of phosphate ions and formation of metal phosphates like chromium orthophosphate, $CrPO_4$, and molybdenum metaphosphate, $Mo(PO_3)_3$. According to Ouerd et al. [65], the transpassive peak increases by increasing phosphate concentration. They reported that this peak is mainly related to the formation of Cr(VI) species by measuring the concentration of CrO_4^{2-} species by UV/vis absorption spectroscopy during 4h oxidation at 0.74 V (SCE) in PBS. Their findings suggested that enhancing phosphate concentration resulted in the formation of higher amounts of chromate ions. Based on their research, in the transpassive range the protective Cr_2O_3 oxide layer dissolved to the soluble CrO_4^{2-} through the following reaction (2.1):

$$Cr_2O_3 + 10OH^- \rightarrow 2CrO_4^{2-} + 6e^- \quad (2.1)$$

At the same time, the presence of the phosphate ions in the solution resulted in the formation of an additional amount of chromate ions (via reaction 2.2), as also detected by the enhanced current density of the peak in the transpassive range.

$$CrPO_4 + 8OH^- \rightarrow CrO_4^{2-} + 4H_2O + PO_4^{3-} + 3e^- \quad (2.2)$$

Higher concentrations of CrO_4^{2-} species were also obtained by increasing the immersion time likely due more abundant formation of a $CrPO_4$ underlayer, under the Cr_2O_3 oxide [65].

In other studies, the deposition of chromium orthophosphate was investigated in-vitro after immersion of CoCrMo alloys into human serum [155] and in-vivo in the periprosthetic tissue of the hip prostheses [156]. Other authors [153] studied the behavior of CoCrMo alloy in 0.14 M NaCl solution and saline phosphate buffer solution (SPBS). They confirmed the presence of phosphate in the oxide layer by XPS. They also conducted electrochemical impedance spectroscopy and reported that in both solutions, the EIS diagrams show a typical passive state shape. It was monitored that the addition of phosphate increased the value of R_{ct} (the charge transfer resistance) and CPE_{dl} (the double-layer capacitance) in the EIS spectra. This increase was more pronounced in the passive region (potential of -0.1 V_{SCE}) than at the open circuit potential, i.e., by two to three orders of magnitude compared to a slight increase at the open circuit potential. These results confirmed that the outer layer formed in the presence of phosphate increases the corrosion resistance. Given this, the formation of a phosphate-rich layer covered the alloy surface and operated as a barrier for mass transport of oxygen or reaction products to and from the surface [153]. According to the mechanism proposed by Muňoz and Mischler, there is a mixed potential theory to interpret the effect of phosphate on corrosion current and corrosion potential. They suggested that phosphate ions act as anodic inhibitors by decreasing the corrosion current density and shifting the potential to more positive values [153].

The effect of phosphate concentration on the formation of oxide layer was confirmed by EIS data, reflecting the adsorption and blockage of the surface by phosphate ions at the electrode-electrolyte interface. They also reported that the charge transfer resistance, R_{ct}, increased with increasing immersion time as well as phosphate concentration [65].

Complexing agents like ethylenediaminetetraacetic acid (EDTA) and citrate establish a simple model of physiological conditions which mimic the in vivo situation. Previous studies on CoCrMo have reported that in SPS solution, the addition of EDTA caused a decrease in thickness of the oxide layer on CoCrMo alloy from 2.1 nm to 1.6 nm at 0.1 V_{SCE} and from 13.5 nm to 7.5 nm at 0.6 V_{SCE} [41]. The content of Co-, Ni- and Mo-oxide in the passive layer was lower in the presence of EDTA, thus indicating increased

solubility associated with higher stability constants for complexes of metal cations with this complexing agent [41]. In particular, the logarithms of the stability constants (log K_{st}) for EDTA complexes with Co^{2+} and Co^{3+} were 16.3 and 41.4, respectively, while the log K_{st} for citrate complexes with Co^{2+} was 5 [157]. Therefore, in comparison to citrate, EDTA more strongly stimulates the anodic process on Co [158]. In principle, as for Co, EDTA is expected to form strong complexes with Cr^{3+} ions too, but the dissolution of the strongly protective Cr_2O_3 layer is a very slow process, so that the amount of dissolved Cr(III) species available for complexing is small [157].

Biological macromolecules can affect the corrosion behaviour by interfering in different ways with the anodic or cathodic reactions. Proteins adsorbs onto the implant surface and may change its chemical characteristics by oxidation and/or hydrolytic reactions. However, even if many studies deal with the effects of proteins on the corrosion behaviour of biomaterials, yet the conclusions are ambiguous. This is probably due to the different experimental procedures adopted, but also due to the fact that a specific protein may act differently when in contact with different metals and alloys [159,160].

The effects of proteins on the corrosion behaviour of biomaterials can be the following [160,161]:

1) Proteins can bind to metal ions and transport them away from the implant surface. This will destabilize the equilibrium across the electrical double layer and trigger further dissolution of the metal.

2) Proteins can affect the electrode potential due to their electron-carrying capability.

3) The adsorption of proteins onto the surface of biomaterials could limit the diffusion of oxygen to certain regions of the surface, thus causing preferential corrosion of oxygen-deficient regions and breakdown of the passive layer.

4) An adsorbed protein layer could act as a barrier between the metal surface and the environment, thus inhibiting corrosion.

5) In the case of wear or wear-assisted corrosion reactions, proteins can act as lubricants on the surface.

Human serum albumin is the most abundant protein in human blood plasma. Indeed, half of the blood serum protein is made of albumin and is mainly responsible for the maintenance of blood pH and osmotic pressure. Bovine serum albumin (BSA) is considered as a widely used model protein in biocompatibility studies. Muňoz et al. [153] reported that the addition of BSA to NaCl solution slightly enhances the current

density of CoCrMo alloy in the whole potential range. However, their experiments in PBS solution in presence of albumin identified a more pronounced increase of current density. In particular, the addition of 0.5 g l^{-1} BSA to PBS increased the value of i_{corr} approximately fivefold, while the same BSA concentration in NaCl solution induced an increase of i_{corr} values by a factor of 1.2. They found that albumin acts as a cathodic inhibitor because its adsorption impedes the access of the oxidant to the metal surface, but at the same time it catalyses the anodic process by complexation, so explaining the corrosion behavior in NaCl solution. In PBS, it more significantly increases the dissolution rate of CoCrMo because it limits the surface adsorption of phosphates [153].

2.3.2.2. Effect of inflammation conditions; Reactive Oxygen Species (ROS)

Recent findings highlight the importance of inflammatory cells, individual body chemistry, Fenton chemistry, and electrosurgery in surgical applications [162–166]. Therefore, it is becoming increasingly clear that using simple solutions (simulating the ionic strength, chloride content, and pH of physiological conditions) for corrosion tests or immersion tests is insufficient to predict in-vivo corrosion properties of biomaterials.

ROS are chemical species, including intermediates of oxygen reduction, which are potent oxidizing and highly reactive agents. Peroxides, superoxides, hypochlorous acid, and hydroxyl radical are among the most recognized ROS agents which are present in the living body system and can be formed from the normal metabolism of oxygen. They are involved in the inflammatory response of the body, in which the inflammatory cells produce acid and ROS species to attack invading foreign bodies [167–169]. The adhesion and activation of microphages form particularly aggressive microenvironments between the material surface and the cell membrane [170] which can make the surface of metallic biomaterials susceptible to potentially high concentrations of oxidizing agents [171–173]. ROS play a crucial role during healing of wound and inflammation, in terms of signal transfer, cleaning up debris, and in cell proliferation [174,175]. Since there is a close relation between metal implants with cells and ROS, these factors should be considered during in-vitro investigations of metallic implants to understand interactions between corrosion and inflammation, connected to bioimplantation. As an example, Steinemann [176] attempted to investigate the corrosion rates of a series of metals and alloys including CoCrMo in vivo, using a rabbit model. He observed that in vivo corrosion rates in tissues can differ up to 3 orders of magnitude from in vitro results.

Although CoCr alloys are not as biocompatible as Ti-based alloys, they are often used in biomedical applications. It is reported that Cr (VI), Cr (III), and Co (II/III) with its compounds are respectively classified as group 1, group 3, and group 2B carcinogens, respectively [177,178]. However, on the other side, Cr and Co are important microelements for living system functions, i.e., Cr plays a role in glucose metabolism, and Co (III) is important for activities of vitamins (B12) [178]. The toxicity of Co and Cr is directly related to their concentration, and when they are in trace quantities, they do not show toxicity to biological targets. The studies of metal implant failure indicated significant amounts of metal wear debris and corrosion products around periprosthetic tissues as well as considerable amounts of macrophage infiltrate [178]. Macrophages play an essential role in corrosion-related implant failure. Evidence of cell-induced corrosion was hypothesized by Gilbert et al. [179], who found cell-like corrosion patterns on the surface of retrieved CoCrMo hip implants. They reported that a distinct rise (40 to 100-fold) in corrosion susceptibility of CoCrMo alloy was observed when it was subjected to PBS solution in the presence of inflammatory conditions (addition of HCl and H_2O_2) [179]. In another work, Liu and Gilbert [180] investigated the corrosion behavior of CoCrMo alloys in simulated inflammatory conditions. The PBS solution was modified by the addition of different concentrations of HCl, H_2O_2 and Fe^{3+}. They stated that an increase in the concentration of H_2O_2 and a decrease in pH values significantly influence the open circuit potential, corrosion current, and impedance of the surface oxide film. Addition of 30 mM H_2O_2 in PBS at pH=7.4 increased the open circuit potential (OCP) from -0.250 $V_{(Ag/AgCl)}$ to 0.355 $V_{(Ag/AgCl)}$; however, in PBS at pH=1, this value reached 0.650 $V_{(Ag/AgCl)}$. EIS measurements confirmed a decrease in resistance of oxide film in PBS in the presence of inflammatory conditions. Attempts have been made by the same authors [162] to investigate the effect of inflammatory conditions on dissolution behaviour and surface oxide on CoCrMo alloy, by using electrochemical atomic force microscopy (ECAFM). A phosphate buffer solution in the presence of 30mM of H_2O_2 was used as the simulated biological solution. In-situ ECAFM analysis, along with surface roughness values and potentiostatic polarization measurements showed a correlation between surface oxide morphology, loss of passivity, and electrochemical behavior CoCrMo alloy. The presence of H_2O_2 induced higher current densities, positive shifts of OCP and less increase in surface roughness in comparison to PBS-only condition. They also showed that in the transpassive region, carbide boundaries and metal

grain boundaries were preferential sites for oxide dissolution [181]. Lin et al. [182] reported that the as-polished CoCrMo is protected by an oxide layer mainly consisting of Cr_2O_3. However, the produced macrophage cells and their released ROS altered the alloy surface oxide compositions through oxidation and nitration reactions. They reported that ROS such as H_2O_2, O_2^- and NO formed by activated macrophages thickened the surface oxide film. Perhaps oxygen formed by reduction of H_2O_2 further reacted with the metal, or H_2O_2 participated in the formation of hydroxyl radicals in the presence of metal or metal ions, thus promoting oxidation [186]. In an in vivo research conducted by Muñoz et al. [183], the electrochemical corrosion behavior of CoCrMo biomedical alloys was studied in fluids extracted from patients with different articular pathologies and prosthesis revisions, using various electrochemical measurements (OCP measurements, polarization resistance, potentiodynamic polarization curves, EIS). Their findings revealed that the corrosion behavior of CoCrMo alloys in synovial fluids not only depended on the material reactivity but also on the specific reactions with the synovial fluid components, most likely involving ROS. In some patients the latter species were found to determine the whole cathodic and anodic electrochemical response. Depending on patients, corrosion rates varied significantly between 50 and 750 mg dm^{-2} $year^{-1}$.

2.4. Electrochemical behaviour of CoCrMo alloys and nature of surface passive films

In recent years, many studies have investigated the behavior of CoCrMo alloys due to the unceasing growth of the number of implanted CoCrMo alloys in biomedical applications (artificial joints). The high biocompatibility of the CoCrMo is directly related to the spontaneous formation of an oxide film which protects the bio metallic implants from the surrounding physiological environment. In general, it is believed that the electrochemical and mechanical properties of the bioimplants and consequently, its durability into the human body are directly affected by this protective oxide layer. Moreover, the interaction of this oxide layer with the surrounding tissues and the environment as well as its physico-chemical properties control the corrosion behavior and biocompatibility of the implanted material. Once the oxide film is formed on the alloy surface, the electrochemical and corrosion behavior of the implanted metal has been strongly correlated with the protectiveness and stability of this oxide film [44,184–187]. The

electrochemical behavior of the alloy is also highly dependent on the alloying elements and service external conditions (i.e., temperature, potential…).

The first histopathological and metallurgical investigation of a failed hip prosthesis consisting of dissimilar metals, a Vitallium (CoCrMo) acetabular cup and a stainless steel femoral head (metal-on-metal combination), was carried out by Gruen and Amstutz [188]. They reported that the main reason for implant failure was a severe abrasive wear and fretting corrosion, suggesting this combination should not be used as a bearing in the body. Thereafter, attempts have been made to change the quality of materials and design for biomedical implants. It is reported that various types of localized corrosion may occur when CoCrMo alloys are subjected to in vivo condition, e.g., galvanic corrosion in the junction of two metals, fretting corrosion due to the micromotions of the metal components, and crevice corrosion from occluded areas in specific parts of the implant components [143,189]. The degradation of CoCrMo cemented hip implants after implantation in sheep was investigated [190]. Auger depth profiles confirmed the presence of a Cr-rich oxide, which was thinner on the retrieved prostheses than on the virgin surface. The ratio of the chemical elements on the metal surface was not significantly changed, but the ratio in the surrounding tissue showed preferential dissolution of cobalt.

The passive layer formed on CoCrMo alloy mainly consists of high content in Cr (mainly Cr(III) and smaller amount of $Cr(OH)_3$) with a minor contribution of Co and Mo oxides [153,183,191]. The protectiveness of this layer and consequently the electrochemical behavior of the alloys is influenced by the solution composition, applied potential, and alloying elements [191]. According to Milosev and Strehblow [191], the thickness of this passive film is directly related to the applied potential (increasing around 1 nm V^{-1} in the passive domain).

It is well known that in contact with electrolytes the passive layers undergo a continuous process of partial dissolution and reformation from the microscopic viewpoint. Co was preferentially dissolved from the passive layer during immersion in Hanks' solution, leaving a passive layer mainly consisting of Cr-oxide with small amounts of Mo-oxides. It is also reported that in 0.15 M NaCl, the air formed molybdenum species are not stable and are replaced by $Co(OH)_2$, and Cr_2O_3 may be partially transformed to $Cr(OH)_3$. Due to the spontaneous formation of this oxide layer, CoCrMo alloys maintain passivity in solution without experiencing an active-passive transition [141].

It is stated that the protectiveness of this oxide layer, estimated by the polarization resistance values, is two orders of magnitude higher for CoCrMo alloy compared to pure cobalt and three times higher than for pure chromium [150,181,185].

Lin et al. [142] conducted a research in which they investigated the changes in surface oxides on CoCrMo alloy in a real biological environment. The results showed that the in-vivo corrosion resistance of the alloy increased at increasing surface oxide thickness. They found that the thickness increased if a preventive nitric acid passivation treatment was applied, so decreasing the corrosion rate [143,144]. An experimental characterization of the oxide film formed on the surface of CoCrMo alloys in various environments was carried out by Hanawa et al. [141]. Their X-ray photoelectron spectroscopy (XPS) results demonstrated that chromium and molybdenum were more widely distributed in the inner layer of the oxide film, while the Co was dissolved from the film, reaching a thickness of 2.5-2.9 nm. Another study by Hiromoto et al. investigated the corrosion behaviour and microstructure of low-Ni Co29Cr6.8Mo alloys and a conventional Co29Cr6Mo1Ni alloy in Hanks' solution and in a cell culture medium [150]. The lower current densities reported for the low-Ni alloys demonstrate that in the human body these alloys have higher corrosion resistance than conventional ASTM alloy.

Other studies evidenced that the alloying elements play an important role in the electrochemical behaviour of the alloy. Metikos et al. [150] found that the corrosion behaviour of the passive alloy is determined by the presence of Cr, although its corrosion resistance is higher due to the beneficial effect of the Mo on the passivation properties.

Li et al [74] reported that the passive film (composed by Cr and Co elements) protects the underlying Mo from further oxidation and reaction with electrolyte. Moreover, in work done by Metikos et al. [185], they also observed that at lower potentials the Cr species play major role in the passivation of the alloy while at higher potentials Co species take on these roles. At the same time Cr also contributes to increase the corrosion resistance of the alloy.

It is stated that the major dissolving specie from the alloy is Co which strongly depends on the electrochemical conditions [80]. In a study aiming at determining the incorporation of cobalt in the film formed on CoCrMo in saline phosphate buffer solution (SPBS), Karimi et al. [194] found that cobalt is released mainly into the solution and does not significantly contribute to the oxide layer growth. This is confirmed by Contu et al. [192]

that the differences on the polarization resistance of the alloy immersed in serum is mainly due to Co dissolution from the protective oxide film.
On the other hand, the chemical composition of the electrolyte plays a crucial role on the exact chemistry of the passive layer [153].

2.5. Conventional manufacturing techniques for CoCrMo alloys

2.5.1. Casting

Casting is a near-net-shape processing, which is recognized as the most common and widely used manufacturing technique for surgical implants. This is mainly because the method is virtually cheap and straightforward, particularly concerning the costly machinery process. Precision casting is beneficial for the fabrication of parts with complex shapes, particularly dental and biomedical prostheses like crowns, inlays, bridges, and dentures. Irrespective of these advantages of casting processes, it is noteworthy to point out that the strength and ductility of the cast CoCrMo alloys are not as good as what is required for implants. Inherent casting defects, like large initial grain size, pores and shrinkages, solidification defects, precipitation, and coarse microstructures, are the main factors that resulted in low mechanical properties [64].

2.5.2. Hot forging

Forging is one of the oldest metalworking processes in which compressive forces are applied through various dies and tools to shape the workpiece. Unlike other metal forming operations, which generally fabricate continuous plates, sheets, strips, or various structural cross-sections, forging is predominantly used for the production of discrete parts.
Advances in the hot forging manufacturing of CoCrMo alloys have resulted in a significant increase in mechanical properties in comparison to cast alloys due to the smaller grain size, which contributes to produce homogeneous structures. The advantage of the good combination of tensile properties and elongation makes this method a widely used technique [193]. Nevertheless, the difficulty in producing complex shapes like mesh structure prevents the application of this method for the fabrication of complex implants [194].

Thus, both mechanical properties and fabrication of complex shapes have become essential and increasingly critical to the implants industry.

2.6. Additive manufacturing techniques

From 2009 on, ASTM subcommittee F42.91 [195] collected all additive processing methods under the category of Additive Manufacturing. AM technology provides an outstanding opportunity for fabricating complex, customized, and cost-effective components with acceptable mechanical properties.

According to the definition provided by the American Society for Testing and Materials (ASTM International), additive manufacturing is defined as the "*Process of joining materials to make object from 3D model data, usually layer upon layer, as opposed to subtractive manufacturing methodologies*" [196].

The additive manufacturing approach has a number of attractive features compared to conventional methods. One advantage of AM technology is that it is capable of producing intricate designs from either traditional or newly developed materials. Given this, it makes it possible to fabricate parts containing various elements within the same design. The other advantage of using the AM method is that it allows the manufacturing of multi-directional composite structures and makes it possible to optimize the design of parts [197]. Moreover, through the AM process, new properties, forms, and functionalities can be developed by processing new materials.

In addition to polymers, metals, and ceramics, AM technology opens the door to produce composites and complex materials. The high flexibility in sketching and design freedom in AM technology allows the manufacturer to design parts with complex geometries or even to apply topology optimization to fabricate structures with the desired dimensions, complexities, and properties. On the other hand, AM technology permits the fabrication of parts with different materials or functionally graded objects. The possibility to supply various feedstocks in some of the AM techniques permits the production of multi-material parts and functionally graded materials (FGMs). The term FGMs refers to those structures having a gradual variation of material properties along one component direction. Recycling and eco-friendliness are the other reasons making AM commercially attractive, benefitting business growth, and reducing pollution. Nowadays, additive manufacturing methods have been integrated into a palette of technologies that result in structurally

strong products with highly accurate dimensions, shapes, and sizes for custom-made (i.e., patient-specific) medical devices and biomedical implants [198].

Additive manufacturing involves integrating a computer with a machine that builds the component according to a required model by performing a series of operations. The generic AM process phases are illustrated in Figure 2.10.

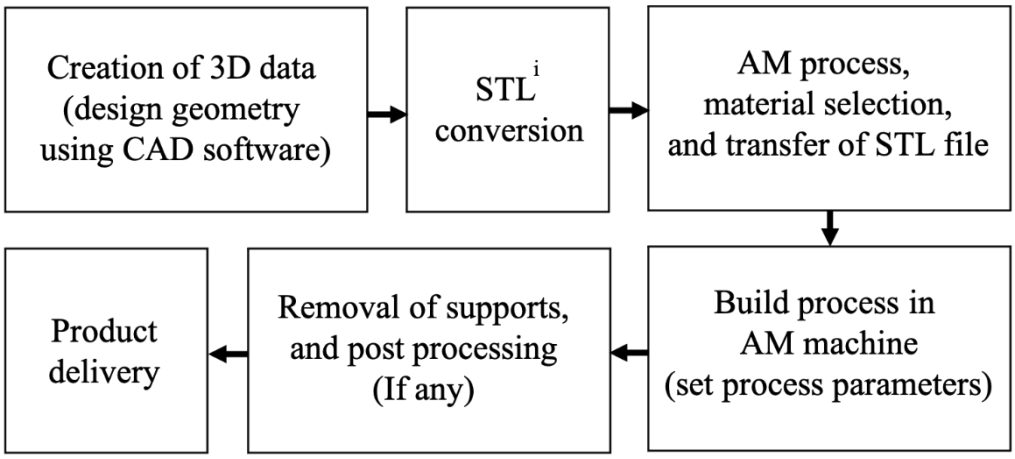

[i] "STL-Standard Triangle Language" describes the surface geometry of a three-dimensional object

Figure 2.10. Additive manufacturing process phases.

AM methods have the capability of processing metals and non-metals in solid, liquid, and semi-solid forms. The map of AM technologies can be divided into two major categories, based on how the material is bonded to a structure: Thermal and Chemical. Processes standing into the thermal branch use heat to produce additive manufactured structures, while technologies falling into the chemical category, form the final structure through a chemical process. Various additive manufacturing processes, their process similarities as well as bonding modes have been arranged in a schematic diagram, represented in Figure 2.11.

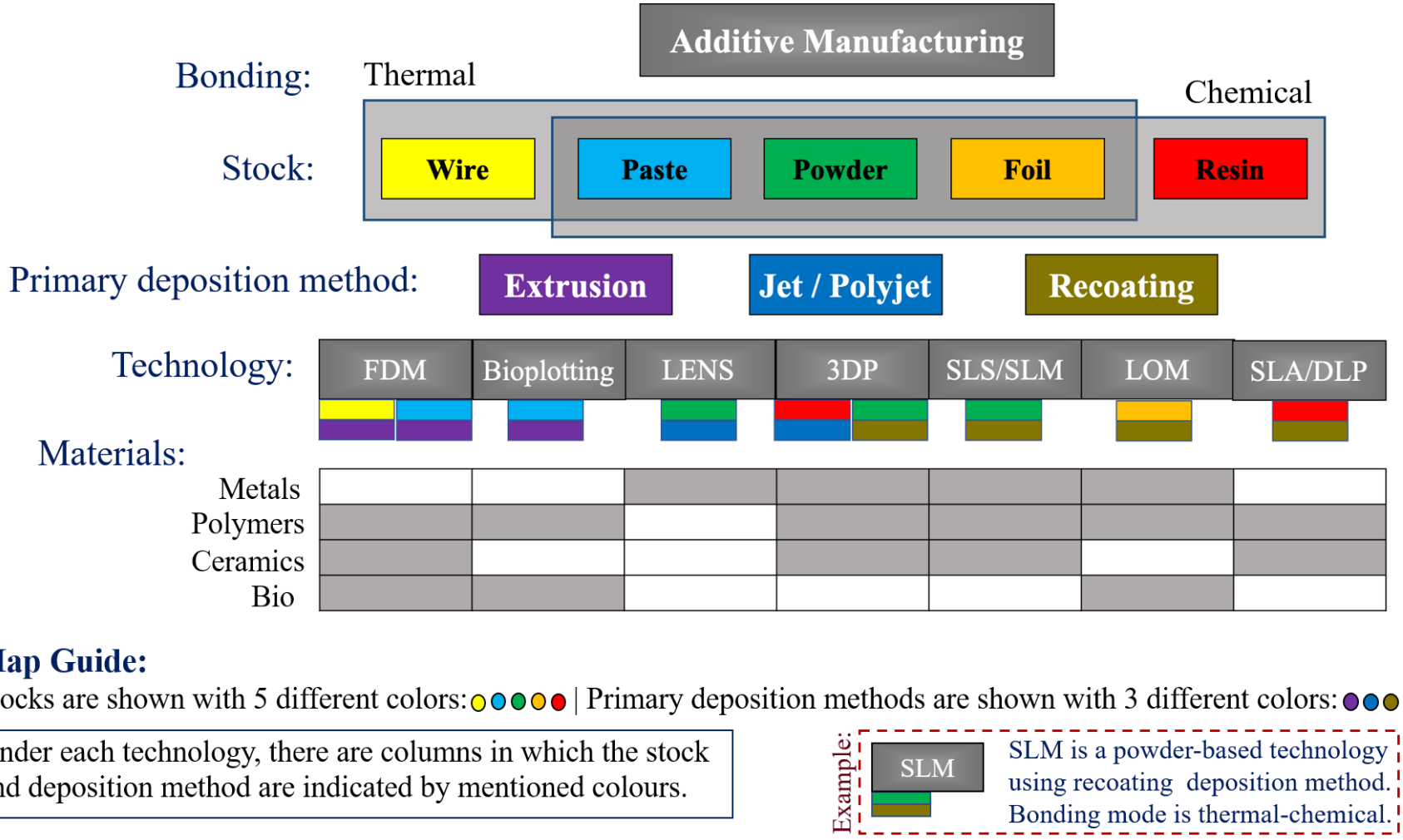

Figure 2.11. Additive Manufacturing Process categories and Branches, adapted from [199].

2.6.1. Metal powders for additive manufacturing

Dynamic control of input energy and process parameters makes AM processing a promising method for attaining stability under high temperature and phase transformation.

Stereo-lithography was the first rapid prototyping process, in which UV curable resins were used as the raw materials, and thereafter research has much focused on the processing of plastics. During 1990-2000, metal was introduced as raw material in the AM field. Metal AM has some tremendous advantages due to higher laser absorption power and stability of metals under higher temperatures. Presently, various metallic materials are available for additive manufacturing processing, including stainless steel, tool steels, Ti and its alloys, Inconel, CoCr alloys, Al alloys, etc. [200]. In order to achieve the required density and mechanical properties of the final products, process parameters and powder reuses are the primary concerns. It is reported that the density and mechanical properties of AM built parts are comparatively equivalent to those fabricated by conventional techniques [201]. Among all metal powders, Ti alloys and CoCr alloys have attracted considerable attention in biomedical applications such as dental implants, prostheses, etc. [200].

Table 2.6 shows the applications and advantages achieved by using different metal powders in additive manufacturing, while Table 2.7 lists the advantages and disadvantages of AM processing compared to conventional manufacturing methods.

Table 2.6. Metals in additive manufacturing [202,203]**.**

Metal	Co Alloys	Ti alloys	Stainless steels	Inconel	Al alloys	Cu alloys
Presently used	Co29Cr6Mo Co-based alloys	Ti6Al4V Pure titanium (CpTi)	316L 17-4PH	625 718	AlSi10Mg AlSi2	CuSn10 Bronze
Application	Dental implants; Medical prosthetics; Gas turbines.	Dental implants; Medical prosthetics; Aerospace industry.	Oil and gas industry	Turbine engine components; Chemical process equipment; Fuel exhaust systems.	Aerospace industry; automotive industry.	Cooling channels; Tool inserts
Advantages	High strength, Good corrosion and wear-resistant, High hardness	High bio-compatible properties	Good mechanical properties and corrosion resistance	Non-magnetic, Good corrosion resistant	Low weight, Good thermal and mechanical properties	Good thermal conductivity

Table 2.7. Comparison of AM and conventional manufacturing methods in metal component production [203]**.**

Factor	Additive manufacturing processes	Conventional manufacturing processes
Part complexity	Offering high flexibility in fabricating complex geometries and customized products	Required assembly for complex designs
Part design	AM brings opportunity in manufacturing lightweight parts (i.e., hollow or lattice structures)	Conventional manufacturing methods are not applicable for hollow and/or lattice structures
Material distribution	The material distribution within a part the structure could be varied	The material distribution within a part is almost uniform
Production volume	Low production volumes	Large production volumes
Production size	Ability to produce low and medium size parts	Providing the production of large-size components
Post-processing	Depending on the AM method, it can be mandatory or optional	Optional
Assembly	Reduction of the assembly stages and number of parts	Requiring assembly
Material cost	High	Low
Material waste	Reduces the material waste	A high amount of material waste

2.6.2. Types of additive manufacturing methods

In the past two decades, several AM technologies have been developed for the fabrication of different materials, including Selective Laser Sintering, Selective Laser Melting (SLS/SLM) and Electron Beam Melting (EBM) for sintering or melting of a powder, either thermoplastic resin or metal or ceramic, in a powder-bed; Directed Energy Deposition (DED) characterized by local material supply; Bioplotting for deposition of biological material and biomaterials in a similar way as FDM; Laminated Object Manufacturing (LOM) for contour tracing and layered manufacturing of any material in sheet form; Binder Jetting for 3D printing; Stereo Lithography (SLA) and Direct Light Projection (DLP) for photocurable polymer resins and composites with ceramic, to name a few [199,203,204]. The development of AM technology has stimulated and improved the fabrication of bioimplants [205–210].

SLS/SLM, DED, EBM are the most commonly applied techniques for manufacturing metallic parts [204,209,210].

A brief description of each technology is provided in the following sections. SLM process will be described more extensively, because it is the technique adopted to manufacture the CoCrMo alloys investigated in this research.

2.6.2.1. Powder Bed Fusion (PBF)

The powder bed fusion (PBF) technique refers to a class of AM technology, which uses a high-energy power source to melt or sinter a metallic powder bed selectively. PBF can be further classified on the basis of the powder source into two major techniques: SLS/SLM which uses a high-intensity laser, and EBM, which uses an electron beam. In principle, these two processes are similar; even though, the processing steps are quite different.

2.6.2.1.1. Selective Laser Sintering (SLS)

Polymer-based and Metal-based SLS are founded on the same manufacturing principle for the production of polymer and metallic parts from a powder. In SLS, the structure is built by applying subsequent layers of powder material on top of each other and consolidating each layer with a laser beam, which scans the powder layer according to the CAD geometry. Layer-by-layer, the powder is supplied on the previously bonded layer

until a 3D structure is formed (Figure 2.12). A finely grained thermoplastic granulate is used as a feedstock in polymer-based SLS system. Then, the temperature of the building chamber raises near to the sintering temperature of the granulate and the powder is selectively sintered to a consolidated component by a laser beam of moderate intensity. Since the powder temperature in the heated chamber is close to its sintering temperature, little to no thermal stresses are accumulated in the built structure [211]. Metal-based SLS is adapted from the polymer-based technique by introducing a protective gas into the build chamber, to prevent unwanted oxidation of the metal powder during sintering. Since in metal-based SLS, it is not viable to preheat the whole chamber to a temperature near the sintering temperature, thermal stresses accumulate within the structures as they are built. SLS-produced parts, whether metal-based or polymer-based, show a high level of porosity. Since the starting powder is sintered in the SLS system, the individual powder grains persist static, and are barely altered within the sintering process. Given this, the powders merely stick to the adjacent ones [199].

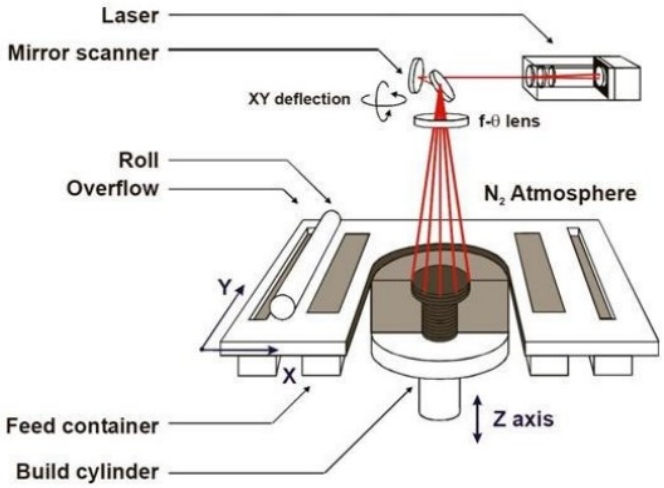

Figure 2.12. Schematic of SLS system. Reprinted from [211].

2.6.2.1.2. Selective Laser Melting (SLM)

SLM is one of the leading commercial rapid prototyping techniques that allow the fabrication of fully customized and controllable components through a laser beam on the basis of a layer-by-layer growth. SLM is regarded as the most versatile AM process because it can process a broad spectrum of materials, including Al-based alloys [212–

214], Ti-based alloys [215–217], Fe-based alloys [218–220], Ni-based alloys [221–223], Co-based alloys [224–226], Cu-based alloys [227], and their composites [228–231]. Also, SLM tends to produce amorphous materials [108] due to the high cooling rates achieved during the process [232,233].

The metal powder-based SLM technique was developed from SLS technique, by using a higher energy laser (beam energy up to 1 kW, beam scanning rate up to ~15 m/s). It can be distinguished from non-metal based SLM by the adoption of a protective gas flow (e.g. N_2 or Ar, depending on the reactivity of the metal powders) into the build chamber which, under proper overpressure conditions, aims at avoiding undesirable oxidation of the metal powders during the melting process [234]. After a powder layer is selectively melted, the build platform shifts downwards, and a recoating blade or brush supplies another layer of fresh powder from the powder tank to the top of the previous layer, then the computer-controlled laser scan process starts again [235,236]. Due to the lack of preheating of the machine chamber, SLM structures exhibit a significant accumulation of residual thermal stresses. Hence, to reduce warping and curling inside the build platform, support structures are used. By now, a wide range of materials, including metals, polymers, and ceramics [231,233,237–241], have been used for various applications. Both solid parts and complex porous structures fabricated by the SLM process exhibit acceptable mechanical properties without subsequent treatment [242,243].

Many process factors are involved during the SLM process. As illustrated in Figure 2.13, the process factors of the SLM process can be classified into four major groups: laser-related, scan-related, powder-related, and temperature-related.

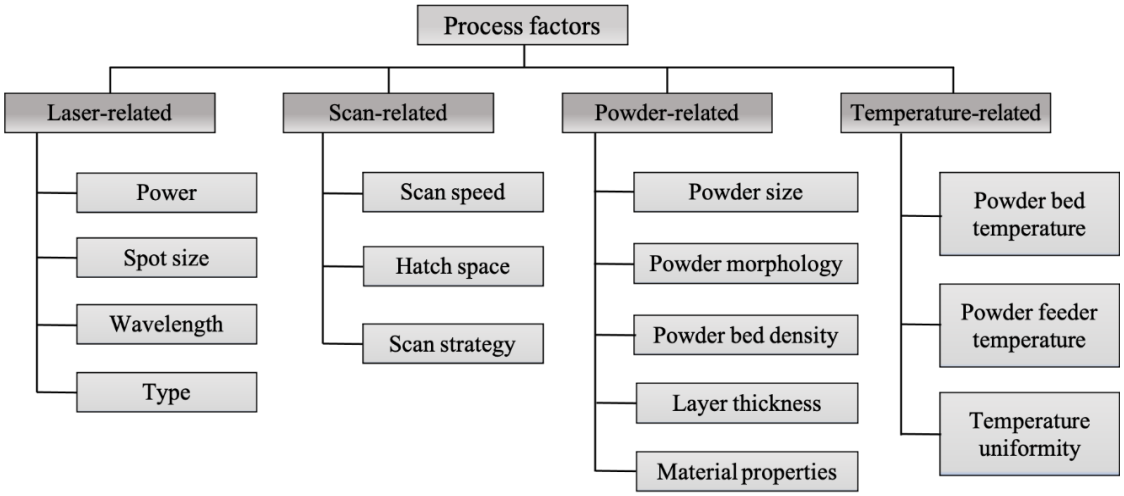

Figure 2.13. Process factors involved in selective laser melting technique. Reprinted from [244]**.**

Several process parameters have to be taken into consideration to fabricate a defect-free and high-quality part. Some parameters, like laser wavelength and laser operating mode, are fixed in a specific SLM system. Even the powder properties, such as the surface tension and the thermal conductivity, cannot be changed so determining the boundary conditions for the specific SLM process. Instead, the manufacturing or process parameters, can be set and optimized [245]. The most important process parameters are laser power, laser scan speed, hatch distance, hatch overlaps and hatch style [232,246].

The volume energy density (energy density of the laser), E, applied to a specific volume of powder material through SLM, is described by:

$$E = \frac{P}{vth} \tag{2.3}$$

where P is the laser power, v is the scan speed, t is the layer thickness, and h is the hatch space. According to the above equation (Eq. 2.3), increasing the laser power (P) and/or decreasing the scan speed (v), layer thickness (t) or hatch spacing (h) induce a rise in the laser energy density, thereby increasing the temperature of the melt pool. A higher laser energy density results in a larger melting volume and thus a higher final density [247]. In general, a range of energy density values, rather than a fixed value, optimizes the material performances.

Figure 2.14 shows graphical representation of the above-mentioned SLM process parameters, according to the Equation 2.3. Besides, in Figure 2.15 the basic working principle of SLM process is depicted, in which all steps starting from the first 3D design to last SLM fabricated part are illustrated.

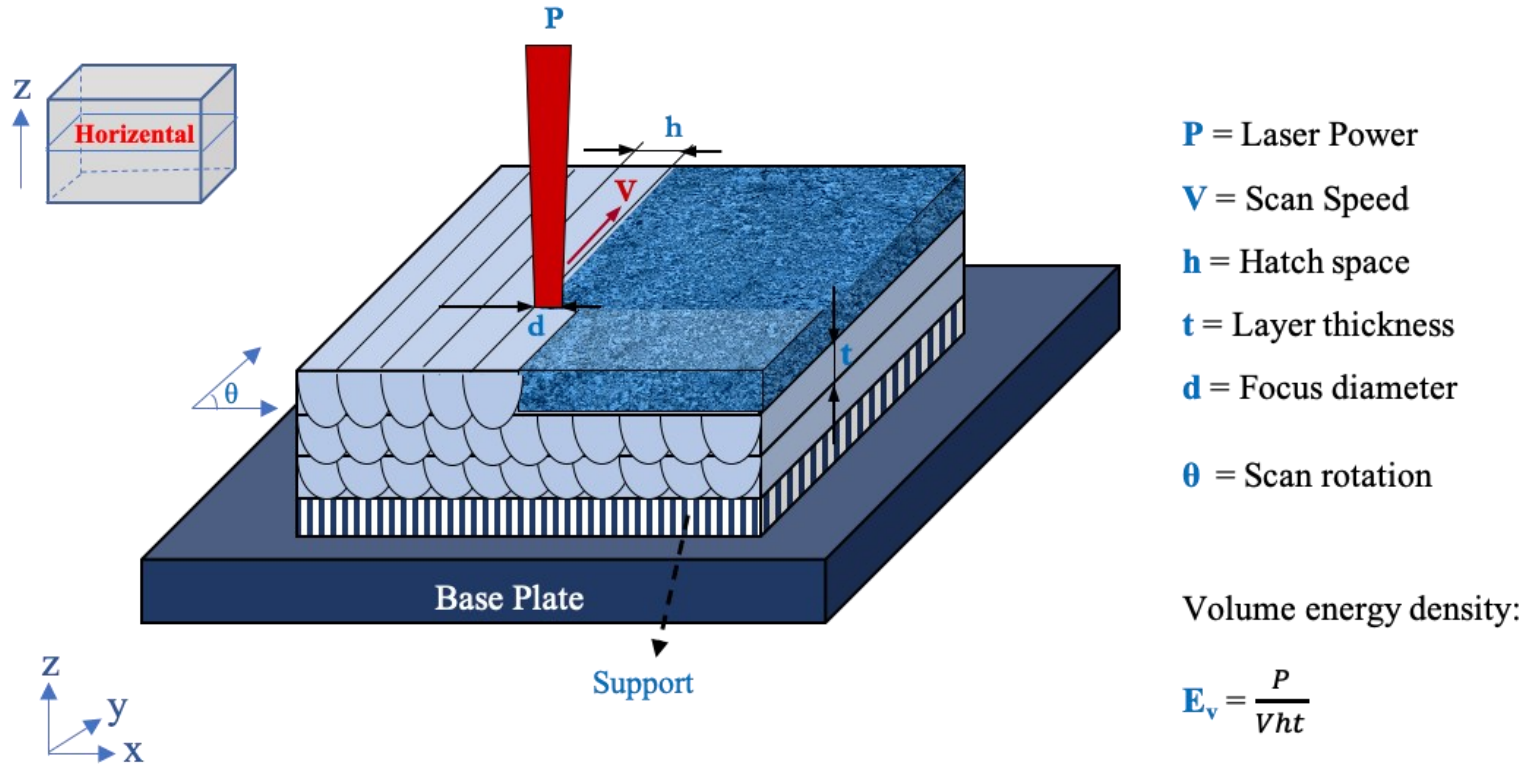

Figure 2.14. A graphical representation of the selective laser melting process parameters. Reprinted from [248].

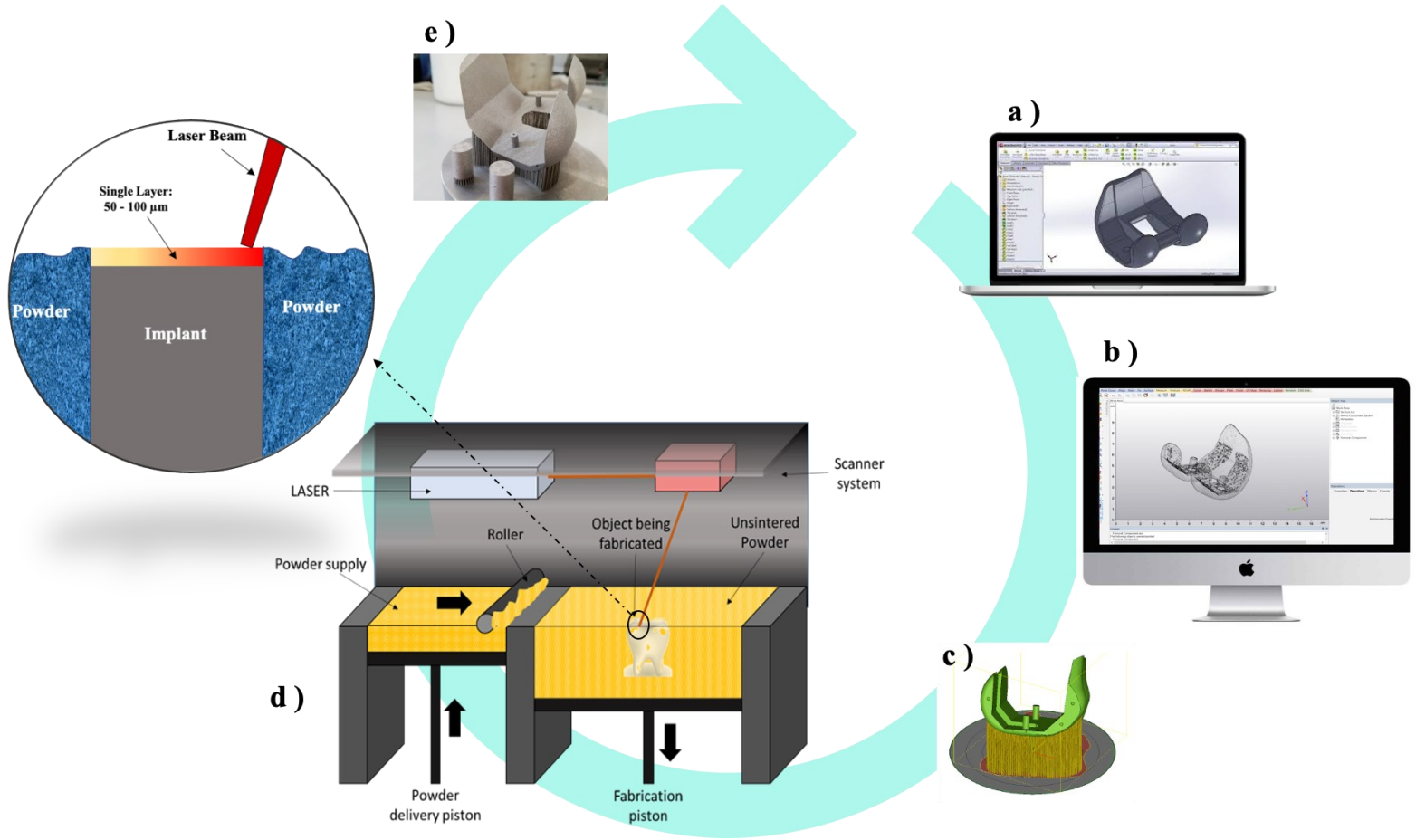

Figure 2.15. The basic working principle of SLM process, a) CAD design, b) Creating STL format, c) import design for SLM machine, d) SLM fabricating and e) final product.

During the SLM process, the laser beam moves over the powder bed at a constant scan speed (v), which controls the SLM manufacturing time. A higher scan speed obviously involves a shorter production time, but this may cause lower part densities [237,248,249]. Even a higher layer thickness accelerates the production time, but a too large layer thickness impairs the inter-layer bonding, due to the re-melting of the inter-layer zone. In the presence of thick layers, high energy input may overcome these problems, but can lead to increased surface roughness and lower dimensional accuracy.

Several scanning strategies for the fabrication of SLM parts can be applied, as shown in Figure 2.16. These scanning strategies may affect the relative density and mechanical properties; as an example, the relative density of SLM-produced parts using a chessboard scanning pattern can reach 99.9% [209,226,248,250].

There is no consensus about the mechanical behavior of metallic components fabricated by SLM methods in comparison to those obtained by conventional manufacturing processes, because of the dependence of these properties on SLM processing parameters. Table 2.8 listed some pros and cons of the SLM process.

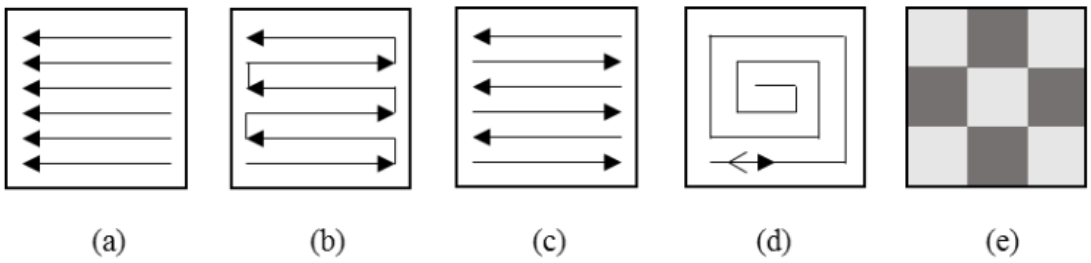

Figure 2.16. Some possible scanning strategies: (a) unidirectional, (b) bidirectional with continuous path, (c) bidirectional, (d) spiral and (e) checkerboard. Reprinted from [248]**.**

Table 2.8. Advantages and disadvantages to selective laser melting process [246,251]**.**

Advantages	Disadvantages
Powders can theoretically be reused repeatedly	Relatively slow process (because of the process speed limitations)
Reduces the wastage of raw materials and hence leads to a greener environment.	Acute size restriction
The use of a large range of materials the ability to tune properties during the processing of the parts	High power usage (the optimization of the process parameters are time-consuming)
Increased functionality	The powder handling can be tricky
Relatively low cost	High initial costs
Production of near-net-shaped components ready to use	The produced parts may have rough surfaces (depending on the powder size and the process parameters)

2.6.2.1.3. Electron Beam Melting (EBM)

EBM is another powder-based AM system equipped with an electron beam launching device, which can produce nearly fully dense parts in a vacuum environment. It resembles the more common SLM system, using an electron beam instead of the laser beam. Both SLM and EBM are powder bed-based methods, in which a powder layer is applied in a building area and selectively molten layer-by-layer, using a moving heat source. Nevertheless, SLM and EBM show distinct differences due to the diverse nature of the chamber atmosphere and heat source [252,253].

The working principle and process of electron beam melting are shown in Figure 2.17 [254,255]. The EBM process is performed in a vacuum chamber at a pressure of 10^{-4} – 10^{-5} mbar, to avoid electron scattering and reduce contamination of the metals and alloys which have high affinity with gases. However, to hinder the powder electrostatic charging, a small helium pressure of 10^{-3} mbar is applied, so allowing powder spreading. A hot tungsten filament or a lanthanum hexaboride LaB_6 cathode are used for emission of electrons, which are then accelerated in an electric field up to energies of 60 KeV, then

the beam is focused and deflected by electromagnetic lenses. The very first layer is applied to the pre-heated substrate. Subsequently, the electron beam scans the powder layer at velocities typically around 4 m/s and melts the powder particles where necessary [253,256]. The differences in beam energy input (heat source) and chamber environment of EBM and SLM result in the different properties of the final products, i.e., different microstructures (like melt pool size, phase-type, and grain size) and mechanical properties (such as hardness, compressive, tensile, and fatigue properties) [254].

The high densification rate (up to 10^5 ms^{-1}) and microstructural homogeneity of the EBM built part induce an improvement in relative density and mechanical properties in comparison to those fabricated by SLM [257,258]. Moreover, compared to other laser-based AM systems, the EBM process usually induces lower residual stresses [259]and coarser microstructure due to the reduced cooling rates and temperature gradients [260].

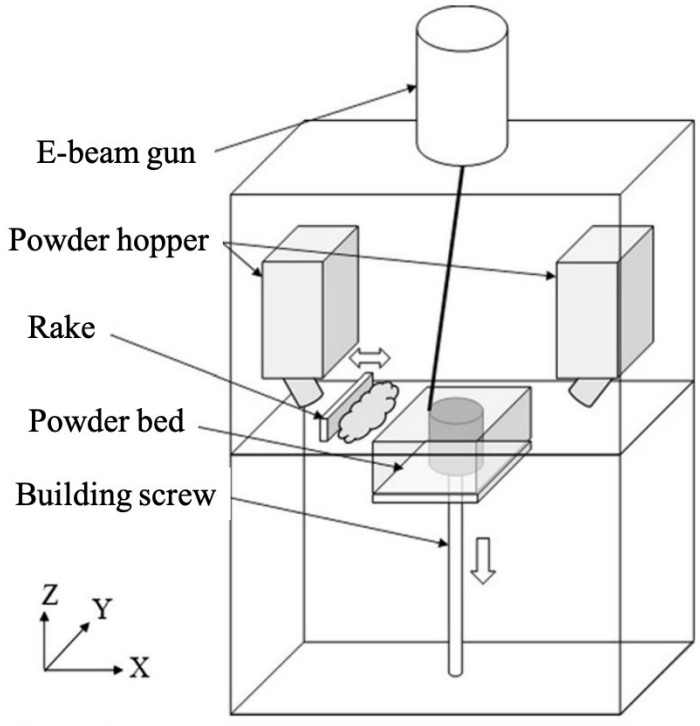

Figure 2.17. Schematic of electron beam melting process. Reprinted from [254]**.**

2.6.2.2. Directed Energy Deposition (DED)

DED is another well-developed additive manufacturing technique in which, instead of having a metal powder bed, an injected metal powder flows or a metal wire is fed through a nozzle and then the material is selectively deposited on a substrate and is simultaneously melted by a laser or an electron beam [261,262].

Using DED processes makes it possible not only to deposit multiple materials in one process step but also to reface or add layers onto objects (cladding or hard-facing) [262]. DED forms a mobile melt pool on the substrate and determines cooling rates substantially dependent on the powder feeding [263].

In the DED process, the laser/deposition head and/or the substrate can be moved in all directions, demonstrating the feasibility of 3D manufacturing by this process. A schematic illustration of the DED technique is demonstrated in Figure 2.18. As shown in this figure, the powder feeding nozzles are situated alongside the laser and can move with the laser if needed. Different DED machines use a various number of nozzles and can be equipped with single or multiple nozzles. Laser-substrate relative velocity (traverse speed), laser power and beam diameter, hatch spacing, powder feeding rate, and scanning strategy are the most critical process parameters that need to be optimized during the DED process. Due to the control flexibilities of the laser beam and powder deposition, DED is a promising method in which the existing parts can be repaired, or new structures can be added to the currently fabricated parts. In addition, parts with different materials or functionally graded objects can be also manufactured by using this technology. In terms of feedstocks, DED can be classified into two categories. In the first category (including Electron Beam Freeform Fabrication (EBF^3), which developed from the traditional welding technique, a metal wire is used as a feedstock, while in the second category (including the Laser Engineered Net Shaping (LENS) method [264] a powder flow is provided. The Electron Beam Freeform Fabrication (EBF^3) process is a DED method which firstly developed by NASA [265] for space-based applications. In this technique, the front end of the metal wire is melted by the electron beam and is then selectively sprayed on the top of the substrate to form a layer of material.

In the LENS process, a laser beam focuses on a point on the building substrate using a lens system and simultaneously the metal powder is injected to the point through a powder nozzle. A layer of material is fabricated when the melted powder and the materials beneath undergo a rapid solidification. After each layer fabrication, the laser lenses, as well as the powder nozzle, move up, and the processes of laser heating and powder injection are repeated for the next layer [264].

Plasma Deposition Manufacturing (PDM) also belongs to the DED group of AM techniques. In the PDM process, a continuous powder feed is supplied to a plasma-melted zone where the powder gets melted and then consolidated. Like the SLM process, an inert

gas such as argon, helium, or nitrogen was supplied into the PDM chamber to avoid or reduce oxidation of metallic powders. The 3D built parts are metallurgically acceptable; however, further experiments are necessary to optimize this process [266].

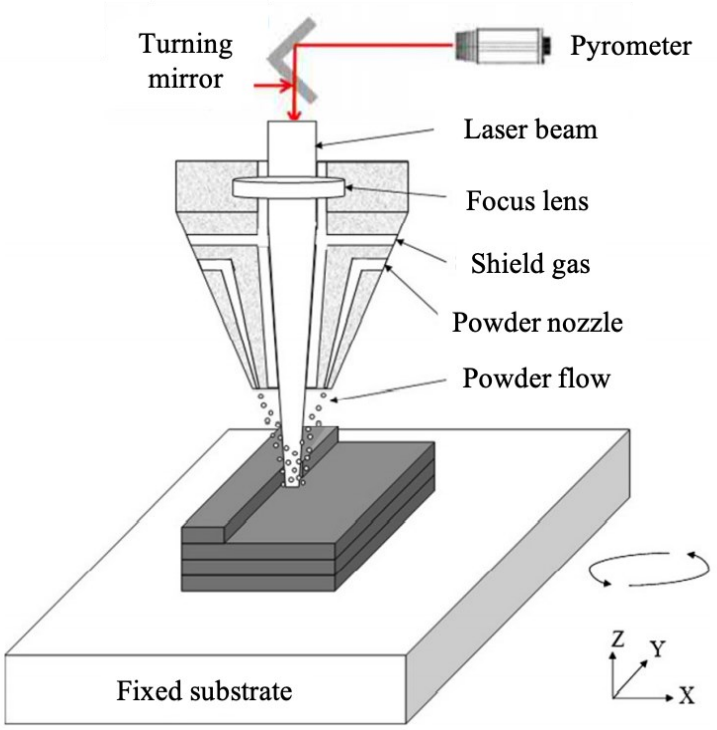

Figure 2.18. Schematic of the directed energy deposition (DED) process. Reprinted from [267]**.**

2.6.2.3. Fused deposition modeling (FDM)

FDM is one of the extrusion-based AM technologies which is commonly used for modeling, prototyping, and manufacturing applications. The basic principle of the FDM process is shown in Figure 2.19. In the FDM process, the material (usually a thermoplastic polymer) is passed through a liquefier head, in which the material is softened by heating elements, then through an extrusion nozzle and finally it is selectively deposited as a strand on the built structure., The extrusion nozzle tracks the cross-sectional geometry of the parts in a layer-by-layer mode on the basis of a CAD design to fabricate the 3D structure. Since the extruded material is still above the liquidus temperature when it contacts the building structure, it partially remelts the previous layer, favouring the inter-layer bonding [268].

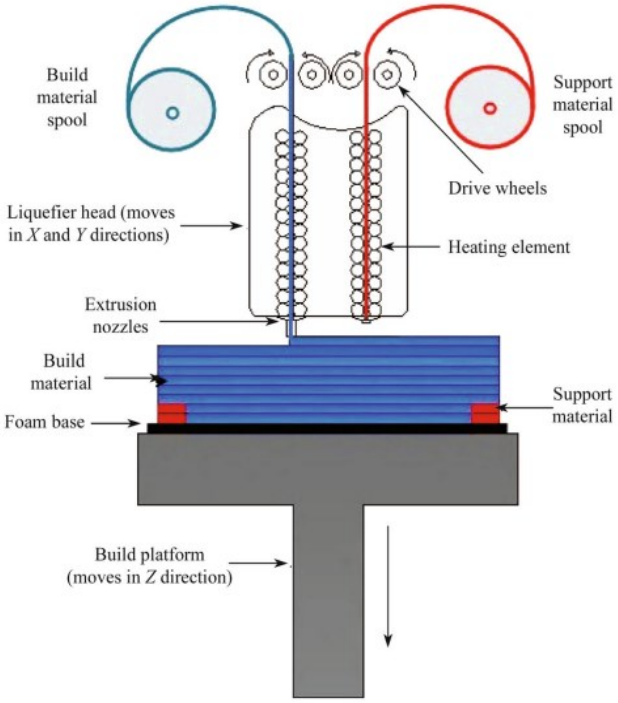

Figure 2.19. Schematic of the directed energy deposition process. Reprinted from [268]**.**

2.6.2.4. Bio plotting

Bio plotting is a novel extrusion-based AM method used for tissue engineering since living and nonliving biomaterials can be incorporated directly into the manufacturing process [269–272]. Bio plotting is a derivative of the FDM technology, involving the pneumatic extrusion of a biomaterial, which melts in the form of strands through a heated extrusion nozzle. The nozzle moves according to the CAD design along the building substrate, on which the strands of the biomaterial are deposited to progressively manufacture the 3D part (Figure 2.20). Unlike traditional FDM, bio plotting also permits plotting by more materials of comparable viscosity, developing a range of applicable materials [273].

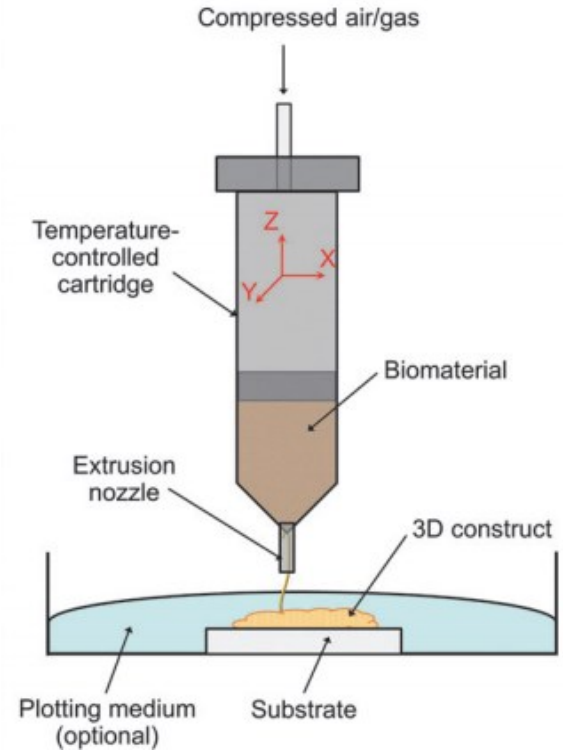

Figure 2.20. Schematic of bio plotting process. Reprinted from [273]**.**

2.6.2.5. Laminated Object Manufacturing (LOM)

LOM is an AM technique in which stock material comes in sheets or is fed endless by rolls. LOM uses the "bond-then-cut" principle in which a sheet of materials is laminated and bonded to the previously laid by using a hot roller. The heat and pressure are applied to the materials by this roller when it is passes over the sheet, which is covered by a thin layer of thermoplastic adhesive on its down-facing surface [274]. A focused beam of CO_2 laser cut the contour of the part when the new layer is bonded. The power of this laser is precisely adjusted to cut through only one lamination layer. Then, the built material is cut into small pieces with a crosshatch pattern, called "tiles", for easy removal (Figure 2.21). The stacked sheets are bonded layer-by-layer until the final layer is completed. Once all layers have been laminated, the product is cut from the base plate, and the waste material is removed, so called de-cubing. In some cases, the final product is polished for better surface finishing [274,275].

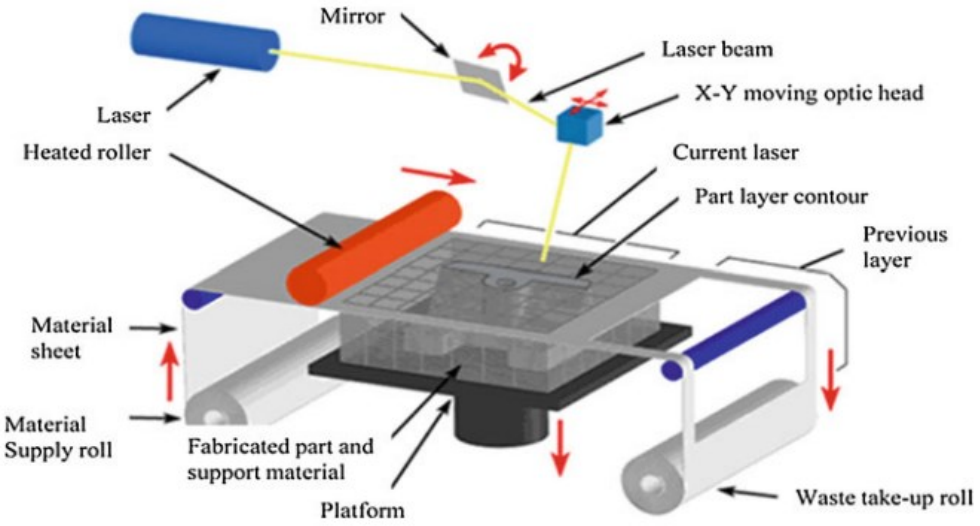

Figure 2.21. Schematic of laminated object manufacturing (LOM) process. Reprinted from [275]**.**

2.6.2.6. Binder jetting

Binder jetting, also named powder bed and inkjet head 3D printing, is basically developed to extend the normal two-dimensional printing to the third dimension. In practice, one or more nozzles are utilized to inject a liquid binder on the top of a powder bed, sticking the powder together. The nozzles move accordingly until they form a thin layer of bonded powders. This process continues until a three-dimensional structure is formed by stacking of layers [276,277].

As shown in Figure 2.22, the binder jetting system contains a building platform and a powder tank for supplying materials. First, a thin layer of powder is distributed on the platform by a leveling roller. Afterward, the inject nozzle moves along with the building platform for distribution and adhesion of powders. When the first layer of powder is bonded, the building platform moves downward to distribute and adhere to the next layer of powder. The repetition of this process in each layer resulted in the manufacturing of the 3D glued object. Then, the built structure is extracted from the powder bed for the following post-processing. The post-processing of the binder jetted parts is usually more complicated than that for other AM systems, in particular for metallic parts [277].

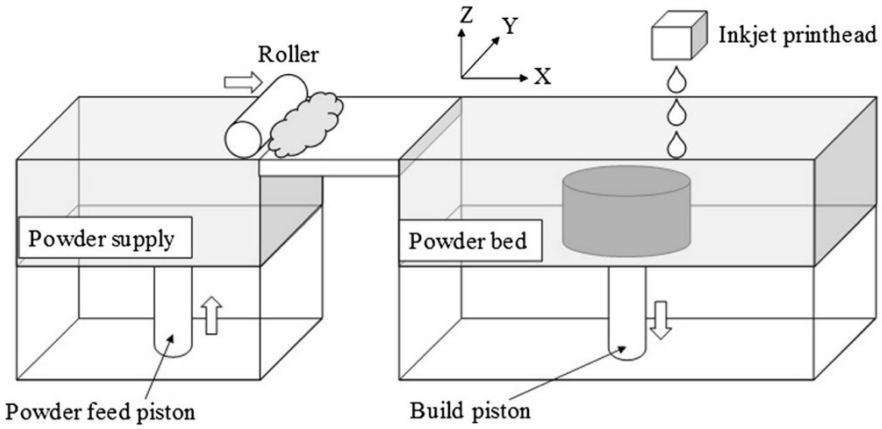

Figure 2.22. Schematic of binder jetting 3D process. Reprinted from [278]**.**

2.6.2.7. Stereo Lithography (SLA) and Direct Light Projection (DLP)

SLA was among the first additive manufacturing techniques based on the spatially controlled solidification of a liquid resin by photo-polymerization [279]. Like other freeform manufacturing methods, stereolithography is a process that allows the production of structures from a CAD file. In this process, layers of the liquid precursor in a vat are consecutively exposed to ultraviolet (UV) light and selectively solidified. After photo-polymerization of the first layer, a fresh resin film is applied, recoated the built layer, irradiated, and cured in the same manner. These steps are repeated until the solid 3D part are incrementally fabricated in a layer-by-layer manner. After draining and washing-off excess resin, the final structure is obtained. The required light for consolidation of the resin can be applied in two different ways, either from above (the free surface approach) or from below through a transparent vat (the constrained surface approach) [279,280]. In the latter case, the technique is also called DLP. The principle of the SLA process is illustrated schematically in Figure 2.23.

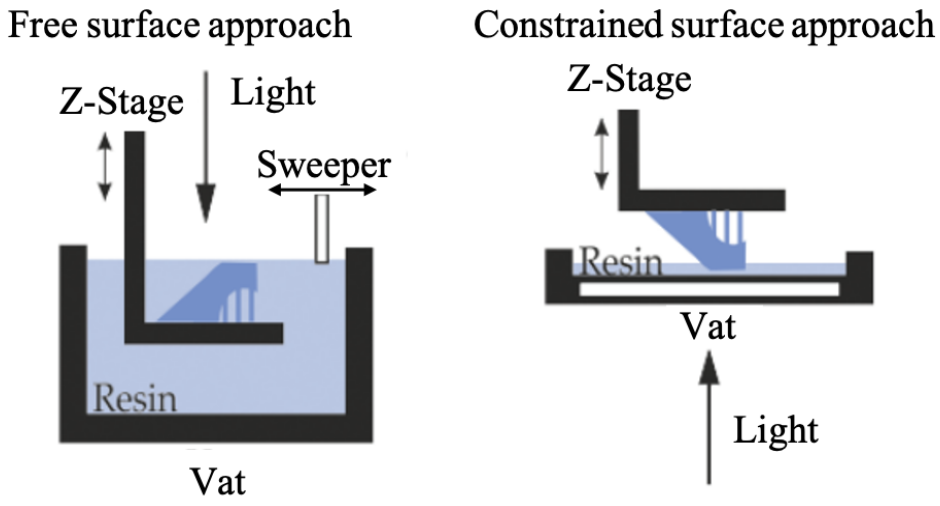

Figure 2.23. Schematic of stereolithography process. Reprinted from [279]**.**

2.7. Properties of metallic parts fabricated by SLM process

2.7.1. Surface characteristics

As previously shown, one of the advantages of the SLM is that it can fabricate parts with complex geometry. However, if compared with the precision forging and machining process, the surface quality of SLM fabricated parts is less satisfactory, due to a higher surface roughness (around 10–15 μm) [281]. In the SLM process, the molten pool tracks have a half-cylinder shape owing to surface tension effects. A number of molten pool tracks accumulated during solidification, and thus the surface morphology is the result of peak and valley overlapping [282], as shown in Figure 2.24a. Moreover, during the cooling process, un-melted particles remain adsorbed on the material surface, leading to high surface roughness (Figure 2.24b) [282,283]. Decreasing scan spacing and scanning speeds determine a more stable molten pool morphology and overlapping characteristics, which can effectively reduce surface roughness. Laser remelting can significantly decrease the surface roughness up to 80% by reducing the liquid contraction during solidification which is widely known as balling phenomenon. For industrial applications, the standard roughness of the parts should be less than 0.8 μm in order to prevent failures in the service [284]. However, in medical applications, a high surface roughness is reported to contribute to good biological properties. For example, according to Zhang et al. [285], the SLM-built Ti-6Al-4V implant with high surface roughness can favour bone

growth. In SLM-fabricated CoCr alloy dentures a high surface roughness was found to enhance the adhesive strength between the metal and the ceramics [286].

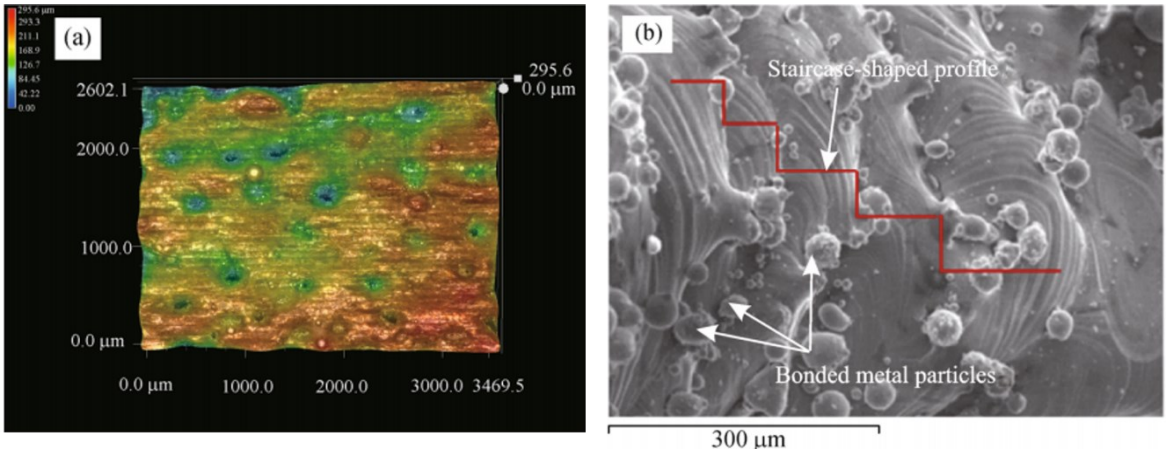

Figure 2.24. Surface morphology of the SLM fabricated parts. a) top view, b) surface view [275].

2.7.2. Microstructure

In SLM process, a laser beam scans the metal powders in a layer-by-layer fashion [287], and forms micro melt pools [288], which cools very fast (cooling rates from 10^3 to 10^8 K s^{-1}), resulting thereafter in a consolidated material. Rapid cooling not only compels a non-equilibrium solidification process but also favours solid solubility, refinement of grains, and possible formation of new metastable phases, even amorphous phases [289]. The complex heat-transfer conditions and large temperature gradients in the molten pools cause the formation of heterogeneous structures, such as overlapped arc-shaped molten pool boundaries (MPBs, Figure 2.25a) and microcellular dendritic structures (Figure 2.25b). Micron-size grains are often observed within each laser track, which tend to grow and change in morphology under higher laser energy density (Equation 2.1), lower scanning speed and lower hatch space [290–292]. It is reported that pores, cracks, and residual stresses are the main defects in SLM manufactured materials [215,293,294]. Two types of pores can be identified in SLM parts, including spherical pores and irregular pores (Figure 2.25c) [215]. The formation of spherical pores can be attributed to the presence of gas in the SLM chamber. This ambient gas present among the powder particles has no time to overflow from the micro-molten pools, resulting in pore formation. The irregular pores which more seriously impair the material mechanical properties are caused by the instability of the molten pool shape.

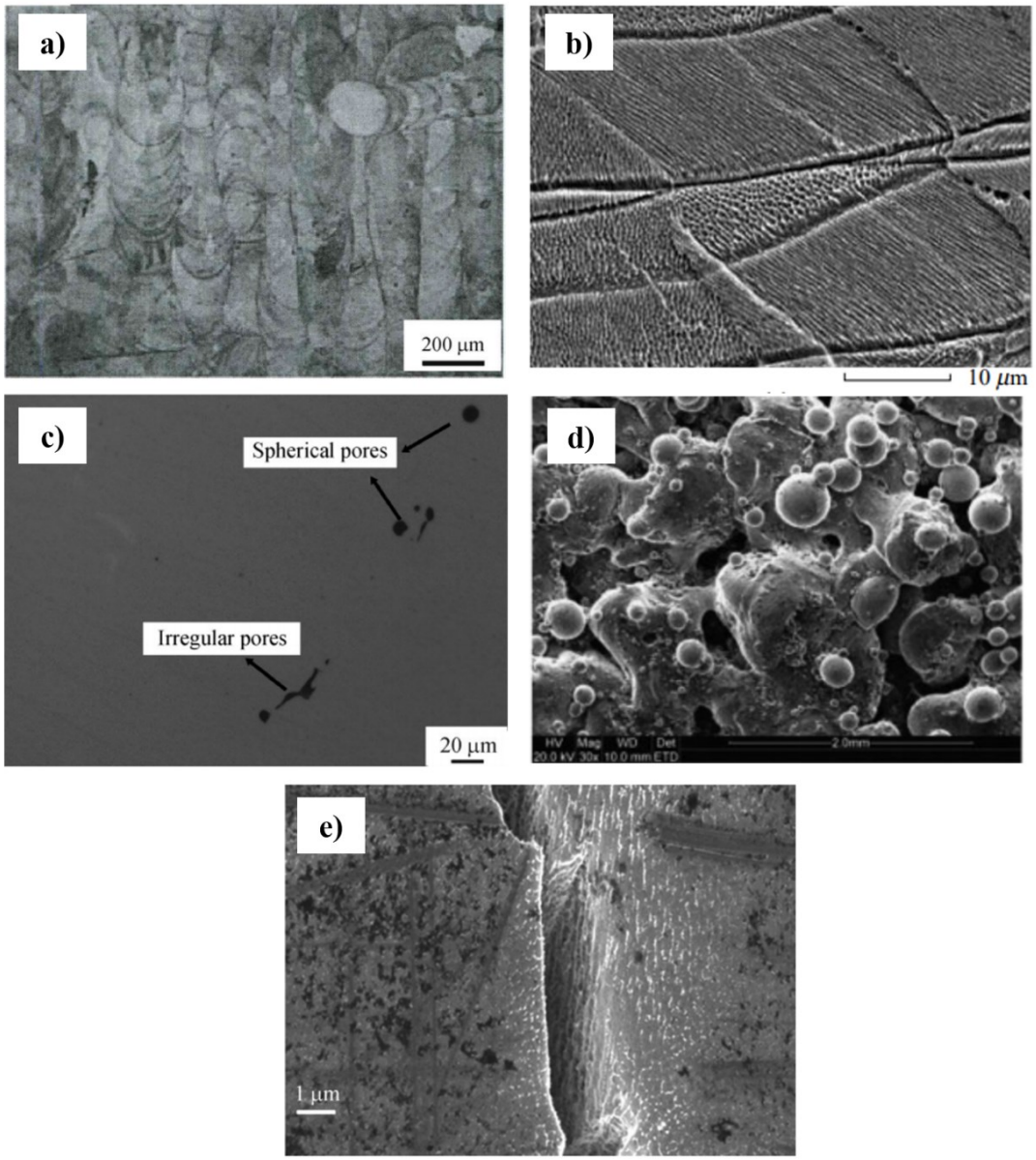

Figure 2.25. Microstructure and typical defects of SLM manufactured parts; a) Morphology of the cross-section parallel to the laser scanning direction [282]**; b) morphology of the cross-section perpendicular to the scanning direction** [281]**; c) porosities** [215]**; d) balling phenomenon** [295]**; cracks** [282]**.**

Liquid contraction during solidification lead to the balling phenomenon which is another common defect in SLM parts (Figure 2.25d). The origin of the balling phenomenon is generally connected to poor wetting between the liquid material and the substrate, but the complete formation mechanism has still to be elucidated. It can lead to discontinuous tracks and incomplete interline bonding, reducing the material density and even interrupting the building process [295]. Optimizing the process parameters [281,296],

improving the powder material properties, and controlling the quality of the building chamber atmosphere [297,298], can effectively suppress the balling effects.

The formation of cracks is another major concern in the SLM process and is connected to the rapid heating and cooling cycles, large solidification shrinkage and high coefficients of thermal expansion [299]. These cracks can be formed due to internal (micro-defects in the SLM parts) and external reasons (residual stress) [300]. Given their complicated forming mechanisms, it is usually very challenging to eliminate cracks by only optimizing SLM process parameters [301,302] (Figure 2.25e).

2.7.3. Mechanical properties

Considering the particular microstructure, complex crystal growth direction, and defects, the mechanical properties of the parts manufactured by SLM differ from those of casting or wrought parts. SLM components exhibit higher ultimate tensile strength, yield strength and hardness, lower ductility, and stronger anisotropy as compared to the wrought alloys. The possible explanation for this improvement is mainly attributed to the grain refinement in the SLM parts [237,300]. The strong anisotropy in mechanical properties is connected by some researchers [301], to the residual stresses induced by the complex thermal history experienced by SLM parts and by others to the anisotropy in microstructure [287,303,304].

2.7.4. Corrosion and electrochemical behaviour of SLM CoCrMo bioimplants

As described before, the corrosion behavior of the bioimplants directly affects their biocompatibility. Thus, corrosion behavior is the main feature for SLM fabricated bioimplants too and must be carefully assessed to validate the capability of SLM-built parts for biomedical applications. In order to achieve this validation, it is necessary to study and control the evolution of corrosion properties of SLM bioimplants in the body environment.

An experimental demonstration of the biocompatibility of CoCrMoW alloy fabricated by SLM was carried out by Xin et al. [305]. They used inductively coupled plasma atomic emission spectroscopy (ICP-AES) to measure the release of Co, Cr, and Mo for SLM specimens after immersion in artificial saliva solution at 37°C for 7 days. The SLM alloy showed significantly lower release of Co ions and higher proliferation of cells with

normal morphology than cast specimens, indicating higher biocompatibility of the SLM prepared alloy. In the same way, the in vitro biocompatibility of CoCrMo dental alloys manufactured by SLM was studied by Hedberg et al. [306]. They reported that the SLM CoCrMo alloys have lower corrosion and susceptibility to metal ion release if compared with the cast alloy. This was attributed to the fine cellular structure of the former alloys, having Mo-enriched (and Co-depleted) cell boundaries, no carbide precipitation and ε-phase formation at the alloy surface. They applied different SLM process parameters and revealed that the increased area of laser melt pool boundaries enhanced the susceptibility of the alloy for corrosion and metal release. In a recent study, Dong et al. [307] performed electrochemical tests to investigate the effect of microstructure on the corrosion behavior of SLM and cast CoCrMoW alloys. Their findings revealed that SLM alloy has higher corrosion resistance, in comparison to the cast alloy. This was mainly attributed to the microstructure (content and structure distribution of precipitates). The higher content of precipitates in cast alloy can cause severe microsegregation phenomena and inhomogeneities, which are the main reason for the inferior corrosion resistance. In addition, the segregated large precipitates work as effective micro-cathode, resulting pitting corrosion and increased corrosion rate. In another study, two different scanning strategies were applied to determine the properties of SLM fabricated CoCr based alloys for dental applications. They used line and island scanning strategies and revealed that the alloys fabricated through island scanning strategy offered better corrosion resistance, i.e., a lower amount of metal release in PBS solution [207]. In contrast, Xin et al. [225] reported that the SLM-fabricated and cast CoCrMo alloys exhibited no differences in their corrosion properties in artificial saliva solution where the corrosion rates resulted acceptable.

2.7.5. Effect of post-processing (heat treatments and HIP processing) on the properties of AM CoCrMo alloys

An investigation about the microstructural and mechanical property evolution of SLM CoCrMo after heat treatments at various temperatures was carried out by Kajima et al. [308]. They reported that an increase in heat-treatment temperature from 750 °C to 1150 °C resulted in an increase in the ductility of the alloy and a decrease in 0.2% offset yield strength and Vickers hardness. They observed that all heat-treated specimens consisted of both γ- and ε-phases, with the ε-phase volume fraction decreasing at elevating the heat-

treatment temperature. They also reported that after heating at a temperature as high as 1150 °C, the formation of equiaxed grains and a drastic relief of residual stresses occurred simultaneously, followed by an increase in elongation and a decrease in alloy strength. This indicated a complete specimen recrystallization driven by residual stresses. These findings were consistent with those of other researchers [309] which found that also in the case of CoCrMo samples obtained by direct metal laser-sintering (the SLS technique) and solution heat-treated at 1150°C, a complete recrystallization occurred, characterized by the formation of equiaxed grains with an average grain size of 40 μm. This was accompanied by a reduction of the tensile strength from 1378 MPa (as-printed) to 1114 MPa (sample treated at 1150°C). This was attributed to the increase in grain size from 0.6-1 μm (column width) to ~40 μm (grain size). In a recent work [310], the heat treatment of SLM CoCrMo at 1150°C for 1 h produced recrystallization and the disappearance of molten pool boundaries. Another study by Hitzler et al. [311] showed that the tensile properties, as well as the Vickers hardness, improved after a short and cost-effective heat treatment of 20 min at 800°C, while this treatment did not affect the homogenization of the microstructure. The aging behavior of SLM-built CoCrMo alloys was the central focus of a study by Zhang et al. [312], in which the authors observed an increase in the ε-phase content of the alloy at increasing aging time at both 750 and 900 °C and a nearly complete transformation in ε-phase after a 10 h aging at 900 °C. Moreover, during the heat treatments they observed the formation of honeycomb precipitates of $M_{23}C_6$ at the boundaries of the cellular structures of the original SLM alloy. The $M_{23}C_6$ precipitates and martensitic $\gamma \rightarrow \varepsilon$ transformation were found to be the reason for a microhardness enhancement at increasing aging times. The highest microhardness was obtained after aging at 900 °C for 10 h. In another work of the same authors [313], the effect of heat treatments of SLM-CoCrMo alloys on corrosion, mechanical properties and bacteria adhesion was studied. Their study showed that the SLM900 samples (annealed at 1200°C for 1 hour, then aged at 900°C) had the best corrosion resistance in artificial saliva and the least surface propagation and overall quantity of bacteria. However, its elongation did not meet the ASTM F75 standard requirements due to the high ε-phase content, which induced a brittle fracture. Conversely, as-SLM and SLM1200D (annealed at 1200°C for 1 h followed by quenching in water) exhibited a quasi-cleavage fracture mechanism and higher tensile strength, yield strength, and elongation than those indicated in ASTM F75 standard. In a study aiming at

assessing the effect of heat treatment on the properties of a binder jet 3D-printed CoCr based alloy, Mostafaei et al. [314] found that solid-state sintering occurred at temperatures below 1280 °C and involved the precipitation of Cr-rich carbides within the grains; instead, super solidus liquid phase sintering occurred at 1290 °C and higher temperature with formation of Co-rich solid solution regions surrounded by eutectic carbides. Subsequent aging at 900 °C for 10 h, resulted in the martensitic $\gamma \rightarrow \varepsilon$ transformation as well as in an increase in eutectic carbide precipitation at grain boundaries and nano-sized carbide formation within grains, where the average hardness reached 491 ± 58 HV at grain boundaries and 322 ± 29 HV within grains.

Other studies focused on the HIP treatment capability to reduce porosity and on the consequent mechanical properties. This treatment was found to reduce the number of locations where failure may initiate, extending the component lifetime, and significantly improving the fatigue resistance, yield strength and ultimate tensile strength [315].

To determine the effect of HIP applied to SLM build CoCrMo alloys on mechanical properties, Haan et al. [316] studied the as-SLM and SLM+HIP CoCrMo alloys. They confirmed that post-densification treatment by HIP resulted in the closure of all remaining pores and complete recrystallization of the microstructure, improving the mechanical properties of the alloy in terms of fatigue strength. In another study by Kircher [317], the effect of HIP processing on the properties of EBM CoCrMo alloy was investigated. They reported that as-EBM CoCrMo alloy exhibited brittle characteristics and anisotropic mechanical behavior, while the applied post-processing HIP treatment determined the dissolution of carbides and the removal of the alloy anisotropy.

References

[1] D.F. Williams, D.F. Williams, The Williams Dictionary of Biomaterials, Liverpool University Press, 1999.

[2] G. Manivasagam, D. Dhinasekaran, A. Rajamanickam, Biomedical Implants : Corrosion and its Prevention - A Review, (2010) 40–54.

[3] B.J.C. Luthringer, F. Feyerabend, R. Willumeit-römer, Magnesium-based implants : a mini-review, (2015).

[4] M.J. Yaszemski, D.J. Trantolo, K. Lewandrowski, V. Hasirci, D.E. Altobelli, D.L. Wise, Biomaterials in Orthopedic s, 2004.

[5] D.F. Williams, On the mechanisms of biocompatibility., Biomaterials. 29 (2008) 2941–2953.

[6] J. Walczak, F. Shahgaldi, F. Heatley, In vivo corrosion of 316L stainless-steel hip implants: morphology and elemental compositions of corrosion products, Biomaterials. 19 (1998) 229–237.

[7] M. Prikryl, S.C. Srivastava, G.R. Viviani, M.B. Ives, G.R. Purdy, Role of corrosion in Harrington and Luque rods failure, Biomaterials. 10 (1989) 109–117.

[8] C.P. Case, V.G. Langkamer, C. James, M.R. Palmer, A.J. Kemp, P.F. Heap, L. Solomon, Widespread dissemination of metal debris from implants, J. Bone Joint Surg. Br. 76-B (1994) 701–712.

[9] M. Sumita, T. Hanawa, I. Ohnishi, T. Yoneyama, Failure processes in biometallic materials, (2003).

[10] M. Niinomi, T. Narushima, M. Nakai, B. Reactions, Advances in Metallic Biomaterials, n.d.

[11] Q. Chen, G.A. Thouas, Metallic implant biomaterials, Mater. Sci. Eng. R Reports. 87 (2015) 1–57.

[12] P. Wiles, The surgery of the osteo-arthritic hip, BJS (British J. Surgery). 45 (1958) 488–497.

[13] P. Wiles, The Surgery of the Osteo-Arthritic Hip, (2003) 3–16.

[14] M. Taira, E.P. Lautenschlagert, In vitro corrosion fatigue of 316L cold worked stainless steel, 26 (1992) 1131–1139.

[15] T. Roland, D. Retraint, K. Lu, J. Lu, Fatigue life improvement through surface nanostructuring of stainless steel by means of surface mechanical attrition treatment, 54 (2006) 1949–1954.

[16] T.S. Sudarshan, T.S. Srivatsan, D.P. Harvey, Fatigue processes in metals—role of aqueous environments, Eng. Fract. Mech. 36 (1990) 827–852.

[17] R. Ebara, Procedia Engineering Corrosion fatigue crack initiation behavior of stainless steels, Procedia Eng. 2 (2010) 1297–1306. https://doi.org/10.1016/j.proeng.2010.03.141.

[18] N.R. Patel, P.P. Gohil, A Review on Biomaterials : Scope , Applications & Human Anatomy Significance, 2 (2012).

[19] J.R. Davis, Handbook of Materials for Medical Devices. 2003, Mater. Park. Ohio ASM Int. (n.d.).

[20] J. Alvarado, R. Maldonado, J. Marxuach, R. Otero, Biomechanics of hip and knee prostheses, Appl. Eng. Mech. Med. GED–University Puerto Rico Mayaguez. (2003) 1–20.

[21] A. Balamurugan, S. Rajeswari, G. Balossier, A.H.S. Rebelo, J.M.F. Ferreira, Corrosion aspects of metallic implants — An overview, Mater. Corros. 59 (2008) 855–869.

[22] C.-W. Kang, F.-Z. Fang, State of the art of bioimplants manufacturing: part I, Adv. Manuf. 6 (2018) 20–40.

[23] R.M. Pilliar, Metallic biomaterials, in: Biomed. Mater., Springer, 2009: pp. 41–81.

[24] M.R. Menezes, C. Godoy, V.T.L. Buono, M.M.M. Schvartzman, J.C.A.-B. Wilson, Effect of shot peening and treatment temperature on wear and corrosion resistance of sequentially plasma treated AISI 316L steel, Surf. Coatings Technol. 309 (2017) 651–662.

[25] M. Talha, C.K. Behera, O.P. Sinha, A review on nickel-free nitrogen containing austenitic stainless steels for biomedical applications, Mater. Sci. Eng. C. 33 (2013) 3563–3575.

[26] M. Liu, C. Li, L. Liu, Y. Ye, D. Dastan, H. Garmestani, Inhibition of stress corrosion cracking in 304 stainless steel through titanium ion implantation, Mater.

Sci. Technol. 36 (2020) 284–292.

[27] K. Majid, T. Crowder, E. Baker, K. Baker, D. Koueiter, E. Shields, H.N. Herkowitz, Analysis of in vivo corrosion of 316L stainless steel posterior thoracolumbar plate systems: a retrieval study, Clin. Spine Surg. 24 (2011) 500–505.

[28] J. Buhagiar, A. Spiteri, M. Sacco, E. Sinagra, H. Dong, Augmentation of crevice corrosion resistance of medical grade 316LVM stainless steel by plasma carburising, Corros. Sci. 59 (2012) 169–178.

[29] J. Buhagiar, H. Dong, Corrosion properties of S-phase layers formed on medical grade austenitic stainless steel, J. Mater. Sci. Mater. Med. 23 (2012) 271–281.

[30] T. Yamamuro, Patterns of osteogenesis in relation to various biomaterials, J Jpn Soc Biomater. 7 (1989) 19–23.

[31] D.M. Brunette, P. Tengvall, M. Textor, P. Thomsen, Titanium in Medicine: Material Science, Surface Science, Engineering, Biological Responses and Medical Applications, Springer Berlin Heidelberg, 2012.

[32] M. Niinomi, T. Hattori, K. Morikawa, T. Kasuga, A. Suzuki, H. Fukui, S. Niwa, Development of low rigidity β-type titanium alloy for biomedical applications, Mater. Trans. 43 (2002) 2970–2977.

[33] N. Sumitomo, K. Noritake, T. Hattori, K. Morikawa, S. Niwa, K. Sato, M. Niinomi, Experiment study on fracture fixation with low rigidity titanium alloy, J. Mater. Sci. Mater. Med. 19 (2008) 1581–1586.

[34] M. Niinomi, M. Nakai, J. Hieda, Acta Biomaterialia Development of new metallic alloys for biomedical applications, Acta Biomater. 8 (2012) 3888–3903.

[35] J. Bronzino, J. Park, Biomaterials: principles and applications, (2002).

[36] N.S. Manam, W.S.W. Harun, D.N.A. Shri, S.A.C. Ghani, T. Kurniawan, M.H. Ismail, M.H.I. Ibrahim, Study of corrosion in biocompatible metals for implants: A review, J. Alloys Compd. 701 (2017) 698–715.

[37] M. Niinomi, C.J. Boehlert, Titanium alloys for biomedical applications, in: Adv. Met. Biomater., Springer, 2015: pp. 179–213.

[38] C. Veiga, J.P. Davim, A.J.R. Loureiro, Properties and applications of titanium

alloys: a brief review, Rev. Adv. Mater. Sci. 32 (2012) 133–148.

[39] S.J.L. Sullivan, L.D.T. Topoleski, Surface Modifications for Improved Wear Performance in Artificial Joints: A Review, JOM. 67 (2015) 2502–2517.

[40] V. Peretti, S. Ferraris, G. Gautier, C. Hellmich, O. Lahayne, B. Stella, S. Yamaguchi, S. Spriano, Surface treatments for boriding of Ti6Al4V alloy in view of applications as a biomaterial, Tribol. Int. 126 (2018) 21–28.

[41] A. Kocijan, I. Milošev, B. Pihlar, Cobalt-based alloys for orthopaedic applications studied by electrochemical and XPS analysis, J. Mater. Sci. Mater. Med. 15 (2004) 643–650.

[42] M. Jenko, M. Gorenšek, M. Godec, M. Hodnik, B.Š. Batič, Č. Donik, J.T. Grant, D. Dolinar, Surface chemistry and microstructure of metallic biomaterials for hip and knee endoprostheses, Appl. Surf. Sci. 427 (2018) 584–593.

[43] F. Contu, B. Elsener, H. Böhni, Corrosion behaviour of CoCrMo implant alloy during fretting in bovine serum, Corros. Sci. 47 (2005) 1863–1875.

[44] L. Wang, J. Luo, Electrochemical behavior of CoCrMo implant in Ringer ' s solution, (2013) 1323–1328. https://doi.org/10.1002/sia.5281.

[45] B. Stojanović, C. Bauer, C. Stotter, T. Klestil, S. Nehrer, F. Franek, M. Rodríguez Ripoll, Tribocorrosion of a CoCrMo alloy sliding against articular cartilage and the impact of metal ion release on chondrocytes, Acta Biomater. 94 (2019) 597–609.

[46] S. Pramanik, A.K. Agarwal, K.N. Rai, Chronology of total hip replacement and materials development Chronology of Total Hip Joint Replacement and Materials Development, (2005).

[47] E.J. Evans, I.T. Thomas, The in vitro toxicity of cobalt-chrome-molybdenum alloy and its constituent metals., Biomaterials. 7 (1986) 25–29.

[48] J. Alvarado, R. Maldonado, J. Marxuach, R. Otero, To succeed in life, humor does not cost --- Goyal BIOMECHANICS OF HIP AND KNEE PROSTHESES 1 Jorge Alvarado, Ricardo Maldonado, Jorge Marxuach and Ruben Otero 2, (2003) 6–22.

[49] C. Valero Vidal, A. Igual Muñoz, Electrochemical characterisation of biomedical alloys for surgical implants in simulated body fluids, Corros. Sci. 50 (2008) 1954–1961.

[50] V. CV, M. AI, Effect of thermal treatment and applied potential on the electrochemical behaviour of CoCrMo biomedical alloy, Electrochim. Acta. 54 (2009) 1798–1809. https://doi.org/10.1016/j.electacta.2008.10.018.

[51] O. Öztürk, Metal ion release from nitrogen ion implanted CoCrMo orthopedic implant material, 200 (2006) 5687–5697.

[52] E. Bettini, C. Leygraf, C. Lin, P. Liu, J. Pan, Influence of grain boundaries on dissolution behavior of a biomedical CoCrMo alloy: in-situ electrochemical-optical, AFM and SEM/TEM studies, J. Electrochem. Soc. 159 (2012) C422.

[53] C. Valero Vidal, Study of the degradation mechanisms of the CoCrMo biomedical alloy in physiological media by electrochemical techniques and surface analysis, (2012).

[54] J.R. Davis, A.S.M.I.H. Committee, Nickel, Cobalt, and Their Alloys, ASM International, 2000.

[55] C.T. Sims, N.S. Stoloff, W.C. Hagel, superalloys II, Wiley New York, 1987.

[56] C.R. Brooks, O.: A.S. for M. Metals Park, ASM, Heat treatment, structure and properties of nonferrous alloys, Metals Park, Ohio, 1982.

[57] H. Baker, H. Okamoto, ASM Handbook. Vol. 3. Alloy Phase Diagrams, ASM Int. Mater. Park. Ohio 44073-0002, USA, 1992. 501. (1992).

[58] Y. Yan, A. Neville, D. Dowson, Tribo-corrosion properties of cobalt-based medical implant alloys in simulated biological environments, 263 (2007) 1105–1111.

[59] A.J. Saldívar-García, H.F. López, Microstructural effects on the wear resistance of wrought and as-cast Co-Cr-Mo-C implant alloys, J. Biomed. Mater. Res. Part A An Off. J. Soc. Biomater. Japanese Soc. Biomater. Aust. Soc. Biomater. Korean Soc. Biomater. 74 (2005) 269–274.

[60] S. Kurosu, H. Matsumoto, A. Chiba, Isothermal phase transformation in biomedical Co-29Cr-6Mo alloy without addition of carbon or nitrogen, Metall. Mater. Trans. A. 41 (2010) 2613–2625.

[61] K. Yoda, Suyalatu, A. Takaichi, N. Nomura, Y. Tsutsumi, H. Doi, S. Kurosu, A. Chiba, Y. Igarashi, T. Hanawa, Effects of chromium and nitrogen content on the

microstructures and mechanical properties of as-cast Co-Cr-Mo alloys for dental applications, Acta Biomater. 8 (2012) 2856—2862.

[62] P. V Muterlle, M. Zendron, M. Perina, R. Bardini, A. Molinari, Microstructure and tensile properties of metal injection molding Co–29Cr–6Mo–0.23 C alloy, J. Mater. Sci. 45 (2010) 1091–1099.

[63] O.S. Iron, C. Alloys, A. Castings, H.R. Steels, H. Steels, I. Alloys, C. Alloys, ASTM F1537-11: Standard Specification for Wrought Cobalt-28Chromium-6Molybdenum Alloys for Surgical Implants, i (2011) 1–4.

[64] C. Requirements, O.S. Iron, C. Alloys, H.R. Steels, H. Steels, I. Alloys, C. Alloys, ASTM F75-12: Cobalt-28 Chromium-6 Molybdenum Alloy Castings and Casting Alloy for Surgical Implants (UNS R30075), (2012) 1–4.

[65] A. Ouerd, C. Alemany-Dumont, B. Normand, S. Szunerits, Reactivity of CoCrMo alloy in physiological medium: Electrochemical characterization of the metal/protein interface, Electrochim. Acta. 53 (2008) 4461–4469.

[66] R. Varano, Wear behaviour of cobalt-chromium-molybdenum alloys used in metal-on-metal hip implants., (2005).

[67] R. Varano, Structure-Property investigation of Co-Cr-Mo alloys used in metal-metal total hip replacements, (1998).

[68] V. Hasirci, N. Hasirci, Fundamentals of biomaterials, Springer, 2018.

[69] H.S. Dobbs, J.L.M. Robertson, Heat treatment of cast Co-Cr-Mo for orthopaedic implant use, J. Mater. Sci. 18 (1983) 391–401.

[70] S.B. Goodman, E. Gómez Barrena, M. Takagi, Y.T. Konttinen, Biocompatibility of total joint replacements: A review, J. Biomed. Mater. Res. Part A. 90A (2009) 603–618.

[71] A.T. Kuhn, Corrosion of Co-Cr alloys in aqueous environments, Biomaterials. 2 (1981) 68–77.

[72] M.X. Yao, J.B.C. Wu, W. Xu, R. Liu, Metallographic study and wear resistance of a high-C wrought Co-based alloy Stellite 706K, Mater. Sci. Eng. A. 407 (2005) 291–298.

[73] E. Bettini, T. Eriksson, M. Boström, C. Leygraf, J. Pan, Influence of metal carbides

on dissolution behavior of biomedical CoCrMo alloy: SEM, TEM and AFM studies, Electrochim. Acta. 56 (2011) 9413–9419.

[74] Y.-S. Li, K. Wang, P. He, B.X. Huang, P. Kovacs, Surface-enhanced Raman spectroelectrochemical studies of corrosion films on implant Co-Cr-Mo alloy in biosimulating solutions, J. Raman Spectrosc. 30 (1999) 97–103.

[75] M.A. Wimmer, J. Loos, R. Nassutt, M. Heitkemper, A. Fischer, The acting wear mechanisms on metal-on-metal hip joint bearings: in vitro results, Wear. 250 (2001) 129–139.

[76] R. Varano, J.D. Bobyn, J.B. Medley, S. Yue, The effect of microstructure on the wear of cobalt-based alloys used in metal-on-metal hip implants, Proc. Inst. Mech. Eng. Part H J. Eng. Med. 220 (2006) 145–159.

[77] K. Ueda, K. Nakaie, S. Namba, T. Yoneda, K. Ishimizu, T. Narushima, Mass Loss and Ion Elution of Biomedical Co–Cr–Mo Alloys during Pin-on-Disk Wear Tests, Mater. Trans. (2013) ME201316.

[78] Y. Chen, Y. Li, S. Kurosu, K. Yamanaka, N. Tang, Y. Koizumi, A. Chiba, Effects of sigma phase and carbide on the wear behavior of CoCrMo alloys in Hanks' solution, Wear. 310 (2014) 51–62.

[79] T. Narushima, S. Mineta, Y. Kurihara, K. Ueda, Precipitates in Biomedical Co-Cr Alloys, JOM. 65 (2013) 489–504.

[80] T. Narushima, New-generation metallic biomaterials, in: Met. Biomed. Devices, Elsevier, 2019: pp. 495–521.

[81] T. Narushima, S. Mineta, K. Ueda, π-phase and χ-phase: new precipitates in biomedical Co–Cr–Mo alloys, in: Interface Oral Heal. Sci. 2011, Springer, 2012: pp. 72–80.

[82] T. Narushima, S. Mineta, S. Namba, T. Yoneda, K. Ueda, Precipitates in biomedical Co-Cr-Mo-C-Si-Mn alloys, in: Adv. Mater. Res., Trans Tech Publ, 2011: pp. 51–58.

[83] S. Mineta, S. Namba, T. Yoneda, K. Ueda, T. Narushima, Precipitates in biomedical Co-28Cr-6Mo-(0–0.41) C alloys heat-treated at 1473 K to 1623 K (1200 C to 1350 C), Metall. Mater. Trans. A. 43 (2012) 3351–3358.

[84] M. Pohl, O. Storz, Sigma-phase in duplex-stainless steels, Zeitschrift Für Met. 95 (2004).

[85] J.-M. Joubert, Crystal chemistry and Calphad modeling of the σ phase, Prog. Mater. Sci. 53 (2008) 528–583.

[86] J.S. Kasper, The ordering of atoms in the chi-phase of the iron-chromium-molybdenum system, Acta Metall. 2 (1954) 456–461.

[87] J.-M. Joubert, M. Phejar, Crystal chemistry and Calphad modelling of the χ phase, Prog. Mater. Sci. 54 (2009) 945–980.

[88] M. Kikuchi, S. Nagakura, S. Oketani, Crystal structures of transition metal carbides, Tetsu-to-Hagané. 57 (1971) 1009–1053.

[89] J.M. Guilemany, J.M. De Paco, J.R. Miguel, J. Nutting, Characterization of the W 2 C phase formed during the high velocity oxygen fuel spraying of a WC+ 12 pct Co powder, Metall. Mater. Trans. A. 30 (1999) 1913–1921.

[90] D.S. Janisch, M. Garel, A. Eder, W. Lengauer, K. Dreyer, H. van den Berg, Sintering, characterisation, and analysis of functional gradient hardmetals, Int. J. Refract. Met. Hard Mater. 26 (2008) 179–189.

[91] A.J. Clemow, B.L. Daniell, Solution treatment behavior of Co-Cr-Mo alloy., J. Biomed. Mater. Res. 13 (1979) 265–279.

[92] T. Kilner, R.M. Pilliar, G.C. Weatherly, C. Allibert, Phase identification and incipient melting in a cast Co-Cr surgical implant alloy, J. Biomed. Mater. Res. 16 (1982) 63–79.

[93] S. Mineta, S. Namba, T. Yoneda, K. Ueda, T. Narushima, Precipitates in as-cast and heat-treated ASTM F75 Co-Cr-Mo-C alloys containing Si and/or Mn, Metall. Mater. Trans. A. 42 (2011) 1941–1949.

[94] J. V Giacchi, O. Fornaro, H. Palacio, Microstructural evolution during solution treatment of Co–Cr–Mo–C biocompatible alloys, Mater. Charact. 68 (2012) 49–57.

[95] J.R. Lane, N.J. Grant, Carbide reactions in high temperature alloys, Trans. Am. Soc. Met. 44 (1952) 113–137.

[96] H. Mancha, J.I. Escalante, G. Mendoza, M. Méndez, E. Carranza, F. Cepedal, E. Valdés, M 23 C 6 carbide dissolution mechanisms during heat treatment of ASTM

F-75 implant alloys, Metall. Mater. Trans. A. 32 (2001) 979–984.

[97] P.C. Noble, Special materials for the replacement of human joints, in: Met. Forum, 1983: pp. 59–80.

[98] M. Gomez, H. Mancha, A. Salinas, J.L. Rodriguez, J. Escobedo, M. Castro, M. Mendez, Relationship between microstructure and ductility of investment cast ASTM F-75 implant alloy, J. Biomed. Mater. Res. An Off. J. Soc. Biomater. Japanese Soc. Biomater. 34 (1997) 157–163.

[99] J.W. Weeton, R.A. Signorelli, Effect of heat treatment upon microstructures microconstituents and hardness of a wrought cobalt-base alloy, Trans ASM. 47 (1955) 815–845.

[100] R.N.J. Taylor, R.B. Waterhouse, A study of the ageing behaviour of a cobalt based implant alloy, J. Mater. Sci. 18 (1983) 3265–3280.

[101] L. Zhuang, E.W. Langer, Carbide Precipitation in Cast Co--Cr--Mo Alloys Used for Surgical Implants, Z. Met. 80 (1989) 251–257.

[102] C. Montero-Ocampo, H. Lopez, M. Talavera, Effect of alloy preheating on the mechanical properties of as-cast Co-Cr-Mo-C alloys, Metall. Mater. Trans. A. 30 (1999) 611–620.

[103] J. Escobedo, J. Méndez, D. Cortés, J. Gómez, M. Méndez, H. Mancha, Effect of nitrogen on the microstructure and mechanical properties of a Co□ Cr□ Mo alloy, Mater. Des. 17 (1996) 79–83.

[104] M. Caudillo, M. Herrera–Trejo, M.R. Castro, E. Ramírez, C.R. González, J.I. Juárez, On carbide dissolution in an as-cast ASTM F-75 alloy, J. Biomed. Mater. Res. An Off. J. Soc. Biomater. Japanese Soc. Biomater. Aust. Soc. Biomater. Korean Soc. Biomater. 59 (2002) 378–385.

[105] H.F. López, A.J. Saldivar-Garcia, Martensitic transformation in a cast Co-Cr-Mo-C alloy, Metall. Mater. Trans. A. 39 (2008) 8–18.

[106] S. Mineta, S. Namba, T. Yoneda, K. Ueda, T. Narushima, Carbide formation and dissolution in biomedical Co-Cr-Mo alloys with different carbon contents during solution treatment, Metall. Mater. Trans. A. 41 (2010) 2129–2138.

[107] S.-H. Lee, N. Nomura, A. Chiba, Significant improvement in mechanical

properties of biomedical Co-Cr-Mo alloys with combination of N addition and Cr-enrichment, Mater. Trans. (2008) 801150296.

[108] H.R. Lashgari, S. Zangeneh, F. Hasanabadi, M. Saghafi, Microstructural evolution during isothermal aging and strain-induced transformation followed by isothermal aging in Co-Cr-Mo-C alloy: A comparative study, Mater. Sci. Eng. A. 527 (2010) 4082–4091.

[109] J. V Giacchi, C.N. Morando, O. Fornaro, H.A. Palacio, Microstructural characterization of as-cast biocompatible Co–Cr–Mo alloys, Mater. Charact. 62 (2011) 53–61.

[110] S. Mineta, S. Namba, T. Yoneda, K. Ueda, T. Narushima, Phase and formation/dissolution of precipitates in biomedical Co-Cr-Mo alloys with nitrogen addition, Metall. Mater. Trans. A. 44 (2013) 494–503.

[111] K. Yamanaka, M. Mori, S. Kurosu, H. Matsumoto, A. Chiba, Ultrafine grain refinement of biomedical Co-29Cr-6Mo alloy during conventional hot-compression deformation, Metall. Mater. Trans. A. 40 (2009) 1980–1994.

[112] S. Kurosu, H. Matsumoto, A. Chiba, Grain refinement of biomedical Co–27Cr–5Mo–0.16 N alloy by reverse transformation, Mater. Lett. 64 (2010) 49–52.

[113] K. Yamanaka, M. Mori, A. Chiba, Origin of significant grain refinement in Co-Cr-Mo alloys without severe plastic deformation, Metall. Mater. Trans. A. 43 (2012) 4875–4887.

[114] K. Yamanaka, M. Mori, A. Chiba, Mechanical properties of as-forged Ni-free Co–29Cr–6Mo alloys with ultrafine-grained microstructure, Mater. Sci. Eng. A. 528 (2011) 5961–5966.

[115] J. Cawley, J.E.P. Metcalf, A.H. Jones, T.J. Band, D.S. Skupien, A tribological study of cobalt chromium molybdenum alloys used in metal-on-metal resurfacing hip arthroplasty, Wear. 255 (2003) 999–1006.

[116] J.J. Jacobs, R.M. Latanision, R.M. Rose, S.J. Veeck, The effect of porous coating processing on the corrosion behavior of cast Co–Cr–Mo surgical implant alloys, J. Orthop. Res. 8 (1990) 874–882.

[117] S. Hiromoto, E. Onodera, A. Chiba, K. Asami, T. Hanawa, Microstructure and

corrosion behaviour in biological environments of the new forged low-Ni Co–Cr–Mo alloys, Biomaterials. 26 (2005) 4912–4923.

[118] M.T. Mathew, J.J. Jacobs, M.A. Wimmer, Wear-corrosion synergism in a CoCrMo hip bearing alloy is influenced by proteins, Clin. Orthop. Relat. Res. 470 (2012) 3109–3117.

[119] J.B. Vander Sande, J.R. Coke, J. Wulff, A transmission electron microscopy study of the mechanisms of strengthening in heat-treated Co-Cr-Mo-C alloys, Metall. Trans. A. 7 (1976) 389–397.

[120] Z. Oksiuta, J.R. Dabrowski, Rotary cold re-pressing and heat treatment of sintered materials from Co–Cr–Mo alloy powder, Powder Metall. 45 (2002) 63–66.

[121] H. V Atkinson, S. Davies, Fundamental aspects of hot isostatic pressing: an overview, Metall. Mater. Trans. A. 31 (2000) 2981–3000.

[122] H.D. Hanes, D.A. Seifert, C.R. Watts, Metals, C.I.C. (U.S.), Hot Isostatic Processing, Battelle Press, 1979.

[123] K.D. Timmerhaus, High-Pressure Science and Technology: Volume 1: Physical Properties and Material Synthesis / Volume 2: Applications and Mechanical Properties, Springer US, 2013. https://books.google.it/books?id=NRLrBwAAQBAJ.

[124] N.L. Loh, K.Y. Sia, An overview of hot isostatic pressing, J. Mater. Process. Technol. 30 (1992) 45–65.

[125] H. Yamada, Strength of biological materials, Williams & Wilkins, Baltimore, 1970.

[126] F.S. Georgette, Effect of hot isostatic pressing on the mechanical and corrosion properties of a cast, porous-coated Co-Cr-Mo alloy, in: Quant. Charact. Perform. Porous Implant. Hard Tissue Appl., ASTM International, 1987.

[127] D.F. Williams, Biocompatibility of clinical implant materials, CRC Press, Boca Raton, Fla., 1981.

[128] M. Niinomi, Fatigue characteristics of metallic biomaterials, Int. J. Fatigue. 29 (2007) 992–1000.

[129] S.H. Teoh, Fatigue of biomaterials : a review, 22 (2000) 825–837.

[130] M. Mori, K. Yamanaka, H. Matsumoto, A. Chiba, Evolution of cold-rolled microstructures of biomedical Co-Cr-Mo alloys with and without N doping, Mater. Sci. Eng. A. 528 (2010) 614–621.

[131] Y.P. Li, J.S. Yu, S. Kurosu, Y. Koizumi, H. Matsumoto, A. Chiba, Role of nitrogen addition in stabilizing the γ phase of Biomedical Co–29Cr–6Mo alloy, Mater. Chem. Phys. 133 (2012) 29–32.

[132] A.J. Dempsey, R.M. Pilliar, G.C. Weatherly, T. Kilner, The effects of nitrogen additions to a cobalt-chromium surgical implant alloy, J. Mater. Sci. 22 (1987) 575–580.

[133] K. Yamanaka, M. Mori, A. Chiba, Effects of nitrogen addition on microstructure and mechanical behavior of biomedical Co–Cr–Mo alloys, J. Mech. Behav. Biomed. Mater. 29 (2014) 417–426. https://doi.org/https://doi.org/10.1016/j.jmbbm.2013.10.006.

[134] K. Yamanaka, M. Mori, A. Chiba, Nanoarchitectured Co–Cr–Mo orthopedic implant alloys: Nitrogen-enhanced nanostructural evolution and its effect on phase stability, Acta Biomater. 9 (2013) 6259–6267.

[135] A. Chiba, S.-H. Lee, H. Matsumoto, M. Nakamura, Construction of processing map for biomedical Co–28Cr–6Mo–0.16 N alloy by studying its hot deformation behavior using compression tests, Mater. Sci. Eng. A. 513 (2009) 286–293.

[136] N.J. Hallab, A review of the biologic effects of spine implant debris: Fact from fiction, SAS J. 3 (2009) 143–160.

[137] A. Sargeant, T. Goswami, Hip implants–paper VI–ion concentrations, Mater. Des. 28 (2007) 155–171.

[138] J.L. Tipper, P.J. Firkins, E. Ingham, J. Fisher, M.H. Stone, R. Farrar, Quantitative analysis of the wear and wear debris from low and high carbon content cobalt chrome alloys used in metal on metal total hip replacements, J. Mater. Sci. Mater. Med. 10 (1999) 353–362.

[139] A. Chiba, K. Kumagai, N. Nomura, S. Miyakawa, Pin-on-disk wear behavior in a like-on-like configuration in a biological environment of high carbon cast and low carbon forged Co–29Cr–6Mo alloys, Acta Mater. 55 (2007) 1309–1318.

[140] J.L. Gilbert, 1.2 Electrochemical Behavior of Metals in the Biological Milieu, in: P. Ducheyne (Ed.), Compr. Biomater. II, Elsevier, Oxford, 2017: pp. 19–49.

[141] T. Hanawa, S. Hiromoto, K. Asami, Characterization of the surface oxide film of a Co–Cr–Mo alloy after being located in quasi-biological environments using XPS, Appl. Surf. Sci. 183 (2001) 68–75.

[142] B.D. Ratner, A.S. Hoffman, F.J. Schoen, J.E. Lemons, Biomaterials Science: An Introduction to Materials in Medicine, Elsevier Science, 2012.

[143] S. Virtanen, I. Milošev, E. Gomez-Barrena, R. Trebše, J. Salo, Y.T. Konttinen, Special modes of corrosion under physiological and simulated physiological conditions, Acta Biomater. 4 (2008) 468–476.

[144] D.F. Williams, Titanium: epitome of biocompatibility or cause for concern, J. Bone Joint Surg. Br. 76 (1994) 348–349.

[145] J. Black, G. Hastings, Handbook of Biomaterial Properties Edited by, (n.d.).

[146] I. Milošev, CoCrMo Alloy for Biomedical Applications in Biomdical Applications, Springer, Boston, MA, 2012.

[147] A.C. Lewis, M.R. Kilburn, I. Papageorgiou, G.C. Allen, C.P. Case, Effect of synovial fluid, phosphate-buffered saline solution, and water on the dissolution and corrosion properties of CoCrMo alloys as used in orthopedic implants, J. Biomed. Mater. Res. - Part A. 73 (2005) 456–467.

[148] F. Kauser, Corrosion of CoCrMo alloys for biomedical applications, (2007).

[149] F. Contu, B. Elsener, H. Böhni, Electrochemical Behavior of CoCrMo Alloy in the Active State in Acidic and Alkaline Buffered Solutions, J. Electrochem. Soc. 150 (2003) 419–424.

[150] M. Metikoš-Huković, Z. Pilić, R. Babić, D. Omanović, Influence of alloying elements on the corrosion stability of CoCrMo implant alloy in Hank's solution, Acta Biomater. 2 (2006) 693–700.

[151] M. Metikos-Hukovic, R. Babić, D. Omanović, I. Milošev, The Role of Alloying Elements in the Corrosion of Cobalt-based Alloys, ECS Trans. 2 (2007) 43.

[152] F. Özçelik, F. Gulen, A. AKDOGAN, S. PISKIN, Electrochemical study of the corrosion behaviour of Co-Cr-Mo orthopedic implants, (1999).

[153] A.I. Muñoz, S. Mischler, Interactive effects of albumin and phosphate ions on the corrosion of CoCrMo implant alloy, J. Electrochem. Soc. 154 (2007) 562–570.

[154] Y. Liu, J.L. Gilbert, The effect of simulated inflammatory conditions and Fenton chemistry on the electrochemistry of CoCrMo alloy, J. Biomed. Mater. Res. Part B Appl. Biomater. 106 (2018) 209–220.

[155] Y. Liao, R. Pourzal, P. Stemmer, M.A. Wimmer, J.J. Jacobs, A. Fischer, L.D. Marks, A.C. Lewis, M.R. Kilburn, I. Papageorgiou, G.C. Allen, C.P. Case, New insights into hard phases of CoCrMo metal-on-metal hip replacements, J. Biomed. Mater. Res. - Part A. 73 (2005) 456–467.

[156] R.M. Urban, J.J. Jacobs, J.L. Gilbert, J.O. Galante, Migration of corrosion products from modular hip prostheses. Particle microanalysis and histopathological findings., JBJS. 76 (1994) 1345–1359.

[157] A.E. Martell, R.M. Smith, Critical stability constants, Springer, 1974.

[158] A. Kocijan, I. Milošev, D.K. Merl, B. Pihlar, Electrochemical study of Co-based alloys in simulated physiological solution, J. Appl. Electrochem. 34 (2004) 517–524.

[159] S. Virtanen, Corrosion of biomedical implant materials, Corros. Rev. 26 (2008) 147–171.

[160] N. Eliaz, Degradation of implant materials, Springer Science & Business Media, 2012.

[161] B.D. Ratner, A.S. Hoffman, F.J. Schoen, J.E. Lemons, Biomaterials science: an introduction to materials in medicine, Elsevier, 2004.

[162] Y. Liu, J.L. Gilbert, Effect of simulated inflammatory conditions and potential on dissolution and surface oxide of CoCrMo alloy: In situ electrochemical atomic force microscopy study, Electrochim. Acta. 262 (2018) 252–263.

[163] J.L. Gilbert, Corrosion in the Human Body: Metallic Implants in the Complex Body Environment, Corrosion. 73 (2017) 1478–1495.

[164] G.W. Kubacki, S. Sivan, J.L. Gilbert, Electrosurgery Induced Damage to Ti-6Al-4V and CoCrMo Alloy Surfaces in Orthopedic Implants In Vivo and In Vitro., J. Arthroplasty. 32 (2017) 3533–3538.

[165] C.M. Arnholt, D.W. MacDonald, A.L. Malkani, G.R. Klein, C.M. Rimnac, S.M. Kurtz, I.R.C.W. Committee, S.B. Kocagoz, J.L. Gilbert, Corrosion Damage and Wear Mechanisms in Long-Term Retrieved CoCr Femoral Components for Total Knee Arthroplasty, J. Arthroplasty. 31 (2016) 2900–2906.

[166] A. Igual Munoz, J. Schwiesau, B.M. Jolles, S. Mischler, In vivo electrochemical corrosion study of a CoCrMo biomedical alloy in human synovial fluids., Acta Biomater. 21 (2015) 228–236.

[167] J.M. Anderson, A. Rodriguez, D.T. Chang, Foreign body reaction to biomaterials, Semin. Immunol. 20 (2008) 86–100.

[168] G.M. Rosen, S. Pou, C.L. Ramos, M.S. Cohen, B.E. Britigan, Free radicals and phagocytic cells, FASEB J. 9 (1995) 200–209.

[169] D.L. Laskin, K.J. Pendino, Macrophages and inflammatory mediators in tissue injury, Annu. Rev. Pharmacol. Toxicol. 35 (1995) 655–677.

[170] I.A. Silver, R.J. Murrills, D.J. Etherington, Microelectrode studies on the acid microenvironment beneath adherent macrophages and osteoclasts, Exp. Cell Res. 175 (1988) 266–276.

[171] C.C. Winterbourn, M.B. Hampton, J.H. Livesey, A.J. Kettle, Modeling the reactions of superoxide and myeloperoxidase in the neutrophil phagosome implications for microbial killing, J. Biol. Chem. 281 (2006) 39860–39869.

[172] M.B. Hampton, A.J. Kettle, C.C. Winterbourn, Inside the neutrophil phagosome: oxidants, myeloperoxidase, and bacterial killing, Blood, J. Am. Soc. Hematol. 92 (1998) 3007–3017.

[173] J.M. Anderson, Biological responses to materials, Annu. Rev. Mater. Res. 31 (2001) 81–110.

[174] A.E.K. Loo, Y.T. Wong, R. Ho, M. Wasser, T. Du, W.T. Ng, B. Halliwell, Effects of hydrogen peroxide on wound healing in mice in relation to oxidative damage, PLoS One. 7 (2012) e49215.

[175] C. Wittmann, P. Chockley, S.K. Singh, L. Pase, G.J. Lieschke, C. Grabher, Hydrogen peroxide in inflammation: messenger, guide, and assassin, Adv. Hematol. 2012 (2012).

[176] S.G. Steinemann, Metal implants and surface reactions, Injury. 27 (1996) S/C16-S/C22.

[177] A.D. Dayan, A.J. Paine, Mechanisms of chromium toxicity, carcinogenicity and allergenicity: review of the literature from 1985 to 2000, Hum. Exp. Toxicol. 20 (2001) 439–451.

[178] B. Scharf, C.C. Clement, V. Zolla, G. Perino, B. Yan, S.G. Elci, E. Purdue, S. Goldring, F. Macaluso, N. Cobelli, Molecular analysis of chromium and cobalt-related toxicity, Sci. Rep. 4 (2014) 5729.

[179] J.L. Gilbert, S. Sivan, Y. Liu, S.B. Kocagöz, C.M. Arnholt, S.M. Kurtz, Direct in vivo inflammatory cell-induced corrosion of CoCrMo alloy orthopedic implant surfaces, J. Biomed. Mater. Res. Part A. 103 (2015) 211–223.

[180] Y. Liu, J.L. Gilbert, The effect of simulated inflammatory conditions and Fenton chemistry on the electrochemistry of CoCrMo alloy, (2017) 209–220.

[181] E.N. Codaro, P. Melnikov, I. Ramires, A.C. Guastaldi, Corrosion behavior of a cobaltchromium-molybdenum alloy, Russ. J. Electrochem. 36 (2000) 1117–1121.

[182] H.-Y. Lin, J.D. Bumgardner, Changes in the surface oxide composition of Co–Cr–Mo implant alloy by macrophage cells and their released reactive chemical species, Biomaterials. 25 (2004) 1233–1238.

[183] A.W.E. Hodgson, S. Kurz, S. Virtanen, V. Fervel, C.-O.A. Olsson, S. Mischler, Passive and transpassive behaviour of CoCrMo in simulated biological solutions, Electrochim. Acta. 49 (2004) 2167–2178.

[184] L.C. Lucas, R.A. Buchanan, J.E. Lemons, C.D. Griffin, Susceptibility of surgical cobalt-base alloy to pitting corrosion, J. Biomed. Mater. Res. 16 (1982) 799–810.

[185] M. Metikoš-Huković, R. Babić, Passivation and corrosion behaviours of cobalt and cobalt–chromium–molybdenum alloy, Corros. Sci. 49 (2007) 3570–3579.

[186] M. Metikoš-Huković, J. Katić, Z. Grubač, I. Škugor Rončević, Electrochemistry of CoCrMo Implant in Hanks' Solution and Mott-Schottky Probe of Alloy's Passive Films, CORROSION. 73 (2017) 1401–1412.

[187] W.A. Badawy, F.M. Al-Kharafi, J.R. Al-Ajmi, Electrochemical behaviour of cobalt in aqueous solutions of different pH, J. Appl. Electrochem. 30 (2000) 693–

704.

[188] T.A. Gruen, H.C. Amstutz, A failed vitallium/stainless steel total hip replacement: A case report with histological and metallurgical examination, J. Biomed. Mater. Res. 9 (1975) 465–477.

[189] I. Milošev, Metallic materials for biomedical applications: laboratory and clinical studies, Pure Appl. Chem. 83 (2010) 309–324.

[190] A.W. Hodgson, S. Mischler, B. Von Rechenberg, S. Virtanen, An analysis of the in vivo deterioration of Co-Cr-Mo implants through wear and corrosion, Proc. Inst. Mech. Eng. Part H J. Eng. Med. 221 (2007) 291–303.

[191] I. Milošev, H.H. Strehblow, The composition of the surface passive film formed on CoCrMo alloy in simulated physiological solution, Electrochim. Acta. 48 (2003)

[192] F. Contu, B. Elsener, H. Böhni, Characterization of implant materials in fetal bovine serum and sodium sulfate by electrochemical impedance spectroscopy. I. Mechanically polished samples, J. Biomed. Mater. Res. An Off. J. Soc. Biomater. Japanese Soc. Biomater. Aust. Soc. Biomater. Korean Soc. Biomater. 62 (2002) 412–421.

[193] T. Altan, G. Ngaile, G. Shen, Cold and hot forging: fundamentals and applications, ASM international, 2004.

[194] K. Lange, Cost Minimization in Small Quantity Production of Stepped Shafts by Combined NC-Radial Forging and NC-Turning. A New Approach to Flexible Manufacturing Systems, CIRP Ann. 34 (1985) 549–555.

[195] ASTM F42 Committee on Additiv emanufacturing technologies, n.d.

[196] ASTM F42-19 Committee on Additiv emanufacturing technologies, n.d. https://www.astm.org/COMMITTEE/F42.htm#:~:text=ASTM Committee F42 on Additive Manufacturing Technologies was formed in 2009.&text=The Committee%2C with a current,of ASTM Standards%2C Volume 10.04 .

[197] Z. Quan, A. Wu, M. Keefe, X. Qin, J. Yu, J. Suhr, J.-H. Byun, B.-S. Kim, T.-W. Chou, Additive manufacturing of multi-directional preforms for composites: opportunities and challenges, Mater. Today. 18 (2015) 503–512.

[198] G. Barucca, E. Santecchia, G. Majni, E. Girardin, E. Bassoli, L. Denti, A. Gatto, L.

Iuliano, T. Moskalewicz, P. Mengucci, Structural characterization of biomedical Co–Cr–Mo components produced by direct metal laser sintering, Mater. Sci. Eng. C. 48 (2015) 263–269.

[199] D.B. Pedersen, Additive manufacturing: multi material processing and part quality control, (2013).

[200] M. Qian, Metal powder for additive manufacturing, Jom. 67 (2015) 536–537.

[201] V. Sriram, V. Shukla, S. Biswas, Metal Powder Based Additive Manufacturing Technologies—Business Forecast, in: 3D Print. Addit. Manuf. Technol., Springer, 2019: pp. 105–118.

[202] T. Wohlers, 3D printing and additive manufacturing state of the industry, Annu. Worldw. Prog. Report. Wohlers Assoc. (2014).

[203] L.J. Kumar, P.M. Pandey, D.I. Wimpenny, 3D printing and additive manufacturing technologies, Springer, 2019.

[204] S. Kumar, Additive Manufacturing Processes, n.d.

[205] L.C. Zhang, H. Attar, M. Calin, J. Eckert, F. Brenne, T. Niendorf, H.J. Maier, T. Dikova, Additively manufactured cellular structures: Impact of microstructure and local strains on the monotonic and cyclic behavior under uniaxial and bending load, J. Mater. Process. Technol. 213 (2018) 1558–1564.

[206] X. Tan, Y. Kok, Y.J. Tan, M. Descoins, D. Mangelinck, S.B. Tor, K.F. Leong, C.K. Chua, Graded microstructure and mechanical properties of additive manufactured Ti–6Al–4V via electron beam melting, Acta Mater. 97 (2015) 1–16.

[207] Y. Lu, S. Wu, Y. Gan, J. Li, C. Zhao, D. Zhuo, J. Lin, Investigation on the microstructure, mechanical property and corrosion behavior of the selective laser melted CoCrW alloy for dental application, Mater. Sci. Eng. C. 49 (2015) 517–525.

[208] X. Zhao, S. Li, M. Zhang, Y. Liu, T.B. Sercombe, S. Wang, Y. Hao, R. Yang, L.E. Murr, Comparison of the microstructures and mechanical properties of Ti–6Al–4V fabricated by selective laser melting and electron beam melting, Mater. Des. 95 (2016) 21–31.

[209] I. Gibson, D.W. Rosen, B. Stucker, Design for additive manufacturing, in: Addit.

Manuf. Technol., Springer, 2010: pp. 299–332.

[210] Y.J. Liu, H.L. Wang, S.J. Li, S.G. Wang, W.J. Wang, W.T. Hou, Y.L. Hao, R. Yang, L.C. Zhang, Compressive and fatigue behavior of beta-type titanium porous structures fabricated by electron beam melting, Acta Mater. 126 (2017) 58–66.

[211] J.-P. Kruth, G. Levy, R. Schindel, T. Craeghs, E. Yasa, Consolidation of polymer powders by selective laser sintering, in: Proc. 3rd Int. Conf. Polym. Mould. Innov., 2008: pp. 15–30.

[212] T. Kimura, T. Nakamoto, M. Mizuno, H. Araki, Effect of silicon content on densification, mechanical and thermal properties of Al-xSi binary alloys fabricated using selective laser melting, Mater. Sci. Eng. A. 682 (2017) 593–602.

[213] K.G. Prashanth, R. Damodaram, S. Scudino, Z. Wang, K.P. Rao, J. Eckert, Friction welding of Al–12Si parts produced by selective laser melting, Mater. Des. 57 (2014) 632–637.

[214] L. Thijs, K. Kempen, J.-P. Kruth, J. Van Humbeeck, Fine-structured aluminium products with controllable texture by selective laser melting of pre-alloyed AlSi10Mg powder, Acta Mater. 61 (2013) 1809–1819.

[215] L. Thijs, F. Verhaeghe, T. Craeghs, J. Van Humbeeck, J.-P. Kruth, A study of the microstructural evolution during selective laser melting of Ti–6Al–4V, Acta Mater. 58 (2010) 3303–3312.

[216] W. Xu, E.W. Lui, A. Pateras, M. Qian, M. Brandt, In situ tailoring microstructure in additively manufactured Ti-6Al-4V for superior mechanical performance, Acta Mater. 125 (2017) 390–400.

[217] S. Li, H. Hassanin, M.M. Attallah, N.J.E. Adkins, K. Essa, The development of TiNi-based negative Poisson's ratio structure using selective laser melting, Acta Mater. 105 (2016) 75–83.

[218] K. Kempen, E. Yasa, L. Thijs, J.-P. Kruth, J. Van Humbeeck, Microstructure and mechanical properties of Selective Laser Melted 18Ni-300 steel, Phys. Procedia. 12 (2011) 255–263.

[219] L.E. Murr, E. Martinez, J. Hernandez, S. Collins, K.N. Amato, S.M. Gaytan, P.W. Shindo, Microstructures and properties of 17-4 PH stainless steel fabricated by

selective laser melting, J. Mater. Res. Technol. 1 (2012) 167–177.

[220] Y. Zhu, J. Zou, X. Chen, H. Yang, Tribology of selective laser melting processed parts: Stainless steel 316 L under lubricated conditions, Wear. 350 (2016) 46–55.

[221] Y. Lu, S. Wu, Y. Gan, T. Huang, C. Yang, L. Junjie, J. Lin, Study on the microstructure, mechanical property and residual stress of SLM Inconel-718 alloy manufactured by differing island scanning strategy, Opt. Laser Technol. 75 (2015) 197–206.

[222] P. Kanagarajah, F. Brenne, T. Niendorf, H.J. Maier, Inconel 939 processed by selective laser melting: Effect of microstructure and temperature on the mechanical properties under static and cyclic loading, Mater. Sci. Eng. A. 588 (2013) 188–195.

[223] P. Wang, B. Zhang, C.C. Tan, S. Raghavan, Y.-F. Lim, C.-N. Sun, J. Wei, D. Chi, Microstructural characteristics and mechanical properties of carbon nanotube reinforced Inconel 625 parts fabricated by selective laser melting, Mater. Des. 112 (2016) 290–299.

[224] E. Liverani, A. Fortunato, A. Leardini, C. Belvedere, S. Siegler, L. Ceschini, A. Ascari, Fabrication of Co–Cr–Mo endoprosthetic ankle devices by means of Selective Laser Melting (SLM), Mater. Des. 106 (2016) 60–68.

[225] X. zhen Xin, J. Chen, N. Xiang, B. Wei, Surface Properties and Corrosion Behavior of Co-Cr Alloy Fabricated with Selective Laser Melting Technique, Cell Biochem. Biophys. 67 (2013) 983–990.

[226] Y.S. Hedberg, B. Qian, Z. Shen, S. Virtanen, I. Odnevall Wallinder, In vitro biocompatibility of CoCrMo dental alloys fabricated by selective laser melting, Dent. Mater. 30 (2014) 525–534.

[227] S. Scudino, C. Unterdörfer, K.G. Prashanth, H. Attar, N. Ellendt, V. Uhlenwinkel, J. Eckert, Additive manufacturing of Cu–10Sn bronze, Mater. Lett. 156 (2015) 202–204.

[228] H. Attar, K.G. Prashanth, L.-C. Zhang, M. Calin, I. V Okulov, S. Scudino, C. Yang, J. Eckert, Effect of powder particle shape on the properties of in situ Ti–TiB composite materials produced by selective laser melting, J. Mater. Sci. Technol. 31 (2015) 1001–1005.

[229] Q. Shi, D. Gu, M. Xia, S. Cao, T. Rong, Effects of laser processing parameters on thermal behavior and melting/solidification mechanism during selective laser melting of TiC/Inconel 718 composites, Opt. Laser Technol. 84 (2016) 9–22.

[230] B. Zhang, G. Bi, S. Nai, C. Sun, J. Wei, Microhardness and microstructure evolution of TiB2 reinforced Inconel 625/TiB2 composite produced by selective laser melting, Opt. Laser Technol. 80 (2016) 186–195.

[231] K.G. Prashanth, S. Scudino, A.K. Chaubey, L. Löber, P. Wang, H. Attar, F.P. Schimansky, F. Pyczak, J. Eckert, Processing of Al–12Si–TNM composites by selective laser melting and evaluation of compressive and wear properties, J. Mater. Res. 31 (2016) 55–65.

[232] J. Suryawanshi, K.G. Prashanth, S. Scudino, J. Eckert, O. Prakash, U. Ramamurty, Simultaneous enhancements of strength and toughness in an Al-12Si alloy synthesized using selective laser melting, Acta Mater. 115 (2016) 285–294.

[233] H.Y. Jung, S.J. Choi, K.G. Prashanth, M. Stoica, S. Scudino, S. Yi, U. Kühn, D.H. Kim, K.B. Kim, J. Eckert, Fabrication of Fe-based bulk metallic glass by selective laser melting: A parameter study, Mater. Des. 86 (2016) 703–708.

[234] L.C. Zhang, D. Klemm, J. Eckert, Y.L. Hao, T.B. Sercombe, Manufacture by selective laser melting and mechanical behavior of a biomedical Ti–24Nb–4Zr–8Sn alloy, Scr. Mater. 65 (2011) 21–24.

[235] H. Schwab, K.G. Prashanth, L. Löber, U. Kühn, J. Eckert, Selective laser melting of Ti-45Nb alloy, Metals (Basel). 5 (2015) 686–694.

[236] P. Laakso, T. Riipinen, A. Laukkanen, T. Andersson, A. Jokinen, A. Revuelta, K. Ruusuvuori, Optimization and simulation of SLM process for high density H13 tool steel parts, Phys. Procedia. 83 (2016) 26–35.

[237] T. Koutsoukis, S. Zinelis, G. Eliades, K. Al-Wazzan, M. Al Rifaiy, Y.S. Al Jabbari, Selective laser melting technique of Co-Cr dental alloys: a review of structure and properties and comparative analysis with other available techniques, J. Prosthodont. 24 (2015) 303–312.

[238] J. Wilkes, Y. Hagedorn, W. Meiners, K. Wissenbach, Additive manufacturing of ZrO2-Al2O3 ceramic components by selective laser melting, Rapid Prototyp. J. (2013).

[239] D.A. Ramirez, L.E. Murr, E. Martinez, D.H. Hernandez, J.L. Martinez, B.I. Machado, F. Medina, P. Frigola, R.B. Wicker, Novel precipitate–microstructural architecture developed in the fabrication of solid copper components by additive manufacturing using electron beam melting, Acta Mater. 59 (2011) 4088–4099.

[240] S.-H. Sun, Y. Koizumi, S. Kurosu, Y.-P. Li, A. Chiba, Phase and grain size inhomogeneity and their influences on creep behavior of Co–Cr–Mo alloy additive manufactured by electron beam melting, Acta Mater. 86 (2015) 305–318.

[241] D. Riedlbauer, M. Drexler, D. Drummer, P. Steinmann, J. Mergheim, Modelling, simulation and experimental validation of heat transfer in selective laser melting of the polymeric material PA12, Comput. Mater. Sci. 93 (2014) 239–248.

[242] K.G. Prashanth, S. Scudino, H.J. Klauss, K.B. Surreddi, L. Löber, Z. Wang, A.K. Chaubey, U. Kühn, J. Eckert, Microstructure and mechanical properties of Al–12Si produced by selective laser melting: Effect of heat treatment, Mater. Sci. Eng. A. 590 (2014) 153–160.

[243] N.W. Hrabe, P. Heinl, B. Flinn, C. Körner, R.K. Bordia, Compression-compression fatigue of selective electron beam melted cellular titanium (Ti-6Al-4V), J. Biomed. Mater. Res. Part B Appl. Biomater. 99 (2011) 313–320.

[244] N.T. Aboulkhair, N.M. Everitt, I. Ashcroft, C. Tuck, Reducing porosity in AlSi10Mg parts processed by selective laser melting, Addit. Manuf. 1 (2014) 77–86.

[245] H. Attar, L. Löber, A. Funk, M. Calin, L.C. Zhang, K.G. Prashanth, S. Scudino, Y.S. Zhang, J. Eckert, Mechanical behavior of porous commercially pure Ti and Ti–TiB composite materials manufactured by selective laser melting, Mater. Sci. Eng. A. 625 (2015) 350–356.

[246] K.G. Prashanth, S. Scudino, J. Eckert, Defining the tensile properties of Al-12Si parts produced by selective laser melting, Acta Mater. 126 (2017) 25–35.

[247] Y.J. Liu, X.P. Li, L.C. Zhang, T.B. Sercombe, Processing and properties of topologically optimised biomedical Ti–24Nb–4Zr–8Sn scaffolds manufactured by selective laser melting, Mater. Sci. Eng. A. 642 (2015) 268–278.

[248] E. Liverani, Studio e ottimizzazione del processo di fabbricazione additiva (SLM) per applicazioni in ambito biomedicale: produzione di protesi e strutture reticolari,

(2017).

[249] C. Lin, T. Wirtz, F. LaMarca, S.J. Hollister, Structural and mechanical evaluations of a topology optimized titanium interbody fusion cage fabricated by selective laser melting process, J. Biomed. Mater. Res. Part A An Off. J. Soc. Biomater. Japanese Soc. Biomater. Aust. Soc. Biomater. Korean Soc. Biomater. 83 (2007) 272–279.

[250] M. Seyedi, F. Zanotto, C. Monticelli, A. Balbo, E. Liverani, A. Fortunato, Microstructural characterization and corrosion behaviour of SLM CoCrMo alloy in simulated body fluid, Metall. Ital. 110 (2018) 45–50.

[251] L.C. Ardila, F. Garciandia, J.B. González-Díaz, P. Álvarez, A. Echeverria, M.M. Petite, R. Deffley, J. Ochoa, Effect of IN718 recycled powder reuse on properties of parts manufactured by means of Selective Laser Melting, Phys. Procedia. 56 (2014) 99–107.

[252] L.E. Murr, S.M. Gaytan, A. Ceylan, E. Martinez, J.L. Martinez, D.H. Hernandez, B.I. Machado, D.A. Ramirez, F. Medina, S. Collins, Characterization of titanium aluminide alloy components fabricated by additive manufacturing using electron beam melting, Acta Mater. 58 (2010) 1887–1894.

[253] L. Zhang, Y. Liu, S. Li, Y. Hao, Additive manufacturing of titanium alloys by electron beam melting: a review, Adv. Eng. Mater. 20 (2018) 1700842.

[254] Y. Zhang, L. Wu, X. Guo, S. Kane, Y. Deng, Y.-G. Jung, J.-H. Lee, J. Zhang, Additive Manufacturing of Metallic Materials: A Review, J. Mater. Eng. Perform. 27 (2018) 1–13.

[255] J. Parthasarathy, B. Starly, S. Raman, A. Christensen, Mechanical evaluation of porous titanium (Ti6Al4V) structures with electron beam melting (EBM), J. Mech. Behav. Biomed. Mater. 3 (2010) 249–259.

[256] Y. Zhong, L.-E. Rännar, L. Liu, A. Koptyug, S. Wikman, J. Olsen, D. Cui, Z. Shen, Additive manufacturing of 316L stainless steel by electron beam melting for nuclear fusion applications, J. Nucl. Mater. 486 (2017) 234–245.

[257] Y. Liu, S. Li, W. Hou, S. Wang, Y. Hao, R. Yang, T.B. Sercombe, L.-C. Zhang, Electron beam melted beta-type Ti–24Nb–4Zr–8Sn porous structures with high strength-to-modulus ratio, J. Mater. Sci. Technol. 32 (2016) 505–508.

[258] Y.J. Liu, S.J. Li, H.L. Wang, W.T. Hou, Y.L. Hao, R. Yang, T.B. Sercombe, L.C. Zhang, Microstructure, defects and mechanical behavior of beta-type titanium porous structures manufactured by electron beam melting and selective laser melting, Acta Mater. 113 (2016) 56–67.

[259] L.M. Sochalski-Kolbus, E.A. Payzant, P.A. Cornwell, T.R. Watkins, S.S. Babu, R.R. Dehoff, M. Lorenz, O. Ovchinnikova, C. Duty, Comparison of residual stresses in Inconel 718 simple parts made by electron beam melting and direct laser metal sintering, Metall. Mater. Trans. A. 46 (2015) 1419–1432.

[260] M. Ramsperger, L. Mújica Roncery, I. Lopez-Galilea, R.F. Singer, W. Theisen, C. Körner, Solution Heat Treatment of the Single Crystal Nickel-Base Superalloy CMSX-4 Fabricated by Selective Electron Beam Melting, Adv. Eng. Mater. 17 (2015) 1486–1493.

[261] K.-H. Shin, H. Natu, D. Dutta, J. Mazumder, A method for the design and fabrication of heterogeneous objects, Mater. Des. 24 (2003) 339–353.

[262] M. Zhong, W. Liu, Laser surface cladding: the state of the art and challenges, Proc. Inst. Mech. Eng. Part C J. Mech. Eng. Sci. 224 (2010) 1041–1060.

[263] D.D. Gu, W. Meiners, K. Wissenbach, R. Poprawe, Laser additive manufacturing of metallic components: materials, processes and mechanisms, Int. Mater. Rev. 57 (2012) 133–164.

[264] R.P. Mudge, N.R. Wald, Laser engineered net shaping advances additive manufacturing and repair, Weld. JOURNAL-NEW YORK-. 86 (2007) 44.

[265] M.S. Domack, K.M. Taminger, M. Begley, Metallurgical mechanisms controlling mechanical properties of aluminium alloy 2219 produced by electron beam freeform fabrication, in: Mater. Sci. Forum, Trans Tech Publ, 2006: pp. 1291–1296.

[266] H. Zhang, J. Xu, G. Wang, Fundamental study on plasma deposition manufacturing, Surf. Coatings Technol. 171 (2003) 112–118.

[267] S.M. Thompson, L. Bian, N. Shamsaei, A. Yadollahi, An overview of Direct Laser Deposition for additive manufacturing; Part I: Transport phenomena, modeling and diagnostics, Addit. Manuf. 8 (2015) 36–62.

[268] O.A. Mohamed, S.H. Masood, J.L. Bhowmik, Optimization of fused deposition modeling process parameters: a review of current research and future prospects, Adv. Manuf. 3 (2015) 42–53.

[269] F. Wang, L. Shor, A. Darling, S. Khalil, W. Sun, S. Güçeri, A. Lau, Precision extruding deposition and characterization of cellular poly-ε-caprolactone tissue scaffolds, Rapid Prototyp. J. (2004).

[270] M.E. Hoque, Y.L. Chuan, I. Pashby, Extrusion based rapid prototyping technique: an advanced platform for tissue engineering scaffold fabrication, Biopolymers. 97 (2012) 83–93.

[271] C. Carvalho, R. Landers, U. Hübner, R. Schmelzeisen, R. Mülhaupt, Fabrication of soft and hard biocompatible scaffolds using 3D-BioplottingTM, Virtual Model. Rapid Manuf. Res. Virtual Rapid Prototyp. (2005) 97–102.

[272] M.G. Li, X.Y. Tian, X.B. Chen, A brief review of dispensing-based rapid prototyping techniques in tissue scaffold fabrication: role of modeling on scaffold properties prediction, Biofabrication. 1 (2009) 32001.

[273] P. Sheshadri, R.A. Shirwaiker, Characterization of material–process–structure interactions in the 3D bioplotting of polycaprolactone, 3D Print. Addit. Manuf. 2 (2015) 20–31.

[274] B.G. Mekonnen, G. Bright, A. Walker, A study on state of the art technology of laminated object manufacturing (LOM), in: CAD/CAM, Robot. Factories Futur., Springer, 2016: pp. 207–216.

[275] C. Y.Y., L. Y.S., Laser path planning of burn-out rule for LOM process, Rapid Prototyp. J. 9 (2003) 201–211..

[276] I. Gibson, D. Rosen, B. Stucker, Binder jetting, in: Addit. Manuf. Technol., Springer, 2015: pp. 205–218.

[277] M. Ziaee, N.B. Crane, Binder jetting: A review of process, materials, and methods, Addit. Manuf. 28 (2019) 781–801.

[278] Y. Zhang, L. Wu, X. Guo, S. Kane, Y. Deng, Y.-G. Jung, J.-H. Lee, J. Zhang, Additive Manufacturing of Metallic Materials: A Review, J. Mater. Eng. Perform. 27 (2018) 1–13.

[279] C. Schmidleithner, D.M. Kalaskar, Stereolithography, in: IntechOpen, 2018.

[280] F.P.W. Melchels, J. Feijen, D.W. Grijpma, A review on stereolithography and its applications in biomedical engineering, Biomaterials. 31 (2010) 6121–6130.

[281] E. Yasa, J. Deckers, J. Kruth, The investigation of the influence of laser re-melting on density, surface quality and microstructure of selective laser melting parts, Rapid Prototyp. J. (2011).

[282] B. Song, X. Zhao, S. Li, C. Han, Q. Wei, S. Wen, J. Liu, Y. Shi, Differences in microstructure and properties between selective laser melting and traditional manufacturing for fabrication of metal parts: A review, Front. Mech. Eng. 10 (2015) 111–125.

[283] K. Mumtaz, N. Hopkinson, Top surface and side roughness of Inconel 625 parts processed using selective laser melting, Rapid Prototyp. J. (2009).

[284] K. Alrbaey, D. Wimpenny, R. Tosi, W. Manning, A. Moroz, On optimization of surface roughness of selective laser melted stainless steel parts: a statistical study, J. Mater. Eng. Perform. 23 (2014) 2139–2148.

[285] S. Zhang, Q. Wei, L. Cheng, S. Li, Y. Shi, Effects of scan line spacing on pore characteristics and mechanical properties of porous Ti6Al4V implants fabricated by selective laser melting, Mater. Des. 63 (2014) 185–193.

[286] S. Zhang, Y. Li, L. Hao, T. Xu, Q. Wei, Y. Shi, Metal-ceramic bond mechanism of the Co-Cr alloy denture with original rough surface produced by selective laser melting, Chinese J. Mech. Eng. 27 (2014) 69–78.

[287] W. Shifeng, L. Shuai, W. Qingsong, C. Yan, Z. Sheng, S. Yusheng, Effect of molten pool boundaries on the mechanical properties of selective laser melting parts, J. Mater. Process. Technol. 214 (2014) 2660–2667.

[288] B. Song, S.J. Dong, H.L. Liao, C. Coddet, Morphology evolution mechanism of single tracks of FeAl intermetallics in selective laser melting, Mater. Res. Innov. 16 (2012) 321–325.

[289] D.-G. Ahn, Applications of laser assisted metal rapid tooling process to manufacture of molding & forming tools—state of the art, Int. J. Precis. Eng. Manuf. 12 (2011) 925–938.

[290] B. Song, S. Dong, S. Deng, H. Liao, C. Coddet, Microstructure and tensile properties of iron parts fabricated by selective laser melting, Opt. Laser Technol. 56 (2014) 451–460.

[291] D. Gu, W. Meiners, Y.-C. Hagedorn, K. Wissenbach, R. Poprawe, Bulk-form TiCx/Ti nanocomposites with controlled nanostructure prepared by a new method: selective laser melting, J. Phys. D. Appl. Phys. 43 (2010) 295402.

[292] D. Gu, H. Wang, G. Zhang, Selective laser melting additive manufacturing of Ti-based nanocomposites: the role of nanopowder, Metall. Mater. Trans. A. 45 (2014) 464–476.

[293] P. Mercelis, J. Kruth, Residual stresses in selective laser sintering and selective laser melting, Rapid Prototyp. J. (2006).

[294] J.-P. Kruth, P. Mercelis, J. Vaerenbergh, L. Froyen, M. Rombouts, Binding Mechanisms in Selective Laser Sintering and Selective Laser Melting, Rapid Prototyp. J. 11 (2005) 26–36.

[295] D. Gu, Y. Shen, Balling phenomena in direct laser sintering of stainless steel powder: Metallurgical mechanisms and control methods, Mater. Des. 30 (2009) 2903–2910.

[296] K. Wei, M. Gao, Z. Wang, X. Zeng, Effect of energy input on formability, microstructure and mechanical properties of selective laser melted AZ91D magnesium alloy, Mater. Sci. Eng. A. 611 (2014) 212–222.

[297] M. Song, X. Lin, G. Yang, X. Cui, H. Yang, W. Huang, Influence of forming atmosphere on the deposition characteristics of 2Cr13 stainless steel during laser solid forming, J. Mater. Process. Technol. 214 (2014) 701–709.

[298] B. Zhang, H. Liao, C. Coddet, Selective laser melting commercially pure Ti under vacuum, Vacuum. 95 (2013) 25–29.

[299] B. Zhang, Y. Li, Q. Bai, Defect formation mechanisms in selective laser melting: a review, Chinese J. Mech. Eng. 30 (2017) 515–527.

[300] A. Hussein, L. Hao, C. Yan, R. Everson, Finite element simulation of the temperature and stress fields in single layers built without-support in selective laser melting, Mater. Des. 52 (2013) 638–647.

[301] L.N. Carter, K. Essa, M.M. Attallah, Optimisation of selective laser melting for a high temperature Ni-superalloy, Rapid Prototyp. J. (2015).

[302] L.N. Carter, M.M. Attallah, R.C. Reed, Laser powder bed fabrication of nickel-base superalloys: influence of parameters; characterisation, quantification and mitigation of cracking, Superalloys. 2012 (2012) 577–586.

[303] S. Leuders, T. Lieneke, S. Lammers, T. Tröster, T. Niendorf, On the fatigue properties of metals manufactured by selective laser melting-the role of ductility, J. Mater. Res. 29 (2014) 1911.

[304] A. Riemer, S. Leuders, M. Thöne, H.A. Richard, T. Tröster, T. Niendorf, On the fatigue crack growth behavior in 316L stainless steel manufactured by selective laser melting, Eng. Fract. Mech. 120 (2014) 15–25.

[305] X.Z. Xin, N. Xiang, J. Chen, B. Wei, In vitro biocompatibility of Co-Cr alloy fabricated by selective laser melting or traditional casting techniques, Mater. Lett. 88 (2012) 101–103.

[306] Y.S. Hedberg, B. Qian, Z. Shen, S. Virtanen, I. Odnevall Wallinder, In vitro biocompatibility of CoCrMo dental alloys fabricated by selective laser melting, Dent. Mater. 30 (2014) 525–534.

[307] X. Dong, Q. Sun, Y. Zhou, Y. Qu, H. Shi, B. Zhang, S. Xu, W. Liu, N. Li, J. Yan, Influence of microstructure on corrosion behavior of biomedical Co-Cr-Mo-W alloy fabricated by selective laser melting, Corros. Sci. 170 (2020) 108688.

[308] Y. Kajima, A. Takaichi, N. Kittikundecha, T. Nakamoto, T. Kimura, N. Nomura, A. Kawasaki, T. Hanawa, H. Takahashi, N. Wakabayashi, Effect of heat-treatment temperature on microstructures and mechanical properties of Co–Cr–Mo alloys fabricated by selective laser melting, Mater. Sci. Eng. A. 726 (2018) 21–31.

[309] K.K. Bawane, D. Srinivasan, D. Banerjee, Microstructural Evolution and Mechanical Properties of Direct Metal Laser-Sintered (DMLS) CoCrMo After Heat Treatment, Metall. Mater. Trans. A. 49 (2018) 3793–3811.

[310] E. Seki, Y. Kajima, A. Takaichi, N. Kittikundecha, H.H.W. Cho, H.L. Htat, H. Doi, T. Hanawa, N. Wakabayashi, Effect of heat treatment on the microstructure and fatigue strength of CoCrMo alloys fabricated by selective laser melting, Mater. Lett. 245 (2019) 53–56.

[311] L. Hitzler, F. Alifui-Segbaya, P. Williams, B. Heine, M. Heitzmann, W. Hall, M. Merkel, A. Öchsner, Additive Manufacturing of Cobalt-Based Dental Alloys: Analysis of Microstructure and Physicomechanical Properties, Adv. Mater. Sci. Eng. 2018 (2018) 8213023.

[312] M. Zhang, Y. Yang, C. Song, Y. Bai, Z. Xiao, An investigation into the aging behavior of CoCrMo alloys fabricated by selective laser melting, J. Alloys Compd. 750 (2018) 878–886.

[313] M. Zhang, Y. Yang, C. Song, Y. Bai, Z. Xiao, Effect of the heat treatment on corrosion and mechanical properties of CoCrMo alloys manufactured by selective laser melting, Rapid Prototyp. J. (2018).

[314] A. Mostafaei, P. Rodriguez De Vecchis, M.J. Buckenmeyer, S.R. Wasule, B.N. Brown, M. Chmielus, Microstructural evolution and resulting properties of differently sintered and heat-treated binder-jet 3D-printed Stellite 6, Mater. Sci. Eng. C. 102 (2019) 276–288.

[315] A. Bose, W.B. Eisen, Hot Consolidation of Powders & Particulates, Metal Powder Industries Federation, 2003.

[316] J. Haan, M. Asseln, M. Zivcec, J. Eschweiler, R. Radermacher, C. Broeckmann, Effect of subsequent hot isostatic pressing on mechanical properties of ASTM F75 alloy produced by selective laser melting, Powder Metall. 58 (2015) 161–165.

[317] R. Kircher, A. Christensen, K. Wurth, Electron beam melted (EBM) Co-Cr-Mo alloy for orthopaedic implant applications, Austin Solid Free Form Fabr. 436 (2009).


3

CHAPTER THREE

Materials and Methods

In this chapter, an overview of the materials and experimental methodology employed for approaching the objectives of the present doctoral thesis is described. The basic principles and the experimental set-up concerning each technique are detailed.

3.1. Experimental Plan

The focus of this Ph.D. research is to characterize the electrochemical and corrosion characteristics of selective laser melted CoCrMo alloy in simulated body fluids by reproducing physiological and inflammation conditions. The research plan can be divided into four parts according to the type of the applied experimental methods as represented in Figure 3.1. In Part I, the microstructure of the studied materials was investigated by SEM, EDS, and FIB. In this part, also a more in-depth investigation on the surface film nature and characteristics were performed by associating surface analysis techniques such as SEM, TEM, and AFM. Part II dealt with the study of the corrosion behavior of the CoCrMo alloys produced by SLM, on the basis of electrochemical techniques such as monitoring of the open circuit potential and recording of polarization curves at different immersion times. The composition and protectiveness of the surface films were investigated by conducting electrochemical investigation by means of open circuit potential (OCP), cyclic polarization curves (CP), cyclic voltammetry (CV) and electrochemical impedance spectroscopy (EIS). These results were compared with those obtained from CoCrMo produced by a traditional method. Part III stands with a mechanical study of SLM alloys based on Vickers microhardness (HV) and tensile tests. The experimental plan then moved onto the study of the mutual effect of electrochemical and mechanical processes on the alloy behavior by employing slow strain rate test (SSRT) technique.

Part IV of this research project investigated the effect of the post-processing heat treatment on the microstructural and electrochemical behavior of the studied materials.

A general introduction to each technique applied during this project is given in the following sections.

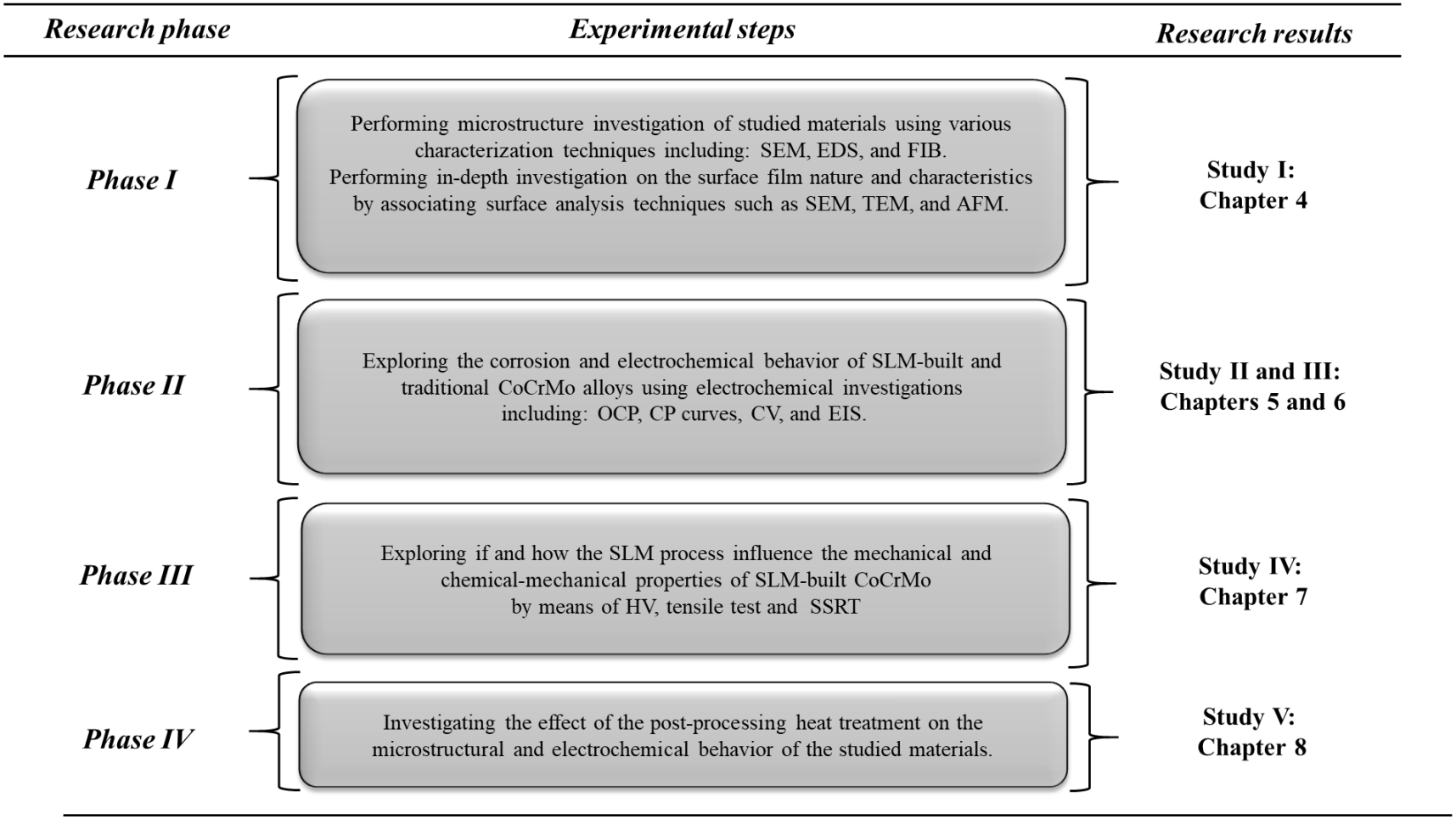

Figure 3.1. Overview of the reaech phases of the present study.

3.2. Materials

3.2.1. Selective laser melting fabricated CoCrMo alloys

Selective laser melted CoCrMo (named SLM CoCrMo in the following text) samples were obtained from a commercial powder (LPW Technology Ltd, Runcorn Cheshire, UK) having the composition reported in Table 3.1. The morphology and microstructure of the starting powders are shown in Figure 3.2 and Figure 3.3. The average particle size of the starting powders is about 20 μm.

Table 3. 1. The chemical composition of CoCrMo powder was obtained by Energy Dispersion Spectroscopy (EDS) analysis.

(wt. %)	C	N	Al	Si	Cr	Mn	Fe	Co	Ni	Mo	La
Average	≤0.04	0.009	0.05	0.77	28.06	0.68	0.12	64.23	Nd.	5.92	0.07

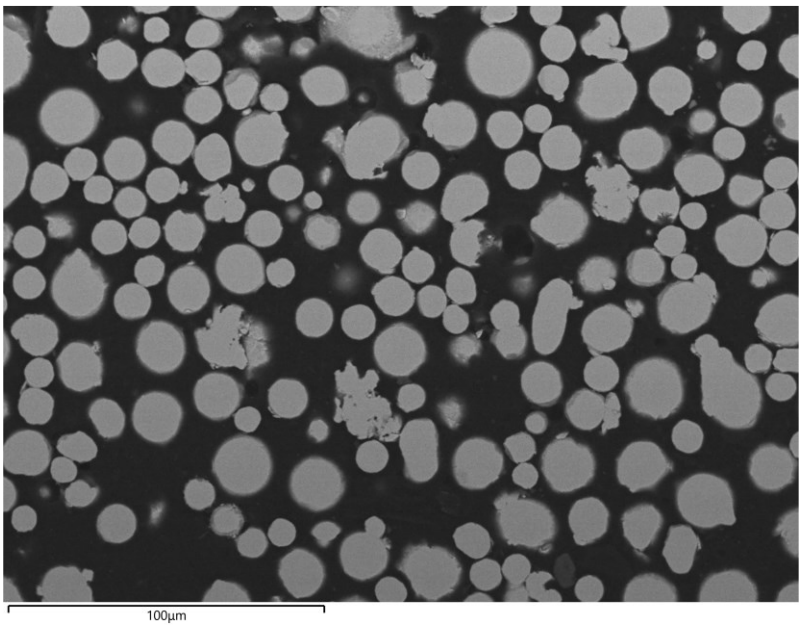

Figure 3. 2. The morphology and microstructure of the starting CoCrMo powders.

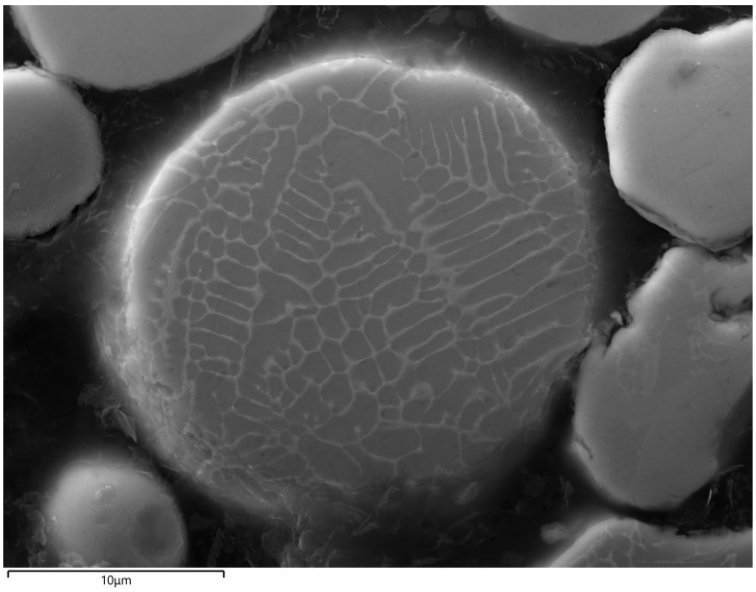

Figure 3. 3. Magnified morphology of CoCrMo starting powder.

The SLM samples were built up by a SISMA MYSINT100 machine (Sisma, Piovene Roccheta, Italy) with the specifications collected in Table 3.2. These specifications may help the reproduction of our results by other commercial machines.

Table 3. 2. Technical specifications of the SLM machine "SISMA: MYSINT100" [1].

MYSINT100 Technical Specifications	
Dimension of chamber	Φ100 mm x h 100 mm
Laser source	Fiber laser, λ = 1030 nm
Precision optics	Quartz F - Theta Lens
Spot diameter	50 µm
Layer thickness (adjustable)	20-30 µm
Power supply	230 V - 50/60 Hz - 1 Ph
Maximum absorbed power	1.53 kW
Oxygen concentration	< 0.1%
Inert gases	Nitrogen, Argon
Inert gas consumption	<0.31/min @ 0.5% Oxygen
Filter unit	Removable
Machine dimensions	1390*777*1600 mm (L*W*H)
Net Weight	650 Kg

The SLM manufacturing procedure began with a CAD design of the desired specimen saved in STL format. The CAD file was then processed by a dedicated software package, MARCAM AutoFab, which subdivided the solid component into layers (figure 3.4). The material process parameters and scanning strategy were then designed with the same software.

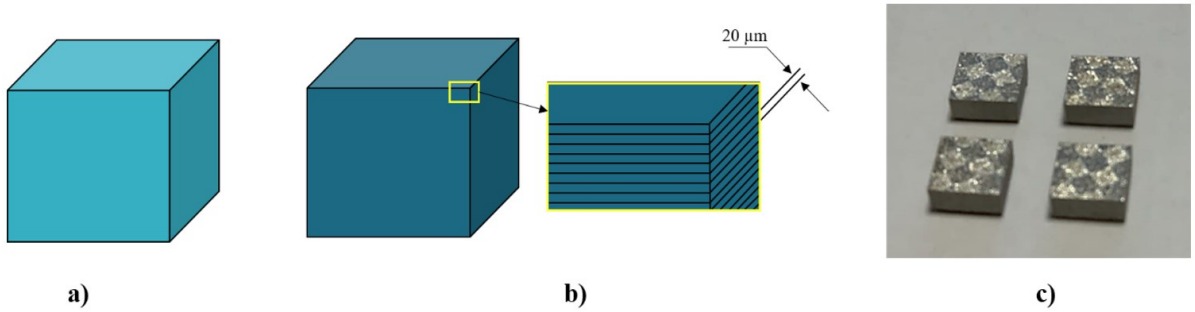

Figure 3. 4. Operation sequence for manufacturing of the SLM specimens: a) schematic of the STL-3D design, b) division of the 3D design into layers for SLM fabrication process, and c) final components.

In this study, SLM specimens were produced by adopting a chessboard scanning strategy, in which each layer was divided into 3 mm × 3 mm square blocks: firstly, the laser beam melted powders in the white blocks then in the black blocks (Figure 3.5). In each block, the laser beam scanned the surface along parallel lines with an offset equal to the hatch distance of 0.06 mm (space between two adjacent laser tracks as described in Figure 2.14), and with scanning direction perpendicular to that of adjacent blocks.

The correlation between the laser paths in several successive layers is evident in both Figure 3.5 and 3.6, where it is clearly shown that each layer was rotated by 45° with respect to the layers above and below. At the completion of each layer, the laser moved along the perimeter twice, in order to melt un-melted powders still present on the surface of the component.

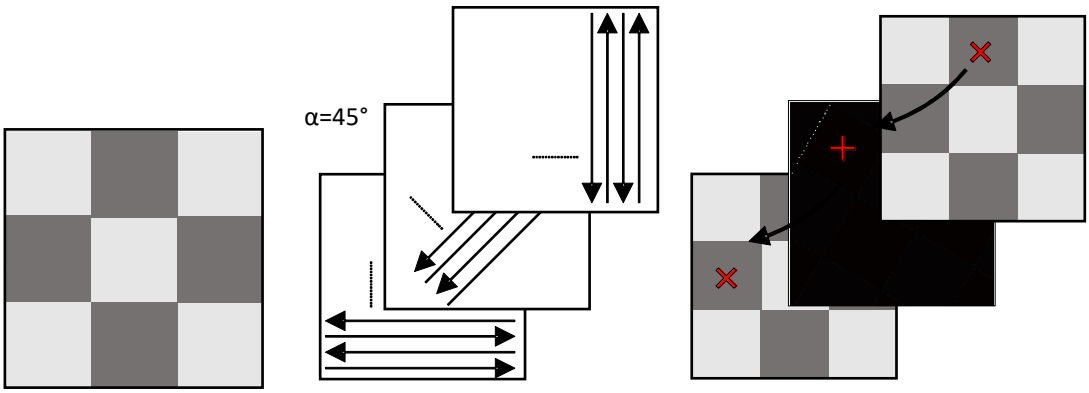

Figure 3. 5. Block melting sequence based on the chessboard strategy, Reprinted, and modified from [1].

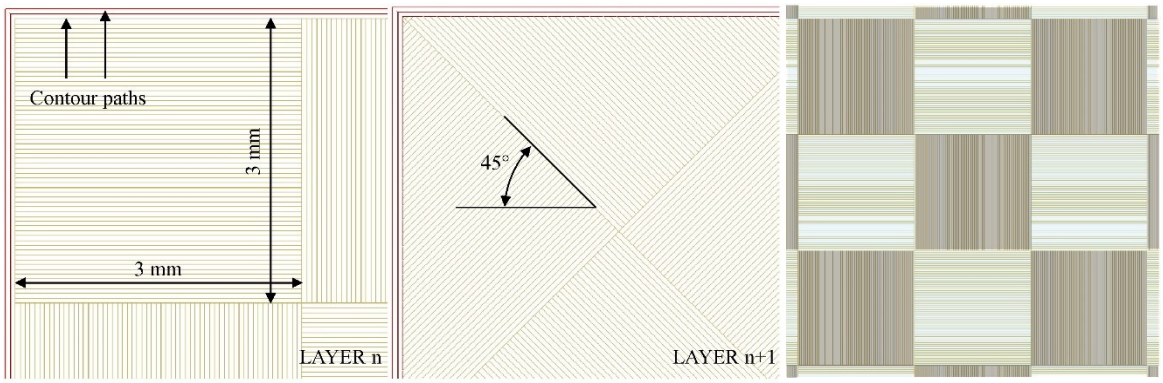

Figure 3. 6. Chessboard laser scanning strategy and (b) block melting sequence reprinted from [1].

As mentioned in the previous chapter, the SLM process can produce specific properties and characteristics by applying different process parameters.

In the present work, two series of samples were produced by applying two parametric building processes: relatively high power and low scanning speed (high fluence) to reproduce the fabrication of the final prosthetic component bulk and low power and high scanning speed (relatively low fluence) to reproduce the fabrication of the component surface. The SLM parameters adopted for the building of the samples are collected in Table 3.3. Using these process parameters, two different series of samples were obtained:

B1: with the maximum density, in order to obtain the highest mechanical strength (high fluence production strategy, for the bulk of the prostheses).

B2: with higher scanning speed and lower power, so reducing the time and cost of the procedure as well as reaching a relatively porous structure, which could help osseointegration with the surrounding tissues and bones (low fluence strategy, for the shell of the prostheses).

Table 3. 3. SLM process parameters and related relative density of CoCrMo samples.

Sample	Power (W)	Scan speed (mm/s)	Fluence (J/mm^3)	Relative density (%)
B1	150	900	138.8	99.8
B2	90	1200	53.6	95

3.2.2. Post-processing heat treatment of SLM CoCrMo alloys

In order to study the effect of post-processing heat treatment on the corrosion behaviour of CoCrMo alloys, samples were produced with different SLM process parameters than those reported in the previous section. These different process parameters are listed in Table 3.4. To understand the effect of post-processing on the corrosion behavior, both as-built samples (from now on C1 and C2) and samples heat-treated at 850 °C for 180 min (henceforth C1HT and C2HT) were investigated. The corrosion behavior of SLM samples was compared to that of specimens extracted from a Real Prosthesis, fabricated by a conventional method.

Table 3.4. Process parameters adopted for the fabrication of samples for corrosion tests

Samples	Laser Power [W]	Scanning velocity [mm s^{-1}]	Layer Thickness [mm]	Hatching Space [mm]	LED [J mm^{-3}]
C1, C1HT	90	500	0.02	0.06	150
C2, C2HT	150	500	0.03	0.06	167

3.2.3. Conventional wrought CoCrMo alloys

The biomedical wrought CoCrMo alloy (WRO) selected for comparison studies was supplied by ARCONIC in the form of a 16 mm diameter rod and was prepared according to ASTM F1537+ISO 5382.12 standard (nominal chemical composition in Table 3.5).

Table 3. 5. The nominal chemical composition (wt. %) of the studied conventional wrought CoCrMo alloy.

(wt. %)	N	Al	Si	Cr	Mn	Fe	Co	Ni	Mo	La	C
Average	0.162	0.01	0.76	27.8	0.75	0.13	64.77	0.066	5.43	0.07	0.048

3.2.4. Pure metals

Cyclic voltammetry tests (CVs) were also performed on pure Co (99.9 wt. % purity), Cr (99.7 wt.% purity) and Mo (99.9 wt. % purity) samples in the form of cylinders cut from rods with

10 mm, 8 mm, and 10 mm diameter, respectively, purchased from Goodfellow Cambridge Limited.

3.3. Test solutions

In order to study the corrosion behavior of SLM and WRO CoCrMo alloys, three types of test solutions were used in this work:

I – Phosphate buffered saline (PBS) solution, pH, 7.4 *(simulating normal physiological conditions).*

II – Phosphate buffered saline (PBS) solution, pH, 4 *(simulating inflammatory conditions).*

III – Phosphate buffered saline (PBS) solution, pH, 4 and 30 mM hydrogen peroxide, H_2O_2 *(simulating more severe inflammatory conditions).*

The composition of these solutions is reported in Table 3.6. The acid pH of solutions II and III was obtained by adding some drops of diluted HCl solution to the plain PBS and, in order to keep the chloride concentration unaltered, the quantities of KCl and NaCl were reduced, keeping the $[Na^+]/[K^+]$ ratio constant. The solutions were freshly prepared from deionized water and Sigma-Aldrich analytical grade chemicals. The test temperature was kept at 37 ºC by using a thermostat.

Table 3. 6. Chemical composition of the test solutions (g/L).

Chemical compounds	Solution I	Solution II	Solution III
Na_2HPO_4 (g/L)	1.42	1.42	1.42
KH_2PO_4 (g/L)	0.245	0.245	0.245
KCl (g/L)	0.2	0.18	0.18
NaCl (g/L)	8.8	8.32	8.32
Total Cl^- (M)	0.15	0.15	0.15
H_2O_2 (mM)	-	-	30
pH	7.4	4.00	4.00
Electrical conductivity (mS/cm^2)	17.15	16.56	16.56

3.4. Sample preparation

3.4.1 Electrochemical specimens

SLM CoCrMo samples for electrochemical tests (polarization curve recording, electrochemical impedance spectroscopy, and cyclic voltammetry) were square parallelepipeds. From these samples, electrodes were prepared by connecting insulated copper wires to the back of the parallelepiped. Then, they were painted by a two-component epoxy varnish in order to avoid crevice corrosion under the test condition and finally they were embedded in epoxy so that the resulting exposed section was perpendicular to the SLM building direction (Figure 3.7). The area of the exposed surface was 1 cm^2.

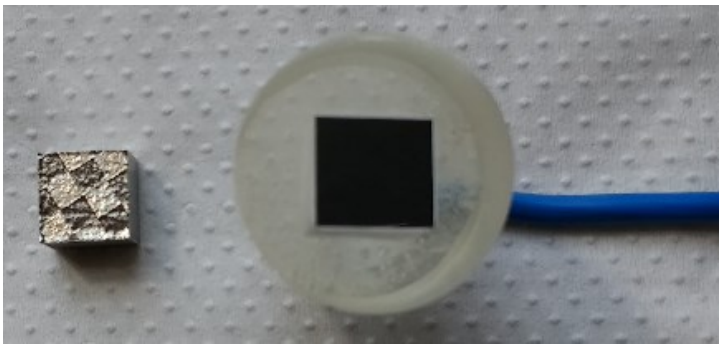

Figure 3. 7. SLM CoCrMo sample and corresponding electrode for electrochemical investigations.

In the case of wrought CoCrMo and pure Co, Cr, and Mo electrodes, cylindrical samples were prepared, and final electrodes, embedded in epoxy with the same method, exposed surface areas of 2.01, 0.79, 0.52, and 0.80 cm^2, respectively (see Table 3.7).

Table 3.7. Exposed surface area of final wrought CoCrMo, pure Co, pure Cr and pure Mo electrodes, embedded in epoxy.

Cylindrical sample	Exposed surface area (cm^2)
Wrought CoCrMo alloy	2.01
Pure Co	0.79
Pure Cr	0.52
Pure Mo	0.80

Prior to each test, the specimens were wet ground by grit SiC paper from no. 600 down to no. 1200. Afterward, they were mirror-polished using 6 µm, 3 µm, and 1 µm diamond pastes on the respective polishing clothes. The specimens were then washed with distilled water under

ultrasounds, then degreased by ethanol, dried by hot air, and finally immersed in the test solution.

3.4.2 Tensile specimens

Tensile specimens were built with a 6 mm circular cross-section diameter, 25 mm gauge length and a 5 mm transition radius between the threaded gripped ends and the gauge length, as illustrated in Figure 3.8. Figure 3.10 evidences the building direction for these specimen types.

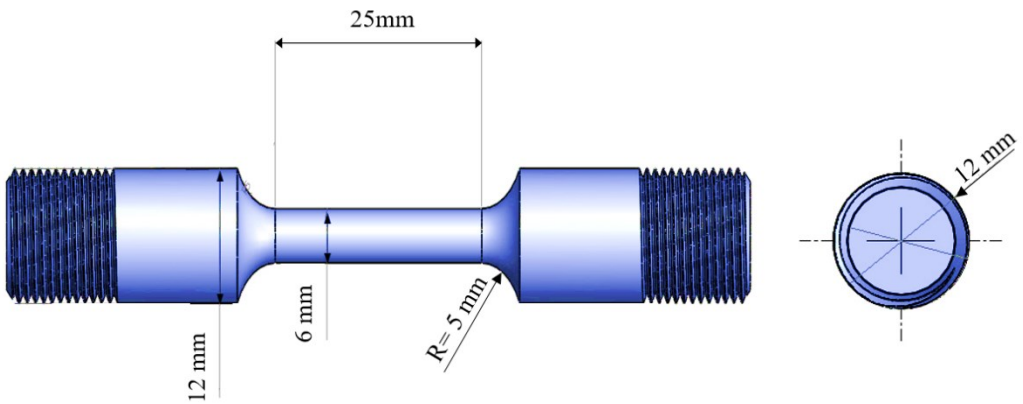

Figure 3. 8. The CAD design and the specifications of the tensile sample.

These specimens were obtained from B1 and B2 SLM alloys but some tensile specimens were also prepared according to a double strategy (B1+B2 samples,): the core (diameter of 3 mm) was built up with the process parameters of B1 (characterized by higher relative density and higher strength), while the external shell (thickness of 1.5 mm) with the process parameters of B2 (better corrosion behaviour, easier osseointegration).

3.4.3. Slow Strain Rate Testing (SSRT) specimens

In the case of Slow Strain Rate Tests, B1 and B2 tensile specimens with an overall length of 90 cm and a gauge portion of 25 mm diameter were produced. The samples were then ground parallel to the stress direction by using SiC-papers from #120 down to #2500, then they were degreased, dried and screened by a two-component epoxy varnish, so leaving only the gauge portion exposed to the solution. The CAD design and specifications of the SSRT sample are

shown in Figure 3.9, while the building direction in the specimens is evidenced in Figure 3.10.

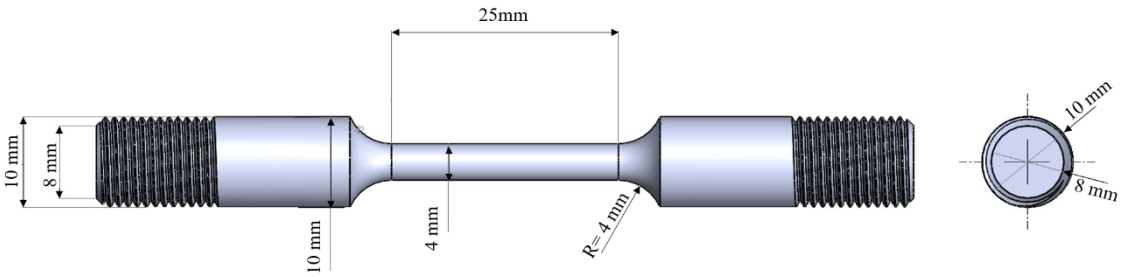

Figure 3. 9. The CAD design and the specifications of the SSRT sample.

3.4.4 Microhardness test specimens

Small plate-shape B1 and B2 SLM samples with dimensions of 10 mm x 10 mm x 5 mm were used for microhardness measurements. The square-shape surface was perpendicular to the building direction (Figure 3.10). On WRO CoCrMo alloy, microhardness tests were performed on the cross-section surface of rods with diameter of 20 mm and height of 5 mm. Before measurements, the specimen surface was ground, polished, degreased and dried as described for electrochemical test electrodes (sect. 3.4.1).

Building direction during SLM process as well as differences between different samples using for mechanical/mechanical-chemical investigations are illustrated in Figure 3.10.

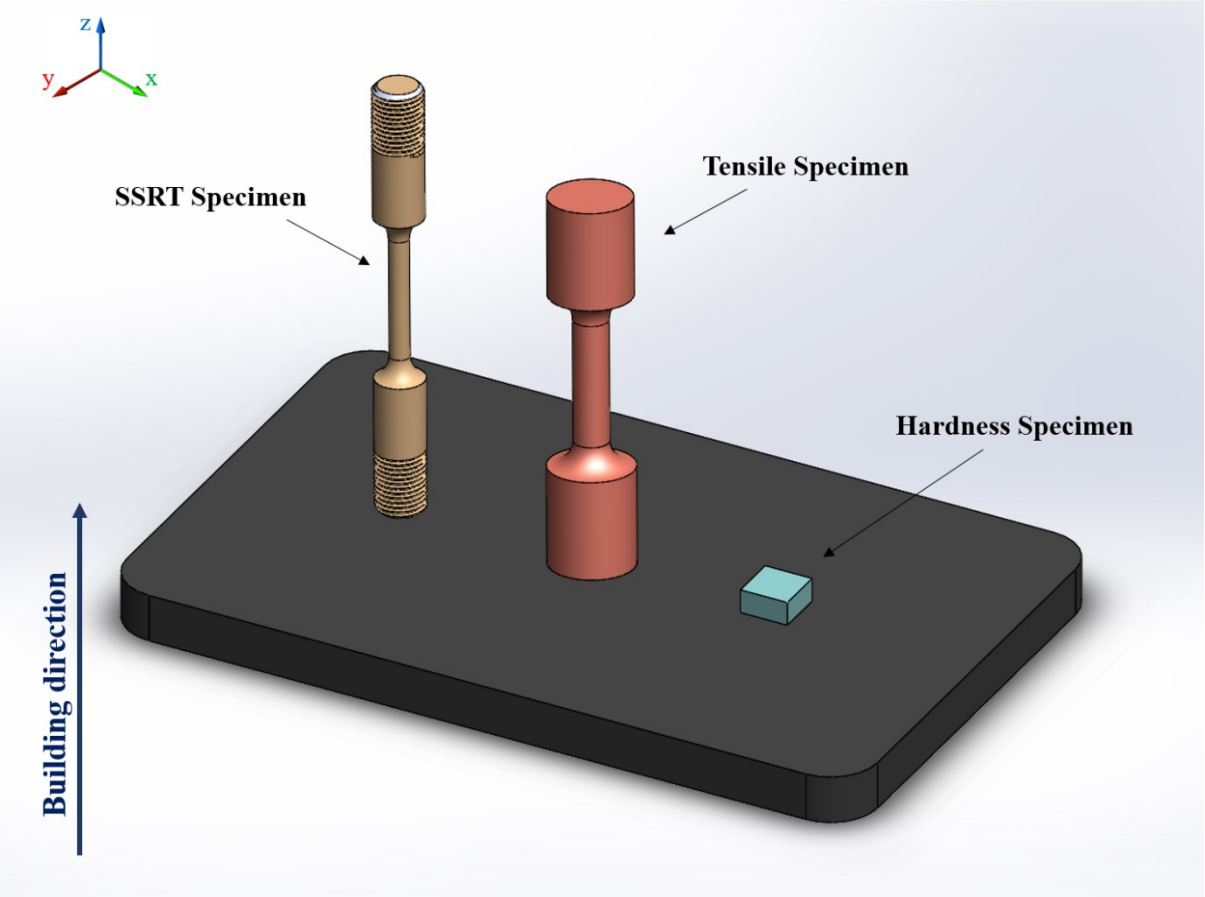

Figure. 3.10. Schematic and orientation of SLM fabricated counterparts.

3.5. Electrochemical techniques

The electrochemical techniques were conducted using a PAR 2263 potentiostat/FRA/ galvanostat (for Electrochemical Impedance Spectroscopy (EIS)) and with a PAR 273A potentiostat/galvanostat (for polarization curves (PC) recording and cyclic voltammetry (CV) tests). The measurements were carried out using the basic configuration of the conventional three-electrode cell consisting of working, counter, and reference electrode.

The working electrode (WE): The working electrode is made of the material to be investigated (in this research, CoCrMo biomaterials and pure metals).

The counter electrode (CE), or auxiliary electrode (AE): The potentiostat applies a potential difference between WE and CE, such that it brings the potential of the WE with respect to RE to the desired value. The CE is usually made of an inert/noble material (such as graphite, platinum, gold) or, more rarely, a material that will not introduce contaminating ions into the electrolyte, such as stainless steel. A platinum electrode was used as the counter electrode in this experimental work.

The reference electrode (RE): The reference electrode (RE) is an electrode with a stable and known potential versus the standard hydrogen electrode (SHE), used to measure and control the potential of the WE. The main properties of a satisfying reference electrode are i) presence of a constant reproducible potential due to involvement in well-defined electrochemical equilibria, ii) non-polarizability (insensitivity to current flow between WE and CE), and iii) ease of use. The standard Saturated Calomel Electrode (SCE) and the saturated silver/silver chloride electrode (Ag/AgCl) respectively showing potentials of +0.244 V and +0.199 V versus SHE, were used in the present work. However, all potentials reported in this thesis are converted versus SCE.

The schematic configuration of the electrochemical cell and connection to the potentiostat are shown in Figure 3.11.

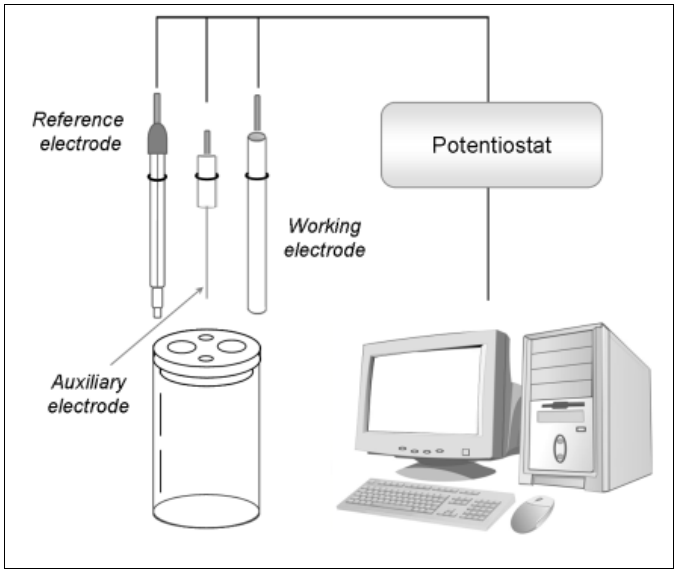

Figure 3. 11. Principal components of the electrochemical test.

3.5.1. Corrosion potential (E_{corr}) and cyclic polarization curves [2]

Unless localized corrosion occurs, passive metals like CoCrMo alloys in aerated, acidic, near neutral, or alkaline solutions behave like noble metals. They exhibit a noble corrosion potential (E_{corr}) and very low corrosion current densities (i_{corr}), coinciding with the passivity current, (i_p), as depicted in Figure 3.12.

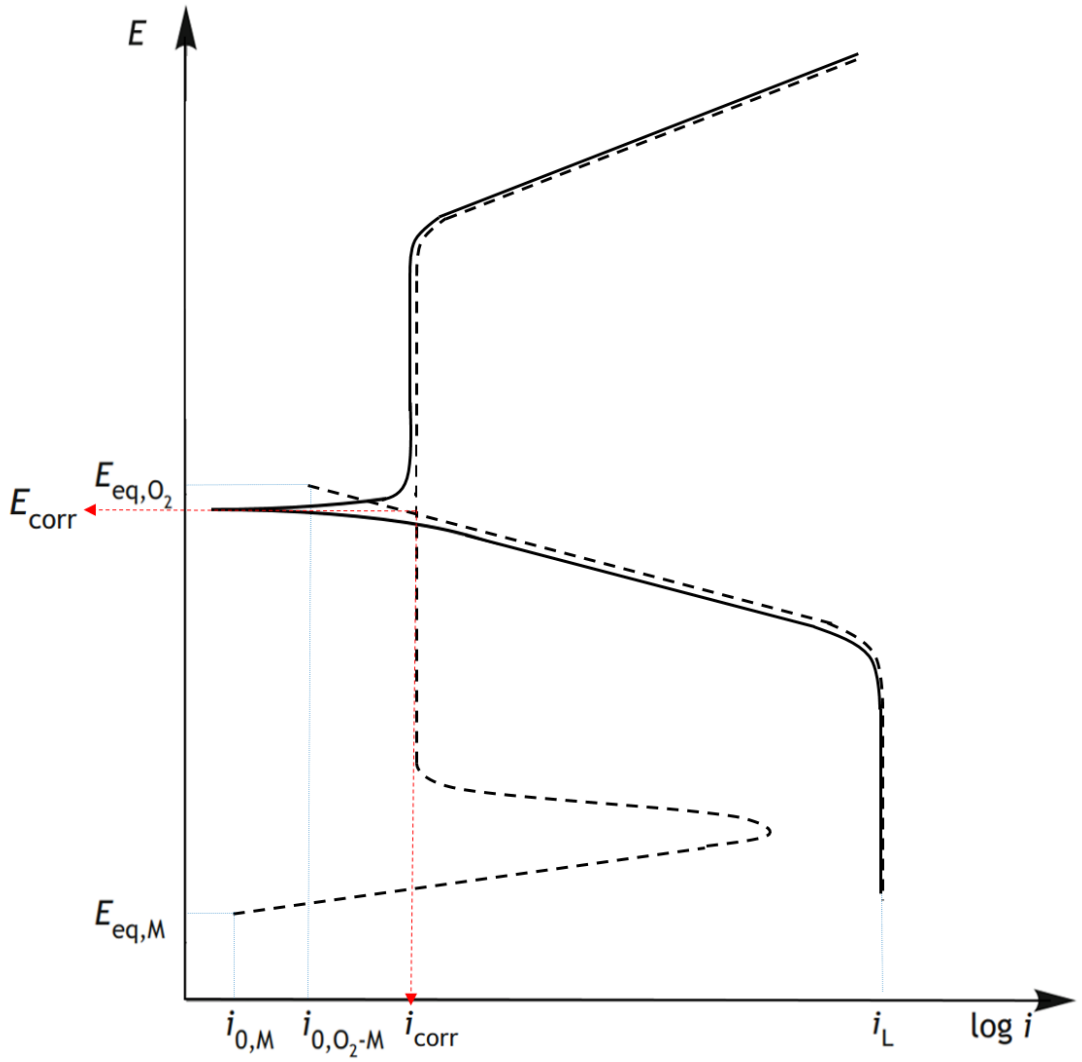

Figure 3. 12. Corrosion conditions of a passive metal in aerated solutions.

E_{cor} of the studied metal (WE) under free corrosion conditions can be easily measured versus a proper RE. Monitoring of E_{cor}, associated to the registration of the polarization curves (PC) at specific immersion times on newly prepared electrodes, can give information on the corrosion mechanism and the evolution of the kinetics of the anodic and cathodic reactions of the corrosion process.

In this research, cyclic potentiodynamic polarizations curves were recorded after 1h and 15 days of immersion at a scan rate of 0.1 mV s^{-1}, always starting at -0.2 V vs E_{cor}. The vertex potential for the cyclic polarization was usually +1 V. The polarization curve recording was stopped at the potential of zero current.

Each electrochemical test was replicated at least three times to assess the data variability, and then representative plots were selected and reported in the figures.

3.5.2. Electrochemical impedance spectroscopy [3]

The electrochemical Impedance Spectroscopy (EIS) is a non-destructive and relatively modern technique in which measurement in the frequency domain is made by applying sinusoidal potential (or current) perturbations of different frequency to a system and measuring the related sinusoidal current (or potential) response.

The impedance measurements are significant if they meet the rules of [4–6]:

• *Causality*: the system must be entirely determined by the applied perturbation;

• *Linearity*: a system is linear if the response to a sum of individual inputs is equal to the sum of individual responses. In order to meet linearity requirements, electrochemical impedance is commonly measured using a small excitation signal;

• *Stability*: a system is stable when it remains stable unless excited by an external source and should return to its original state after excitation;

• *Finite value*: the impedance must have a finite value at both zero and infinite frequency.

The potential excitation signal, expressed as a function of time, has the form

$$E(t) = E_0 \sin \omega t \quad (3.1)$$

where E(t) is the potential at time t, E_0 is the amplitude of the signal, and ω is the radial frequency. The relationship between radial frequency ω (expressed in radians/second) and frequency f (expressed in hertz) is:

$$\omega = 2\pi f. \quad (3.2)$$

In a linear system, the response signal, I(t), is a sinusoid with amplititude I_0 shifted in phase by the phase angle (Φ):

$$I(t) = I_0 \sin (\omega t + \Phi) \quad (3.3)$$

The Ohm's Law allows us to calculate the impedance of the system as:

$$Z = E/I = (E_0 \sin \omega t) / (I_0 \sin (\omega t + \Phi)) \quad (3.4)$$

The impedance is therefore expressed in terms of a magnitude, Z_0, and a phase shift, Φ. With Euler's relationship,

$$\exp(j\,\Phi) = \cos\Phi + j\sin\Phi \quad (3.5)$$

it is possible to express the impedance as a complex function. The potential is described as,

$$E(t) = E_0 \exp(j\omega t) \quad (3.6)$$

and the current response as,

$$I(t) = I_0 \exp(j\omega t - \Phi) \quad (3.7)$$

The impedance is then represented as a complex number,

$$Z(\omega) = E/I = Z_0 \exp(j\omega) = Z_0(\cos\Phi + j\sin\Phi) = Z' + j\,Z'' \quad (3.8)$$

It is composed of a real (Z') and an imaginary (Z") part. If the real part is plotted on the X-axis and the imaginary part is plotted on the Y-axis of a chart, we get the Nyquist plot of the impedance spectrum (Figure 3.13). Notice that in this plot, the Y-axis reports –Z" and that each point on the Nyquist plot is the impedance at one frequency.

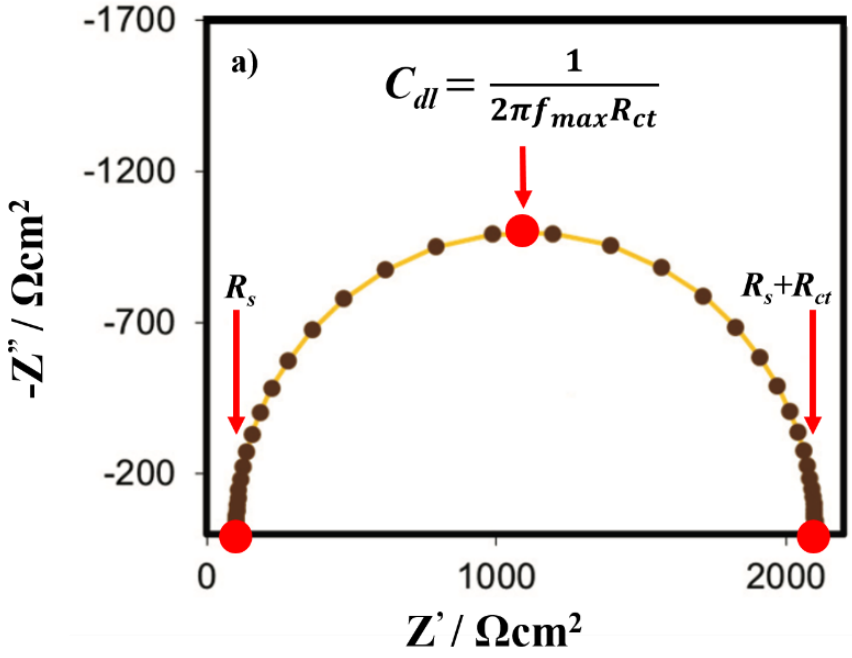

Figure 3. 13. Nyquist diagram representing impedance spectrum of the equivalent circuit in Figure 3.14a.

The spectra are commonly analyzed by fitting them by a proper equivalent electrical circuit. Most of the circuit elements are simple electrical elements such as resistors, capacitors, and inductors (Figure 3.14). To be useful, the circuit elements should have a physical correspondence in the analyzed electrochemical system. As an example, a corrosion process like iron in an acid environment, involving a charge transfer reaction, shows a Nyquist diagram with a single semicircle (a single "time constant") like that in Figure 3.13. This spectrum can be fitted by the simple equivalent circuit (EC) of Figure 3.14a, where R_s is the resistance of the electrolyte between the WE and RE and the electrical connections, R_{ct} is the charge transfer resistance of the corrosion process and C_{dl} represents the capacity of the electrochemical double layer. R_{ct} also represents to the overall resistance to the electrochemical corrosion reaction and therefore corresponds to the polarization resistance, R_p.

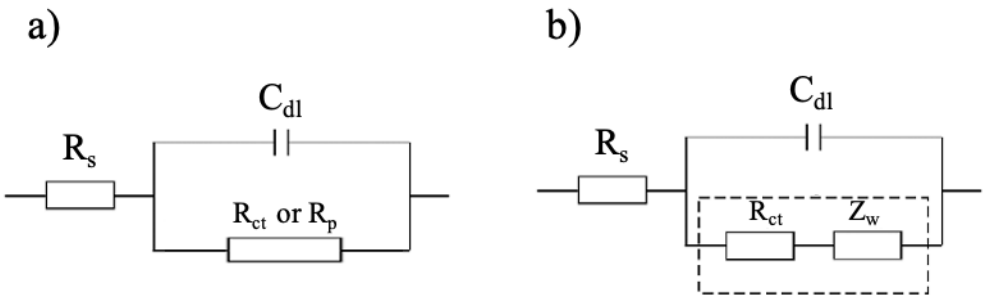

Figure 3. 14. Representation of a) Simplified Randles circuit, b) Randles circuit with Warburg element.

If the impedance spectrum is plotted by reporting the log frequency on the X-axis and both the absolute values of the impedance modulus (|Z|) and the phase angle (Φ) on the Y-axis, the Bode plot representation of the impedance spectrum is obtained. The Bode plot corresponding to the Nyquist plot in Figure 3.13 is shown in Figure 3.15.

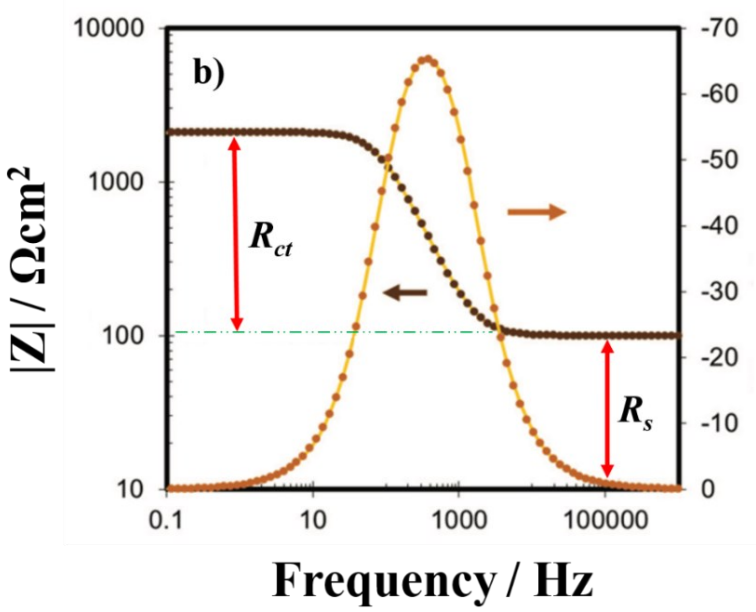

Figure 3. 15. Bode plot of the impedance spectrum of the equivalent circuit in Figure 3.14a.

The Nyquist plots of electrochemical systems often contain more semicircles (and more time constants).

If the low-frequency arc is followed by a straight section, the so-called Warburg element is added to the equivalent circuit, as shown in Figure 3.14b, to take into account the diffusion phenomena. The Nyquist spectrum, in this case, is reported in Figure 3.16.

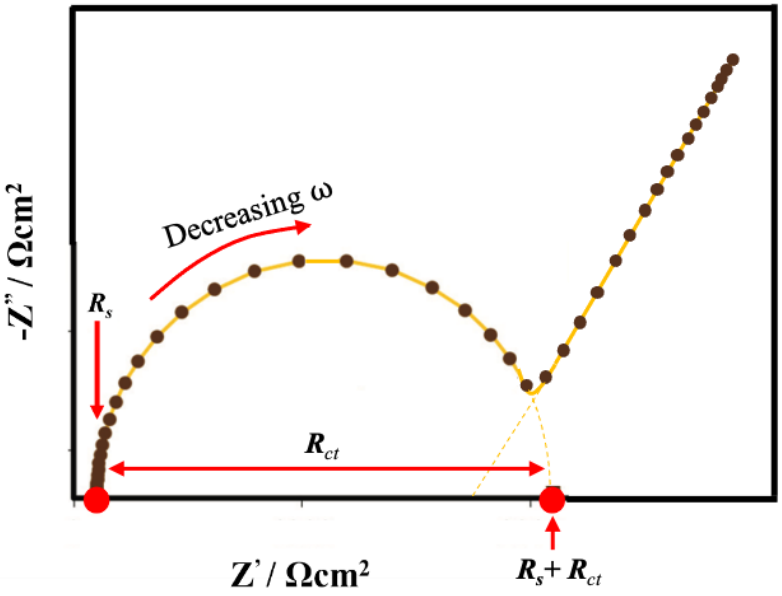

Figure 3. 16. Nyquist diagram representing impedance data of the equivalent circuit in Figure 3.14b.

In this work, Electrochemical Impedance Spectroscopy (EIS) was used to monitor the evolution of the corrosion behavior of the studied metals during the immersion period. The instrumentation used was a PAR 2263 potentiostat/FRA/ galvanostat. The EIS tests were performed at the corrosion potential (E_{corr}) by imposing a 10 mV_{rms} amplitude excitation voltage in the frequency range 10^4 –10^{-3} Hz with five measurements per decade. From each spectrum, the polarization resistance (R_p) value was estimated as the limit of the real part of the impedance at frequency tending to 0. The R_p values were estimated by circle fitting the low frequency portion of the Nyquist spectra and corresponded to the low frequency intercept of the circle with the real axis. Finally, the EIS spectra were analyzed by using the software ZView 3.5D software (Scribner Associates Inc). It should be noted that each electrochemical test was replicated at least three times to assess the data variability, and representative plots were reported in the figures.

3.5.3. Cyclic voltammetry

Cyclic voltammetry (CV) is a widely used method for obtaining qualitative information about the electrochemical behavior of a system. A potential ramp is cyclically applied to the electrode under test at a constant potential scan rate. The voltammogram is obtained by plotting the measured current density versus the applied potential [7].

A current peak in the CV plot is seen at the potential at which any electrochemical reaction takes place on the electrode. The width, height, and position of each peak depend on factors such as the nature of the electrochemical reaction and working electrode material, the scan rate, the concentration of the soluble species involved [8,9]. Figure 3.17 shows a graphical representation of the typical voltammogram obtained in the presence of a single redox couple, with the indication of the corresponding reduction and oxidation peaks. The Figure also evidences the current due to capacitive effects, which rises in proportion to the potential scan rate, $\Delta V/\Delta t$.

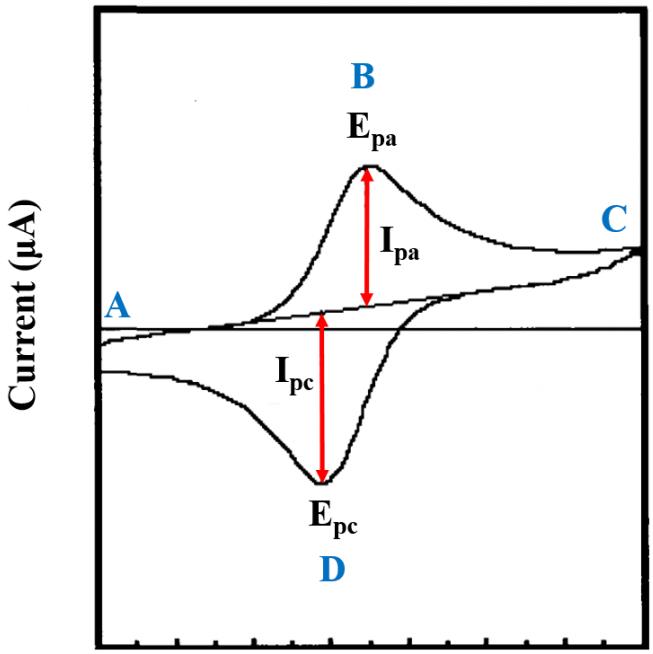

Figure 3. 17. A typical voltammogram of current versus potential. Reprinted and modified from [7].

The CV tests were performed by using a 273A potentiostat/galvanostat controlled by PowerSuite software (Advanced Measurement Technology Inc., AMETEK, Berwyn, Pennsylvania, USA), with a conventional three electrode cell, composed by a working electrode (selected metal/alloy electrodes), a Pt counter electrode and a SCE as reference electrode. The investigate alloys were B1 SLM alloy as well as wrought CoCrMo counterpart. CV tests were also performed on Co (99.9 wt. % purity), Cr (99.7 wt.% purity) and Mo (99.9 wt. % purity) samples. From the alloys and pure metals, proper electrodes were prepared as described in sect. 3.4.1 The exposed surface area of SLM was 1 cm^2 and for other electrodes as depicted in Table 3.6. In the case of SLM electrodes, the exposed section was perpendicular to the building direction.

Each CV test consisted of recording 5 cycles between -1.5 to +0.7 V_{SCE}, at a scan rate of 120 mV s^{-1}, under stirring (magnetic stirrer set at 250 rpm). Before each test, the working electrode was preconditioned at -1.5 V_{SCE} for 80 s to reduce the air-formed passive film. Some tests were also performed in different potential ranges, with the aim to help CV interpretation. All the potential values in the text are referred to SCE. Each electrochemical test was replicated at least three times to assess the data variability and representative plots were reported in the Figures.

3.6. Mechanical testing

Metallic biomaterials are often used to make implants that substitute load-bearing parts of the living body. Thus, the assessment of the mechanical properties is fundamental for the design of these devices with new alloy types.

3.6.1. Vickers microhardness testing (VH)

Hardness testing is the most frequently used method for characterizing the mechanical properties of the materials. Microhardness is a term usually referred to indentation hardness testing made with loads that do not exceed 1 kgf. The majority of microhardness tests involve application of loads of 100-500 gf (1 - 5 N); however, it is also possible to apply loads as light as 1 gf (0.01 N, in nanohardness measurements). In Vickers microhardness test, the hardness value (HV) is determined by pressing an indenter of a well-defined nature and geometry (a diamond pyramid with a square base and an angle of 136°) onto the surface of the sample under a predefined load [10]. Thus, an indentation is produced of pyramidal shape with a square base (Figure 3.18a). The length of the two diagonals of the indentation base is measured with a microscope and the mean value is used to calculate HV by using conversion tables, in accordance with ASTM E384. More specifically, the HV value corresponds to the ratio between the applied test load and the surface of the indentation as shown in equation 3.9.

$$HV = F/S = 1.854\ F/d^2 \quad (3.9)$$

where F is the load (in kgf), S the area of the surface indentation (in mm^2), and d is the mean diagonal length (in mm) of the pyramid square base on the specimen surface. Using different loads results in different indentation sizes, as shown in Figure 3.18b [10].

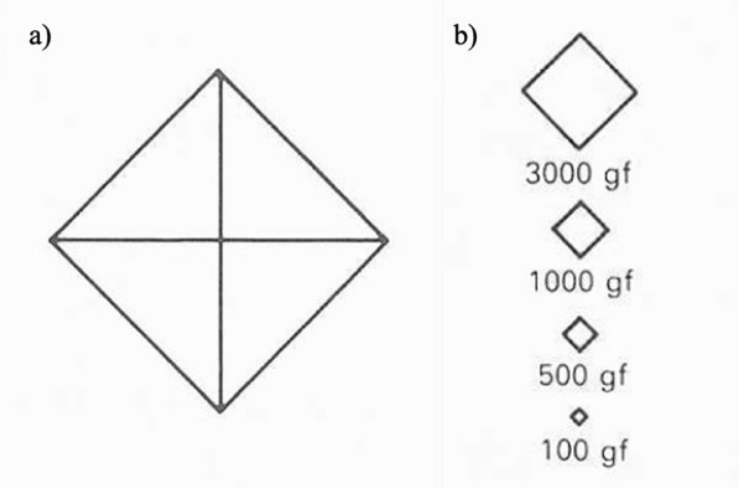

Figure 3.18. Indentation shape made by Vickers indenters. Reprinted from [10]

The principal components of a Vickers microhardness tester machine are shown in Figure 3.19.

In the present study, a Leitz mini-load microhardness tester was utilized to carry out microhardness tests on flat polished samples by applying a load of 300 gf and a dwell time of 15 s. Micrographs of the indentations were obtained by a Leica optical microscope in order to accurately measure the indentation diagonal values.

HV tests were performed on all three alloy types: B1, B2, and the WRO CoCrMo alloys.

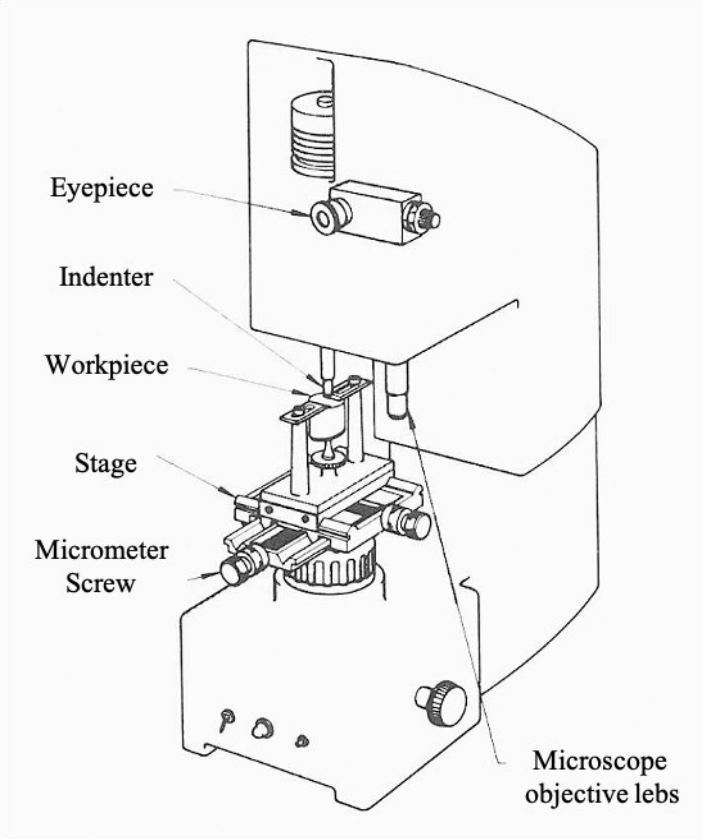

Figure 3.19. Principal components of a Vickers microhardness tester. Reprinted from [10].

3.6.2. Tensile tests [11]

The tensile properties of materials can be obtained by performing the tensile test. The specimens for tensile test consist of a gauge portion with constant section and specific gripping ends, as illustrated in Figure 3.20 and 3.21. The gauge is the region over which measurements are done and is centered within the constant section portion.

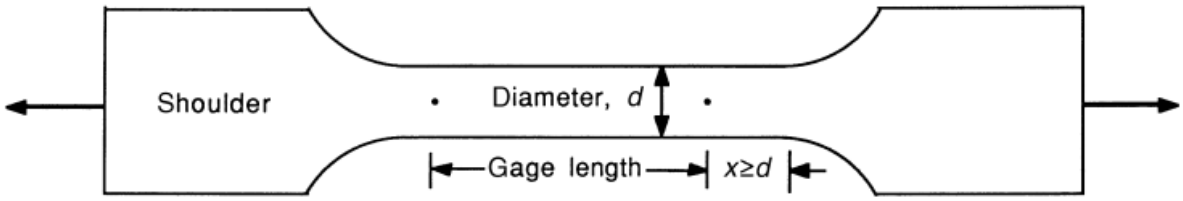

Figure 3.20. Typical tensile specimen, representing a reduced gauge section and enlarged shoulders. Reprinted from [11].

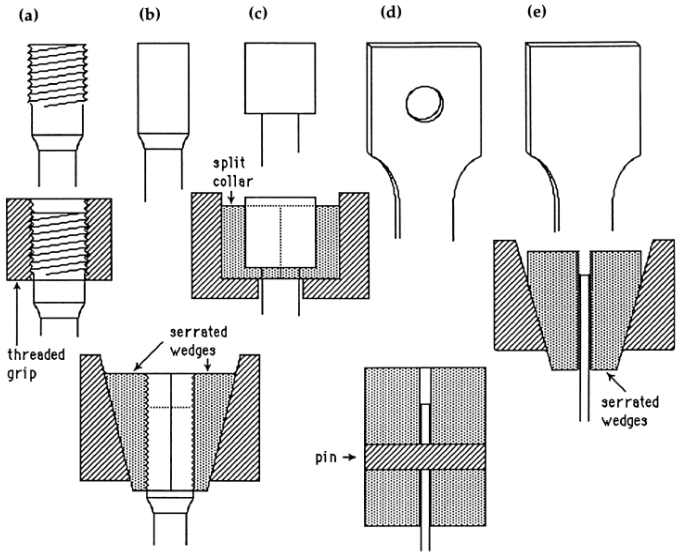

Figure 3. 21. Systems for gripping tensile specimens. For cylindrical specimens; a) threaded grips, b) serrated wedges, c) and, for butt end specimens; c) split collars constrained by a solid collar. For plannar specimens; d) pins, e) serrated wedges. Reprinted from [11].

During the tensile test, the load, F, is monitored as a function of the elongation of the gauge length, Δl, and a stress-strain (σ-ε) curve is obtained, where the stress σ is:

$$\sigma = F/A_0 \tag{3.10}$$

A_0 is the initial constant section area, and the strain ε is:

$$\varepsilon = \Delta l / l_0 \tag{3.11}$$

In Figure 3.22, a typical σ-ε curve of a ductile material is shown. It includes both elastic and plastic deformation regions: in particular, 0-a is the linear elastic deformation region where the stress is proportional to the strain, according to the Hooke's law. The Young modulus of the material can be obtained by calculating the slope of this region. In most metallic materials, the transition between the elastic and plastic deformation is not clearly visible in the σ-ε curve. By convention, the plastic deformation region starts in correspondence of the

yield strength which is taken as the stress at which 0.2% plastic deformation occurs (ordinate of point b). The maximum stress in the plastic deformation region (ordinate of point c), is the ultimate tensile strength (UTS) of the material. The specimen fracture occurs at point d.
Parameters such as percent elongation after fracture and percent reduction of area after fracture are often evaluated as indexes of material ductility.

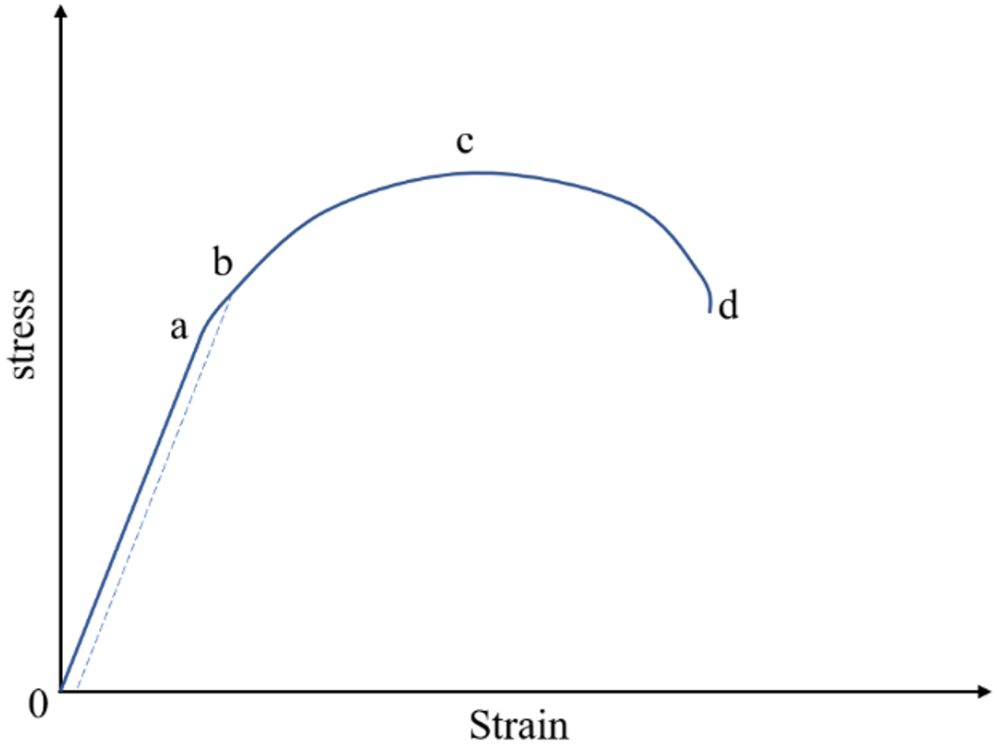

Figure 3.22. Schematic diagram of a tensile stress-strain curve.

Figure 3.23 shows a scheme of a universal tensile machine.
In the present study, tensile tests were performed with a hydraulic testing machine, using a crosshead strain rate of 1 mm/min at room temperature. Stresses were calculated by dividing the applied load by the cross-sectional area of the gauge part, whereas a clip-on extensometer was used for measuring and recording the strain values. The shape and dimensions of the tensile specimens are reported in sect. 3.4.2.

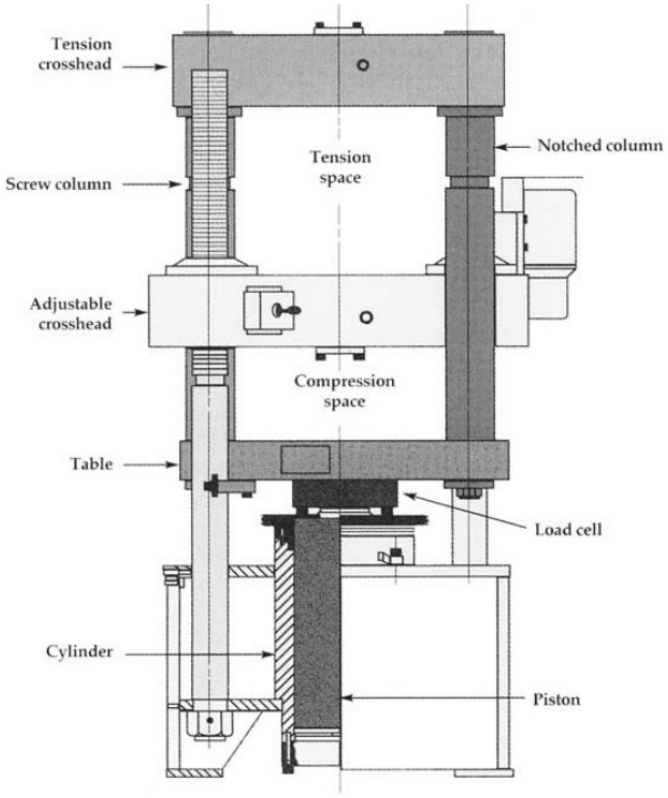

Figure 3.23. Principal components of a tensile testing machine [11].

3.7. Testing combined conditions of corrosion and mechanical loading

3.7.1. Slow strain rate test

The slow strain rate test (SSRT) can predict the susceptibility of an alloy to stress corrosion cracking (SSC) in a specific environment [12,13]. Typically, it involves strain rates in the range 1×10^{-7} s^{-1} - 1×10^{-5} s^{-1}. The tensile behavior is evaluated in the aggressive solution and the results obtained are compared to those obtained in an inert environment, in terms of strain percentage to fracture (ε_f %) and fracture surface morphology. In particular, the SCC susceptibility was evaluated by calculating the ratio, R, between the ε_f % value in the test solution and the corresponding value in air. In the case of stainless steel $R < 0.8$ is usually taken as an indication of SCC susceptibility [13]. The presence of SCC can be also confirmed by the formation of secondary cracks on the specimen surface. During the test in aggressive environment, the time evolution of E_{cor} can be monitored to achieve information on the electrochemical SCC mechanism.

Figure 3.24 shows a scheme of a SSRT machine. In order to study the possible susceptibility of SLM B1 and B2 alloys to stress corrosion cracking in the artificial physiological solution simulating severe inflammation conditions, SSRT were performed in air and in PBS solution with 30 mM H_2O2 at pH 4 at the temperature of 37°C, using strain rate of 10^{-7} s^{-1}. Stresses were calculated by dividing the applied load by the cross-sectional area of the gauge part, whereas a clip-on extensometer was used for measuring and recording the strain values. Besides, strains were the result of the division of the sample elongation, as evaluated from the relative movement of the machine crosshead to its original length.

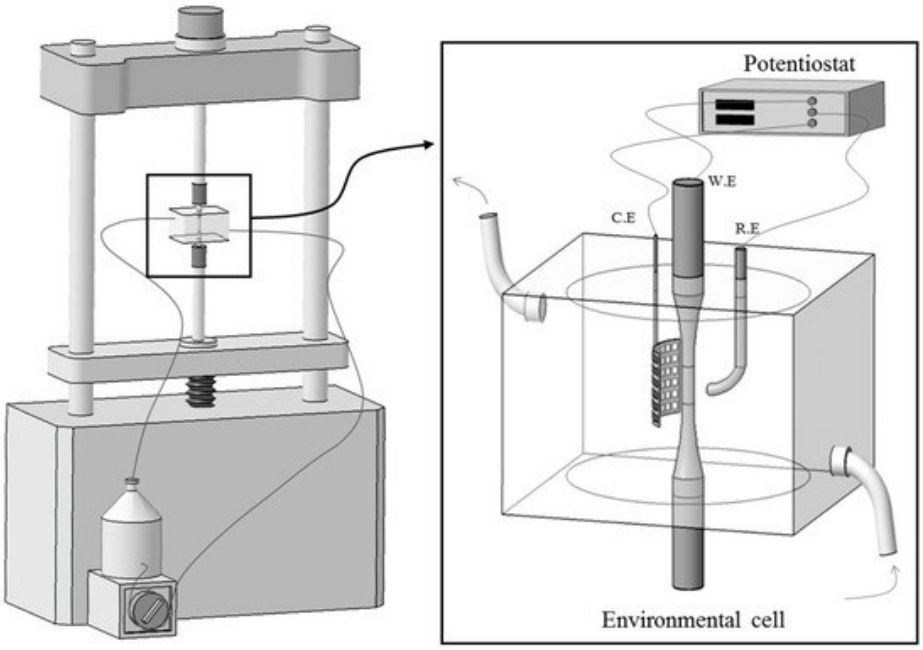

Figure 3.24. Schematic illustration of an SSRT machine and its components. Reprinted from [14].

3.8. Characterization methods

3.8.1. X-Ray Diffraction (XRD)

X-ray diffraction is a powerful non-destructive technique for characterizing crystalline materials. It provides information on structures, phases, preferred crystal orientations texture, and other structural parameters, such as average grain size, crystallinity, strain, presence and crystal defects. XRD peaks are produced by constructive interference of a monochromatic

beam of X-rays scattered at specific angles from each set of lattice planes in a sample, according to the Bragg law:

$$2d \sin \theta = n \lambda \quad (3.16)$$

where d is the interplanar spacing, θ represents the scattering angle, n is a positive integer, and λ is the wavelength of the incident wave (Figure 3.25). The peak intensities are determined by the atomic positions within the lattice planes. Consequently, the XRD pattern is the fingerprint of periodic atomic arrangements in a given material. An online search of a standard database for X-ray powder diffraction patterns enables quick phase identification for a large variety of crystalline samples.

In the present work, X-Ray diffraction was used to characterize CoCrMo powders and SLM and WRO CoCrMo alloys. The Phase identification and structural characterization was carried out with a Bruker D8 Advances diffractometer (Bruker, Billerica USA) equipped with Cu tube, in the 2θ range of 25-125 degree. The quantitative phase analysis and the evaluation of the crystallite size were performed by the Rietveld refinement method implemented in the Topas software (Bruker, Billerica USA) using a spherical harmonics correction (SHPO, 8 terms) to take into account the preferential orientations.

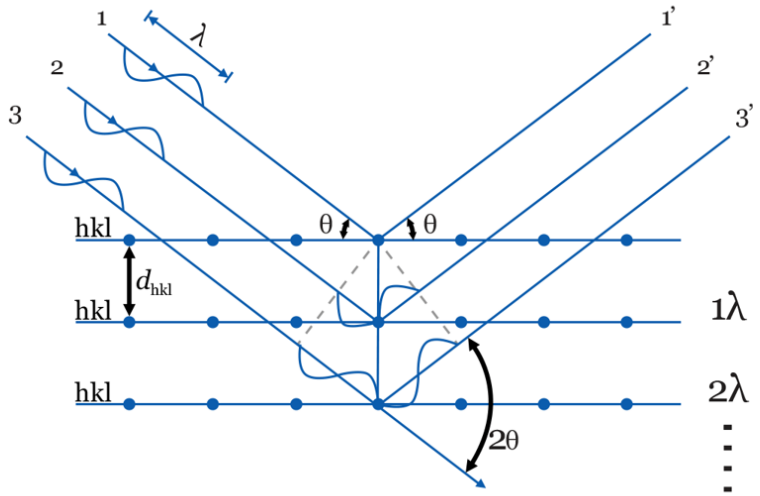

Figure 3.25. Bragg diffraction. Reprinted and modified from [15].

3.8.2. Surface analysis and microscopical characterization

This section gives an introduction and general principles of the various surface characterization methods used in the present Ph.D. thesis.

3.8.2.1 Reflected light optical microscope (LOM)

The light optical microscope, commonly applied to investigate the microstructure of metallic specimens, creates a magnified image of a sample by using the objective lens, and magnification is determined by the lens ability to bend light and focus it on the specimen surface [16]. Optical microscopes are relatively simple and popular devices because they use visible light, so that samples may be directly visualized with the eyes. Originally, images were captured by photographic film but modern developments in complementary metal-oxide-semiconductor and charge-coupled device (CCD) cameras allow the capture of digital images. The principal components of a light optical microscope are schematically depicted in Figure 3.26.

In the present work, the sample microstructures and the corrosion attack morphologies were investigated by using a Leica DMRM microscope. To investigate the sample microstructures, the samples were embedded in cold-mounting resin, then they were automatically ground, polished to 1 μm diamond using a Struers polishing machine, rinsed with distilled water and ethyl alcohol and dried. Finally, the samples were electrolytically etched in a solution containing 100 ml H_2O, 8 ml HCl, 16.75g $FeCl_3$, at an applied potential of 6-7 V for 7-10 s in order to reveal the microstructure of the CoCrMo alloys.

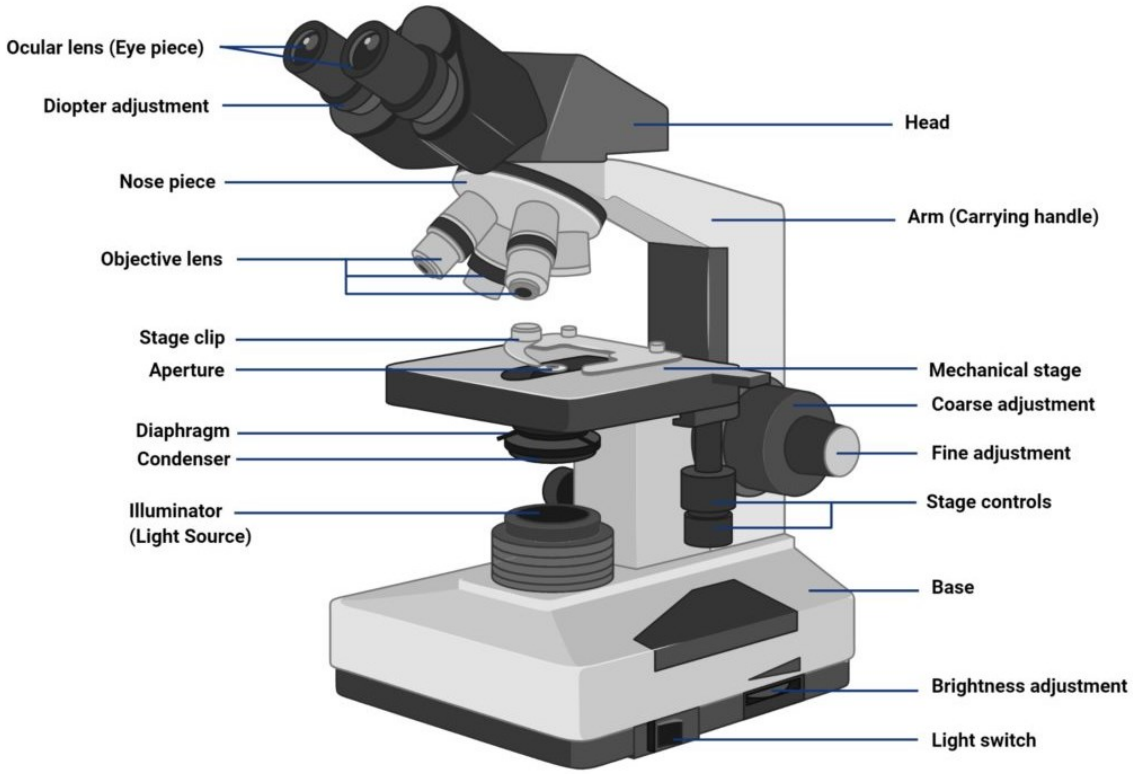

Figure 3.26. Schematic illustration of an optical microscope machine and its components. Reprinted from [17].

3.8.2.2 Scanning electron microscope (SEM)

When an accelerated electron beam interacts with the surface atoms of a material, various signals are produced, as schematically depicted in Figure 3.27. The volume and depth of the interaction region increase at increasing energy of the electron beam and decreasing average atomic number.

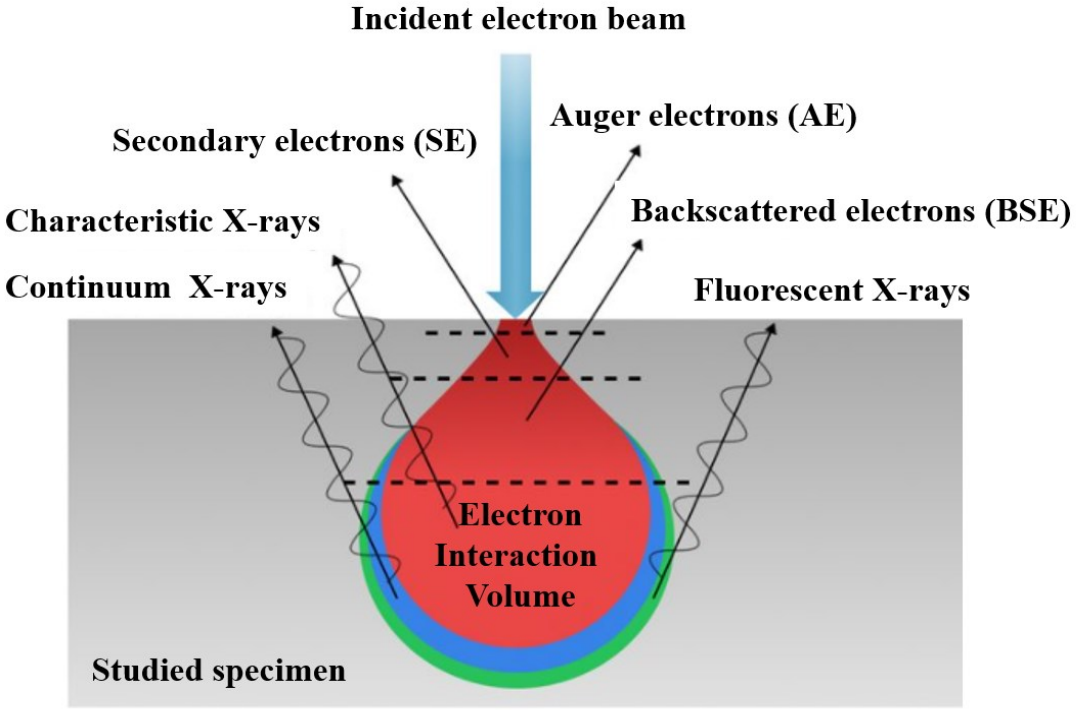

Figure 3.27. The interaction volume of an incident beam of electrons produces a variety of effects at different depths. SEM utilizes the SEs for surface imaging, whereas EDS utilizes characteristic X-rays for elemental analysis. Reprinted and modified from [18].

The electron interaction induces elastic and inelastic scattering events [19,20]. Elastic scattering is characterized by insignificant energy loss as a result of the deflection of the incident negatively charged electrons by the positively charged atom nuclei of the matter. Some of these electrons emerge from the specimen with a large fraction of their incident energy intact after experiencing scattering and deflection by the electric fields of the atoms in the sample. They are known as backscattered electrons (BSEs). By contrast, secondary electrons (SEs) are electrons that escape from the specimen surface after beam electrons have ejected them from atoms in the sample, as a result of inelastic interactions between the electron beam and the sample. Despite the fact that beam electrons have generally high energy, these SEs experience low kinetic energy transfer and consequently escape from the surface of the specimen with very low kinetic energies, in the range 0–50 eV, with the majority of them below 5 eV in energy. Since BSEs come from deeper regions of the sample and SEs originate from surface regions, they carry different types of information and both of them are used for making SEM images. SEs escape from about 5-50 nm below the surface and are useful for obtaining detailed topographic contrast. Instead, BSEs can escape from a depth of 50-300 nm, depending on the energy of the primary electrons and the atomic number

and density of the sample, and are used for obtaining the elemental composition contrast. The ratio of the number of BSEs, which can escape from the sample surface to the total number of the incident electrons, is defined as the backscatter coefficient (η_{BSE}) and depends on the average atomic number in the observed specimen region. Consequently, BSE images show high sensitivity to differences in atomic number; the higher the average atomic number, the brighter the material details appear as compared to regions with lower average atomic numbers [19].

Therefore, SEM images can provide different types of information, concerning [21]:

- *Compositional microstructure*: Generally, BSE can detect compositional variations by 1-unit in average atomic number (Z). Greater sensitivity can be reached for low (Z≈6) and intermediate (Z≈30) atomic numbers. The spatial resolution is generally limited to approximately 10–100 nm, depending on the selected beam energy and composition of the studied specimen.

- *Topography (shape):* Topographic structure can be accessed by SEM imaging with variations in local surface inclination as small as a few degrees. The edges of structures can be localized with a spatial resolution in the range of the incident beam diameter (which can be 1 nm or less, depending on the electron source) up to 10 nm or greater, on the basis of the studied material as well as the geometric nature of the edge (vertical, rounded, tapered, reentrant, etc.).

- *Visualization of the third dimension*: Optimizing for a large depth-of-field allows to visualize the three-dimensional structure of a sample. However, in conventional X-Y image monitoring, the final image is a projection of the three-dimensional information onto a two-dimensional plane, suffering spatial distortion due to foreshortening. It is possible to recover the true three-dimensional nature of the specimen by applying the techniques of stereomicroscopy, which invokes the natural human visual process for stereo imaging, combining two independent views of the same area made with small angular differences.

- *Other properties*: SEM imaging also permits the access to other properties such as crystal structure, including grain boundaries, crystal defects, and crystal deformation effects; magnetic microstructure, including magnetic domains and interfaces; applied electrical fields in engineered microstructures; and electron-stimulated optical

emission (cathodoluminescence), which is sensitive to low energy electronic structure.

Generally, SEM imaging is coupled to energy-dispersive X-ray spectroscopy (EDS) for chemical analysis. In fact, the interaction between the SEM electron beam and the specimen also produces two types of X-ray photon emissions: characteristic X-rays and continuum X-rays. The former spectrum type is generated when a high energy electron collides an atom on the material surface, so dislodging an electron from an inner atomic level. The kicked-out electron leaves the atom as a "free" electron, and the atom becomes excited (unstable state). The ionized atom tends to return to its normal state by filling the inner electron vacancy with an electron from an outer atomic level characterized by a lower binding energy in the atom. The energies of the photons emitted from an atom fall within the X-Ray energies and represent a fingerprint for each element. Instead, the continuum X-Ray spectrum arises because the beam electrons can undergo a deceleration in the Coulombian field of the specimen atoms which corresponds to a loss in electron energy ΔE. Therefore, ΔE is emitted as an electromagnetic radiation, that is as a photon. This radiation is referred to as bremsstrahlung or braking radiation. Since the interactions are random, the electrons may lose any amount of energy in a single deceleration event. Therefore, the bremsstrahlung can take on any energy value from zero up to the original energy of the incident electron (from 0 to E_0), forming a continuous electromagnetic spectrum [20–22].

The characteristic X-ray spectrum emerging from a sample under SEM observation is measured to identify and quantify the specific elements (except for H and He, which do not produce X-rays) present within the beam-excited interaction volume in the sample. The interaction volume has dimensions ranging from approximately 100 nm to 10 μm, depending on composition and beam energy.

A schematic of a SEM system and its components is shown in Figure 3.28. In a conventional-vacuum SEM, the electron-optical column and the specimen chamber must operate under ultra-high vacuum ($< 10^{-4}$ Ps) in order to minimize the unwanted electron scattering and to allow the condenser "lenses " to collimate the electron beam. The sample chamber is equipped with different detectors; at each beam location, the outgoing electron signals are measured using one or more electron detectors. Usually, the SEM system is equipped with an Everhart–Thornley "secondary electron" detector (which is actually sensitive to both SEs and BSEs and used for SEM imaging) and a "dedicated backscattered electron detector" (which is insensitive to SEs and is used for elemental microstructural characterization). Insulating specimens that would accumulate surface electrical charge because of the impact of the beam

electrons must be covered by a conductive coating (in C or Au), properly grounded to provide an electrical discharge path [18,21].

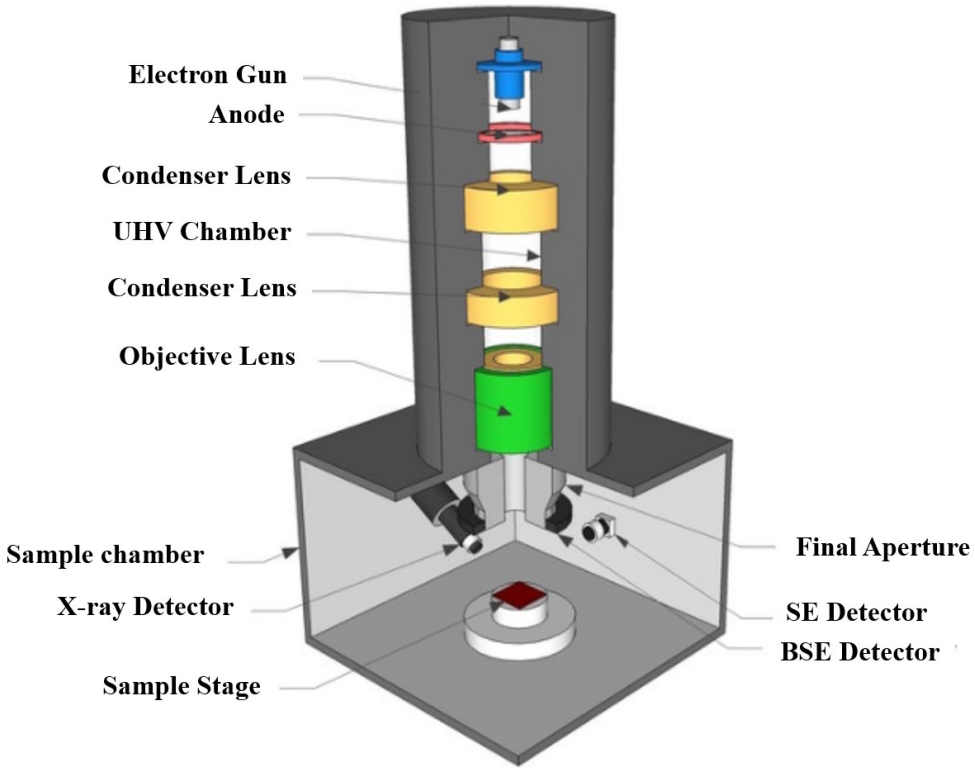

Figure 3.28. The schematic principle of an SEM system and its components. Reprinted and modified from [18].

In the experimental tests described in this thesis, a Zeiss EVO MA15/LaB_6 SEM (Oxford, Inca X-act), coupled with Oxford X-Max/AZTEC EDS system (operating at the University of Ferrara), a FEG-SEM (operating at the University of Bologna) and is a Dual Beam FIB-SEM ZEISS CrossBeam 340 (operating at CNR Bologna) were used for microstructure characterization and elemental analysis of the studied samples. The latter equipped with GEMINI SEM column and thermally assisted (Schottky type) Field Emission Gun and is a dual-beam focused Ga^+ beam-scanning electron microscope systems (FIB-SEM) used for TEM sample preparation and FIB/STEM observations.

Note that SEM micrographs were taken both in the SE-mode, which gives topography, and in the BSE-mode to enhance compositional image contrast. Moreover, the EDS analysis of the sample composition was made. For SEM investigations, electrostatic charge accumulation on resin-embedded samples was avoided: i) for electrodes: by connecting the metallic investigated material to the sample holder through the electrode electrical contact, ii) for

other samples: by providing a conductive bridge connecting the top of the sample to the sample holder.

3.8.2.3. Transmission electron microscope (TEM)

The transmission electron microscope (TEM) allows detailed microstructural imaging and the recording of electron-diffraction patterns, useful for analyzing and identifying the nature of crystalline specimens. In addition, TEM is capable of generating images of material microstructures at a significantly higher magnification and resolution than light and scanning electron microscopes, owing to the small wavelength of electrons. In fact, electrons with an energy of 200 kV are used, having a wavelength of the order of magnitude of ~ 0.025 Å (the wavelength of an electron is inversely proportional to the acceleration voltage), which permits a resolution of ~ 0.1-0.2 nm. Consequently, by TEM it is possible to record images of thin specimens with magnifications in the range 10^3 –10^6. These high performances are due to the TEM electron-optical system including an electron gun, which produces the beam of electrons, and several magnetic lenses, stacked vertically to form a lens column. Considering figure 3.29, the TEM system is divided into three parts [20,23]:

- ***The illumination system,*** consisting of the electron gun together with two or more condenser lenses, which focus the electrons onto the specimen. The design and operation of this part of the TEM column determine the electron beam diameter (often named the illumination) at the specimen and the intensity level of the final TEM image.
- ***The specimen stage*** enables samples to either be held stationary, or else intentionally moved, and to be inserted or withdrawn from the TEM. The specimen holder is placed in between illumination and imaging systems, and its mechanical stability is a crucial factor in determining the spatial resolution of the final TEM image.
- ***The imaging system*** comprises at least three lenses that collectively generate a magnified image (or a diffraction pattern) of the studied sample on a fluorescent screen or on the monitor screen of an electronic camera system. The operation of these imaging lenses is a crucial factor to determine the final magnification of the TEM image, while their design largely determines the spatial resolution which can be reached by the microscope [22,24,25].

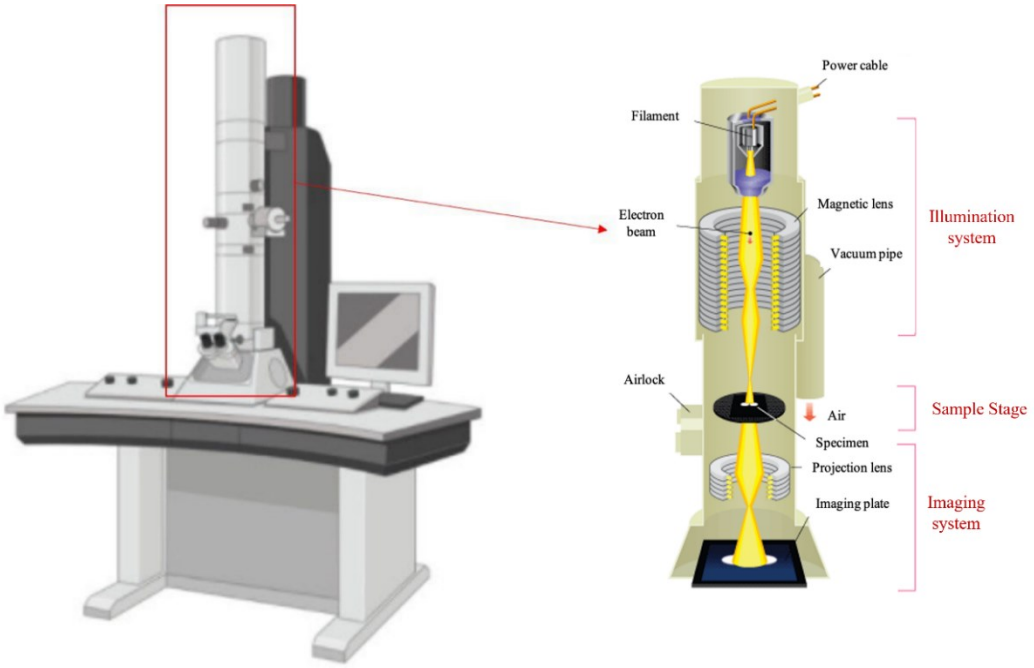

Figure 3.29. The schematic principle of a TEM system and its components [18].

In TEM, the electron source is generally a V-shaped filament made of tungsten wire and the obtained high-interaction-power electrons are employed as a source of illumination that is transmitted through a thin electron transparent sample (foil or lamella). TEM is capable of operating either to produce a diffraction pattern (DP) from a specific region of the sample (diffraction mode) or microstructural images (image mode) so that a clear correlation is achieved between a microstructure and the corresponding crystalline phases. In the diffraction mode, the DP is formed in the back focal plane of the objective lens; instead, in the image mode, an image is created on the image plane of the objective lens. The intermediate lenses below the objective lens are used to focus and magnify either the DP or the image onto a fluorescent screen or charged-coupled device (CCD) detector [23–25].

Focused ion beam-SEM, also known as FIB-SEM, is a potent tool for the preparation of TEM samples (TEM lamella). With this technique, TEM samples of well-localized sites can be prepared, so allowing to directly investigate specific regions of interest, e.g., grain boundaries. In the FIB technique, a Ga^{+} ion beam is moved over a sample surface in the same way as the electron beam in a SEM does. The high-energy ion beam induces the milling of small ditches in the regions of interest. Given this, with the FIB instrument sufficiently thin samples can be cut out of the bulk material for rapid site-specific preparation of cross-section TEM samples, as shown in figure 3.30 [26,27]. However, the FIB-produced lamellas often need further thinning for TEM observation.

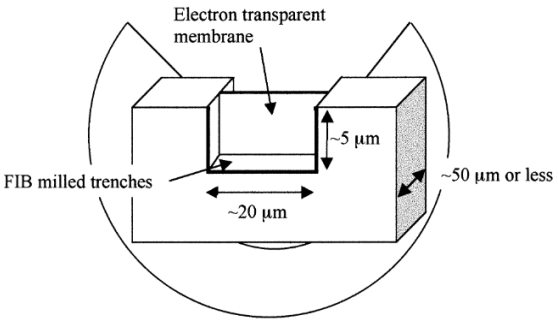

Figure 3.30. Schematic of a FIB lamella to be lifted out for TEM observation (not drawn in scale). Reprinted from [27].

In this study, ultrathin sections for TEM characterization were obtained from selected positions on the surface of SLM alloy after exposure to PBS + H_2O_2 solution at pH 4 under both free corrosion conditions (15 days of immersion) and anodic polarization at + 0.9 V_{SCE} (30 min polarization). TEM lamellas were fabricated using a ZEISS dual-beam system, Focused Ion Beam and Scanning Electron Microscope (CNR Microscopy Center, Bologna). A protective layer of platinum was preliminarily deposited over the region of interest, and a rectangle of 20 µm × 2 µm × 6 µm was cut out with a gallium ion beam at 30 kV. A FEI Tecnai TEM equipped with EDS spectrometer and High-Angle Annular Detector (HAADF) was operated at 200 kV in STEM-HAADF imaging mode to address the compositional analysis of the specimen at the nanoscale.

3.8.2.4 Atomic Force Microscope (AFM)

AFM is a scanning probe microscopy (SPM) technique, in which an ultra-sharp brittle tip mounted on a cantilever spring at the end of the AFM probe sweeps the surface and monitors its topography. Since it was invented by Binnig et al. in 1986 [28,29], the AFM technique has played a crucial role in nano-scale science and technology to image the atomic topography and measure interacting forces. In AFM, the force or the potential energy between the small tip attached to the cantilever and the sample are measured. By pushing the cantilever towards the sample, the local topographic height can be measured, and by pulling it, the interacting force between the tip and the sample can be monitored. The radius of the tip curvature is smaller than 50 nm, and the cantilever spring is 0.1-2 mm in size with a 0.1- 0.01 N/m spring constant [30–33]. There are three common modes of AFM [33–35]: contact mode, non-contact mode, and tapping mode.

In the *contact mode*, the AFM tip scans across a surface at a very low force and is deflected by the repulsive force between the tip and surface atoms. A feedback loop maintains constant

deflection of the cantilever by vertically moving the scanner as it scans laterally across the surface, so that the topographic image of the sample surface is constructed. As the tip always exerts a mechanical load on the sample, which may lead to damage, contact AFM is not suitable for soft biomaterials. In the *non-contact mode*, the tip of the cantilever does not make direct contact with the sample surface. Instead, the cantilever oscillates at a frequency slightly above its resonant frequency, with amplitude of oscillation of typically a few nanometres (<10 nm). The van der Waals force, which is strong from 1 nm to 10 nm above the surface, or any other long-range force which extends above the surface decrease the resonance frequency of the cantilever. This effect combines with the feedback loop system to maintain a constant oscillation amplitude or frequency by adjusting the average tip-to-sample distance. In the tapping mode, also called intermittent contact mode, the cantilever is driven to oscillate up and down near its resonant frequency, similar to that in the non-contact mode. However, the amplitude of this oscillation is much greater than 10 nm, typically 100–200 nm. The tip intermittently touches the surface, and the piezoelectric actuator controls the height in order to maintain a set cantilever oscillation amplitude as the cantilever is scanned over the sample. An image is produced by imaging the force of the intermittent contacts of the tip with the sample surface. Nowadays, using very sharp tips enables AFM to perform topography imaging even at the atomic level. However, unlike SEM-EDS surface imaging and analysis, AFM does not give any elemental information. Therefore, they can be considered complementary techniques. The schematic of the AFM principle is shown in Figure 3.31.

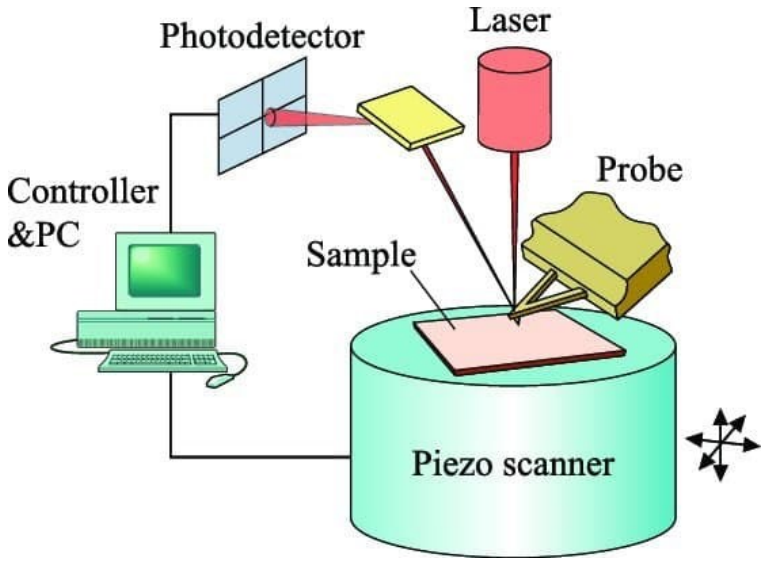

Figure 3.31. Scheme of the AFM principle and its components. Reprinted and modified from [36].

Scanning Kelvin Probe Microscope (SKPFM)

Scanning Kelvin probe microscope (SKPM) is a variation of atomic force microscope (AFM) that makes it possible to assess the practical nobility of a surface. It was introduced as a tool to measure the local contact potential difference between an AFM tip and the sample, thereby mapping the work function or surface potential of the sample with high spatial resolution. Briefly, Volta potential probe microscope is an AFM based apparatus supported by some commercial AFM systems, which measures the surface potential of the sample in addition to the sample topography.

The Volta potential is an electron-sensitive parameter and describes the thermodynamic propensity of a metal to take part in electrochemical reactions [37,38]. Defined as a useful quantity to assess the relative nobility of local microstructures of an alloy, Volta potential has now found widespread acceptance among corrosion researchers, being often used to understand localized corrosion phenomena and galvanic activities at the micro- and nanometer scale [39–43]. It was demonstrated to be in close correlation with the corrosion potential [44]. The Volta potential difference ($\Delta\Psi$) is part of the surface potential difference between the tip and the sample. The vibrating capacitor method, also known as the Kelvin technique, is a common method for measuring the Volta potential difference between two materials, wherein two conductors are set up as a parallel plate capacitor with a small spacing [44]. Given this, in SKPFM, the studied samples and moving probes act as the plates of a capacitor with air dielectric in between. It is reported that two operational modes can be applied in order to map the Volta potential differences: the single-pass mode and the dual-pass mode. In the single-pass mode, an AC voltage is applied to stimulate the electrostatic force interaction between the sample and the conducting probe [45,46]. Then, a DC voltage is used to nullify the measured electrostatic forces, providing the quantitative surface potential [46]. Using the single-pass mode results in a higher resolution due to the immediate proximity of the tip to the sample [46]. On the other side, in dual-pass mode, during the first pass, the topography is scanned, then during the second scan, the tip is lifted to a preselected distance (50–100 nm) at which the potential signal is recorded. The topography signal is used as feedback to maintain a constant elevation ("lift" distance between tip and sample). An AC bias is applied to the tip through the second pass, which generates a time-varying electrostatic force between tip and sample, causing a vertical cantilever oscillation [45]. An external DC bias is also applied to the tip, which is varied during the point-to-point scanning across the surface. The DC bias at any specified X-Y location is chosen via feedback to zero the cantilever oscillation by offsetting the difference in surface potential. Thereby, the

determined DC bias corresponds to the contact potential difference of sample and tip materials in the absence of this bias [45].

In the present work, a Bruker Dimension Icon AFM instrument of the AlbaNova University Centre (Royal Institute of Technology, Stockholm, Sweden) with facilities for Volta potential measurement was used. For Volta potential mapping, a Nanoprobes SPM probe of SCM-PIT type with a resonance frequency of 60-100 kHz and a length of 200-250 μm was utilized. The SKPFM measurements were performed on well-polished sample surfaces down to 0.25μ) to evaluate the morphological features with different nobility.

References

[1] E. Liverani, Studio e ottimizzazione del processo di fabbricazione additiva (SLM) per applicazioni in ambito biomedicale: produzione di protesi e strutture reticolari, (2017).

[2] P. Pedeferri, Corrosion science and engineering, Springer, 2018.

[3] G.I.A. Note, Basics of Electrochemical Impedance Spectroscopy, GamryInstrument, Www. Gamry. Com. (2006).

[4] M. Urquidi-Macdonald, S. Real, D.D. Macdonald, Applications of Kramers—Kronig transforms in the analysis of electrochemical impedance data—III. Stability and linearity, Electrochim. Acta. 35 (1990) 1559–1566.

[5] A. Lasia, Electrochemical impedance spectroscopy and its applications, in: Mod. Asp. Electrochem., Springer, 2002: pp. 143–248.

[6] B.A. Boukamp, J.R. Macdonald, Alternatives to Kronig-Kramers transformation and testing, and estimation of distributions, Solid State Ionics. 74 (1994) 85–101.

[7] P.T. Kissinger, W.R. Heineman, Cyclic voltammetry, J. Chem. Educ. 60 (1983) 702.

[8] E. Gileadi, E. Kirowa-Eisner, J. Penciner, Interfacial electrochemistry: an experimental approach, (1975).

[9] A.J. Bard, L.R. Faulkner, Fundamentals and applications, Electrochem. Methods. 2 (2001) 580–632.

[10] H.E. Boyer, A.S. for M.C. on H. Testing, Hardness Testing, ASM International, 1987.

[11] J.R. Davis, Tensile Testing, 2nd Edition, ASM International, 2004.

[12] ASTM G 129, Standard practice for slow strain rate testing to evaluate the susceptibility of metallic materials to environmentally assisted cracking, American Society for testing of Materials, West Conshohocken, PA, (n.d.).

[13] M. Barteri, N. De Cristofaro, L. [Centro S.M.S. p. A. Scoppio Roma (Italy)], G. Cumino, G.D. [Dalmine T.I.S. r. l. (Italy)] Pina, Corrosion resistance of martensitic stainless steels in moderately sour oilfield environments, NACE International, Houston, TX (United States), United States, 1995.

[14] H.-Y. Ha, C.-H. Lee, T.-H. Lee, S. Kim, Effects of nitrogen and tensile direction on stress corrosion cracking susceptibility of Ni-free FeCrMnC-based duplex stainless steels, Materials (Basel). 10 (2017) 294.

[15] G.S. Schajer, Practical residual stress measurement methods, John Wiley & Sons, 2013.

[16] G.F. Vander Voort, ed., Metallography and Microstructures Handbook, ASM International, 2004.

[17] F. Mokobi, Light Microscope- definition, principle, types, parts, magnification, (2020).

[18] P.J.D. Whiteside, J.A. Chininis, H.K. Hunt, Techniques and challenges for characterizing metal thin films with applications in photonics, Coatings. 6 (2016) 35.

[19] R.F. Egerton, The Scanning electron microscope, Phys. Princ. Electron Microsc. (2010) 125–153.

[20] Y. Leng, Materials characterization: introduction to microscopic and spectroscopic methods, John Wiley & Sons, 2009.

[21] J.I. Goldstein, D.E. Newbury, J.R. Michael, N.W.M. Ritchie, J.H.J. Scott, D.C. Joy, Scanning electron microscopy and X-ray microanalysis, Springer, 2017.

[22] Hawkes, Peter W., J.C.H. Spence, Springer Handbook of Microscopy, 2019.

[23] R.F. Egerton, Physical principles of electron microscopy, Springer, 2005.

[24] S.K. Sharma, D.S. Verma, L.U. Khan, S. Kumar, S.B. Khan, Handbook of Materials Characterization, 2018.

[25] B.J. Inkson, Scanning Electron Microscopy (SEM) and Transmission Electron Microscopy (TEM) for Materials Characterization, Elsevier Ltd, 2016.

[26] M. Jublot, M. Texier, Sample preparation by focused ion beam micromachining for transmission electron microscopy imaging in front-view, Micron. 56 (2014) 63–67.

[27] L.A. Giannuzzi, F.A. Stevie, A review of focused ion beam milling techniques for TEM specimen preparation, Micron. 30 (1999) 197–204.

[28] G. Binnig, C.F. Quate, C. Gerber, Atomic Force Microscope, Phys. Rev. Lett. 56 (1986) 930–933.

[29] Binnig G 1986 US Patent Specification 4,724,318, n.d.

[30] B. Cappella, G. Dietler, Force-distance curves by atomic force microscopy, Surf. Sci. Rep. 34 (1999) 1–104.

[31] R. García, R. Pérez, Dynamic atomic force microscopy methods, Surf. Sci. Rep. 47 (2002) 197–301.

[32] F.J. Giessibl, Advances in atomic force microscopy, Rev. Mod. Phys. 75 (2003) 949–983.

[33] R.J. Colton, Procedures in scanning probe microscopies, John Wiley & Sons, 1998.

[34] H. Wang, P.K. Chu, Chapter 4 - Surface Characterization of Biomaterials, in: A. Bandyopadhyay, S. Bose (Eds.), Charact. Biomater., Academic Press, Oxford, 2013: pp. 105–174.

[35] C.D. Frisbie, Scanning Probe Microscopy, in: R.A. Meyers (Ed.), Encycl. Phys. Sci. Technol. (Third Ed., Third Edit, Academic Press, New York, 2003: pp. 469–484.

[36] N. Ishida, V.S.J. Craig, Direct measurement of interaction forces between surfaces in liquids using atomic force microscopy, KONA Powder Part. J. 36 (2019) 187–200.

[37] R. Hausbrand, M. Stratmann, M. Rohwerder, The physical meaning of electrode potentials at metal surfaces and polymer/metal interfaces: consequences for delamination, J. Electrochem. Soc. 155 (2008) C369.

[38] C. Örnek, C. Leygraf, J. Pan, On the Volta potential measured by SKPFM–fundamental and practical aspects with relevance to corrosion science, Corros. Eng. Sci. Technol. 54 (2019) 185–198.

[39] E. Bettini, T. Eriksson, M. Boström, C. Leygraf, J. Pan, Influence of metal carbides on dissolution behavior of biomedical CoCrMo alloy: SEM, TEM and AFM studies, Electrochim. Acta. 56 (2011) 9413–9419.

[40] N. Sathirachinda, R. Pettersson, S. Wessman, J. Pan, Study of nobility of chromium nitrides in isothermally aged duplex stainless steels by using SKPFM and SEM/EDS, Corros. Sci. 52 (2010) 179–186.

[41] N. Sathirachinda, R. Pettersson, S. Wessman, U. Kivisäkk, J. Pan, Scanning Kelvin probe force microscopy study of chromium nitrides in 2507 super duplex stainless steel—Implications and limitations, Electrochim. Acta. 56 (2011) 1792–1798.

[42] N. Sathirachinda, R. Pettersson, J. Pan, Depletion effects at phase boundaries in 2205 duplex stainless steel characterized with SKPFM and TEM/EDS, Corros. Sci. 51 (2009) 1850–1860.

[43] K.H. Anantha, C. Örnek, S. Ejnermark, A. Medvedeva, J. Sjöström, J. Pan, Correlative microstructure analysis and in situ corrosion study of AISI 420 martensitic stainless steel for plastic molding applications, J. Electrochem. Soc. 164 (2017) C85.

[44] M. Nonnenmacher, M.P. o'Boyle, H.K. Wickramasinghe, Kelvin probe force microscopy, Appl. Phys. Lett. 58 (1991) 2921–2923.

[45] G. Haugstad, Atomic force microscopy: understanding basic modes and advanced applications, John Wiley & Sons, 2012.

[46] S. Magonov, J. Alexander, Compositional mapping of materials with single-pass kelvin force microscopy, Agil. Technol. Appl. Note# 5990-5480EN. (2014).


4

CHAPTER FOUR

SEM, TEM and AFM studies to investigate the microstructure and dissolution behaviour of SLM-built and forged CoCrMo alloys.

4.1 Introduction

In this part, the microstructures of CoCrMo biomedical alloy fabricated with conventional and selective laser melting techniques (WRO, B1 and B2 samples) were investigated by optical microscopy (OM) and scanning electron microscopy (SEM) coupled with energy dispersive X-Ray spectroscopy (EDX) and X ray diffraction technique. Then, SKPFM was used to identify and characterize the changes in Volta potential in correspondence of heterogeneities on both alloys. Focused Ion Beam technique (FIB) associated to Scanning Transmission Electron Microscopy (STEM) were used to investigate the corrosion attack on the surface of the tested alloys.

4.2 Results and discussion

4.2.1. XRD characterization

Figure 4.1 compares the XRD patterns obtained from the starting powders (Powder), the SLM samples (SLM B1, SLM B2) and wrought CoCrMo alloy (WRO) and in Table 4.1 are reported the amount and crystallite size of the detected phases as obtained from the Rietveld refinement. Note that the instrumental contribution to the line (peak) broadening (Instrumental Resolution Function, IRF) was evaluated according to the FP (Fundamentals Parameters) approach by convoluting the contribution of instrumental aberrations [1]. For more information regarding the XRD experimental setup, see sect. 3.8.1.

The results of XRD analysis indicated that the metastable austenitic FCC phase (γ-phase) is the main phase and amounts of hexagonal HCP ε-phase are present in all the samples. First, unlike the starting powder (and wrought alloy), both SLM CoCrMo alloys demonstrate duplex phases of γ-FCC and ε-HCP. What is interesting in this data is that the SLM B2 alloy represents much higher diffraction intensity assigned to ε phase, comparing to the other alloys and starting powder. According to the binary Co-Cr phase diagram, the hexagonal ε phases is the equilibrium phase at room temperature and γ-phase exist, as the stable phase, at higher as the transformation ε→ γ occurs during heating starting from 900-950 °C [2]. However, during the fabrication procedures, the metastable γ-phase is retained at room temperature because the martensitic transformation γ → ε is hindered by fast cooling below the Tc (martensitic transformation critical temperature), a condition commonly achieved during air cooling [3, 4]. The higher amount of γ-phase was detected in B1 SLM samples (93

wt%), while WRO and starting powders showed similar fractions of γ-phase (89 wt% and 83 wt%, respectively) and ε-phase (89 wt% and 83 wt%, respectively). Interesting, the B2 SLM samples showed the higher amounts of ε-phase than both B1 SLM sample and starting powder. This finding might be explained in this way. The ε-phase is formed through γ→ε transformation during cooling above Tc. This condition was probably achieved in the sublayers, during the fabrication process with B2 laser parameters, due to the lower laser scan rate that allowed to maintain, in the sublayers, temperatures above Tc inducing a higher degree of γ→ε transformation [5].

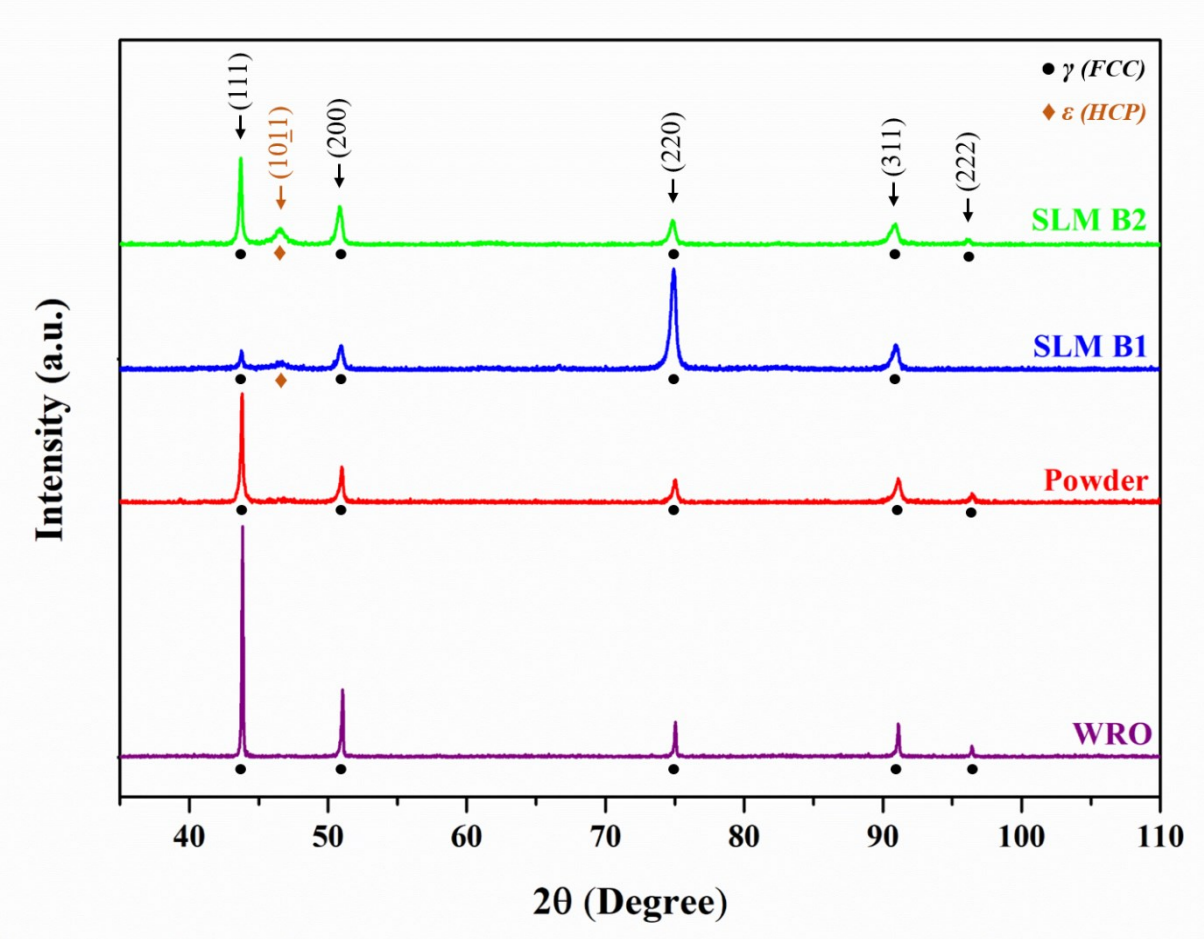

Figure 4.1. The X-ray diffractograms of the wrought CoCrMo alloy (WRO), as-received CoCrMo powder, and selective laser melted CoCrMo alloys (B1 and B2).

Table 4.1. Results of XRD analysis. Amount (wt%) and crystallite size (CS, nm) of γ and ε phases

Sample	γ-phase (Wt%)	CS γ-phase (nm)	ε-phase Wt%	CS - ε-phase (nm)
Powder	83	34	17	3.2
SLM B1	93	23	7	6
SLM B2	71	30	29	7
WRO	89	198	11	6

The XRD pattern of SLM B1 sample (Fig. 4.1, blue curve) exhibited atypical relative intensity of Bragg reflections the intensity of the main peak (111) was lower than those of the (200), (220) and (311) peaks, suggesting a texturing effect due to SLM process that induced an anisotropic microstructure where crystallite mainly grew with a preferred orientation (220). Less evident texturing effect was observed in the SLM B2 sample, where only a little higher intensity was detected for the peak (200).

The Rietveld analysis also provided interesting information on the size of the coherent diffraction domains (crystallites) of the detected phases. All the samples showed similar crystallite size of the ε-phase (in the range of 3-7 nm), suggesting that the transformation γ → ε occurred at many nucleation centers promoting crystals nucleation rather than grain growth. Marked differences are instead observed in the crystallite size of the γ phase. The SLM samples showed lower crystallite size (23nm for B1 and 30 for B2) with respect to the traditional alloy (198 for WRO).

4.2.2. OM and SEM-EDS characterization

Typical OM images of the cross and longitudinal section (with respect to build direction) of SLM samples are shown in Figure 4.2 (see sect. 3.8.2.1. for OM characterization specification). The main microstructural characteristic is represented by the overlap of the melt pools formed by the laser beam scan. The use of the selected process parameters resulted in the complete melting and solidification of the CoCrMo powder particles. It can be assumed that there are similarities between the physical phenomena occurring through SLM and those of the macroscopic welding process [6]. Melt pools are formed when the laser beam irradiates the powder particles, and they grow elongated by moving the laser beam along the powder bed. Subsequently, the induced heat flow changes the shape of these melt pools from round or slightly elliptical to teardrop. The rapid solidification of adjacent scan tracks resulted in the superposition of numerous stripe-shaped melt pools in the cross-plane (Figure 4.2a and c),

and arc-shaped melt pools boundaries in the longitudinal-plane (Figure 4.2b and d), which is the typical morphological characteristic of as-built SLM parts [7,8]. Moreover, the Figure 4.2e showed the fine lamellae texture elongated along in the build direction. Inside the melt pools, different grains are formed, as highlighted by the different contrast areas in the Figures 4.2a-c and 4.2d, for the cross and longitudinal section, respectively. Typical microstructural features of the SLM process are shown in Figure 4.2e where the fine elongated cellular dendritic texture and grains are highlighted by yellow dashed lines and arrow. During the fabrication process fine cellar and lamellar structure are formed and large sized grains (with dimensions of the order of a few hundred microns) grow epitaxially through some melt pool boundaries along the building direction, as observed by previous studies [7]. In fact, the grains in the previous solidified layers acted as nucleation sites for further solidification by heterogeneous nucleation, leading to the formation of the columnar grains. The fine cellar and lamellar structure are formed not only inside the melt pools, but the lamellae grew through them and also through different grains. These results together with the findings of the XRD analyzes showed the microstructural complexity of alloys fabricated with the SLM technique. In fact, it must be assumed that these materials are characterized by a hierarchical microstructure where small crystal domains (crystallites) grow with preferential orientations within fine cellular structures both through large grains and melt pools under the action of thermal gradients.

The Figure 4.3 showed the SEM micrographs of the etched surfaced of the SLM alloys, evidencing the melting pool boundaries and the fine microcellular and lamellar structures. See sect. 3.8.2.2 for SEM characterization descriptions, using in the present work.

As previously mentioned, the SLM process is comparable to that of the macroscopic welding process. It is stated that the direction of maximum temperature gradient is always perpendicular to the melt pool boundary within the welding process [8]. Nevertheless, during SLM process, the loose powder is surrounding the previously melted powders negatively affecting the heat flow. As a consequence, a competitive growth is likely to occur during the dendrite formations, resulting in the different growth directions, as reflected in Figure 4.2e and Figure 4.3b [8]. The cell dimensions vary from sub micrometric to micrometric, while the thickness of the cell boundaries is of the order of magnitude of the tenth of nanometers.

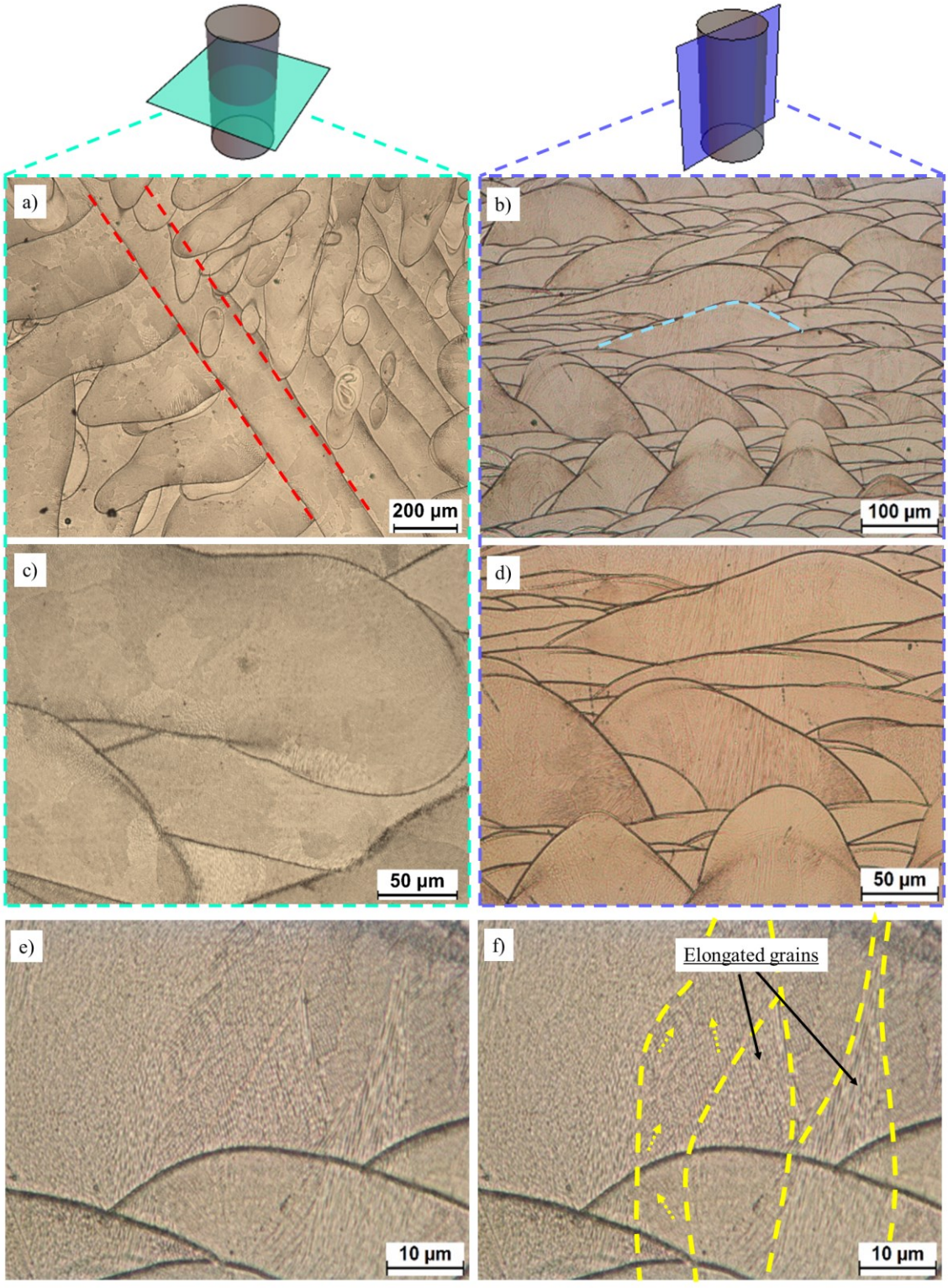

Figure 4.2. Optical macrographs of SLM alloy from transverse cross-section and longitudinal plane. a and c) cross sectional images, b and d) longitudinal images, e) higher magnification of longitudinal image in which elongated grains as well as different cell orientations are visible, f) the specification of different grains and orientation of cellular structure of e.

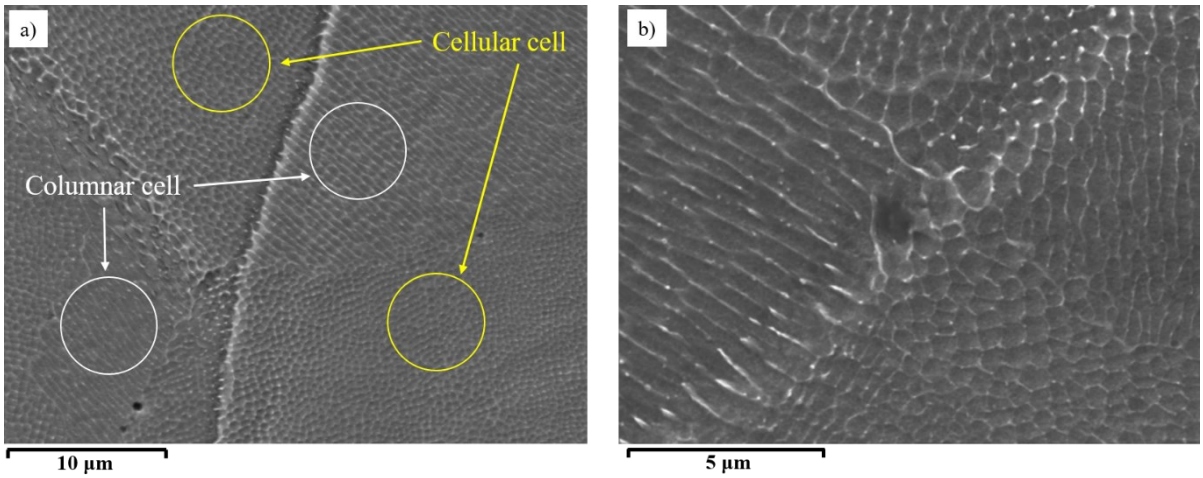

Figure 4.3. a) SEM micrographs of SLM alloy showing microcell structure growing in different directions and melting pool boundaries, b) higher magnification image.

A representative EDS line scanning profile of the main alloying elements across the cell boundaries is reported in Figure 4.4. The analysis reveals a boundary enrichment in Mo, C and Si, and a corresponding depletion in Cr and Co. Especially Mo segregation are expected to play an important role in corrosion behaviour since this element is important for improving the stability of the surface passive films and it was not unexpected that the electrolytic etching used to investigate the alloy microstructure preferentially attacked the dendrite cores, instead of the dendrite boundaries which resulted in relief on the surface.

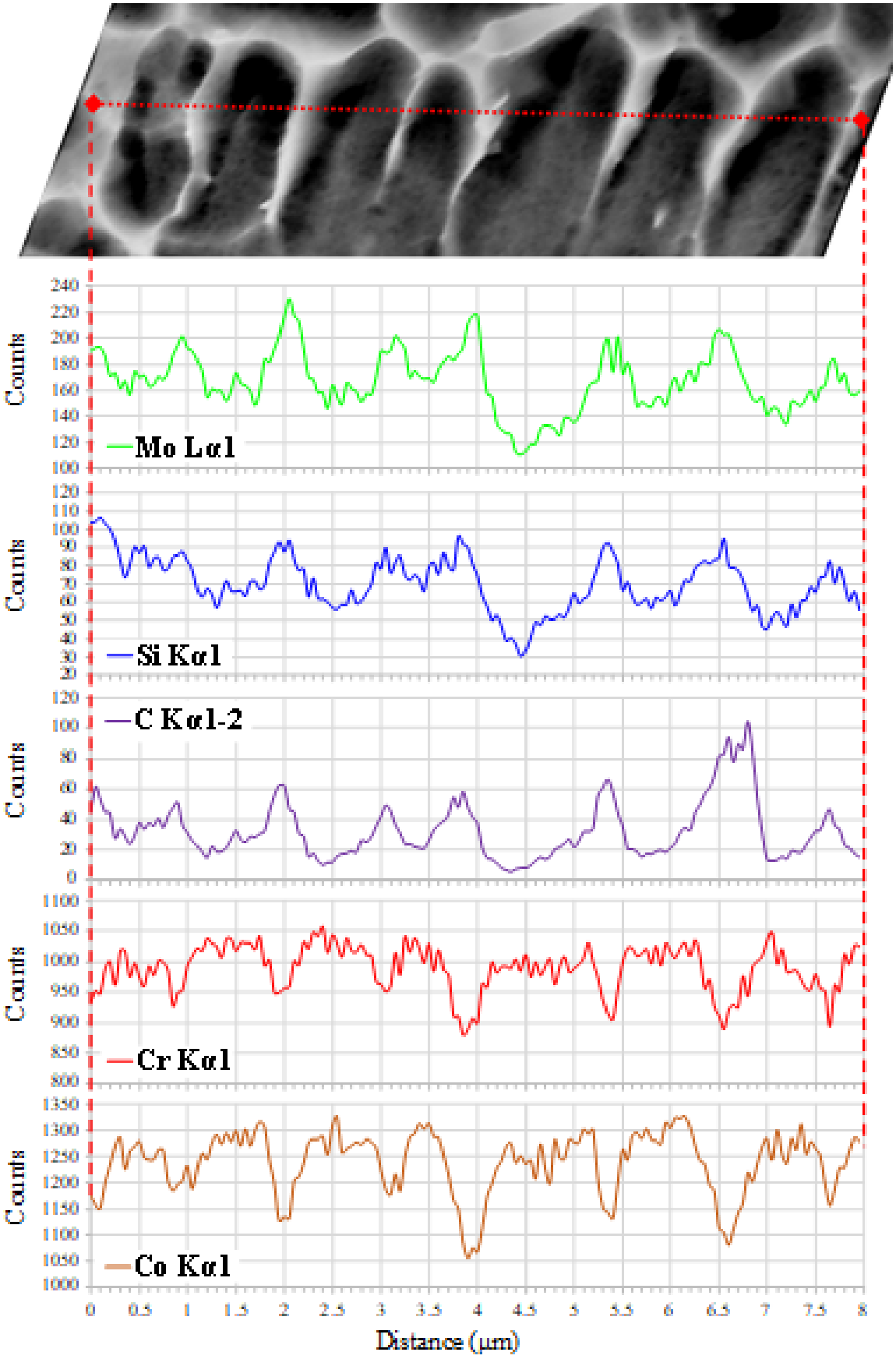

Figure 4.4. a) The cell microstructure of SLM alloy, and b) Co, Si, Mo, and Cr EDS profiles across microcell boundaries (across yellow line in a).

More detailed SEM micrographs of polished and etched surface of the SLM CoCrMo samples are given in Figure 4.5. Due to the different scan parameters of B1 and B2 samples, the features differ from each other. Inconsistency in some tracks not connecting to their adjacent melt tracks as well as local gaps present in track edges of the B2 sample, are shown in figure 4.5b and d. This is almost certainly due to the unstable melt width during fabrication of B2 samples, using a lower power (90 W) with respect to the B1 samples. Everton et al. [9] holds the view that materials discontinuity or lack of fusion (LOF) is a major defect present in AM materials. At the same time, Gong et al. [10] have been reported that such discontinuity formed due to insufficient and low laser energy during SLM process. Accordingly, LOF is a usual defect of SLM materials predominantly stemming from lack of sufficient melting, i.e., higher input power of laser (P) and lower scan speed (v) can give rise melting of a larger amount of powder per manufacturing time unit. In SLM, depending on the volume of melted powder per unit time, a complete melting or partial melting can be defined. This means that the selection of layer thickness (t) and hatch space (h) is crucial. The amount of melting thought the SLM process is directly related to the energy for a unit volume of material per time unit. The relation between process parameters and laser energy can be expressed as mentioned in Equation 2.3. According to this equation, a higher laser energy density resulting in a greater amount of melting area and thus higher final density [11]. It has been demonstrated that high input energy of laser results in higher evaporation but achieving higher density value for the final product. However, it is important to bear in mind that using lower scan speed (to achieve higher energy density) simply results a lower manufacturing rate [12]. Thus, it is an important issue that the energy density should be adequately high to obtain a high-density product and at the same time, a sufficient scan speed should be applied to achieve a higher rate of manufacturing. Taking into account the process parameters for B1 and B2 samples used in the present study, the lower density and higher porosity values of B2 samples was directly related to its lower P and higher v values as h and t values were kept unchanged during SLM process. The process parameters of B1 sample resulted in the fabrication of a dense structure with a relative density of around 99.8% if compared to B1 sample with lower relative density of 95%. However, using lower laser power and higher scan speed for B2 fabrication, simply means a higher production time and decrease of the production time and cost.

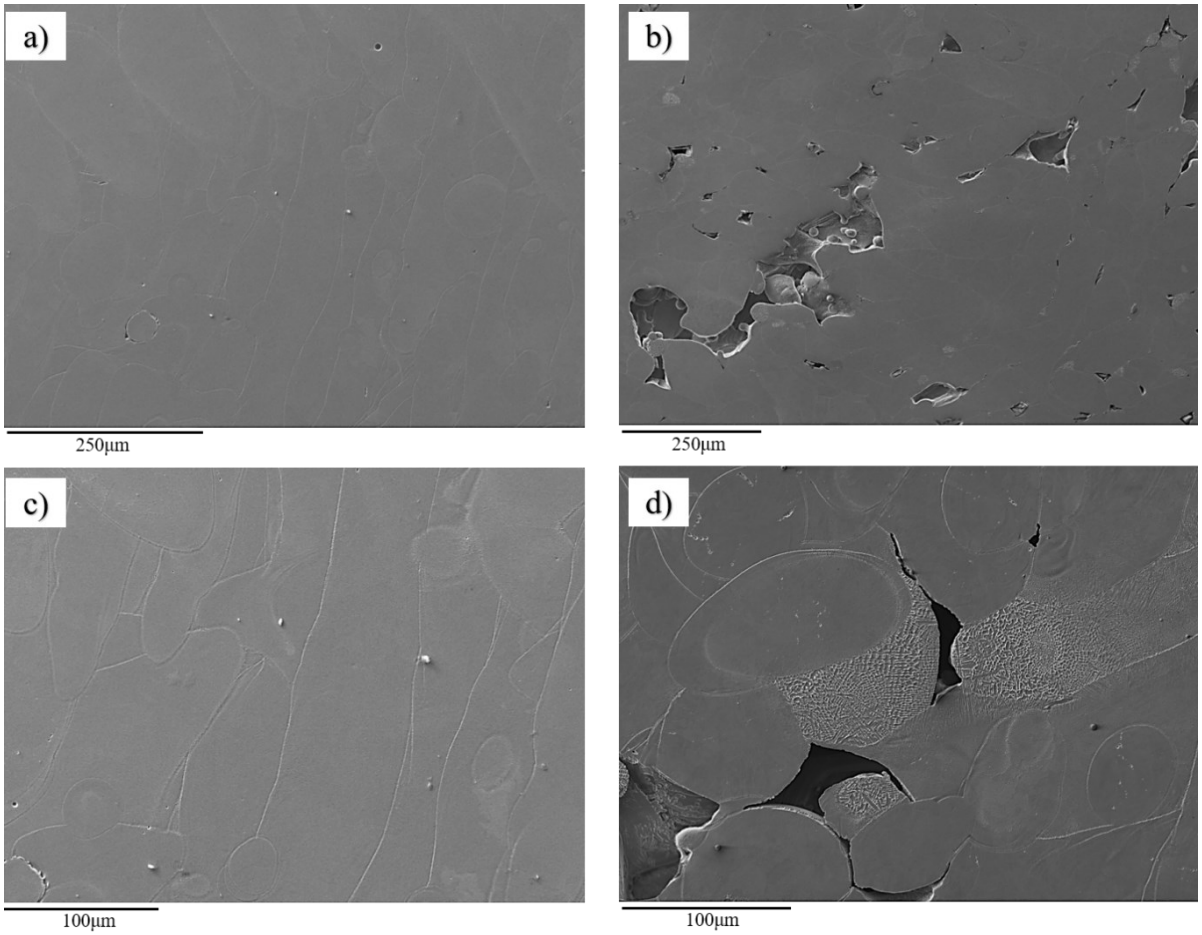

Figure 4.5. SEM images of the top surface of SLM B1 (a and c), and SLM B2 (b and d) samples.

During the solidification process, the transformation from liquid to solid and the solidification microstructure are widely controlled by various parameters such as temperature gradient G, solidification rate R, alloy composition and undercooling ΔT [13]. The correlation of the combined form of temperature gradient and solidification rate (G/R) with the size and the morphology of the solidified microstructure is reported by Lee et al [13,14]. According to Lee [14], planar morphology is possible when R is very low and/or G is very high. The cellular, columnar and then equiaxed dendritic microstructure can be achieved by increasing the value of R. It is a widely held view that the most common modes of solidification in metallic alloys fabricated by SLM methods are cellular or columnar dendritic. The cellular and columnar growth happens when no secondary dendrite arms form during solidification. Moreover, it is believed that if R is extremely low, the growth of crystal structure shifted to the equiaxed growth mode [13,14]. According to the fact that the very small melt pool size and high scan speed, together with high melting and solidification rate

are the distinctive features of SLM technique, G and R values are expected to be very high during SLM manufacturing process [15,16]. Cellular growth and in some extent cellular-dendritic growth are the main microstructural features of the SLM fabricated alloys. Nevertheless, the size and shape of this specific morphology can be affected by SLM process parameters [6,17,18]. According to Kurz and Fisher [19], the primary spacing of cells (λ_1) can be inversely related to G and R values, as follows:

$$\lambda_1 = \frac{4.3.\left(\frac{\Delta T^{\circ}.D_L.\Gamma}{k}\right)^{0.25}}{R^{0.25}.G^{0.5}} \quad (4.1)$$

in which ΔT° is the equilibrium liquidus-solidus interval, D_L is the diffusion coefficient in liquid, Γ Gibbs-Thomson coefficient and k is mass partition ratio.

The cooling rate ($\dot{T}$) can be estimated by means of the following equation:

$$\dot{T} = G \times R \quad (4.2)$$

Based on the equation 4.1, in can be revealed that the higher G and/or R (higher cooling rate) values results in lower (λ_1) values, suggesting finer cellular structures. In Figure 4.6 the microcell sizes for the B1 and B2 SLM samples are compared after electrolytic etching. The measurement of λ_1 indicated values of about 360 nm and 240 nm for B1 and B2 samples suggesting that the different laser parameters adopted for B2 samples induced a microstructure refinement. Since the selected process parameter of v, thus R values, is higher in B2 sample, the smaller value of λ_1 is expected, as expressed in Eq. 4.1. Moreover, the lower laser power thereby results in a decrease of the temperature of the melt pool. It suggests that during B2 fabrication, in each region, the adjacent zone is not affected by a high laser energy during melting, thus the temperature gradient is lower in B2 if compared to B1, due to the shorter persistence at high temperature during the layer build up. Considering also the λ_1 measurements, these findings suggested that higher cooling rate are achieved during the fabrication process of B1 samples. This result agrees with Darvish's [20] findings which studied different works using various process parameters to show the effect of SLM parameters on the cell size.

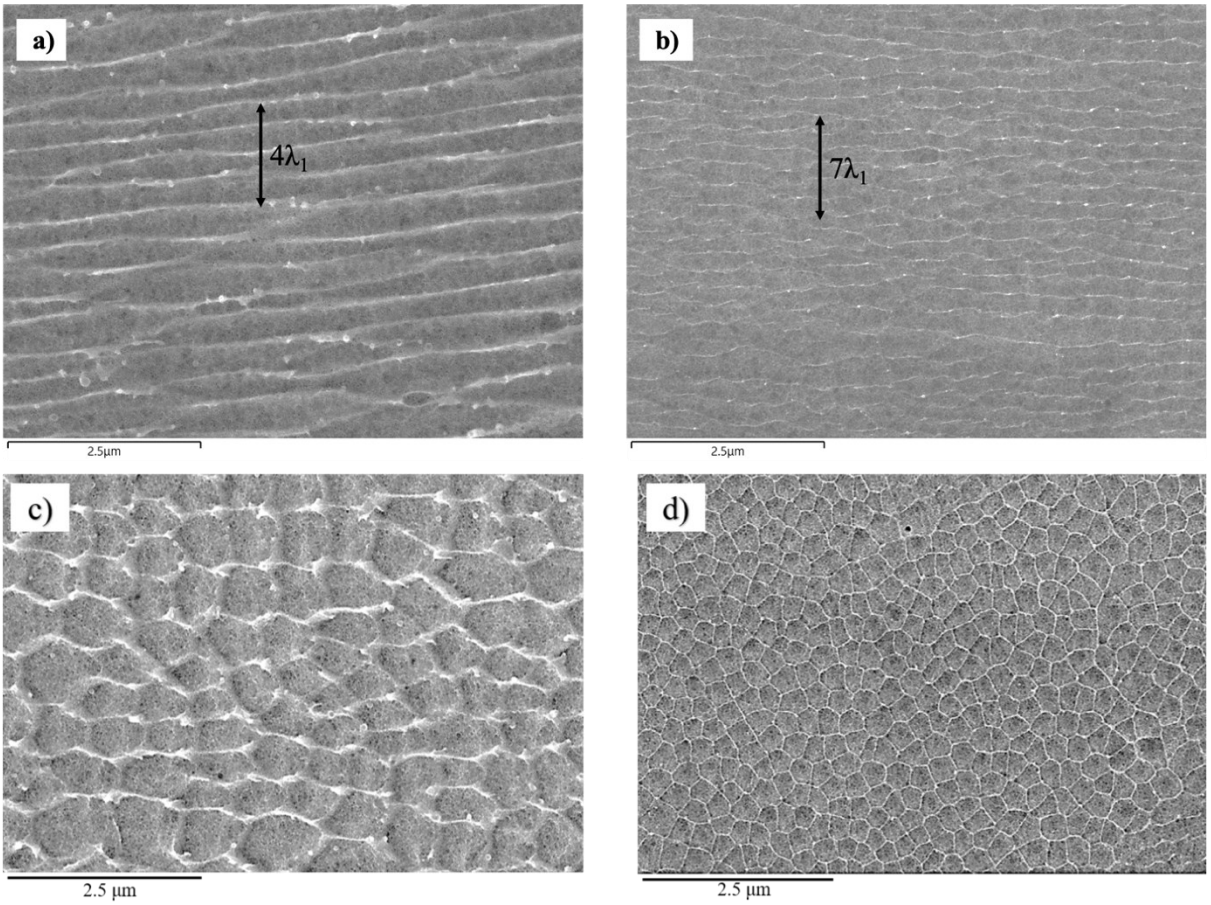

Figure 4.6. SEM micrographs of B1 (a, c) and B2 (b, d) samples, showing the cellular microstructure as well as indication the λ_1 values.

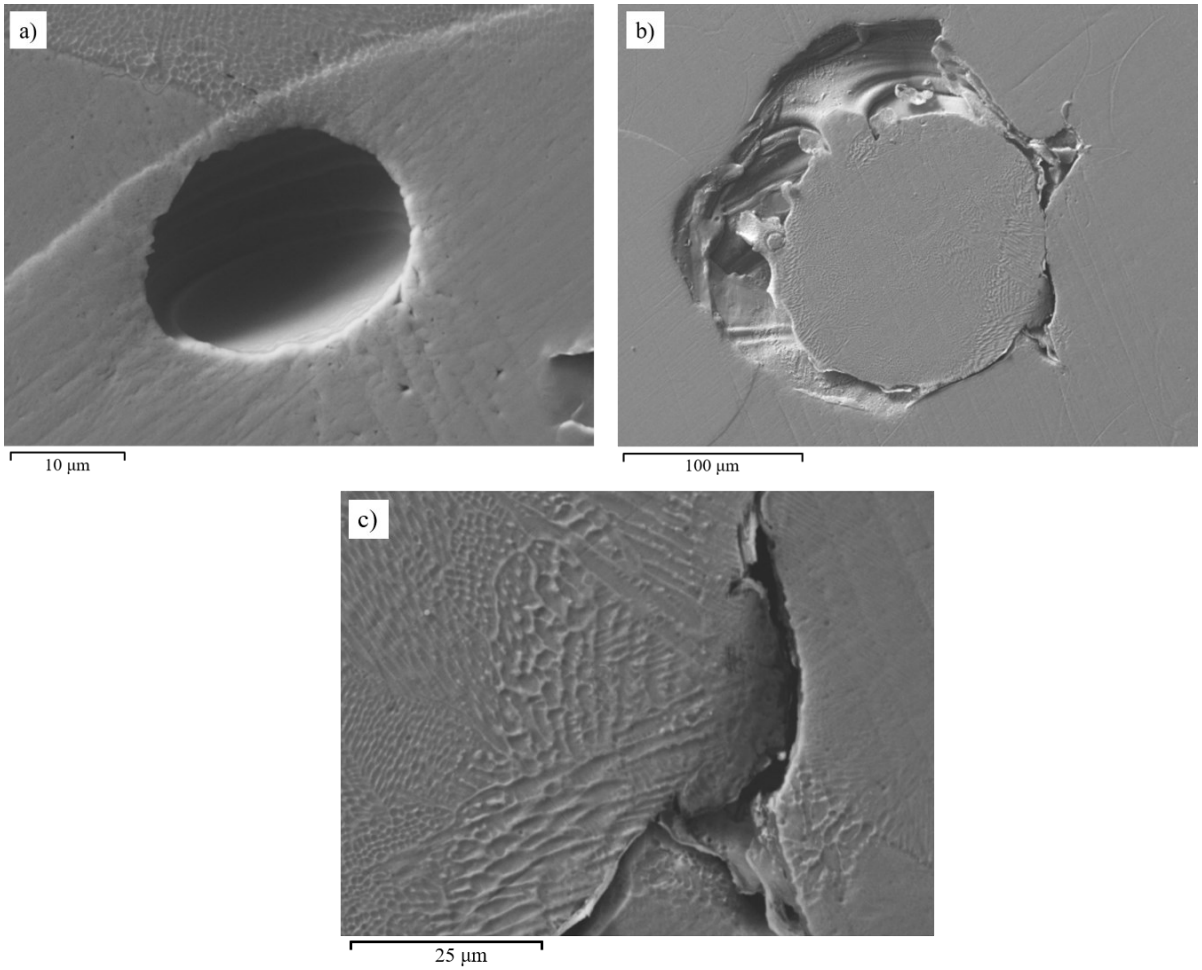

Figure 4.7. Typical defects of CoCrMo SLM alloy, showing spherical pores (a) as well as irregular pores (b) and cracks (c).

Generally, pores and cracks are the typical defects that can be found in SLM alloys [21–24]. As shown in Figure 4.7, two different types of pores are present, specifically spherical pores (Figure 4.7a), due to gas entrapment [25], and irregular ones (Figure 4.7b). The latter pore type is usually attributed to inhomogeneous powder distribution that can lead to an inconsistent melt flow and an unstable molten pool in the successive layers [26]. Liquid contraction during solidification can lead to the balling phenomenon, which is attributed to a poor wetting of the substrate by the liquid material and is perhaps connected to residual oxygen traces in the forming chamber atmosphere [27]. Another example of a common defect of SLM fabricated alloys is crack imperfection due to both internal and external reasons. The internal reasons are related to micro-defects in SLM built samples, while external reasons are connected to residual stresses. These stresses are ascribed to non-uniform shrinkage during cooling, because of high temperature gradients located in the laser affected area, given the Gaussian distribution of laser energy along the horizontal direction. Moreover, residual

stresses may arise because of inadequate heat-transfer between two adjacent layers, again resulting in temperature gradient, which cause compressive stresses in the bottom section and tensile stresses in the upper section [27].

Figure 4.8 collects two representative optical and SEM images of the WRO alloy microstructure characterized by an average grain size of about 5 µm. It shows the typical twins of the FCC structure and a low volume fraction of precipitates randomly distributed throughout the matrix. The scarce amount of carbide precipitates agrees with the low carbon content of the WRO alloy.

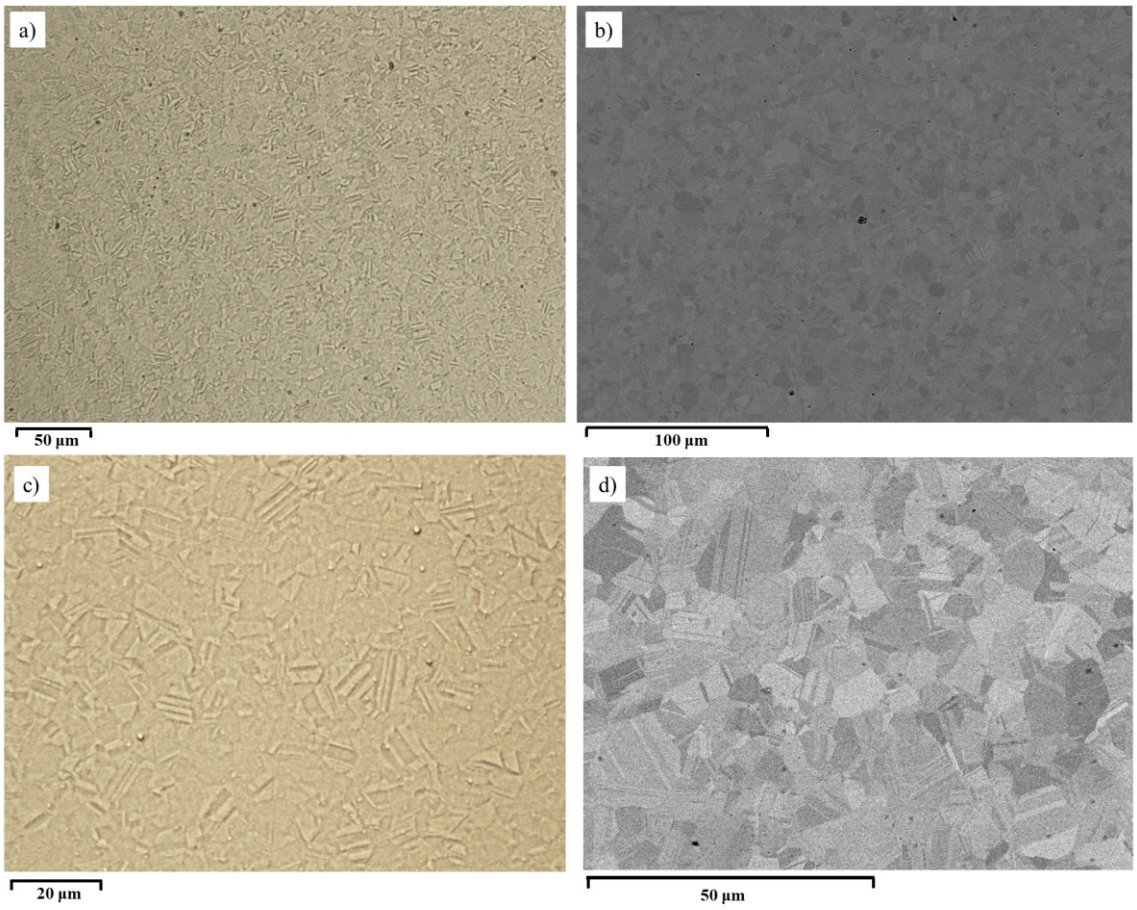

Figure 4.8. a and c) Optical macrographs and b and d) SEM micrographs of WRO CoCrMo alloy; FCC matrix grains are ~ 5 µm in diameter.

4.2.3. AFM-SKPFM characterization

AFM-SKPFM investigations aimed at investigating how heterogeneities in WRO alloy (secondary phases and grain boundaries) and in SLM alloys (micro-and nano-heterogeneities, such as melt pools and cell boundaries) may affect the dissolution behavior of the studied materials. For this purpose, SKPFM measurements were carried out to map the Volta

potential variations over the surfaces of well-polished WRO and SLM samples. The SKPFM technique can be effectively used to evaluate the relative nobility of any heterogeneities compared to the surrounding matrix. So far, different factors have been identified as being potentially important for influencing Volta potential differences. Despite Volta potential values may change due to the experimental conditions (from AFM tip to the surface preparation), a consistent trend is prominent. For instance, the difference between Volta potential of the carbides and the matrix is more noticeable in the presence of the larger carbides. It has been showed that it is not just carbides that acts on Volta potential but also the surrounding matrix may contribute on it [28]. The correlation between the size of an isolated surface feature and its measured Volta potential is described by its size, i.e., the potential of the isolated feature gets closer to the matrix potential when its size reduces [28,29]. The depletion of the alloying elements could be a major factor, if not the only one, affecting the Volta potential difference. In particular, the diffusion of Cr and Mo elements from matrix to the carbide particles and/or to the cell and grain boundaries during cooling process (after casting or through SLM fabrication process) resulted in the formation of a depleted region close to the Cr- and Mo-rich zones. The depleted zone, exhibiting lower nobility, may be capable of acting as an anode and the segregated area (like carbides), being more noble, may become cathode. As a consequence, if the condition is prone to the localized corrosion, an electrochemical cell can be formed in which a micro-galvanic corrosion phenomenon may be initiated and propagated from the depleted zones [28,30].

In order to study the susceptibility to the micro galvanic coupling, SKPFM maps of studied alloys were acquired on the polished surface of the specimens. Figure 4.9a and b respectively show the Volta potential map together with Volta potential profile along the marked white line of the WRO alloy, However the Volta potential map and profile of the B1 SLM fabricated alloy are represented in Figure 4.9c and d, in turn. The SKPFM map and Volta potential profile of WRO alloy (Figure 4.9a) did not show any significant change and showed almost uniform potential (it is in the range of about 20 mV, see Figure 4.9b). This also accords with our earlier observations (Figure 4.8), which showed that the amount of carbides is scare in this sample, as it is a Low Carbon (LC) type, with a C content lower than 0.05%.

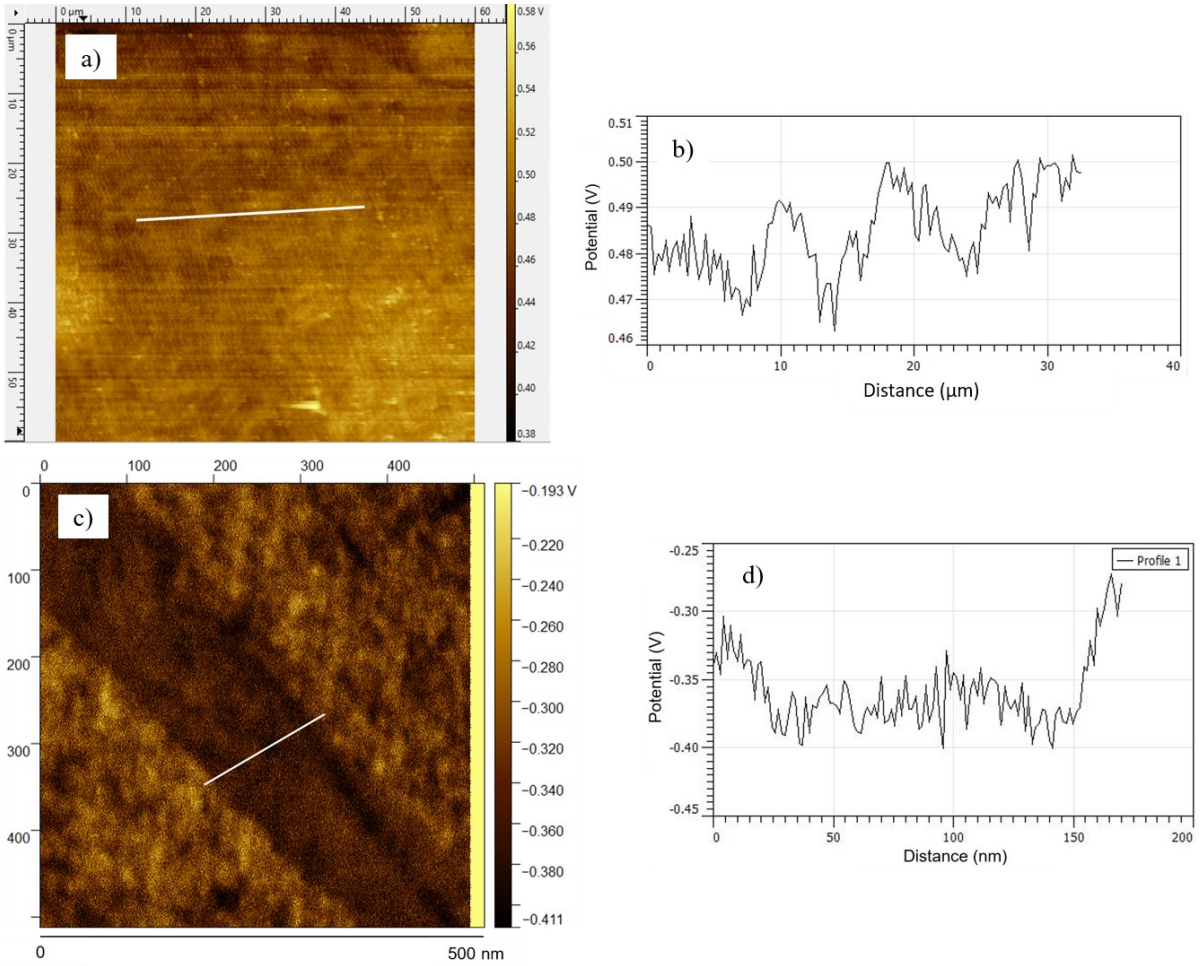

Figure 4.9. a) Volta potential map of WRO alloy; b) Volta potential profile along the white line in a; c) Volta potential map of SLM alloy collected in correspondence of the melt pool boundary, and d) the Volta potential profile along the white line in b.

The Volta potential map and profile were then obtained from B1 SLM samples in correspondence of a melt pool boundary and the results are presented in Figure 4.9 c and d. it is noted that due to the high percentage of porosity of B2 sample, AFM method did not apply to this sample, in order to avoid break of AFM tip during measurements. From the Volta potential map, it was apparent that the boundary region comes out darker, demonstrating a lower relative nobility in comparison to the adjacent matrix which appears brighter. This result indicated that the melt pool boundary may act as a preferential area for corrosion initiation. This less noble area was very narrow (around 0.1-0.2 µm) but exhibits a significantly lower Volta potential in comparison to adjacent regions. The Volta potential difference between boundary and matrix was in the range of about 100mV, that could be a driving force for promoting the selective galvanic corrosion at microscale and justify the greater reactivity of the melt pool boundary as highlighted by the electrolytic etching that

revealed the microstructure by attacking these microstructural features. These differences could be attributed to microsegregation of alloying elements during the SLM fabrication process (as depicted in Figure 4.4).

4.2.4. Surface characterization after anodic polarization by FIB/ STEM

Figure 4.10a shows the surface attack morphology on SLM alloy after 30 min polarization at + 0.9 V_{SCE} in the most severe PBS solution (PBS + 30mM H_2O_2 at pH 4). The specimen is clearly covered by a surface oxide film with cracks preferentially localized at both melt pool and cell boundaries.

Figure 4.10a clearly shows that the melt pool boundaries (characterized by less noble Volta potentials than the matrix) and the core of the cells (where Mo depletion in comparison to the boundaries is detected) correspond to surface valleys due to local preferential corrosion.

From this area, using the FIB technique (see sect. 3.8.2.3), a lamella containing a melt pool boundary was extracted after protecting the surface with a platinum layer (as shown in Figure 4.10b) and after milling the surrounding areas. The extracted lamella is shown in Figure 4.11a and a blue arrow points to the valley corresponding to the melt pool boundary.

On the lamella, parallel lines can be distinguished that seem to correspond to the edges of the dendritic cellular structures (yellow dotted-line in Figure 4.11b). Other linear traces are also observed that cut the previous ones with a different inclination (blue dashed-line in Figure 4.11b) and could be due to the growth of cellular dendrites with different orientation during subsequent passes of the laser beam in the course of the alloy building. However, these features could also be attributed to the introduction of stacking faults into the subsurface, as explained by Wang et al [31].

The lamella was then thinned to reach conditions suitable for STEM analysis of the surface oxide film. The EDS line scan long the direction indicated by the red arrow in Figure 4.11c evidenced that the protective oxide layer formed at +0.9 V_{SCE} (thickness in the range of 100 - 150 nm) mainly consisted of Cr-oxide with traces of Co-oxides. The present findings confirm the results of a voltammetric study (see chapter 5) performed on pure Co, Cr and Mo in the potential range -1.5 to +0.75 V_{SCE} in the same solution here considered. These electrochemical tests evidence that only Cr maintains a kind of passivity up to +0.75 V_{SCE} while the other metals show very high anodic currents at the highest applied anodic potentials suggesting the formation of soluble oxidized species (see chapter 5). This agrees with the STEM results indicating the persistence of only Cr oxides at +0.9 V_{SCE} on the SLM alloy surface.

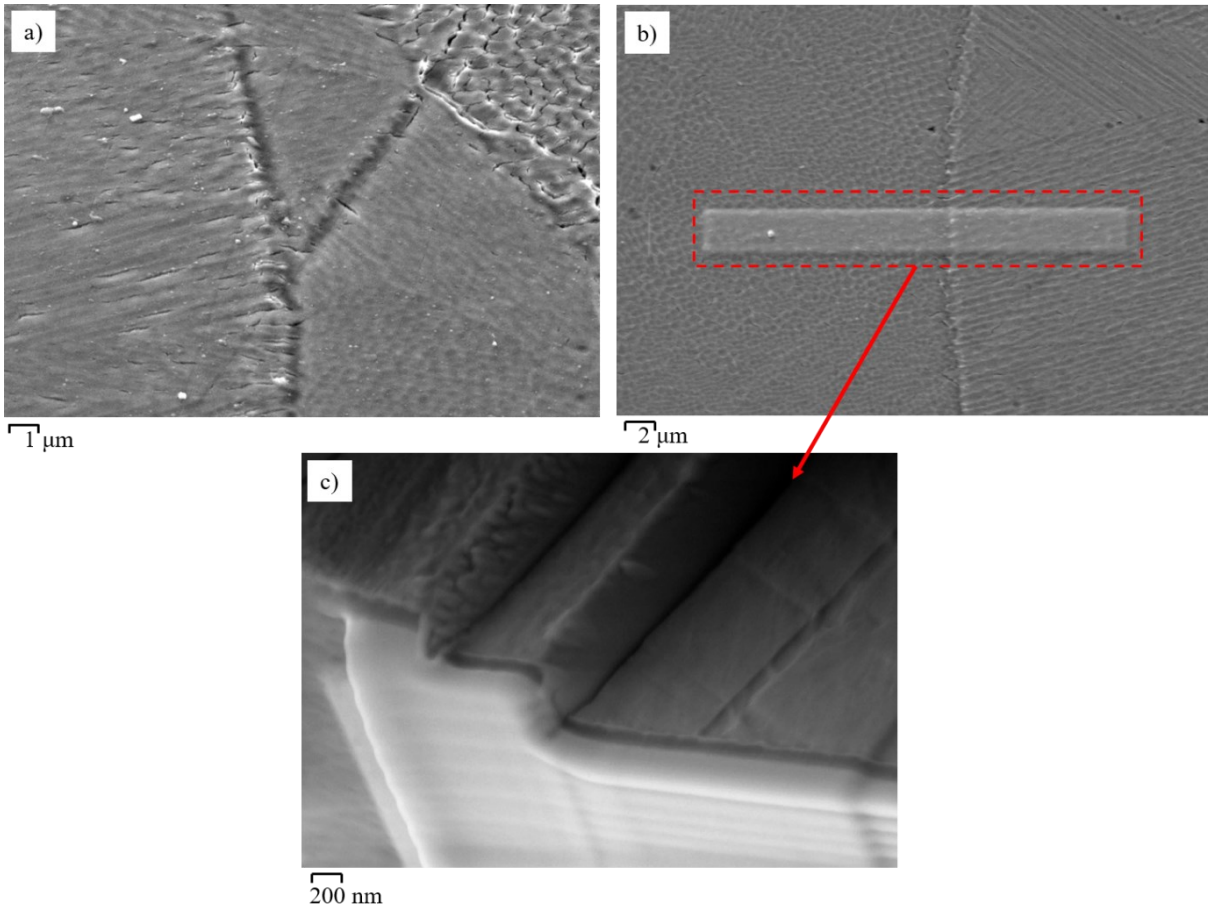

Figure 4.10. SE-SEM images of the SLM CoCrMo alloy polarized for 30 min at a potential of + 0.9 V/SCE in PBS solution pH= 4 at the presence of 30mMol H_2O_2. a) SEM micrograph showing the joint of grain boundaries, b) Region of interest SE-imaging at 1 keV in which the texturing of the microstructure is visible, c) SEM micrograph indicating the oxide layer.

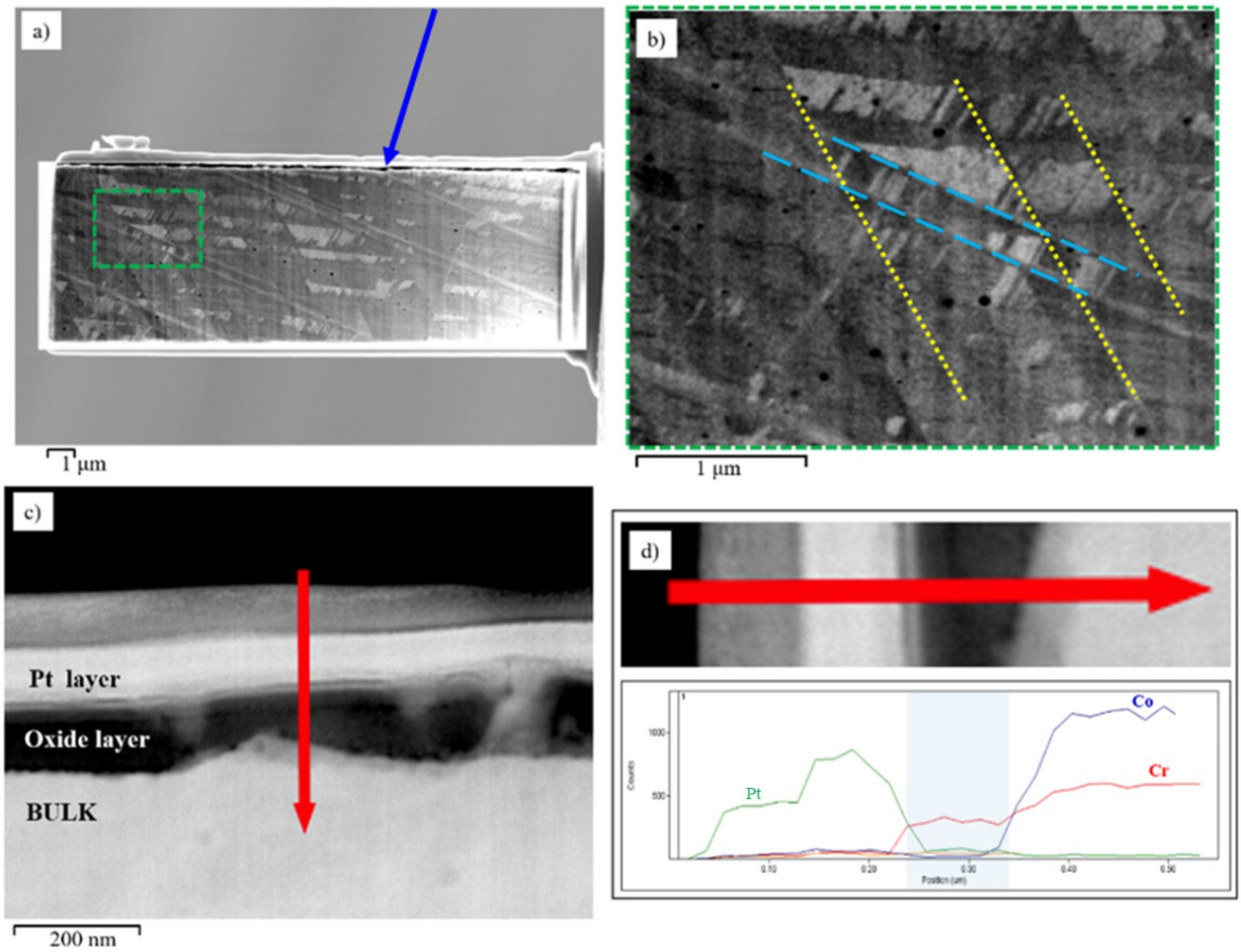

Figure 4.11. a) SE image (e-beam) of the microstructure from the extracted lamella showing the crystalline microstructure, b) indication of the visible parallel lines crossing the sample, c) STEM micrograph representing Pt layer, an oxide layer, and bulk material, d) EDS element peak integrated intensity along with line scan. Note that the light-grey shaded area in the profile plot represented the oxide layer.

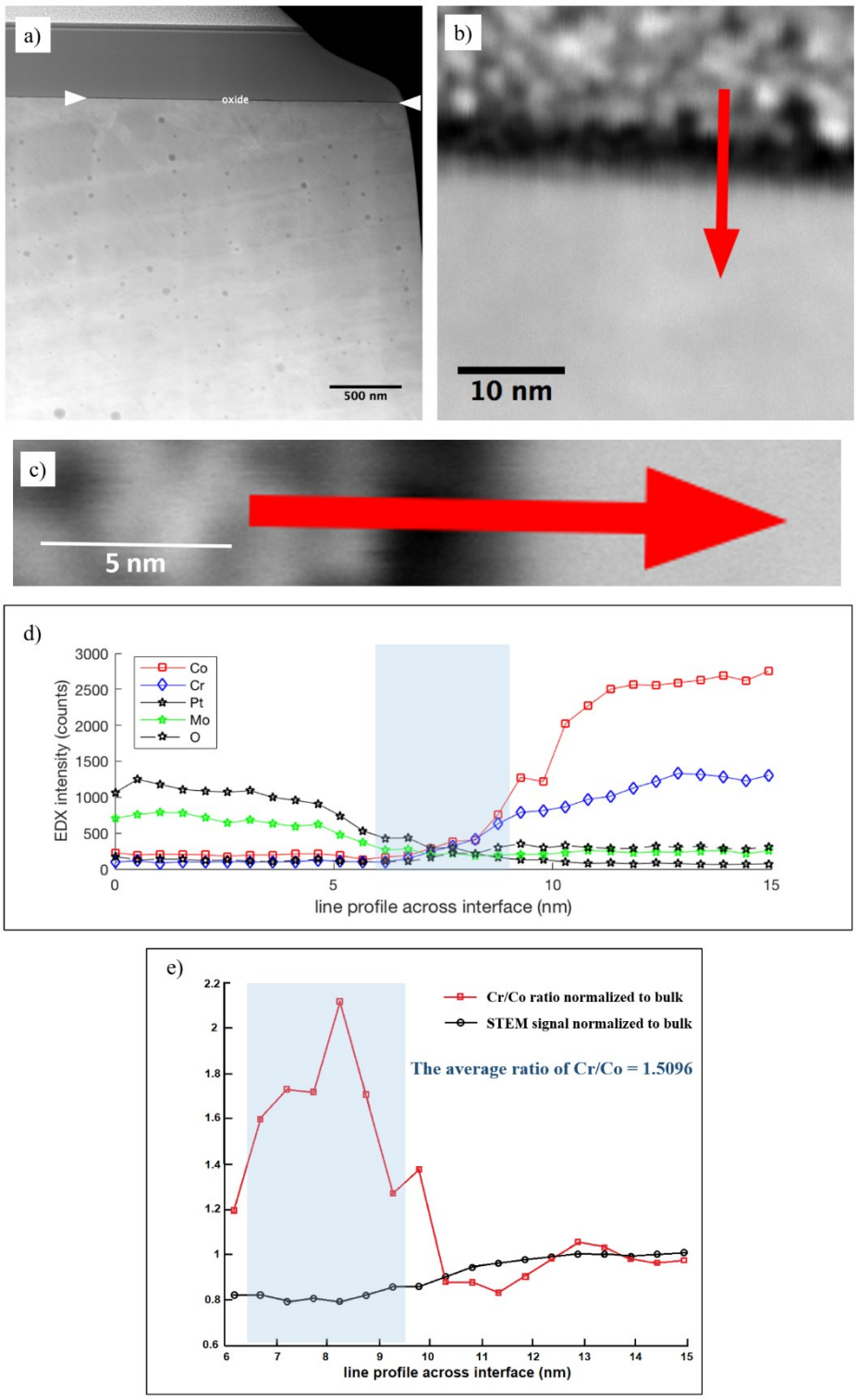

Figure 4.12. a) STEM compositional Imaging of SLM specimen after 15 days in free corrosion condition, b) STEM micrograph representing line profile across the interface, d) EDS compositional scan across the reference line (red line in c.), e) Normalized Cr/Co ratio and STEM signal along with the line scan, not considering Pt area (red line in c). Noted that the highlighted light blue rectangular represented the oxide layer.

The results of STEM analysis performed on a section extracted from a SLM sample after 15 days of immersion in PBS +30 mM H_2O_2 at pH is shown in Figure 4.12.
The STEM image reveals that the alloy is covered by a nano-metric oxide layer of about 4 nm (Figure 4.12b and c). The elemental profiles collected across the oxide layer is shown in figure 4.12c. The Cr and Co percentages correctly increase by passing from the oxide layer to the bulk, as depicted in figure 4.12c and d. The Cr/Co ratio normalized to the abundancy in the bulk confirmed that in the oxide layer Cr has a higher relative content in comparison to the alloy (the estimated normalized average Cr/Co ratio is 1.5096).

4.3 Conclusion

The major goal of this part was to evaluate the microstructure and characteristics of CoCrMo alloys manufactured by selective laser melting. Both SLM alloys and their WRO counterparts were examined using different characterization techniques. Following conclusions can be drawn after analyzing the outcomes:

- The selective laser melting process SLM parameters allow to obtain samples with different microstructural characteristics: the different process parameters lead to fabrication of materials with different residual porosity. Sample B1 obtained under high fluence has a relative density of 99.8% with few residual pores, while the B2 sample fabricated with lower fluence is characterized by a greater porosity percentage and larger pores with a relative density of 95%.
- The XRD analysis showed a higher amount of ε-phase and a smaller crystallite size in the γ-phase in the B2 samples compared to those measured on the B1 samples.
- The SLM technique induced a non-equilibrium microstructure characterized by a cellular structure in which micro and submicro cell growing in specific directions within grains that grow epitassially from n layer to n+1 layer.
- The different laser parameters adopted during the fabrication of the SLM samples induced a finer microstructure in the B2 samples characterized by a finer spacing between the primary dendrites with respect the B1 samples.
- The SLM particular morphlogy is charactrized by a non-unform distribution of alloying elements, representing an enrichment in Mo, and to some extent also for Cr at the cell bundaries and depletion at the center of the cells. B2 sample with finer

structure represents a lower segregation and more unifor distribution of alloying elements if compared to B1.

- CoCrMo alloy fabricated by conventional method already shows the typical twins of the FCC structure and a low volume fraction of precipitates randomly distributed throughout the matrix.
- This SKPFM result indicates that the melt pool boundary of SLM alloys may act as a preferential area for corrosion initiation, demonstrating a lower relative nobility in comparison to the adjacent matrix. However, no significant changes on Volta potential were detected in WRO alloys.
- The application of the FIB technique allowed the estimation of the oxide film thickness which varies between 100 nm and 150 nm after polarization at +0.9 V_{SCE} for 30 minutes. Instead, the thickness of the surface layer in free corrosion condition after 15 days of immersion is much thinner than that of polarized condition and is around 4 nm.
- The EDS line scan long along the surface to bulk of thin lamella extracted by FIB evidenced that the protective oxide layer formed at +0.9 V_{SCE} mainly consisted of Cr-oxide with traces of Co-oxides. The elemental profiles of free corrosion condition suggests that in this case the protective layer is essentially constituted by Cr oxides which their percentages increase by passing from the oxide layer to the bulk.

References

[1] R. E.Dinnebier, A Leineweber, J. S. O. Evans, Rientveld Refinement -practical powder diffraction pattern analysis using Topas. 2019 De Gruyter GmbH , Berlin.

[2] K. Yamanaka, M. Mori, A. Chiba, Effects of carbon concentration on microstructure and mechanical properties of as-cast nickel-free Co–28Cr–9W-based dental alloys, Mater. Sci. Eng. C. 40 (2014) 127–134.

[3] H.F. López, A.J. Saldivar-Garcia, Martensitic transformation in a cast Co-Cr-Mo-C alloy, Metall. Mater. Trans. A. 39 (2008) 8–18.

[4] J.R. Davis, A.S.M.I.H. Committee, Nickel, Cobalt, and Their Alloys, ASM International, 2000.

[5] Y.S. Hedberg, B. Qian, Z. Shen, S. Virtanen, I. Odnevall Wallinder, In vitro biocompatibility of CoCrMo dental alloys fabricated by selective laser melting, Dent. Mater. 30 (2014) 525–534.

[6] X. Zhou, K. Li, D. Zhang, X. Liu, J. Ma, W. Liu, Z. Shen, Textures formed in a CoCrMo alloy by selective laser melting, J. Alloys Compd. 631 (2015) 153–164.

[7] A. Takaichi, Suyalatu, T. Nakamoto, N. Joko, N. Nomura, Y. Tsutsumi, S. Migita, H. Doi, S. Kurosu, A. Chiba, N. Wakabayashi, Y. Igarashi, T. Hanawa, Microstructures and mechanical properties of Co-29Cr-6Mo alloy fabricated by selective laser melting process for dental applications, J. Mech. Behav. Biomed. Mater. 21 (2013) 67–76.

[8] S.L. Sing, S. Huang, W.Y. Yeong, Effect of solution heat treatment on microstructure and mechanical properties of laser powder bed fusion produced cobalt-28chromium-6molybdenum, Mater. Sci. Eng. A. 769 (2020) 138511.

[9] S.K. Everton, M. Hirsch, P. Stravroulakis, R.K. Leach, A.T. Clare, Review of in-situ process monitoring and in-situ metrology for metal additive manufacturing, Mater. Des. 95 (2016) 431–445.

[10] H. Gong, K. Rafi, H. Gu, G.D. Janaki Ram, T. Starr, B. Stucker, Influence of defects on mechanical properties of Ti–6Al–4V components produced by selective laser melting and electron beam melting, Mater. Des. 86 (2015) 545–554.

[11] Y.J. Liu, X.P. Li, L.C. Zhang, T.B. Sercombe, Processing and properties of topologically optimised biomedical Ti–24Nb–4Zr–8Sn scaffolds manufactured by selective laser melting, Mater. Sci. Eng. A. 642 (2015) 268–278.

[12] B. Wälivaara, I. Lundström, P. Tengvall, An in-vitro study of H2O2-treated titanium surfaces in contact with blood plasma and a simulated body fluid, Clin. Mater. 12

(1993) 141–148.
[13] Library, MRS Bull. 28 (2003) 674–675. https://doi.org/DOI: 10.1557/mrs2003.197.
[14] Y. Lee, M. Nordin, S.S. Babu, D.F. Farson, Effect of Fluid Convection on Dendrite Arm Spacing in Laser Deposition, Metall. Mater. Trans. B. 45 (2014) 1520–1529.
[15] L.E. Murr, E. Martinez, J. Hernandez, S. Collins, K.N. Amato, S.M. Gaytan, P.W. Shindo, Microstructures and properties of 17-4 PH stainless steel fabricated by selective laser melting, J. Mater. Res. Technol. 1 (2012) 167–177.
[16] L.C. Zhang, H. Attar, M. Calin, J. Eckert, F. Brenne, T. Niendorf, H.J. Maier, T. Dikova, Additively manufactured cellular structures: Impact of microstructure and local strains on the monotonic and cyclic behavior under uniaxial and bending load, J. Mater. Process. Technol. 213 (2018) 1558–1564.
[17] Z.W. Chen, M.A.L. Phan, K. Darvish, Grain growth during selective laser melting of a Co–Cr–Mo alloy, J. Mater. Sci. 52 (2017) 7415–7427.
[18] Y. Zhang, L. Wu, X. Guo, S. Kane, Y. Deng, Y.-G. Jung, J.-H. Lee, J. Zhang, Additive Manufacturing of Metallic Materials: A Review, J. Mater. Eng. Perform. 27 (2018) 1–13.
[19] W. Kurz, D. Fisher, Fundamentals of Solidification: Fourth Revised Edition, Retrosp. Collect. (1998).
[20] K. Darvish, Z.W. Chen, M.A.L. Phan, T. Pasang, Selective laser melting of Co-29Cr-6Mo alloy with laser power 180–360W: Cellular growth, intercellular spacing and the related thermal condition, Mater. Charact. 135 (2018) 183–191.
[21] K.-H. Shin, H. Natu, D. Dutta, J. Mazumder, A method for the design and fabrication of heterogeneous objects, Mater. Des. 24 (2003) 339–353.
[22] M. Peter, K. Jean-Pierre, Residual stresses in selective laser sintering and selective laser melting, Rapid Prototyp. J. 12 (2006) 254–265.
[23] P. Mercelis, L. Froyen, M. Rombouts, Binding Mechanisms in Selective Laser Sintering and Selective Laser Melting Binding Mechanisms in Selective Laser Sintering and Selective Laser Melting, (2005).
[24] L. Thijs, F. Verhaeghe, T. Craeghs, J. Van Humbeeck, J.-P. Kruth, A study of the microstructural evolution during selective laser melting of Ti–6Al–4V, Acta Mater. 58 (2010) 3303–3312.
[25] K. Monroy, J. Delgado, J. Ciurana, Study of the Pore Formation on CoCrMo Alloys by Selective Laser Melting Manufacturing Process, Procedia Eng. 63 (2013) 361–369.
[26] S.M. Yusuf, Y. Chen, R. Boardman, S. Yang, N. Gao, Investigation on Porosity and

Microhardness of 316L Stainless Steel Fabricated by Selective Laser Melting, (2017) 1–12.

[27] B. Song, X. Zhao, S. Li, C. Han, Q. Wei, S. Wen, J. Liu, Y. Shi, Differences in microstructure and properties between selective laser melting and traditional manufacturing for fabrication of metal parts : A review, 10 (2015) 111–125.

[28] A.W. Adamson, A.P. Gast, Physical Chemistry of Surfaces Sixth Edition, (n.d.).

[29] H.O. Jacobs, H.F. Knapp, S. Müller, A. Stemmer, Surface potential mapping: A qualitative material contrast in SPM, Ultramicroscopy. 69 (1997) 39–49.

[30] T.H. Muster, A.E. Hughes, Applications and Limitations of Scanning Kelvin Probe Force Microscopy for the Surface Analysis of Aluminum Alloys, J. Electrochem. Soc. 153 (2006) B474.

[31] Z. Wang, Y. Yan, Y. Su, L. Qiao, Effect of electrochemical corrosion on the subsurface microstructure evolution of a CoCrMo alloy in albumin containing environment, Appl. Surf. Sci. 406 (2017) 319–329.


5

CHAPTER FIVE

Influence of alloying elements on the electrochemical behaviour of SLM CoCrMo alloy in simulated body fluids – A Cyclic Voltammetry (CV) study.

5.1 Introduction

In this chapter, cyclic voltammetry (CV) tests were used to compare the corrosion behaviour of SLM CoCrMo alloy (that is B1 and B2 samples) to those of a wrought alloy (WRO samples) with similar composition. To evaluate the dependence of the nature of the surface film on CoCrMo alloys with the potential and the environment, cyclic voltammetry tests were conducted on both SLM and WRO alloys and on its main alloying elements, namely pure Co, Cr and Mo (see sect. 3.5.3 for description of CV tests). Pourbaix diagrams of Co, Cr and Mo in water, at 37 °C, were also used to interpret CV tests. The voltammograms were conducted to understand the nature of the reduction peaks and therefore the nature of the compounds and ions formed during the scanning in anodic direction.

5.2 Construction of the Pourbaix diagrams

In order to help interpreting cyclic voltammetry results, the potential-pH (E-pH) equilibrium diagrams of the Co-H_2O, Cr-H_2O and Mo-H_2O systems at three different molarities of soluble species (10^{-6}, 10^{-4} and 10^{-2} M) at 37 °C were calculated. The selected data used in the thermodynamic calculations are reported in the appendix (Table A1, A2 and A3). The E-pH equilibrium diagrams were calculated at the standard state pressure of 1 bar by using the HSC Chemistry 9 software (Outotec, Espoo, Finland). A pH domain from 0 to 10 is established and the potentials referred to the Saturated Calomel Electrode (SCE) (considered to be +244 mV standard hydrogen electrode (SHE) at all temperatures).

The pH dependence of electrochemical potential of the water reduction ($H_2O_{(l)} + e^- = 0.5H_{2(g)} + OH^-$ or $H^+ + e^- = 0.5H_{2(g)}$) and water oxidation reactions ($2H_2O_{(l)} = O_{2(g)} + 4H^+ + 4e^-$ or $4OH^- = O_{2(g)} + 2H_2O + 4e^-$) are represented in the diagrams by the two dotted lines crossing the diagram, a and b, respectively.

5.3. Results and discussion

5.3.1. E-pH diagrams of Co, Cr and Mo – H_2O systems

The E-pH diagram of Co-H_2O systems obtained at 37°C with different Co ion concentrations (10^{-2}, 10^{-4} and 10^{-6} M) is plotted in Figure 5.1.

By considering as stability boundaries of solid species those in equilibrium with ion concentrations of 10^{-6} M, Figure 6 suggests that: Co oxidation is allowed over -0.72 V_{SCE}, at

both pH 7.4 and 4. At pH 7.4, Co oxidation produces Co^{2+}, which is converted into Co_3O_4 at potentials nobler than 0.1 V_{SCE}. However, as Co^{2+} ion concentration increases up to 10^{-2} M or higher, solid $Co(OH)_2$ is thermodynamically allowed, in the potential range -0.6 to -0.3 V_{SCE}. At higher potentials, $Co(OH)_2$ oxidation to Co_3O_4 is possible.

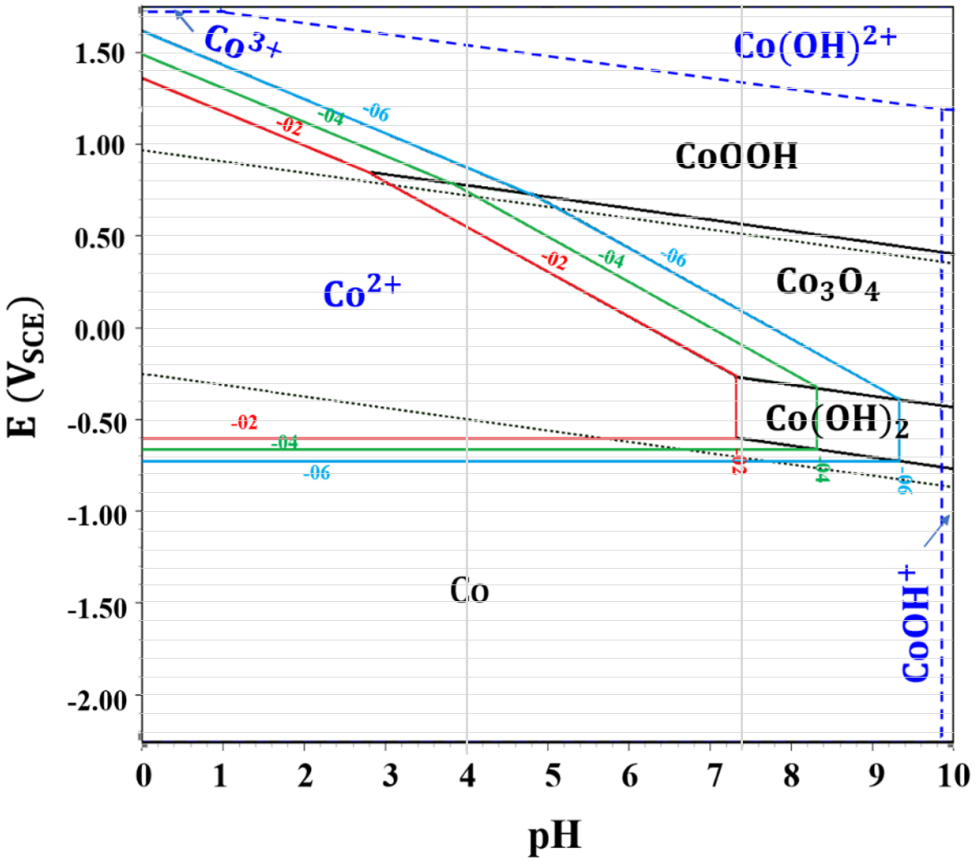

Figure 5. 1. Potential-pH diagram for Co–H_2O system at 37 °C and $[Co]_{total}=10^{-2}$, 10^{-4} and 10^{-6}M.

At pH 4 in the potential range investigated by CV, Co oxidation produces soluble species and in particular, taking into consideration species such as Co^{2+}, $Co(OH)^{+}$, $Co(OH)^{2+}$ and Co^{3+}, only Co^{2+} is thermodynamically allowed. However again, if Co^{2+} ion concentrations increase up to 10^{-2} M or higher, solid Co_3O_4 can form, in a limited potential range (0.55 - 0.7 V_{SCE}).

The E-pH diagram of Cr-H_2O system at 37 °C is plotted in figure 5.2. It shows that at pH 7.4, Cr is immune up to potentials of -1.30 V_{SCE}, then, it is oxidized to Cr_2O_3, stable up to 0.25 V_{SCE}. At even higher potentials the oxide evolves into soluble CrO_4^{2-}. At pH 4, Cr_2O_3 is stable in the range -0.72 V_{SCE} to 0.55 V_{SCE}. At lower potentials, down to -1.28 V_{SCE}, Cr^{2+} prevails, whereas at nobler potentials, $HCrO_4^{2-}$ can form. Mo (VI) anions and molybdic acid have varying degrees of condensation, but equilibria are reached very slowly. Only the species shown in the E/pH diagram were considered in this analysis.

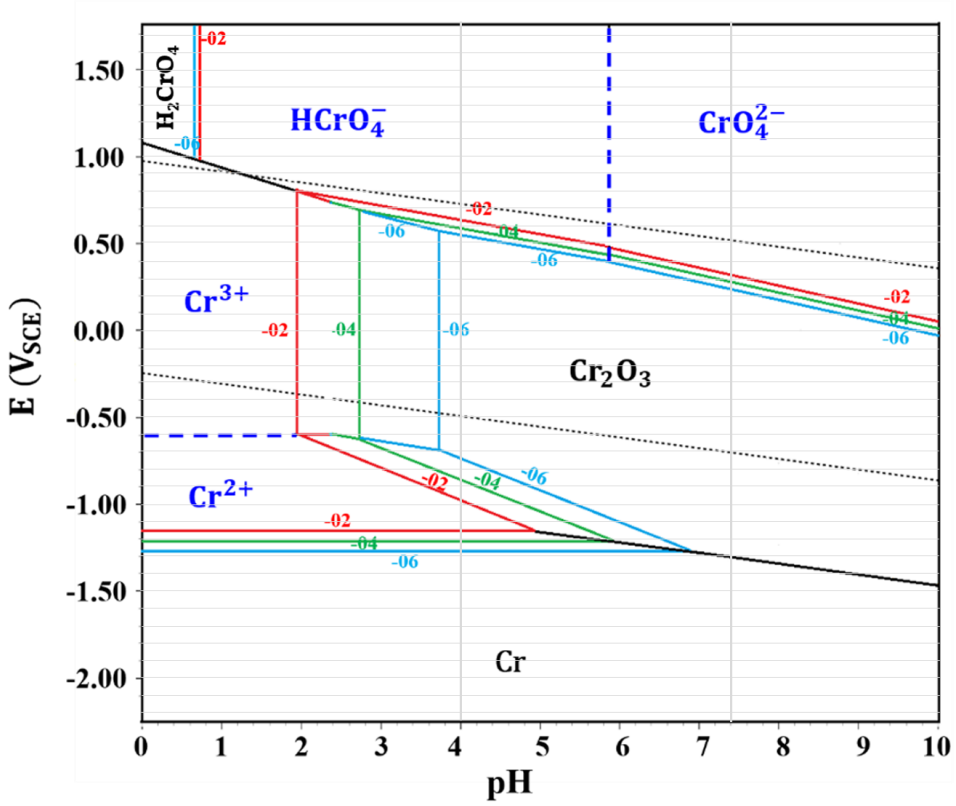

Figure 5. 2. Potential-pH diagram of Cr–H_2O system at 37 °C and [Cr]total=10^{-2}, 10^{-4} and 10^{-6}M.

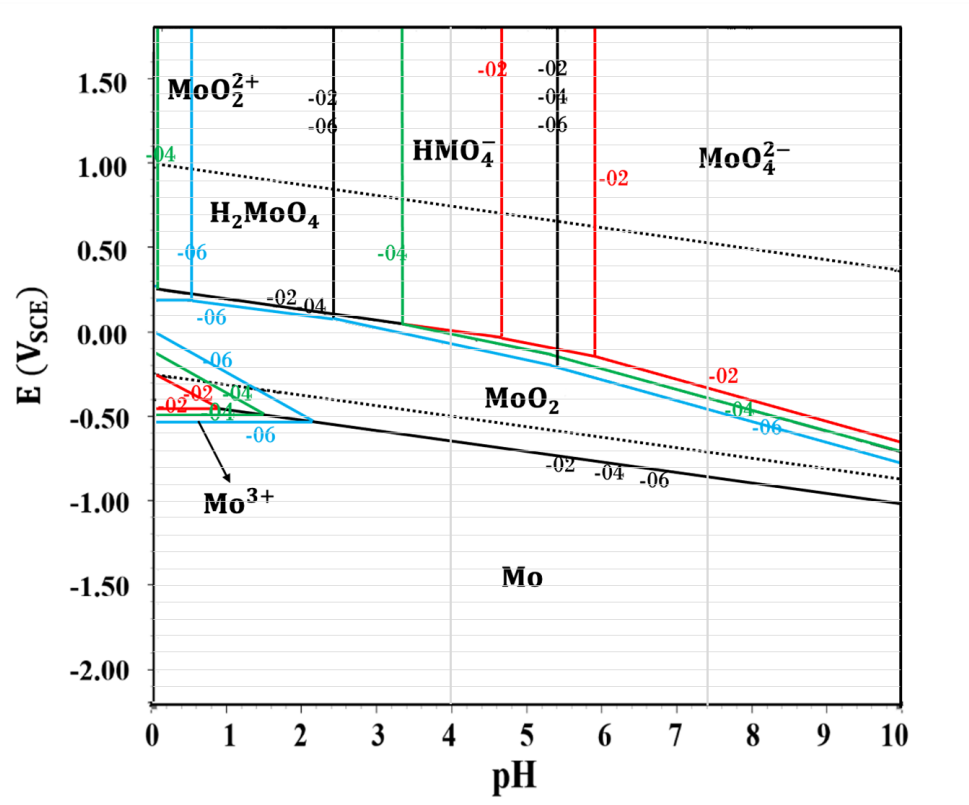

Figure 5. 3. Potential-pH diagram of Mo–H_2O system at 37 °C and [Mo]total=10^{-2}, 10^{-4} and 10^{-6}M.

Figure 5.3 shows the potential-pH diagram for molybdenum. Under ordinary laboratory conditions (P_{O2}=0.2atm) in oxygenated water, Mo(II) ions are not stable and were here not considered. The potential of Mo/MoO_2 equilibrium is -0.85 V_{SCE} and -0.64 V_{SCE} for pH 7.4 and pH 4. At pH 7.4, MoO_2 oxidizes to MoO_4^{2-} at potentials nobler than -0.48, -0.42 and -0.32 V_{SCE}, for ion concentrations equal to 10^{-6}, 10^{-4} and 10^{-2} M respectively. At pH 4 $HMoO_4^-$ can form from MoO_2 oxidation at potential over -0.11 and -0.4V_{SCE} for ion concentrations equal to 10^{-6} and 10^{-4} M respectively.

However, as concentration increases up to 10^{-2} M MoO_2 is oxidized soluble molybdic acid at potential higher than -0.0V_{SCE}. Mo (VI) anions and molybdic acid have varying degrees of condensation, but equilibria are reached very slowly. Only the species shown in the E/pH diagram were considered in this analysis.

5.3.2. CV tests on pure Co

The cyclic voltammograms (1st and 5th cycles) recorded on Co in PBS at pH 7.4 are presented in Figure 5.4. The 1st cycle started with water reduction up to potential values of -1.2 V_{SCE}. Then, very low currents were obtained up to about 0 V_{SCE} suggesting that, despite the thermodynamic information obtained from E-pH diagram, at potentials nobler than those of the immunity region Co passivity occurred since the 1st cycle.

According to some authors [1] this behaviour is connected to the existence of an adsorbed hydrous oxide Co(I) which favours the formation of $Co(OH)_2$ some hundred mV before the expected potential. Other authors operating in a phosphate buffer at pH 7 [2] or in Hank's solution [3–5] suggested that passivity was essentially connected to the formation of a $Co(OH)_2$ or CoO film, but also phosphates were likely incorporated in the surface film to reinforce passivity [3,5]. At higher potentials, the currents of the 1st cycle increased up to the vertex potential of 0.7 V_{SCE}. At this pH value also water oxidation is possible at potentials nobler than 0.51 V_{SCE}. During the reverse scan, pitting occurred, favoured by the presence of chlorides in the aggressive solution and indicated by the presence of higher anodic currents in the backward than in the forward scan. In the cathodic current potential range, a peak at -1.1 V_{SCE} and a shoulder at -1.0 V_{SCE} were detected. The anodic and cathodic currents increased from the 1st to the 5th cycle and the width of the passivity range strongly decreased, indicating a limited surface film protectiveness in this environment. In the last reverse cycle, the reduction peaks merged into a larger one, starting at -0.7 V_{SCE} and centred at -1.28 V_{SCE}.

To attribute specific reduction reactions to the cathodic peaks in the reverse scans and therefore to interpret the anodic behaviour of Co in this environment, CV tests were collected in PBS at pH 7.4 with different maximum vertex potentials (Figure 5.4b). With a vertex potential of -0.6 V_{SCE} (just above the immunity region, not shown) the currents remained cathodic, and no reduction peak was visible, beside that related to water reduction. Vertex potentials of -0.5, -0.4 and -0.3 V_{SCE} produced low slightly increasing anodic currents and the rise of a correspondingly increasing cathodic peak at about -0.8 V_{SCE} (indicated as C1 in Figure 5.4b). Instead, cycles with vertex potentials of -0.2, -0.1 and 0 V_{SCE} exhibited a single cathodic peak at -0.9 V_{SCE}. In view of the stabilization afforded by Co^{2+} ions to the $Co(OH)_2$ film (as suggested by the E-pH diagram), it is possible that below a certain maximum potential, and in particular below -0.3 V_{SCE}, the achieved Co^{2+} concentration was insufficient to produce the hydroxide film. In these CV tests, the reduction of the small produced Co^{2+}

amounts were likely responsible of the C1 peak. In the case of nobler vertex potentials, C2 peak appeared and was attributed to the reduction of the hydrated Co(II) hydroxide film to Co metal. With maximum potentials nobler than 0.1 V_{SCE}, the partial conversion of Co(II) hydroxide to Co_3O_4 film was finally allowed, so that C3 peak (increasing significantly with the increase in maximum potential, Figure 5.4a) was ascribed to the reduction of this mixed oxide.

At pH 4 (Figure 5.4c) the forward scan started with hydrogen evolution reaction. In rather good agreement with thermodynamic information (Figure 5.1), the metal oxidation started at -0.6 V_{SCE}, with the formation of soluble Co^{2+} cations [6,7], then, anodic currents increased steeply up to 0.7 V_{SCE}. During the backward scan, one small reduction peak at -0.78 V_{SCE} (indicated as C1) and a shoulder at about -1.1 V_{SCE} were observed. CV tests with different vertex potentials decreasing regularly from 0.7 to -0.7 V_{SCE} are shown in Figure 5.4d. They clearly evidence that peak C1 was always detected if the maximum potential exceeded -0.3 V_{SCE}, while the shoulder at about -1.1 V_{SCE} never disappeared, even if only cathodic currents were measured on cycling. Therefore, also considering thermodynamic reasons (Figure 5.1), C1 was ascribed to the $Co^{2+} + 2\ e^- \rightarrow Co$ reaction. The reduction potential of C1 was more or less the same of the same peak at pH 7.4, because the reaction is pH independent. The band at -1.1 V_{SCE} was reasonably attributed to a step of hydrogen ion reduction (likely the Volmer hydrogen adsorption step [8]).

The exposure of Co to PBS+H_2O_2 at pH 4 (Figure 5.4e) did not determine any clear passivity region, even if the cyclic voltammograms showed lower anodic currents than those recorded in the absence of H_2O_2 at the same pH value.

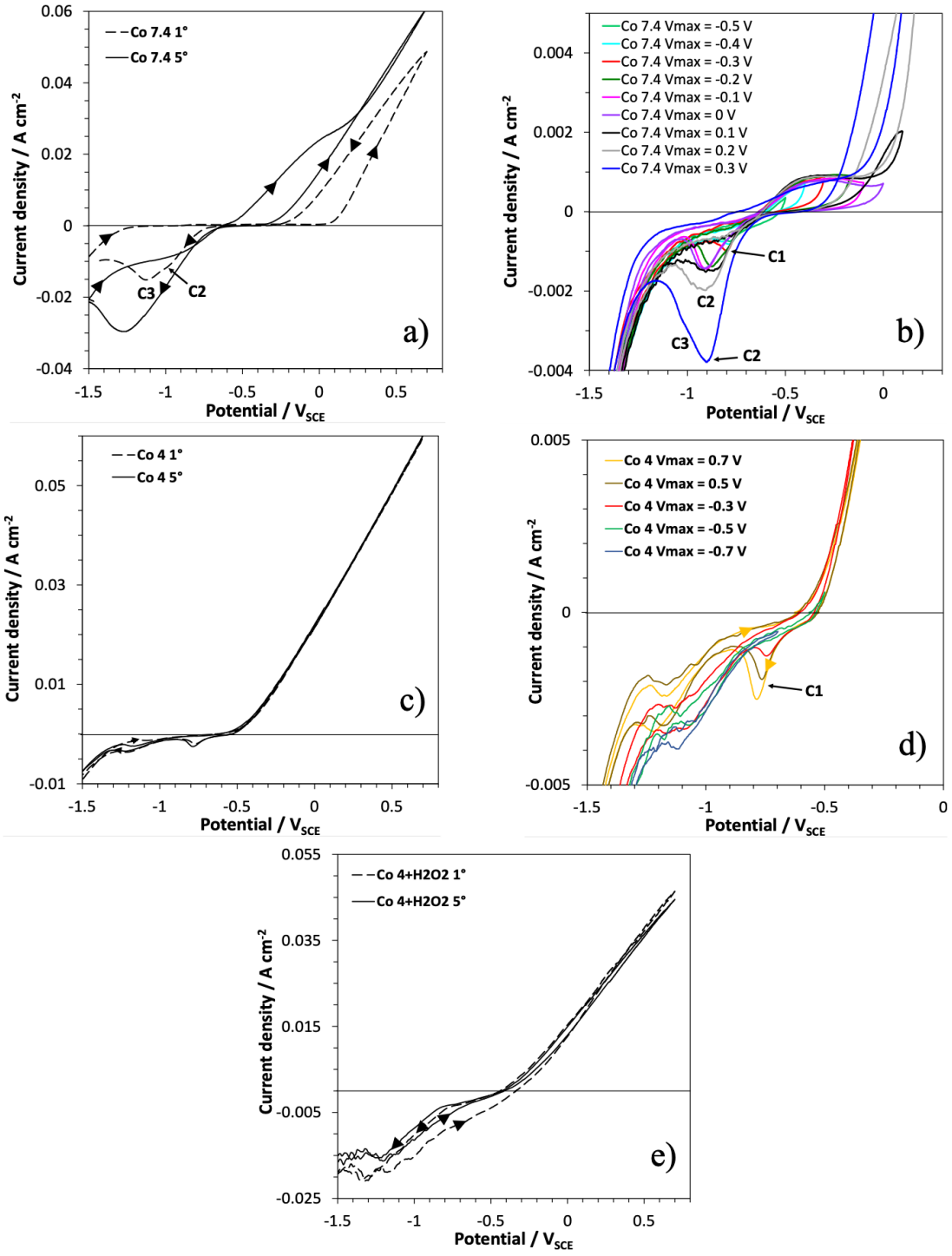

Figure 5. 4. Voltammetry cycles recorded on pure Co in PBS a) at pH 7.4, with maximum potential of 0.7 V_{SCE}, b) at pH 7.4, with different maximum potentials, c) at pH 4, with maximum potential of 0.7 V_{SCE}, d) at pH 4, with different maximum potentials, e) at pH 4, with addition of 30 mM H_2O_2. Dashed line = first cycle. Continuous line = fifth cycle.

This suggests the possible formation of an adsorption oxide layer, induced by the strong oxidative action of the peroxide [9,10]. Under acidic pH, the favourable influence of H_2O_2 on the formation of a protective surface film on CoCrMo was recognized in the other papers [11,12]. The results here obtained suggested that Co in CoCrMo alloy may give a contribution to the film protectiveness in acidic H_2O_2 solutions.
In contrast with Figure 5.4c, Figure 5.4e shows a wide intense cathodic band at potentials below -0.4 V_{SCE} which was attributed to H_2O_2 reduction to H_2O [13].

5.3.3. CV tests on pure Cr

The cyclic voltammograms recorded on Cr in PBS solutions are reported in Figure 5.5.

In all environments after the potential region of prevailing cathodic currents, Cr exhibited a wide passive potential range with currents much lower than those recorded on Co, due to the formation of a protective Cr(III) oxide film. The potential-pH diagram for Cr (Figure 5.2) evidences that passivation is due to Cr_2O_3 formation which, at pH 7.4, can be oxidized to soluble Cr(VI) species at potentials nobler than +0.25 V_{SCE}. Therefore, in neutral solution the sharp current increase over 0.4 V_{SCE} was ascribed to the formation of chromates (with likely some contribution of water oxidation) which were reduced in correspondence of the cathodic peak at 0.07 V in the reverse cycle (Figure 5.5a), in agreement with the findings of previous research studies [14]. At pH 4, chromate ions are stable at nobler potentials, higher than 0.55 V_{SCE}, so that their formation was negligible in the potential investigated range, as indicated by the low anodic currents and absence of reduction peaks in Figure 5.5b. In contrast with Co behavior, the addition of H_2O_2 in PBS at pH 4 induced a slight increase in the anodic currents (Figure 5.5c).
Studies performed on 316L stainless steel evidenced that H_2O_2 favors the surface formation of CrOOH instead of Cr_2O_3, with a consequent marked decrease in the barrier properties of the passive film [15].
On this metal, the passive currents either decreased on cycling in absence of hydrogen peroxide but remained almost constant, in the absence or presence of H_2O_2, suggesting that H_2O_2 induced the formation of less resistant and protective passive film. Even on Cr, H_2O_2 markedly stimulated the cathodic currents due to the peroxide reduction to H_2O.

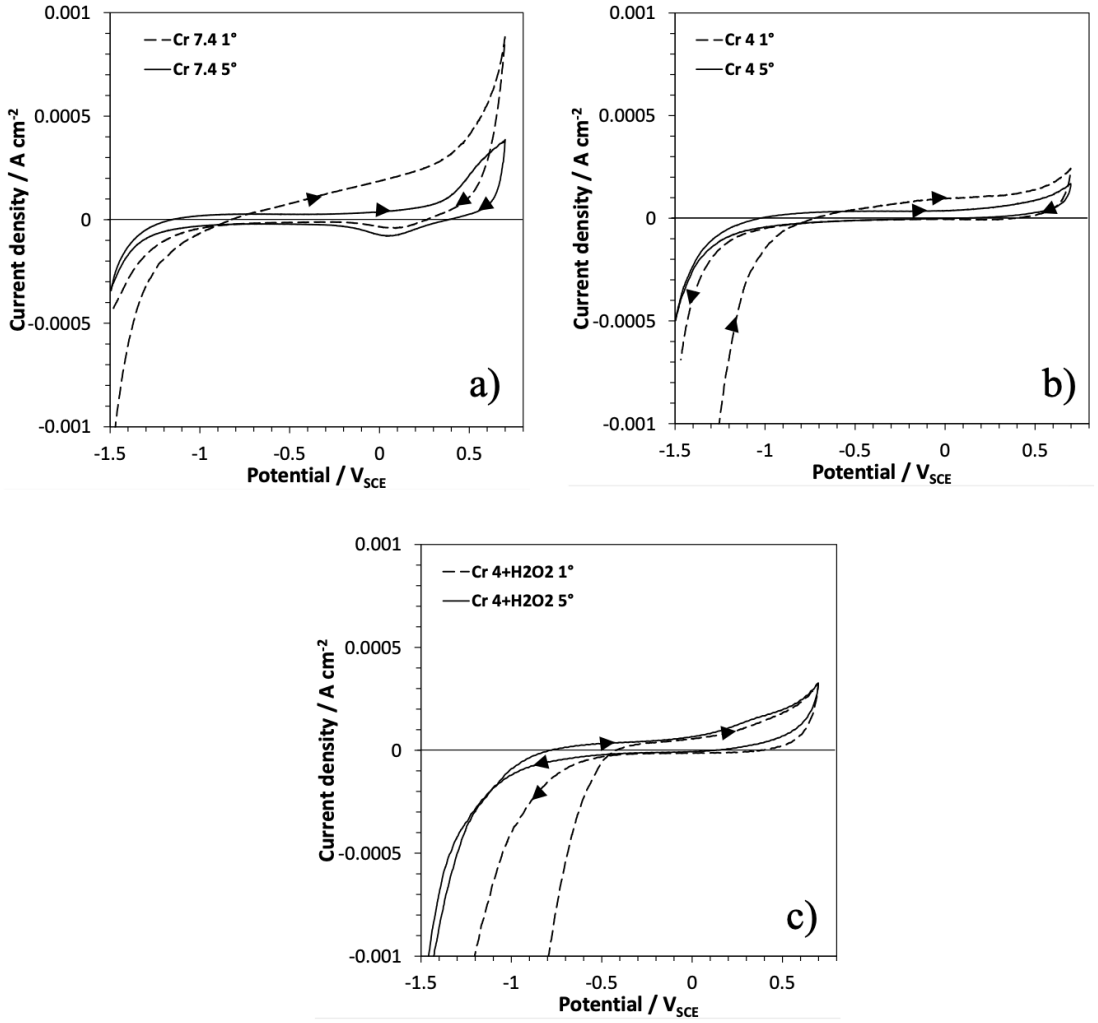

Figure 5. 5. Voltammetry cycles recorded on pure Cr in PBS a) at pH 7.4 b) at pH 4, c) at pH 4 with addition of 30 mM H_2O_2. Dashed line = first cycle. Continuous line = fifth cycle.

5.3.4. CV tests on pure Mo

The results of CV tests on Mo are shown in Figure 5.6. At pH 7.4, after the potential region of water reduction, quite low anodic currents were observed up to about -0.2 V_{SCE}, indicating metal passivity. According to the E-pH diagram (Figure 5.3), at this pH the first oxidation product of Mo is MoO_2, likely formed during the forward cycle in correspondence of the anodic peak centred at about -0.47 V_{SCE}, within the passive region and better visible in the inset of Figure 5.6a [4,14]. At increasing potentials, a shoulder was observed at about -0.1 V_{SCE}, followed by a steep rise of the anodic currents above 0.1 V_{SCE}. According to thermodynamic considerations (Figure 5.3) MoO_2 oxidation is expected to produce Mo (VI) in the form of soluble MoO_4^{2-}.

Other authors [5,14], that conducted tests under comparable conditions, ascribed the shoulder at 0 V_{SCE} to MoO_3 and the subsequent fast current increase to the formation of soluble molybdates (and/or condensed $Mo_7O_{24}^{6-}$), as molybdates are in equilibrium with heptamolybdate species [14,16]. The XPS analyses performed by Ebrahimi et al. [17]. On NiCrMo alloys after exposures to a neutral chloride solution partially confirmed these results.

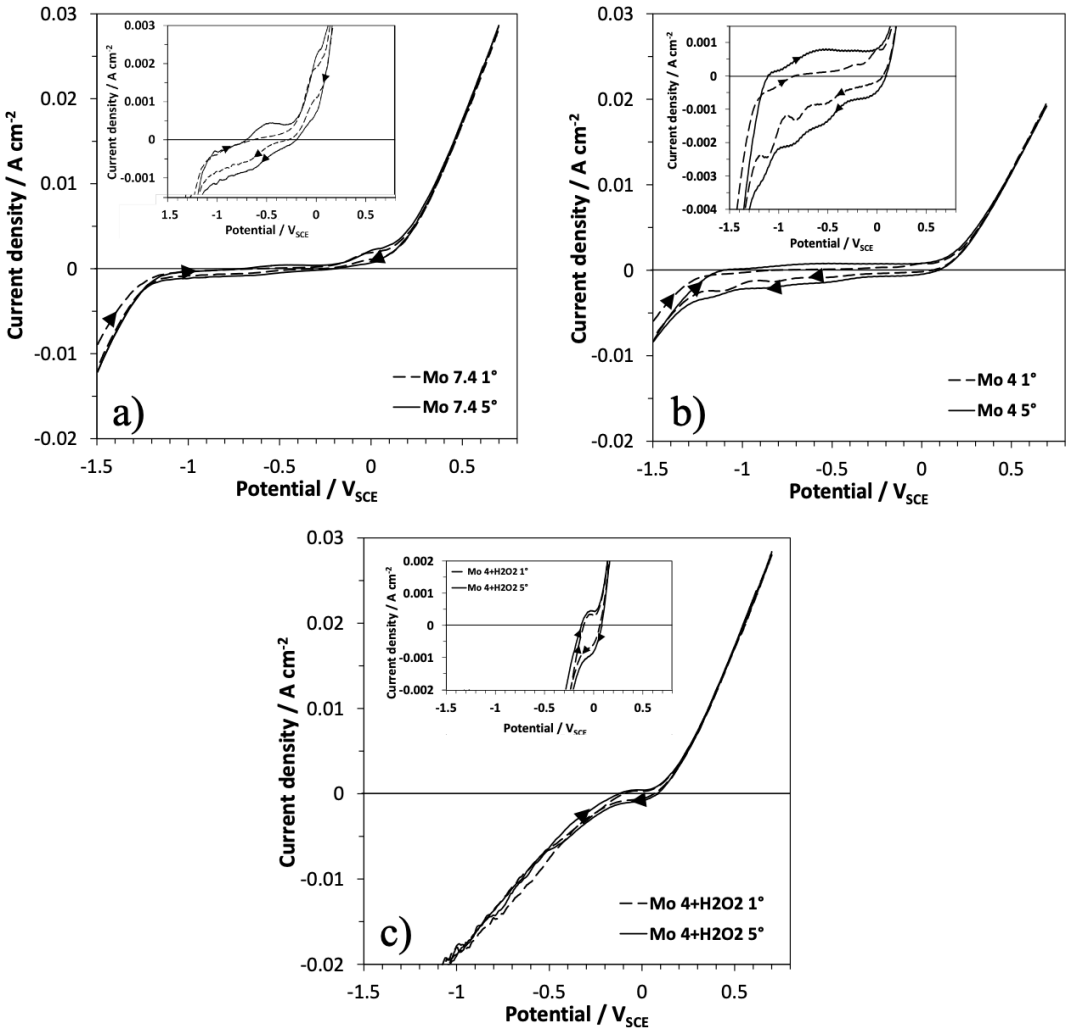

Figure 5.6. Voltammetry cycles recorded on pure Mo in PBS a) at pH 7.4 b) at pH 4, c) at pH 4 with addition of 30 mM H_2O_2. Dashed line = first cycle. Continuous line = fifth cycle.

In fact, after prolonged (some hours) persistence of the alloys at 0.05 V_{SCE}, they detected comparable amounts of Mo(IV), Mo(V) and Mo (VI) compounds in in the passive film (beside oxides of Cr and Ni).

In the reverse scan at pH=7.4 a reduction peak was detected at about -0.65V_{SCE} due to the reduction of Mo(VI) species to MoO_2, thermodynamically allowed already at potential below -0.35V_{SCE} for ion concentrations of 10^{-2}M and at potential below -0.46 V_{SCE} for 10^{-2}M).

At pH 4 (Figure 5.6b), Mo showed a wide passive potential range with slightly increasing anodic currents from the first to the last cycle. From -1.1 to 0 V_{SCE}, many scarcely pronounced anodic peaks were perceivable, in agreement with the literature information suggesting the formation of different intermediate oxidations states and/or metastable oxide forms. The most pronounced peak at -0.55 V_{SCE} was likely connected to MoO_2 formation. In fact, in acidic NaCl solution (pH 4.3), Wang et al. [18] detected Mo_2O_3 (likely) at -1.1 $V_{Ag/AgCl}$, MoO_2 and traces of molybdate at -0.6 $V_{Ag/AgCl}$ and mainly molybdate at -0.1 $V_{Ag/AgCl}$. According to Ürgen et al. [19], in acidic chloride solution of pH 1, the major fraction of the film generated in the passive range (- 0.2 to 0.1 V_{SCE}) was constituted by a Mo(III) species; whereas Mo(IV) and Mo(V) compounds represented a minor fraction at -0.2 V_{SCE} and slightly increased at nobler potential. Mo(VI) species increased more remarkably up to 0.1 V_{SCE}. Similarly, Hull [20] and Lu et al [21], operating in sulphuric and hydrochloric acid electrolytes respectively, found surface species with all oxidation states from Mo(III) to Mo(VI) during their polarization studies. Figure 5.5b shows that transpassivity started at potentials nobler than 0 V_{SCE} at which a sharp current increase occurred, connected to molybdate and/or heptamolybdate ion dissolution [22]. At the vertex potential, transpassivity currents were lower than those at pH 7.4, suggesting the formation of a more protective surface oxide layer. Phosphomolybdates are known to be very stable at this and lower pH values [23] and could contribute to reinforce surface passivity. In the backward cycles, many reduction peaks were detected as a consequence of the multiplicity of oxidized Mo species.

The voltammograms of Mo in PBS+30 mM H_2O_2 at pH 4 are shown in Figure 5.6c. It clearly evidences that H_2O_2 provoked the formation of a very defective oxide film, with a dramatic reduction of a passive range. Transpassive currents were higher than those in the absence of H_2O_2 at the same pH and reached values comparable to those observed at pH 7.4.

5.3.5. CV tests on CoCrMo Alloys

The cyclic voltammograms recorded at pH 7.4 on both SLM and WRO CoCrMo alloys are presented in Figure 5.7a.

The two alloys exhibited a quite similar behaviour with very low anodic currents from -0.9 V_{SCE} up to the vertex potential. This behaviour, largely connected to the protective capability

of Cr_2O_3 [5] (Figures 5.4-5.6), suggested that the barrier properties of the passive film of SLM alloy were quite similar to those of the wrought alloy. In the 1st forward cycle, two anodic peaks were detected at about -0.5 and -0.12 V_{SCE} (the latter one scarcely evident on the WRO alloy) which increased on cycling and merged in a large single peak centred at -0.25 V_{SCE}. This anodic peak was essentially connected to the formation of $Co(OH)_2$, favoured (in the case of this alloy) by a pre-existing Cr_2O_3 oxide layer [3,16]. Traces of MoO_2 were also expected to form [4,5]. At about 0.5 V_{SCE} the currents slightly increased due to transpassivity (dissolution of chromates and molybdates, as reported for pure Cr and Mo, Figures 5.5 and 5.6). All these anodic reactions appeared definitely irreversible, because in the reverse scans the first cathodic peak was detected at -1.1 V_{SCE}.

Considering the 1st cycle obtained at pH 4 (Figure 5.7b), low passive currents with no clear anodic peaks and trends similar to those obtained on Cr at the same pH were detected on both alloys, suggesting the formation of a Cr_2O_3 film, essentially (Figure 5.5b). The limited chromate dissolution at this pH contributed to reinforce the film stability, with anodic currents lower than those at pH 7.4 in the high potential region. The main contribution to the anodic currents at potentials higher than 0.5 V_{SCE} was attributed to Co_3O_4 formation and Co^{2+} dissolution. On cycling, the anodic currents slightly increased, and the passive range became somewhat narrower, particularly on SLM alloy. Two anodic peaks were clearly present in the 5th cycle: a smaller one at about -0.68 V_{SCE} (on the SLM alloy) and -0.5 V_{SCE} (on the WRO alloy) and another one at about -0.07 V_{SCE} on both alloys. They were ascribed to the formation of Mo oxides, likely MoO_2 and molybdates (and perhaps phosphomolybdates [23], in agreement with Figure 5.6b [18]. A single cathodic peak was detected in the potential range -1.2 to -1.0 V_{SCE}, which pointed to a highly irreversible nature of the surface oxide film. Figure 5.7c shows that even with H_2O_2 addition the SLM and WRO alloys exhibited a quite similar electrochemical behaviour. The peroxide scarcely affected the cyclic voltammograms which resulted quite close to those collected in Figure 5.7b. Overall, the alloys kept quite low anodic currents, with two clearly distinguished anodic peaks, likely connected to Mo oxidation at two different oxidation states. In all voltammograms, after the anodic peak at about 0 V_{SCE} a reduction of the anodic current was observed that increased only at potentials higher than 0.6 V_{SCE}. In this potential range for pure alloying elements a strong oxidation of molybdenum and cobalt was observed while in the alloys these processes are strongly reduced, suggesting that the chromium oxide film strengthens the protective capacity of the individual oxides, increasing their stability.

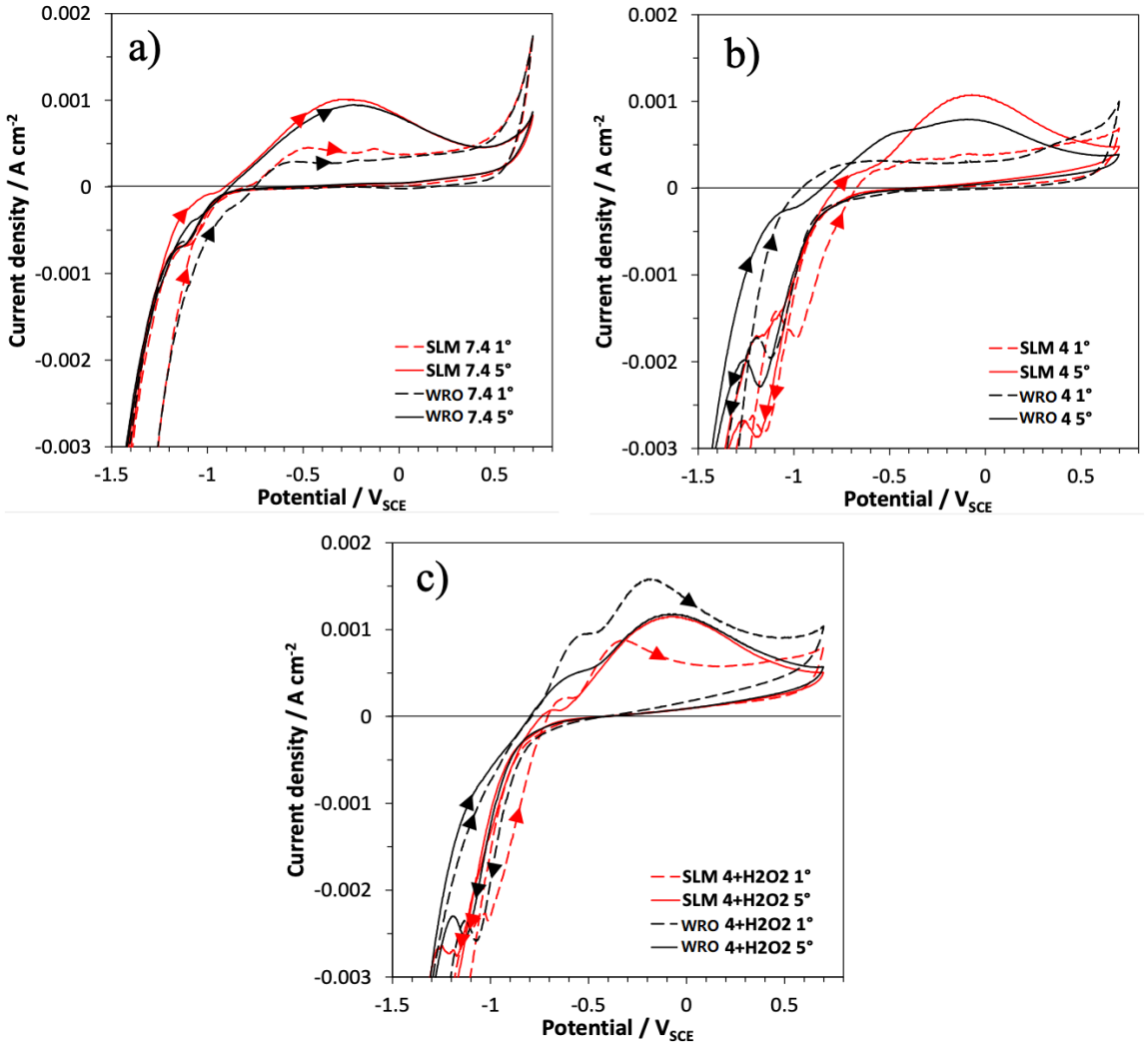

Figure 5. 7. Voltammetry cycles recorded on SLM and WRO CoCrMo alloys in PBS a) at pH 7.4 b) at pH 4, c) at pH 4 with addition of 30 mM H2O2. Dashed line = 1st cycle. Continuous line = 5th cycle

5.4. Conclusions:

- In PBS at neutral pH, Co, undergoes spontaneous passivation because formation of cobalt hydroxide film, which, however, shows a limited protection if aggressive ions such as chlorides are present. The presence of phosphate ions may reinforce the passive film. At pH = 4 the formation of protective film is not allowed, and Co is oxidized to Co^{2+} at potential higher than those of thermodynamic equilibrium.

  No passive region was observed in the presence of H_2O_2, however the lower anode currents than those measured in the absence of hydrogen peroxide suggested the formation of an adsorption oxide layer.

- Chromium is the alloying element that mainly contributes to the high corrosion resistance of the CoCrMo alloy. In the tested environments Cr is spontaneously passive and the formation of a highly protective Cr_2O_3 film produced a large passivity region even in the presence of chlorides. In none of the tested environments is Cr subject to localized corrosion. In the presence of H_2O_2, the probable formation of CrOOH as well as Cr_2O_3 reduces the protection of the passive film.
- In PBS at pH=7.4 and pH=4 Mo showed a wide passive potential range with slightly increasing current on cycling. The passivity of molybdenum was ascribed to the formation of MoO_2. Transpassivity was observed at potentials nobler than -0.1 and 0 V_{SCE} at pH= 7.4 and pH=4 respectively, connected the formation of molybdate and/or heptamolybdate ion. The presence of H_2O_2 induced the formation of a defective oxide film, and a reduction of a passive range.
- The SLM and the WRO alloys showed similar behaviour at pH=7.4 and pH=4 suggesting comparable barrier properties of the passive film, mainly ascribed to the protective capability of Cr_2O_3, reinforced by the presence of MoO_2.

  The H_2O_2 addition scarcely affected the electrochemical behaviour of both SLM and wrought alloys that exhibited a quite similar electrochemical behaviour.

References

[1] L.D. Burke, M.M. Murphy, The electrocatalytic behavior of cobalt (and iron) electrodes at low potential in base, J. Electrochem. Soc. 138 (1991) 88.

[2] W.A. Badawy, F.M. Al-Kharafi, J.R. Al-Ajmi, Electrochemical behaviour of cobalt in aqueous solutions of different pH, J. Appl. Electrochem. 30 (2000) 693–704.

[3] M. Metikoš-Huković, R. Babić, Passivation and corrosion behaviours of cobalt and cobalt-chromium-molybdenum alloy, Corros. Sci. 49 (2007) 3570–3579.

[4] A. Kocijan, I. Milošev, D.K. Merl, B. Pihlar, Electrochemical study of Co-based alloys in simulated physiological solution, J. Appl. Electrochem. 34 (2004) 517–524.

[5] M. Metikoš-Huković, J. Katić, Z. Grubač, I. Škugor Rončević, Electrochemistry of CoCrMo Implant in Hanks' Solution and Mott-Schottky Probe of Alloy's Passive Films, CORROSION. 73 (2017) 1401–1412. https://doi.org/10.5006/2522.

[6] D. Sazou, M. Pagitsas, Polarization behaviour of a cobalt rotating disc electrode in sulphuric acid solutions in the absence and presence of chloride ions, J. Electroanal. Chem. Interfacial Electrochem. 304 (1991) 171–185.

[7] K.M. Ismail, W.A. Badawy, Electrochemical and XPS investigations of cobalt in KOH solutions, J. Appl. Electrochem. 30 (2000) 1303–1311.

[8] W. Sheng, Z. Zhuang, M. Gao, J. Zheng, J.G. Chen, Y. Yan, Correlating hydrogen oxidation and evolution activity on platinum at different pH with measured hydrogen binding energy, Nat. Commun. 6 (2015) 1–6.

[9] P.N. Ross Jr, Oxygen reduction reaction on smooth single crystal electrodes, Handb. Fuel Cells. (2010).

[10] A.K. Singh, V. Chaudhary, A. Sharma, Electrochemical studies of stainless steel corrosion in peroxide solutions, Port. Electrochim. Acta. 30 (2012) 99–109.

[11] Y. Liu, J.L. Gilbert, Effect of simulated inflammatory conditions and potential on dissolution and surface oxide of CoCrMo alloy: In situ electrochemical atomic force microscopy study, Electrochim. Acta. 262 (2018) 252–263.

[12] Y. Liu, J.L. Gilbert, The effect of simulated inflammatory conditions and Fenton chemistry on the electrochemistry of CoCrMo alloy, J. Biomed. Mater. Res. Part B Appl. Biomater. 106 (2018) 209–220.

[13] Y. Liu, J.L. Gilbert, The effect of simulated inflammatory conditions and Fenton chemistry on the electrochemistry of CoCrMo alloy, (2017) 209–220.

[14] I. Milošev, CoCrMo Alloy for Biomedical Applications, 2012.

[15] W. Xu, F. Yu, L. Yang, B. Zhang, B. Hou, Y. Li, Accelerated corrosion of 316L

stainless steel in simulated body fluids in the presence of H2O2 and albumin, Mater. Sci. Eng. C. 92 (2018) 11–19.

[16] M. Metikoš-Huković, Z. Pilić, R. Babić, D. Omanović, Influence of alloying elements on the corrosion stability of CoCrMo implant alloy in Hank's solution, Acta Biomater. 2 (2006) 693–700.

[17] N. Ebrahimi, M.C. Biesinger, D.W. Shoesmith, J.J. Noël, The influence of chromium and molybdenum on the repassivation of nickel-chromium-molybdenum alloys in saline solutions, Surf. Interface Anal. 49 (2017) 1359–1365.

[18] K. Wang, Y.-S. Li, P. He, In situ identification of surface species on molybdenum in different media, Electrochim. Acta. 43 (1998) 2459–2467.

[19] M. Ürgen, U. Stolz, R. Kirchheim, ESCA measurements of films on molybdenum formed in the passive and transpassive region, Corros. Sci. 30 (1990) 377–391. https://doi.org/https://doi.org/10.1016/0010-938X(90)90045-7.

[20] M.N. Hull, On the anodic dissolution of molybdenum in acidic and alkaline electrolytes, J. Electroanal. Chem. Interfacial Electrochem. 38 (1972) 143–157.

[21] Y.C. Lu, C.R. Clayton, An XPS study of the passive and transpassive behavior of molybdenum in deaerated 0.1 M HCl, Corros. Sci. 29 (1989) 927–937.

[22] J.W. Johnson, C.H. Chi, C.K. Chen, W.J. James, The anodic dissolution of molybdenum, Corrosion. 26 (1970) 338–342.

[23] E.A. Nagul, I.D. McKelvie, P. Worsfold, S.D. Kolev, The molybdenum blue reaction for the determination of orthophosphate revisited: opening the black box, Anal. Chim. Acta. 890 (2015) 60–82.

CHAPTER SIX

Towards understanding the corrosion and electrochemical behavior of selective laser melted CoCrMo alloys in simulated body fluids: Polarization Curves (PC) and Electrochemical Impedance Spectroscopy (EIS).

6.1. Introduction

This part of the thesis aims at studying the electrochemical and corrosion behavior of B1 and B2 SLM and WRO CoCrMo alloys in simulated physiological solutions (PBS solutions) on the basis of cyclic polarization curves and electrochemical impedance spectroscopy (EIS) tests performed during 15 days of immersion in artificial body fluids, simulating both the absence and the presence of inflammatory conditions.

6.2. Results and discussion

6.2.1 Polarization curves

The polarization curves (PC) recorded on SLM and WRO CoCrMo alloys after 1h and 15 days in PBS solutions are collected in Figure 6.1 (see sect. 3.5.1 for PC test description). The electrochemical parameters derived from the curves, including the corrosion potential (E_{corr}), the corrosion current density (i_{corr}) and the anodic and cathodic Tafel slopes are shown in Table 6.1.

In all environments and at both immersion times, CoCrMo alloys are passive at E_{corr}, with i_{corr} values always well below 1 μA cm^{-2}. The sudden increase in anodic current densities at the end of the passive region can be attributed to transpassive dissolution and water oxidation, while pitting must be excluded at pH 7.4 and 4, due to the absence of hysteresis loops in the backward curves in these solutions [1,2]. Instead, at pH 4 in the presence of H_2O_2, the anodic currents in the backward curve are definitely higher than those in the forward scan. Therefore, a not negligible hysteresis loop was detected in this solution on all alloys. Since at the end of the polarization tests pitting was not observed on the specimen surface in either of the three environments, pitting is not the cause of the hysteresis loop appearance. It is possible that in the transpassive potential range the passive film suffers a more significant surface damage in the presence of H_2O_2 than in the absence, so making the film less resistant to oxidation during the backward scan, at the same anodic potentials. This would justify the onset of the hysteresis loop in the solution simulating severe inflammation conditions.
In all alloy/environment combinations, the stability of passive films was found to improve with time, so that after 15 days of immersion lower i_{corr} values and E_{corr} ennoblements were detected on all alloy types. In particular, the polarization curves recorded at pH 7.4 show that B1 and B2 shows initial E_{corr} values around -0.320 to -0.350 V, while WRO exhibits more active values (-0.418 V). At increasing immersion times, much nobler E_{corr} values were

obtained, with final values of -0.133 V and -0.063 V for B1 and B2, respectively, and -0.061 for WRO. As suggested by the more active initial E_{corr} value, on WRO the highest initial i_{corr} value was measured (0.209 μA cm^{-2} after 1h immersion), while i_{corr} in the range 0.011 to 0.023 μA cm^{-2} were obtained for all alloys at long immersion times.

At pH 4, nobler E_{corr} values driven by the lower pH were measured: B1 and B2 show initial E_{corr} values around -0.250 to -0.300 V_{SCE}, while WRO shows a E_{corr} value of -0.378 V_{SCE}. During the 15 day immersion, the E_{corr} ennoblement was about 200 - 300 mV for all alloys with SLM alloys reaching the noblest final E_{corr} values. The i_{corr} values were again in accordance, with i_{corr} values decreasing from 0.06 - 0.07 to 0.013 μA cm^{-2} for SLM alloys and from 0.177 μA cm^{-2} to 0.068 μA cm^{-2} for WRO, at the end of the immersion period.

The PBS solution at pH 4 containing H_2O_2 induced much nobler E_{corr} values in comparison to the other solutions, due to the oxidizing nature of the peroxide. After 1 h, values in the range +0.2 V_{SCE} to + 0.26 V_{SCE} were obtained, which ennobled less with time than in other solutions (+ 0.010 V_{SCE} for B1, + 0.180 V_{SCE} for B2 and + 0.008 V_{SCE} for WRO). This environment was more aggressive than the other ones and i_{corr} of 0.09 - 0.28 μA cm^{-2} were measured after 1h which decreased to 0.046 - 0.075 μA cm^{-2} after 15 days of immersion.

The comparison between the different CoCrMo alloys evidence only small differences, but in general B2 appears to be the most corrosion resistant alloy, particularly in PBS+H_2O_2 at pH 4, while WRO the least one. These results are consistent with those of other studies and suggest that the structure refinement ensured by SLM (more pronounced in SLM B2) reduces the alloy inhomogeneities and improves the alloy corrosion resistance [3–6].

Table 6. 1. The polarization parameters extracted from the polarization curves.

CoCrMo sample	Solution	Time	i_{corr} ($\mu A/cm^2$)	E_{corr} (V/SCE)	B_a (V)	B_c (V)
SLM B1	PBS pH= 7.4	1h	0.090	-0.321	0.179	0.199
SLM B1		15d	0.023	-0.133	0.122	0.160
SLM B2		1h	0.170	-0.349	0.231	0.270
SLM B2		15d	0.011	-0.063	0.164	0.212
WRO		1h	0.209	-0.418	0.222	0.234
WRO		15d	0.015	-0.061	0.300	0.296
SLM B1	PBS pH=4	1h	0.071	-0.242	0.116	0.145
SLM B1		15d	0.013	-0.093	0.226	0.162
SLM B2		1h	0.057	-0.299	0.093	0.116
SLM B2		15d	0.013	-0.011	0.224	0.328
WRO		1h	0.177	-0.378	0.269	0.306
WRO		15d	0.068	-0.175	0.599	0.458
SLM B1	PBS pH=4 +H_2O_2	1h	0.278	0.206	0.296	0.291
SLM B1		15d	0.074	0.216	0.318	0.168
SLM B2		1h	0.087	0.264	0.161	0.207
SLM B2		15d	0.046	0.382	0.191	0.375
WRO		1h	0.101	0.252	0.152	0.326
WRO		15d	0.075	0.260	0.172	0.660

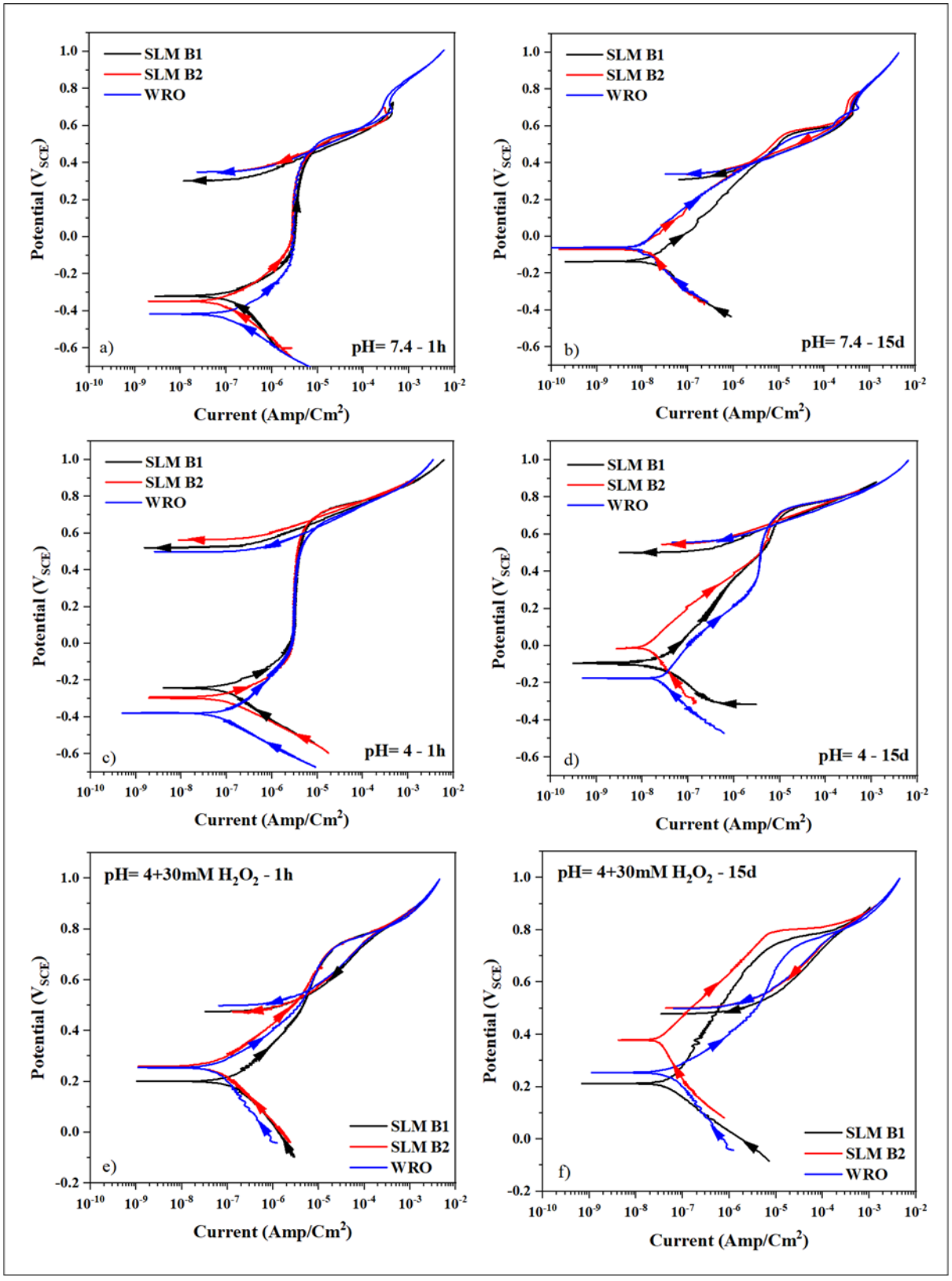

Figure 6.1. The polarization curves of SLM and WRO CoCrMo alloys recorded after 1 hour and 15 days of exposure to 3 different PBS solution.

6.2.2. Electrochemical impedance spectroscopy (EIS)

The Nyquist diagrams and Bode plots of WRO and SLM fabricated CoCrMo alloys after 1 h and 15 days of immersion in the different PBS solutions are collected in Figures 6.2 and 6.3, respectively (see sect. 3.5.2 for description of EIS measurments). The Nyquist diagrams well evidence the low-frequency behavior of the alloys, characterized by one semicircle, with dimension clearly increasing at longer immersion times. This observation agrees with the trends of the i_{corr} values as obtained from the 1h and 15 day polarization curves. The Bode plots in Figures 6.2 b, d, f and 6.3 b, d, f permit to investigate the EIS spectra in the whole frequency range. They show that at very high frequencies, ranging from 10^5 to 10^3 Hz, the absolute impedance values have a resistive character and are approximately independent of the frequency, representing the electrolyte resistance. Moreover, beside the 1 time constant evidenced by the Nyquist plots, a further high-frequency one can be detected at frequencies within 1 – 10^3 Hz, which is better resolved at long immersion times (figure 6.3 b, d, f) and in the most aggressive H_2O_2-containing environment (figure 6.2 f and 6.3 f). The high-frequency time constant is likely connected to the dielectric characteristics of the surface passive film, while the low-frequency one could connected to the charge transfer process at the metal/electrolyte interface at the bottom of the passive film pores [7,8].

Figure 6.4 collects the time dependence of E_{corr} and R_p for SLM and WRO alloys in the three investigated environments. E_{corr} ennoblements are detected during the two first days, then rather stable values are achieved until 15 days of immersion. In spite of some data scattering, similar trends are observed for R_p values, suggesting that stationary final passive conditions are always achieved. In particular, at pH 7.4 and 4 E_{corr} values ennoble from about -0.3 to -0.4 V_{SCE} to -0.1 to 0.1 V_{SCE}, while R_p values increase by one order of magnitude or more, so reaching final values of about 10 MΩ cm^2 in all alloy/environment systems, with the exception of B1 at pH 4, reaching about 0.4 MΩ cm^2.

A definite degradation of the corrosion resistance properties is detected in the presence of H_2O_2. Much nobler E_{corr} values were obtained in this environment, due to the oxidizing power of H_2O_2. During the first day of immersion, E_{corr} quickly ennobled to +0.170 V_{SCE} (for B1) and to +0.39 V_{SCE} (for B2 and WRO), then final E_{corr} of +0.21 V_{SCE} (for B1) and +0.37 V_{SCE} (for B2 and WRO) were obtained. Differences in E_{corr} values between figure 6.4 (open circuit potentials) and figure 6.1 (zero current potentials in the polarization curves) are due to the polarization curve recording method, involving registration of the cathodic and anodic polarization curves starting from -0.2 V versus the open circuit potential up to potentials

above the transpassive region. The R_p values obtained in this environment are well below those obtained in the other environments, as shown as an example by final values of 1.4 MΩ cm^2 for B1, 2.6 MΩ cm^2 for WRO and 6.5 MΩ cm^2 for B2. This suggests that in the presence of metal or metal ions H_2O_2 participated in the formation of aggressive species, such as hydroxyl radicals, thus promoting oxidation and surface film deterioration [9].

Figure 6.4 also shows that among the three different alloys, SLM B1 exhibited the worst performances in all environments, likely due to the significant Mo segregation al the cell boundaries and Mo depletion in the cell cores (sect. 4.3.2). Better corrosion performances are provided by SLM B2 and WRO alloys, the former due to a marked microstructure refinement allowed by SLM parameters that make the alloy more homogeneous, the latter characterized by a fine-grained microstructure with no clear evidence of carbide precipitation. The excellent corrosion performances of B2 appear in contrast with the alloy more porous structure. However, as shown by cyclic polarization curves, no pitting occurs on this alloy and therefore it is reasonable that no occluded cell conditions develop in the pores, so excluding these pores can induce a significant stimulation of the overall corrosion rates.

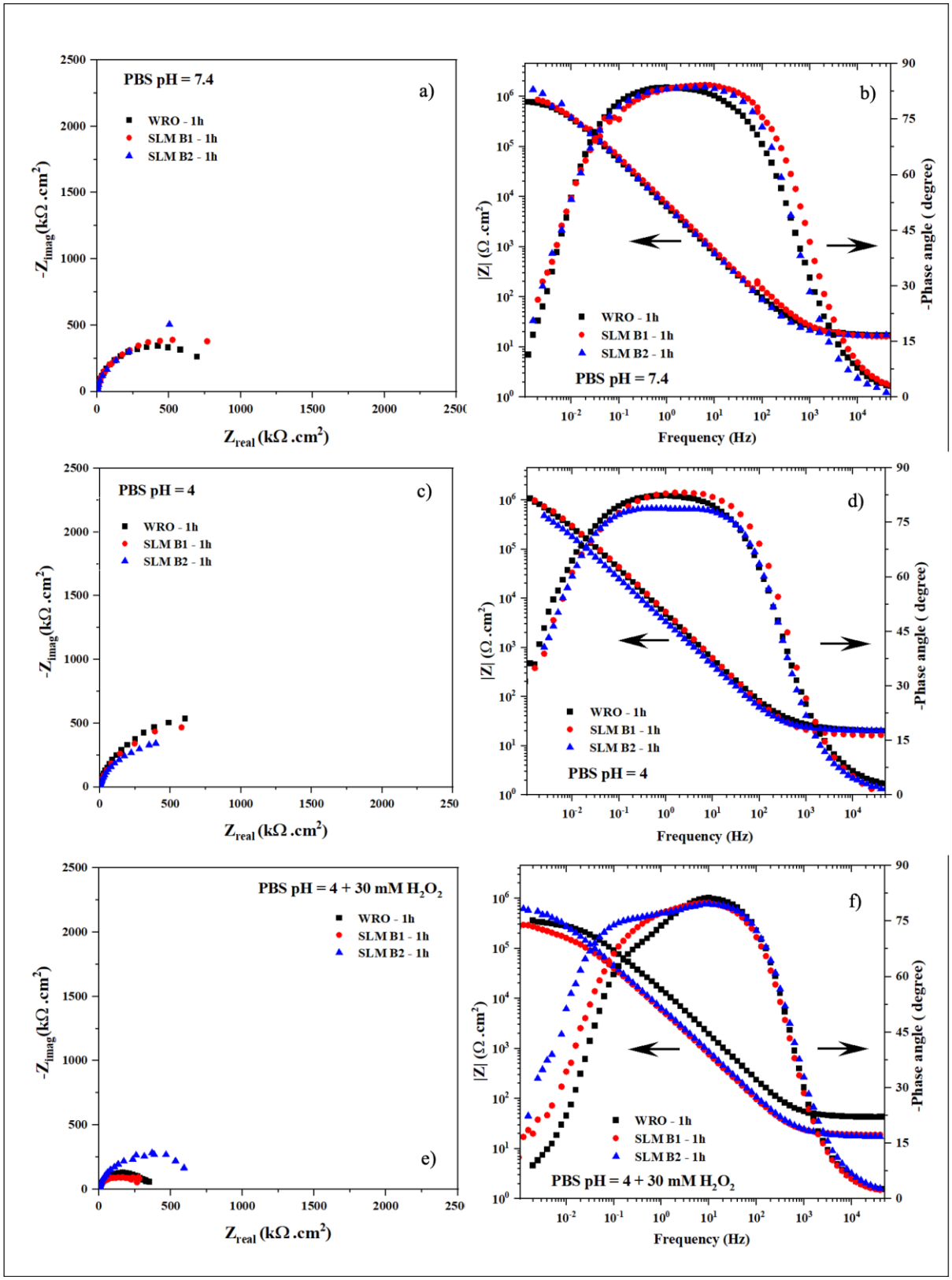

Figure 6.2. Nyquist (a, c, e) and Bode (b, d, f) plots of EIS spectra collected on CoCrMo alloys after 1 hour of immersion in PBS pH=7.4 (a, b), PBS pH=4 (c, d) and PBS pH=4+30 mM H_2O_2 (e, f) at 37 °C.

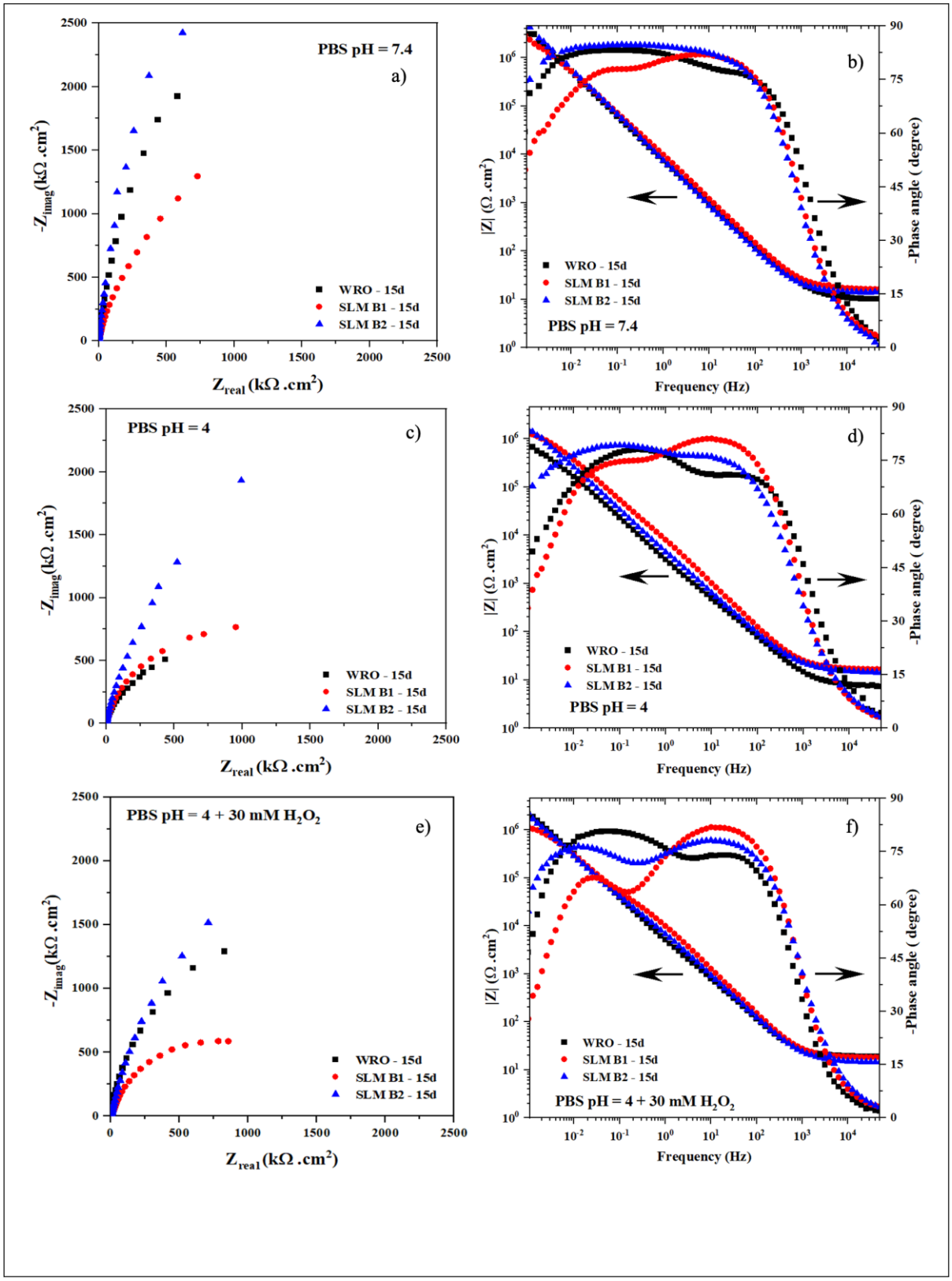

Figure 6.3. Nyquist (a, c, e) and Bode (b, d, f) plots of EIS spectra collected on CoCrMo alloys after 15 days of immersion in PBS pH=7.4 (a, b), PBS pH=4 (c, d) and PBS pH=4+30 mM H_2O_2 (e, f) at 37 °C.

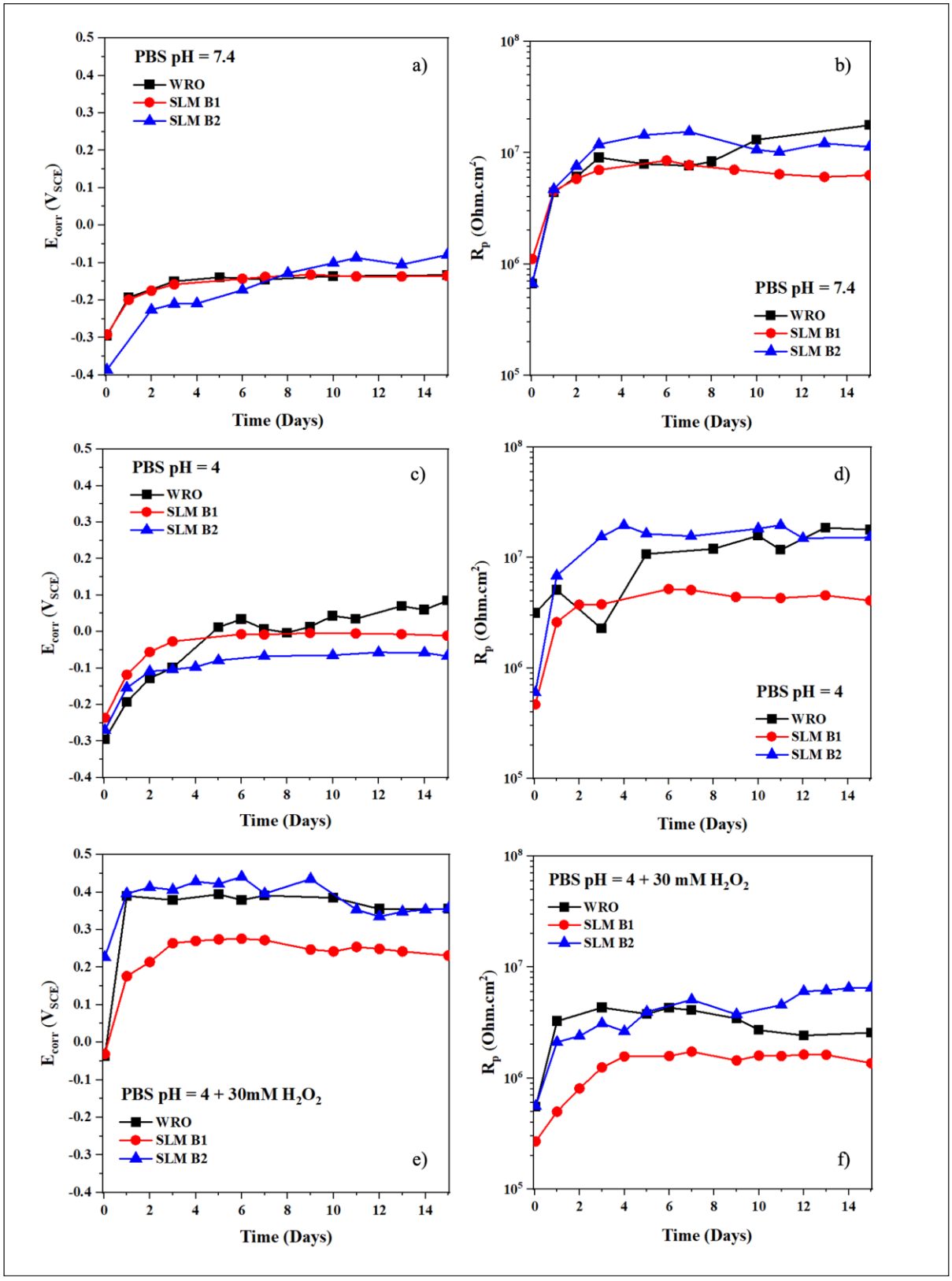

Figure 6.4. E_{cor}/time (a, c, e) and R_p/time (b, d, f) trends for CoCrMo alloys in PBS pH=7.4 (a, b), PBS pH=4 (c, d) and PBS pH=4+30 mM H_2O_2 (e, f), at 37 °C.

6.3. Conclusions

The electrochemical behaviour of the SLM and WRO CoCrMo biomedical alloys was studied in the investigated PBS environments by recording the polarization curves at 1h and 15 days of immersion and by monitoring the alloy corrosion behaviour during the 15-day immersion period by Electrochemical Impedance Spectroscopy. From the obtained results, the following conclusions can be drawn:

- Samples obtained with SLM techniques show low corrosion rates in the tested environments, which result comparable to those measured on WRO alloy in the case of B2 and slightly worse for B1.
- The SLM process parameters affect the corrosion behaviour of SLM alloys: in all tested conditions alloy B2 with its homogeneous fine microstructure exhibits lower corrosion rates than sample B1, characterized by a coarser microstructure and likely more important micro-segregation phenomena. The porosity present in B2 does not affect the alloy corrosion resistance.
- The lower corrosion resistance in the presence of simulated inflammation conditions is likely connected to the strong oxidative properties exhibited by H_2O_2 in the presence of metals or metal ions which are reported to contribute to the formation of aggressive species, such as hydroxyl radicals.

References

[1] E. Bettini, T. Eriksson, M. Boström, C. Leygraf, J. Pan, Influence of metal carbides on dissolution behavior of biomedical CoCrMo alloy: SEM, TEM and AFM studies, Electrochim. Acta. 56 (2011) 9413–9419.

[2] A.W.E. Hodgson, S. Kurz, S. Virtanen, V. Fervel, C.-O.A. Olsson, S. Mischler, Passive and transpassive behaviour of CoCrMo in simulated biological solutions, Electrochim. Acta. 49 (2004) 2167–2178.

[3] D. Sun, J.A. Wharton, R.J.K. Wood, L. Ma, W.M. Rainforth, Microabrasion–corrosion of cast CoCrMo alloy in simulated body fluids, Tribol. Int. 42 (2009) 99–110.

[4] Y. Lu, S. Wu, Y. Gan, J. Li, C. Zhao, D. Zhuo, J. Lin, Investigation on the microstructure, mechanical property and corrosion behavior of the selective laser melted CoCrW alloy for dental application, Mater. Sci. Eng. C. 49 (2015) 517–525.

[5] Y.S. Hedberg, B. Qian, Z. Shen, S. Virtanen, I. Odnevall Wallinder, In vitro biocompatibility of CoCrMo dental alloys fabricated by selective laser melting, Dent. Mater. 30 (2014) 525–534.

[6] C. Valero Vidal, A. Igual Muñoz, Electrochemical characterisation of biomedical alloys for surgical implants in simulated body fluids, Corros. Sci. 50 (2008) 1954–1961.

[7] L. Yang, Q. Zhu, X. Xie, X. Cao, Y. Wu, S. Chen, J. Qu, Electrochemical behavior of CoCrMo alloy for dental applications in acidic artificial saliva containing albumin, Colloids Surfaces B Biointerfaces. 184 (2019) 110492.

[8] J.A. Moreto, A.C. Rodrigues, R.R. da S. Leite, A. Rossi, L.A. da Silva, V.A. Alves, Effect of Temperature, Electrolyte Composition and Immersion Time on the Electrochemical Corrosion Behavior of CoCrMo Implant Alloy Exposed to Physiological Serum and Hank's Solution, Mater. Res. 21 (2018).

[9] Y. Liu, J.L. Gilbert, The effect of simulated inflammatory conditions and Fenton chemistry on the electrochemistry of CoCrMo alloy, (2017) 209–220.


7

CHAPTER SEVEN

Exploring the mechanical and chemical-mechanical behavior of SLM CoCrMo alloys by means of microhardness, tensile and Slow Strain Rate tests.

7.1. Introduction

The mechanical behavior of SLM CoCrMo alloys was investigated by microhardness and tensile tests and the susceptibility to stress corrosion cracking (SCC) was assessed by performing slow strain rate tests (SSRT). Scanning electron microscope observations were carried out to study the fracture surface after tensile and SSRT measurements.

7.2. Results and discussion

7.2.1. Microhardness (HV)

In order to measure the indentation dimensions correctly, the micrographs obtained from a Leica optical microscope were analysed (see Fig. 7.1) and HV values were obtained from the equation 3.9 (sect. 3.4.4.) [1]. Microhardness sample specification and experimental details have been reported in section 3.4.4 and 3.6.1, respectively.

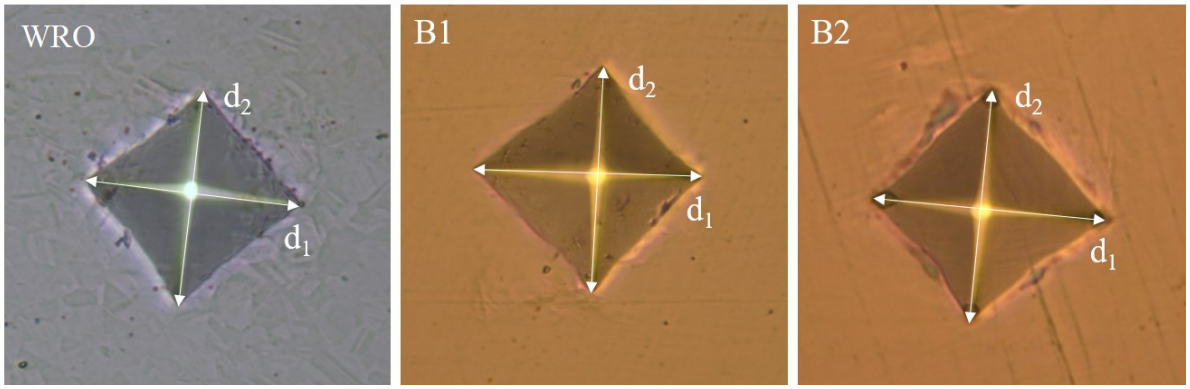

Figure 7.1. Optical microscopy images of the indentation for HV measurements, (A= d_1d_2).

Multiple microhardness measurements were done on B1, B2 and WRO samples and the obtained average results are collected in Figure 7.2. The confidence intervals of the Vickers hardness values were 418±4 for B1, 407±9 for B2 and 428±3 HV for WRO.

These results suggest that SLM B1 has a microhardness only slightly lower than that of the WRO alloy. Among the SLM alloys, B2 exhibited the lowest values, likely due to its lower relative density. The reason why B2 samples have more abundant porosity as compared to B1 is connected to the lower fluence adopted in the building process (53.6 and 138.8 J/mm^3, respectively) which results in the formation of more numerous solidification defects and incomplete powder densification. Similarly, the higher hardness of the wrought alloy is due to a relative density of about 100%.

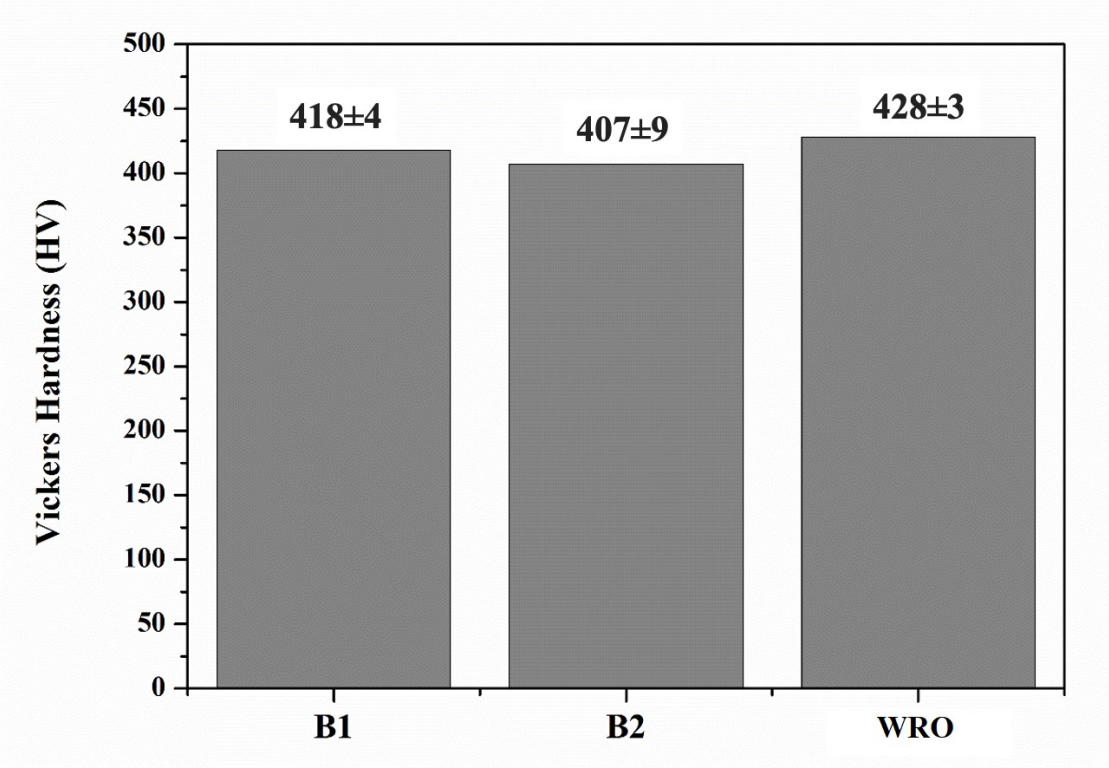

Figure 7.2. Mean hardness values of the studied samples (HV).

Figure 7.3 confirms the presence of pores in B2 samples, while B1 only exhibits tiny holes and small defects.

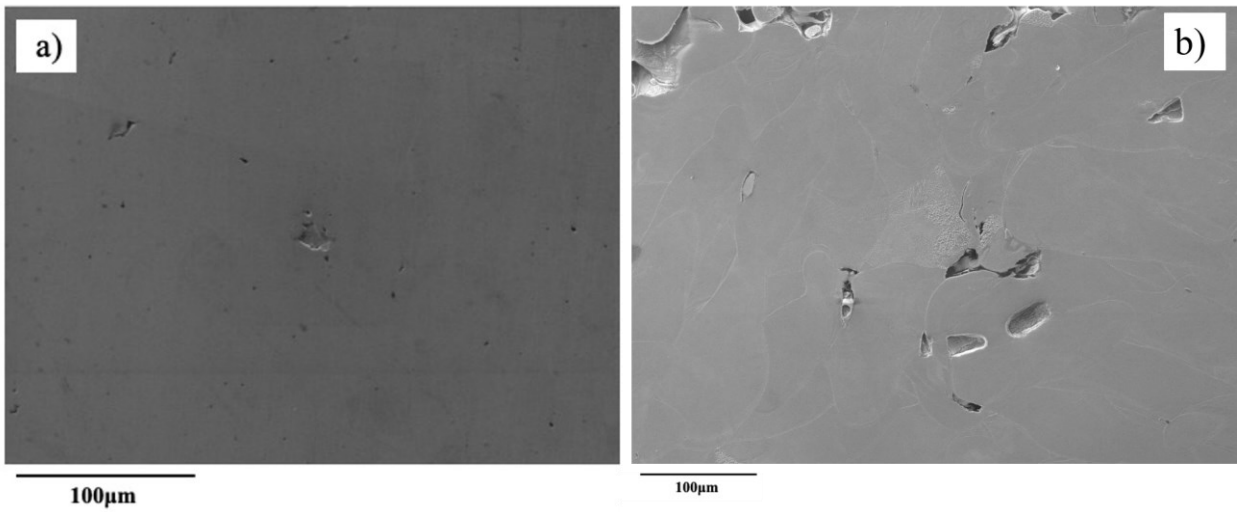

Figure 7.3. SEM micrographs of B1 and B2 samples, indicating their pores and defects.

The results are in relatively good agreement with the findings of other studies, in which two different laser strategies were used for the fabrication of SLM CoCrW alloy for dental application. The authors reported a slightly higher hardness value (570 ± 3.4HV) for the line-formed alloy (characterized by higher density values) as compared with the island-formed

alloy (564 ± 2.9HV). However, it must be stressed that in both cases the relative densities were higher than 99% [2]. Similarly, Henriques et al. [3] found that the hot-pressed biomedical CoCrMo samples demonstrated greater hardness than their cast counterparts. They argued that the higher hardness obtained from hot-pressed samples was due to their lower porosity.

7.2.2. Tensile tests

This test was used to assess the tensile properties of SLM B1, B2 and B1+B2 samples. Tensile sample specification and experimental details have been reported in section 3.4.2. and 3.6.2, respectively. Figure 7.4 shows a preliminary fractographic analysis performed on B1+B2 samples, evidencing the dense core with B1 characteristics and the more porous external B2 shell.

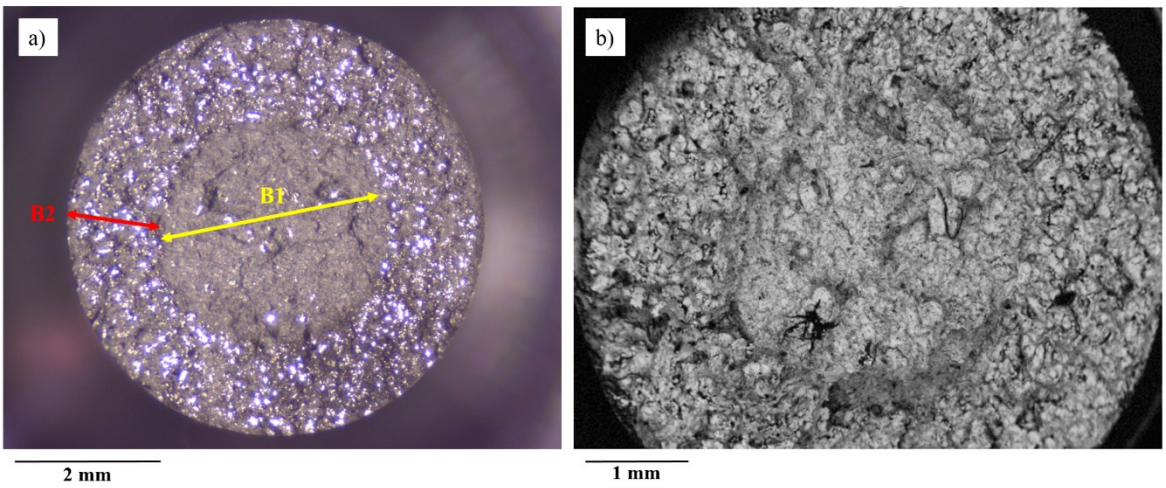

Figure 7.4. a) Optical microscope and b) SEM images of the fracture surface of the B1+B2 sample, showing the mixed fabrication methodology of B1 in the core and B2 in the shell of the built structure.

The typical nominal stress-strain curves are shown in Figure 7.5. After the elastic portions, yielding occurs followed by limited uniform plastic strains. Then, a sudden fracture occurs without any sign of macroscopic necking. There are similarities between such tensile deformation behavior in this study and those observed in the traditional CoCrMo and CoCrW [4,5].

The mechanical properties of the samples obtained from the stress-strain curves in Figure 7.5, namely the Young modulus, the yield strength (σ_y), the ultimate tensile strength (UTS) and the percent elongation, are listed in Table 7.1. The first parameter measures the alloy

stiffness, σ_y and UTS are related to the mechanical strength of the metallic alloys, while the last parameters quantify the alloy ductility.

Figure 7.5 and Table 7.1 evidence the definitely higher mechanical strength properties of B1, while B2 exhibits the worst behaviour. B1 and B2 also exhibits respectively the highest and lowest ductility values. One factor contributing to degrade the performances of B2 is certainly connected to its higher amount of pores and cracks, which may operate as stress concentration factors, so hindering ductility and producing lower UTS values. However, another factor may contribute to these differences. In fact, it has been reported that the formation of ε-phase leads to good wear resistance and strength in CoCr based alloys, but impairs the alloy ductility [6]. Yamanaka [7] maintains that the strain-induced martensite ε-phase intersected with the pre-existent martensite under the tensile test may determines stress concentration at the grain boundaries and/or interfaces of these phases. This stress accumulation seems the cause for premature fracture before the initiation of localized necking [8]. In chapter 4, Figure 4.1 we have evidenced that ε-phase is present in higher amounts in SLM B2, so likely favouring the alloy more brittle behaviour.

Figure 7.5 also shows that combining B1 (in the sample core) and B2 (in the sample surface) structures, as in B1+B2 samples, is a very promising strategy to take advantage of the good mechanical properties of B1 and the interesting corrosion resistance and osseointegration properties of B2. In fact, B1+B2 samples exhibit intermediate stiffness, mechanical strength, and ductility in comparison to B1 and B2. Therefore, this structure combination could represent a viable way to apply SLM for implant production.

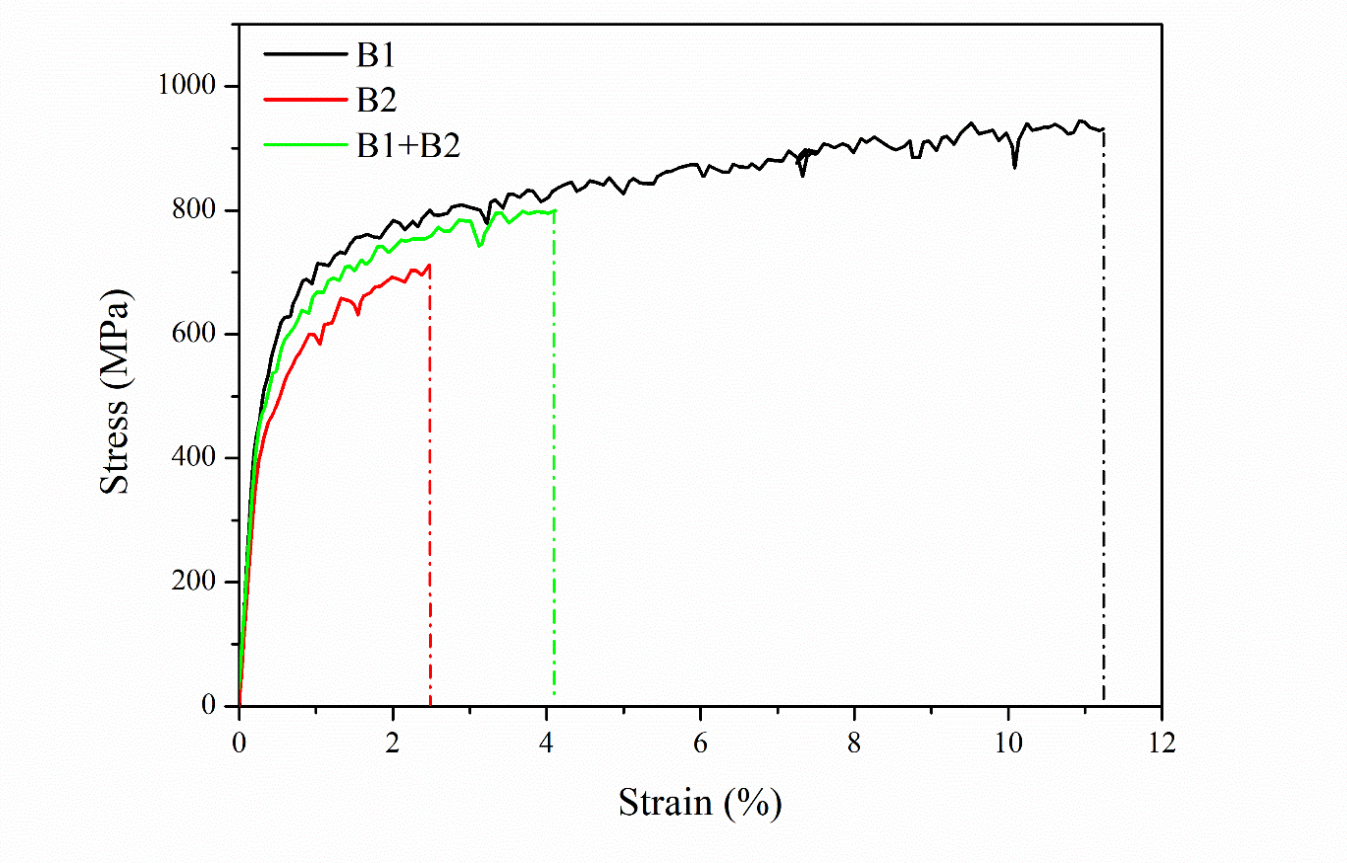

Figure 7.5. Typical stress-strain curves of the SLM fabricated alloys, B1, B2, and B1+B2, at room temperature.

Table 7. 1. The mechanical properties of the B1, B2, and B1+B2 SLM built alloys.

Sample	Young modulus (GPa)	Yield strength σ_y (MPa)	Ultimate tensile strength UTS (MPa)	Strain percentage to fracture ε_f (%)
B1	214	584	944	11.2
B2	168	481	712	2.47
B1+B2	184	533	800	4.11

The micrographs of the fracture surface of the selective laser melted alloys after the tensile test are shown in Figure 7.6.

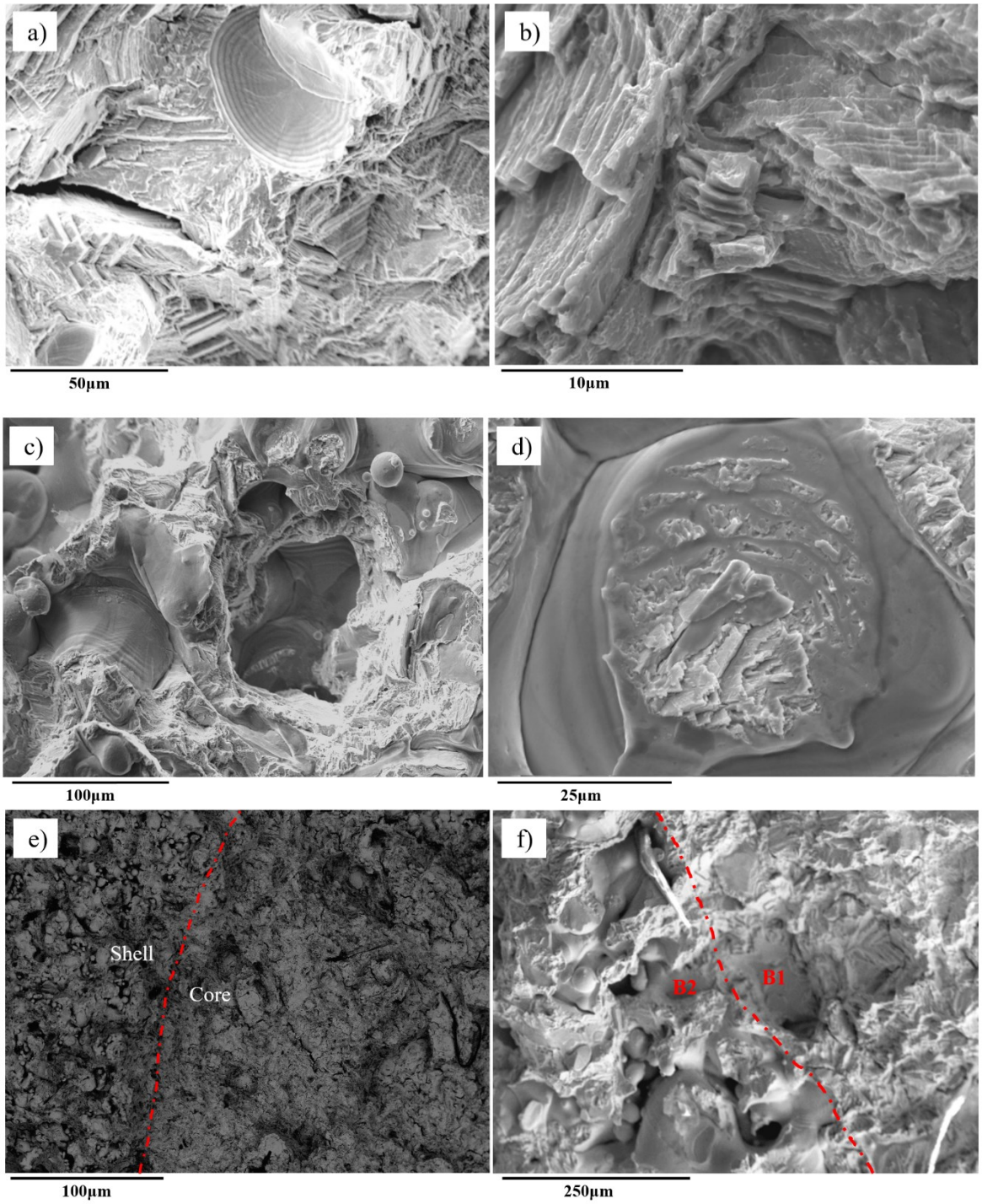

Figure 7.6. SEM micrographs of the fracture surface of the selective laser melted CoCrMo alloys obtained after the tensile test. a) fracture surface of B1 sample, b) the magnified fracture surface of B1, c) fracture surface of B2 specimen, d) the magnified fracture surface of B2, e) fracture surface of B1+B2 sample showing the border of core and shell, f) the magnified fracture surface of B1+B2 sample, indicating B1 and B2 border.

From the fracture surface images of the B1 sample at low magnification (Figure 7.6a), a brittle fracture mode was detected on a fraction of the surface, as suggested by the observed facet-like fracture pattern and the presence of wedge type cracks. There are similarities in the fracture surface observations in this study and those reported in previous reports [2,9,10]. At higher magnification in Figure 7.6b, both wedge-like cracks and dimple-like patterns (due to the fact that the fcc structure of this alloy (Figure 4.1) is not prone to the cleavage fracture mode [5,11]) were highlighted. The former features may be created by the cleavage fracture along the {111} planes, where the stacking faults developed, while the latter was induced by the cellular dendrites [5,12]. Therefore, the observed fracture on this alloy can be identified as a quasi-cleavage fracture, according to the suggestions of Yamanaka [8].

The fracture surface of B2 sample is shown in Figures 7.6c and d. Strong evidence of the presence of un-melted powder and brittle fracture was found. A possible explanation for the persistence of un-melted particle may be the low laser power and high laser scan speed adopted for SLM B2. During the tensile test, these un-melted particles act as susceptible points for the initiation and propagation of the cracks and also contribute to the reduction of B2 ductility, in comparison to B1, together with the higher porosity and more abundant ε-phase.

The fractographic analysis of B1+B2 after the tensile test (Figures 7.6 e and f) indicated the presence of mixed fracture features typical of the two alloys, such as the dimple-like patterns and quasi-cleavage fracture on B1 core, as well as presence of un-melted powders on B2 shell. Wedge like cracks were present on both regions. The most interesting finding was that there is no evidence of the initiation and propagation of the cracks on the junction of B1 and B2 (see Figures 7.7e and f). This finding further supports the idea of the fabrication of complex components using multi-components and/or various process parameters for the optimization of the final product. Indeed, the junction part of the sample in which the process parameters are changed during layer-by-layer fabrication does not weaken the specimen during loading condition. These findings confirm that these multi-structural components could represent a viable way to apply SLM for implant production.

The particular fracture mode of SLM alloys, characterized by the dimple-like patterns and quasi-cleavage fracture is probably a result of the local thermal regimes and induced internal stresses during the selective laser melting process.

7.2.3. Slow strain rate test (SSRT)

All SSRT curves collected in both air and in the aggressive environment are shown in Figure 7.7a. SSRT sample specification and experimental details have been reported in section 3.4.3. and 3.7.1, respectively. It is evident that the large scattering of the results in terms of ε_f% of the alloy in each environment largely prevents to draw conclusions about the alloy susceptibility to SCC. The absence of secondary cracks on the specimen surfaces after exposure to the aggressive solution would suggest the absence of SCC susceptibility of the alloys in this environment, but more tests are needed, in order to gain a clear view of the alloy corrosion behaviour.

The stress-strain curves generally confirmed that fracture always occurs without necking and the overall ductility of the alloys is low, particularly for B2. Quite interestingly, in both alloys a reduction in mechanical strength is generally observed in solution, in comparison to that in air. This was also observed by Gu et al. by applying in-situ tensile tests to brass samples under TEM observations [13]. They found that in aggressive solution a crack tip can emit dislocation under a stress or stress intensity below the critical value, which is necessary to emit the dislocation in the absence of the corrosion solution. That is to say that corrosion can make the dislocation sources operate under a lower stress than that necessary in the absence of the corrosion solution. The reason why corrosion can facilitate the dislocation emission and motion is not clear and needs further study. Perhaps, divacancies resulting from localized anodic dissolution can diffuse into edge dislocation (or mixed dislocation), resulting in dislocation climb and/or multiplication.

Figure 7.7 b shows the E_{corr}/time evolution of B1 and B2 during the SSRT in the acid PBS solution, containing H_2O_2. Fast E_{corr} reactivation events followed by fast ennobling indicate the onset of metastable pitting on the specimen surface, which however does not seem to propagate. Only on specimen B1_I, a more important depassivation event then followed by slow ennobling occurs, just before the final failure. In that case, the depassivation event likely contributed to the final failure propagation.

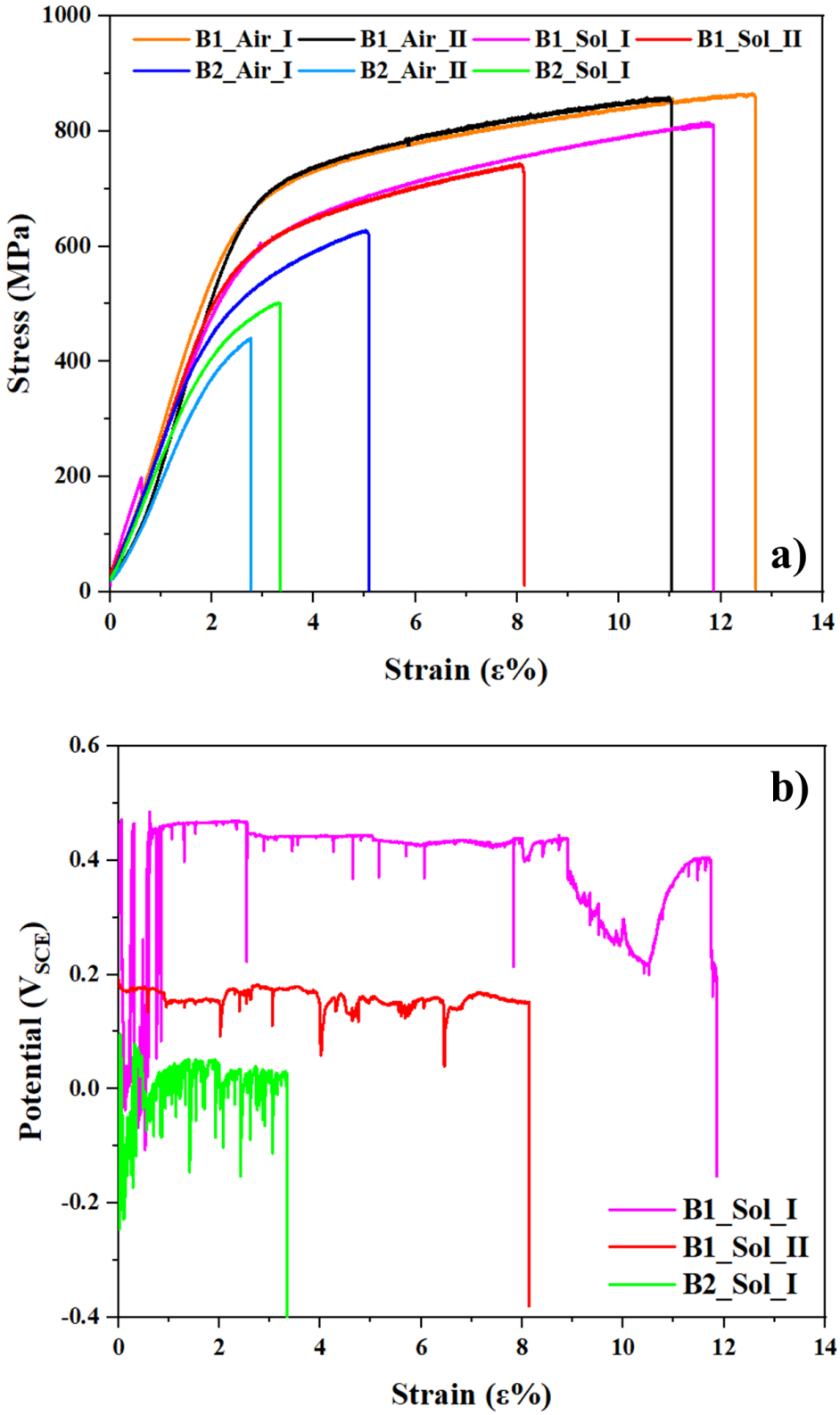

Figure 7.7. a) Stress-strain curves of SLM B1 and B2 obtained by SSRT in air (Air) and in PBS pH= 4+30mM H_2O_2 (Sol), T = 37°C; b) E_{corr} /time values monitored on SLM B1 and B2 during SSRT in PBS pH= 4+30mM H_2O_2 (Sol), T = 37°C.

Figure 7.7 b also evidences that the earlier the specimen failure, the less noble the specimen E_{corr}. This is likely the consequence of a more abundant casual distribution of the surface porosity which may stimulate metastable pitting. The high frequency of depassivation/healing events in the most porous B2 specimen seems to support this hypothesis. This unpredictable surface pore distribution could be responsible of the large scattering of the SSRT results.
Figure 7.8 shows the fractographic analysis of the tensile specimens after failure produced on B1 (Figure 7.8a and b) and B2 (Figure 7.8c and d), in air Figure 7.8a and c) and in solution (Figure 7.8b and d).

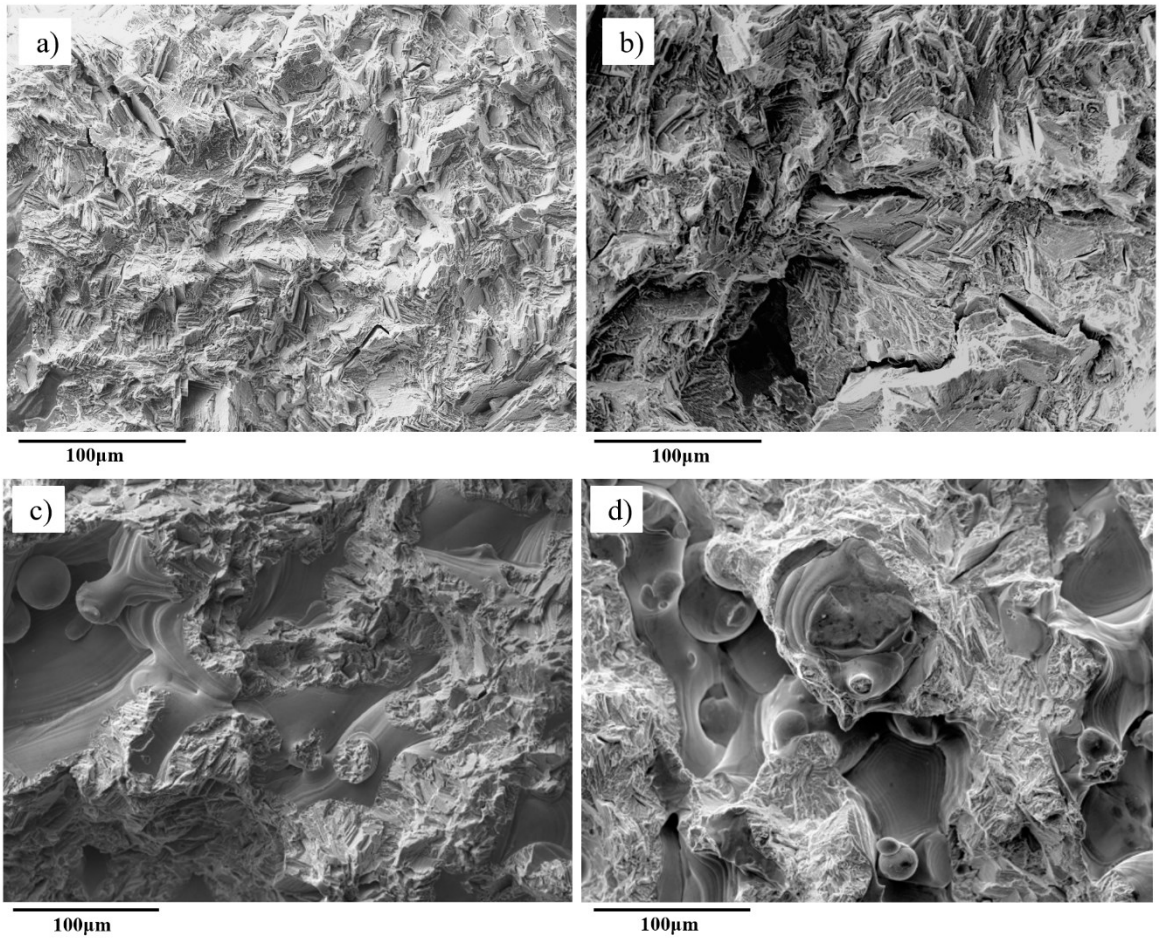

Figure 7.8. The fracture surface of SLM fabricated CoCrMo alloys after slow strain rate testing at 1×10^{-7}, a) B1 SLM in the air, b) B1 SLM in PBS pH= 4+30mMol H_2O_2 (37°C), c) B2 SLM in the air, d) B2 SLM in PBS pH= 4+30mMol H_2O_2 (37°C).

The fracture surface of B1 in both conditions shows a quasi-cleavage type fracture, faceted areas with different dimensions and wedge-type cracks (Figure 7.8 a and b). Furthermore, shear lips on the fracture surface indicated dimple-like patterns as well as parallel dimple belt features. Larger cracks form when the test is carried out in solution (Figure 7.8b). They may

be the result of the aggressiveness of the environment on crack initiation and propagation. At the same time, this figure reveals that mixed dimpled regions and facet-like features are the prone sites for propagation of the cracks. In terms of B2 (Figure 7.8 c and d), apart from quasi-cleavage fracture mode and dimple-like features, the fractography images again shows the presence of powders that are not fully melted on the fracture surface. As mentioned before, these un-melted particles weaken the sample under the loading conditions, resulting in crack initiation and propagation which cause the failure of the sample.

7.3. Conclusions:

The present study was designed to determine the effect of different process parameters of selective laser melting on the mechanical and chemical-mechanical behavior of the biomedical CoCrMo alloys. For this purpose, two CoCrMo alloys namely B1 and B2 were fabricated by the SLM process. Dense B1 was obtained when a lower laser scan speed of 900 mm/s and a higher laser power of 150 W were utilized, while the more porous B2 was built when the scan speed increased to 1200 mm/s and laser power decreased to 90 W. Multiple analysis based on hardness tests, tensile and slow strain rate testing as well as electron microscopy investigation were employed to study the mechanical and chemical-mechanical properties of the studied parts. The following conclusions can be drawn from the present study:

- B1 samples have a relative density of 99.8%, while B2 samples show a lower relative density of 95%.
- The microhardness tests demonstrate that the SLM process can build parts with hardness only slightly lower that of WRO CoCrMo alloy. B1 exhibits relatively higher hardness values than B2. This can be correlated to their different density: higher hardness was afforded by the denser B1 alloy.
- The tensile tests revealed that the stiffness, yield strength, UTS, and strain percentage to fracture of B1 sample are higher than those obtained for B2. The reasons can be connected to the lower fluence adopted during the B2 alloy preparation, which caused higher porosity, higher fraction of the brittle ε phase and significant amount of unmelted powders, entrapped in the consolidated alloy.
- Interesting materials properties are achieved by adopting a double process parameters set in the fabrication of B1+B2 tensile samples. They are characterized by a B1 structure in the bulk and a B2 structure on the surface. The results of the tensile tests

showed that B1+B2 mechanical properties are only slightly lower than those of B1. At the same time, the presence of B2 in the shell of the structure ensures better corrosion resistance (see chapter 6) and better matches with the surrounding porous bone. B2 is also expected to favour osseointegration. In the current study, B1+B2 sample represents the best trade-off between mechanical resistance, corrosion resistance and production time.

- In agreement with the results of the tensile tests, the slow strain rate test suggested that the B1 sample showed slightly better mechanical properties as well as higher ε_f % values, than B2. However, the large data scattering obtained with tests in air and in solution prevented a clear conclusion about the susceptibility of the two SLM alloys to SCC.
- From fractography analysis of SLM alloys after tensile and SSRT testing, in general, the failure type was recognized to be a quasi-cleavage fracture and dimple-like patterns as well as facet-like surface. Moreover, samples exhibited the presence of wedge-like cracks, while B2 samples showed un-melted particles which are sites prone to initiation and propagation of failure cracks.

References

[1] C.T. Duong, J.S. Nam, E.M. Seo, B.P. Patro, J.D. Chang, S. Park, S.S. Lee, Tribological property of the cobalt—chromium femoral head with different regions of wear in total hip arthroplasty, Proc. Inst. Mech. Eng. Part H J. Eng. Med. 224 (2010) 541–549.

[2] Y. Lu, S. Wu, Y. Gan, J. Li, C. Zhao, D. Zhuo, J. Lin, Investigation on the microstructure, mechanical property and corrosion behavior of the selective laser melted CoCrW alloy for dental application, Mater. Sci. Eng. C. 49 (2015) 517–525.

[3] B. Henriques, D. Soares, F.S. Silva, Microstructure, hardness, corrosion resistance and porcelain shear bond strength comparison between cast and hot pressed CoCrMo alloy for metal-ceramic dental restorations, J. Mech. Behav. Biomed. Mater. 12 (2012) 83—92. https://doi.org/10.1016/j.jmbbm.2012.03.015.

[4] K. Yoda, Suyalatu, A. Takaichi, N. Nomura, Y. Tsutsumi, H. Doi, S. Kurosu, A. Chiba, Y. Igarashi, T. Hanawa, Effects of chromium and nitrogen content on the microstructures and mechanical properties of as-cast Co-Cr-Mo alloys for dental applications, Acta Biomater. 8 (2012) 2856—2862. https://doi.org/10.1016/j.actbio.2012.03.024.

[5] K. Yamanaka, M. Mori, A. Chiba, Influence of carbon addition on mechanical properties and microstructures of Ni-free Co–Cr–W alloys subjected to thermomechanical processing, J. Mech. Behav. Biomed. Mater. 37 (2014) 274–285.

[6] K. Yamanaka, M. Mori, Y. Koizumi, A. Chiba, Local strain evolution due to athermal γ→ε martensitic transformation in biomedical CoCrMo alloys, J. Mech. Behav. Biomed. Mater. 32 (2014) 52—61. https://doi.org/10.1016/j.jmbbm.2013.12.019.

[7] K. Yamanaka, M. Mori, A. Chiba, Effects of carbon concentration on microstructure and mechanical properties of as-cast nickel-free Co-28Cr-9W-based dental alloys, Mater. Sci. & Eng. C, Mater. Biol. Appl. 40 (2014) 127—134. https://doi.org/10.1016/j.msec.2014.03.053.

[8] K. Yamanaka, M. Mori, A. Chiba, Mechanical properties of as-forged Ni-free Co–29Cr–6Mo alloys with ultrafine-grained microstructure, Mater. Sci. Eng. A. 528 (2011) 5961–5966.

[9] K. Yamanaka, M. Mori, A. Chiba, Effects of nitrogen addition on microstructure and mechanical behavior of biomedical Co–Cr–Mo alloys, J. Mech. Behav. Biomed. Mater. 29 (2014) 417–426. https://doi.org/https://doi.org/10.1016/j.jmbbm.2013.10.006.

[10] B. Qian, K. Saeidi, L. Kvetková, F. Lofaj, C. Xiao, Z. Shen, Defects-tolerant Co-Cr-Mo dental alloys prepared by selective laser melting, Dent. Mater. 31 (2015) 1435–1444.

[11] M. Jw, Z. Guo, K. CR, Y.-H. Kim, The limits of strength and toughness in steel, ISIJ Int. 41 (2001) 599–611.

[12] A. Takaichi, T. Nakamoto, N. Joko, N. Nomura, Y. Tsutsumi, S. Migita, H. Doi, S. Kurosu, A. Chiba, N. Wakabayashi, Microstructures and mechanical properties of Co–29Cr–6Mo alloy fabricated by selective laser melting process for dental applications, J. Mech. Behav. Biomed. Mater. 21 (2013) 67–76.

[13] B. Gu, J. Zhang, F. Wang, W. Chu, The in-situ TEM observation of corrosion facilitating dislocation emission, multiplication and motion for brass, Scr. Metall. Mater. 32 (1995) 637–640.

CHAPTER EIGHT

Effect of post processing heat treatment on the microstructure and corrosion behaviour of SLM CoCrMo alloys in simulated body fluid.

8.1. Introduction

For SLM Co28Cr6Mo alloy few research works were carried out on heat treatments of mainly focused on high-temperature (1150-1220 °C) solution treatment with and without a following aging treatment (750-900 °C) [1–4], and on long-time annealing (750-1150 °C) [5,6], to assess their effects on microstructure and mechanical properties (tensile and hardness). Studies on the effect of post-process heat treatment on corrosion behavior are currently very limited. A preliminary study conducted on the SLM Co28Cr6Mo alloy showed that the alloy subjected to a solution treatment at 1200 °C, followed by aging at 900 °C for 10 hours, was characterized by a better corrosion resistance than cast, as-built and simply solutionized samples [7].

8.2. Results and discussion

8.2.1. Microstructural characterization

The microstructure of the etched C1 and C2 samples (as-built) are shown in Figure 8.1a and 8.1b, respectively (see sample description in sect. 3.2.2). The SEM images show the typical cellular and/or columnar morphology of the as-built materials due to the non-equilibrium conditions achieved during the SLM process. The comparison of the microstructure of the as-built samples suggested a finer cellular morphology for C1 sample: this refinement could be attributed to the differences in cooling rates. The cooling rate is generally seen as a factor strongly related to the combination of the specific energy and the layer thickness: higher thickness and laser power induce lower cooling rates [8-10]. As higher layer thickness and laser power (and finally higher LED) were used during the fabrication of C2, lower cooling rate are expected for this sample. The cell size or dendrite space measured in C1 samples is approximately one-half of the C2 sample, in agreement with the Kurz and Fisher equation [11], that showed an inverse relationship between the cell size and the cooling rate and lower. Moreover, the SEM images revealed that when the grains have been crossed the melt pool/melt track boundaries, the size and the direction growth of the cells have changed. However, it seems that in some cells adjacent to the melt pool/melt track boundaries, the growth direction is continuous along the boundaries and the cells are growing with the same direction to the neighbour track. These results agree with the findings of other studies [9,12]. Figure 8.1c shows the EDS line profile performed along the cellular structure of as-built sample C1. It is noted that the same results were obtained for C2 sample by EDS analysis. The results showed that an enrichment of Mo, C, and in some extent of Cr and Si is present at

cell boundaries. Similar results were also reported in previous works [13–15]. It is believed that during rapid solidification and formation of CoCr phase, Mo was released into the solid-liquid interface, resulting in its deposition and enrichment along the cell boundaries [3].

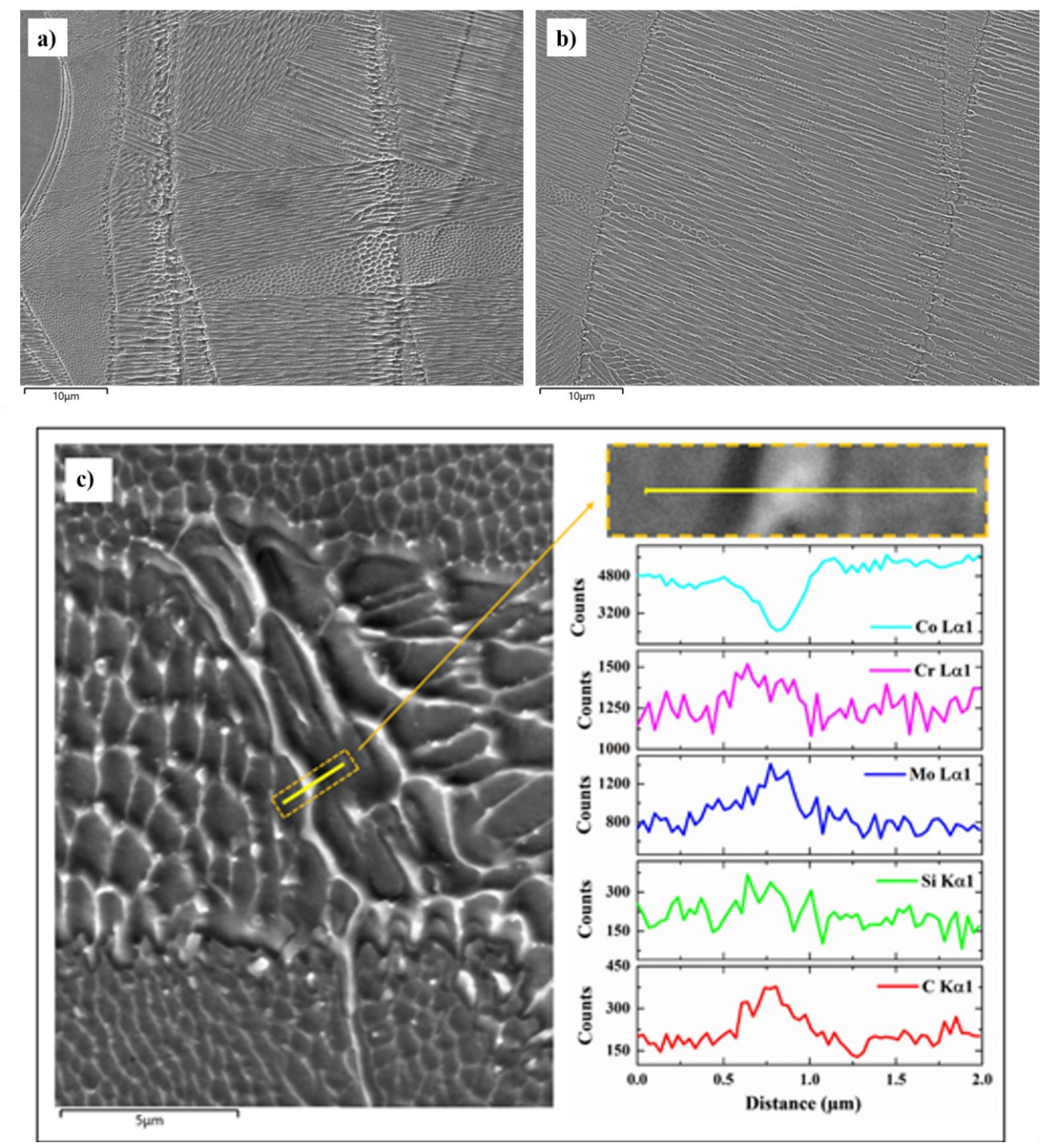

Figure 8.1. SEM/EDS analysis of the as-built SLM CoCrMo alloys after etching. a) C1 sample; b) C2 sample; c) semi-quantitative EDS line profile analysis on as-built C1 sample. Noted that the same EDS results were obtained for C2 as-built sample.

The microstructure of the heat-treated samples is shown in Figure 8.2. The heat treatment at 850°C completely modified the microstructure compared that observed in as-built specimens: the cellular and columnar structures disappeared, and fine globular particles are formed in the matrix, as illustrated in Figure 8.2 a, and b. These results match those observed in earlier studies in CoCrMo alloy after 980 °C annealing for 2 h [16] and Al-12Si alloy after isothermally annealed at 450 °C [17]. The SEM images also showed that the distribution of the precipitated particles is influenced by the growth direction of the cellular/columnar structure present before heat treatment. As schematically drawn in Figure 8.2c, the fine cellular structure seemed start to nucleate at cell boundaries where an enrichment of Mo, Si C and Cr was detected. During the heat treatment the precipitates grow maintaining a distribution that follows the initial orientation of the cellular structure. Moreover, relatively finer particles are observed in C1 if compared to the C2 sample, as consequence of the cellular structure refinement detected on C1 sample.

Based on the EDS analysis of the bright particles after heat treatment (Figure 8.2d), it is revealed that these particles are mainly composed of Mo, N, Cr, C and Si. It should be mentioned that it is quite challenging to determine C and N from EDS. However, the presence of C and N can be justified by the literature regarding conventional CoCrMo alloy [18]. Narushima et al. [18] reported a complete list of phases and precipitates found in conventional biomedical CoCrMo alloys. According to their work, considering a nominal C content of about 0.16 wt.% (Table 3.1), $M_{23}C_6$ and η-phases should be expected, with minor σ- and π-phases. $M_{23}C_6$ is a Cr-rich carbide while η- and π-phases are C-rich carbonitrides and, in particular, Mo-rich M_6X and $M_{12}X$ carbonitrides belong to η-phases. The presence of these secondary phases may justify the local segregation of C and N evidenced by EDS analyses.

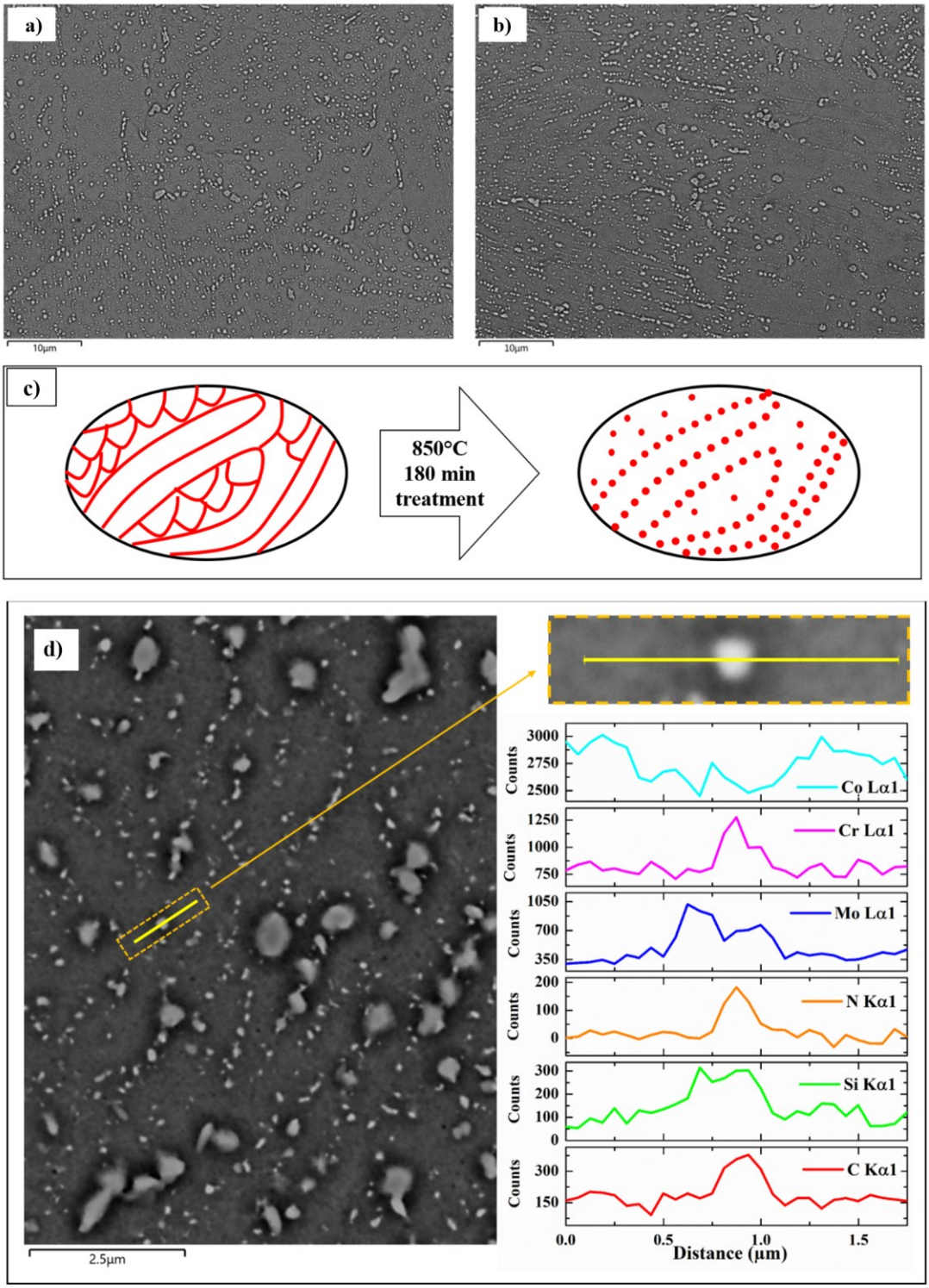

Figure 8.2. SEM/EDS analysis of the Heat treated SLM CoCrMo alloys after etching. a) C1HT sample, b) C2HT sample, c) schematic illustration of the microstructure evolution of the SLM samples during heat treatment, d) semi-quantitative EDS line profile analysis on the C1HT as built sample. Noted that the same EDS results were detected for C2HT sample.

8.2.2. Electrochemical tests

These tests investigated the corrosion behaviour of C samples under both as built conditions (C1 and C2 samples) and heat treated at 850 °C for 180 min (C1HT, C2HT) in comparison to that exhibited by samples extracted from a real prosthesis. The tests consisted in evaluating the time dependence of the sample polarization resistance (R_p) values obtained from EIS spectra, during 15 days of immersion in PBS + 30 mM H_2O_2 at pH 4.

8.2.2.1 Electrochemical impedance spectroscopy

The R_p and E_{corr} values, collected during the electrochemical tests in simulated inflammatory condition solution, are shown in Figure 8.3 a and b, respectively. After one day of immersion the C1, C2, C2HT and real prosthesis showed samples a marked increase of R_p values up values around 5-8×10^5 Ω cm^2, while values close 2MΩ cm^2 were detected in the case of C1HT sample. During the exposure C1HT sample showed continuously increasing R_p values reaching values close 5×10^6 Ω cm^2 after 15 days of immersion. Similar trend was observed in the case of C1sample, but during the medium immersion period, R_p values 2-times lower than C1HT are recorded, and slight R_p drop was observed at the end of exposure. Samples C2 and C2HT also showed a tendency to increase R_p values during exposure, reaching values close to 1 MΩ cm^2 after 15 days of exposure. The highest corrosion resistance was achieved by the heat-treated C1HT sample that showed higher corrosion resistant also of the real prosthesis during all immersion periods.

The corrosion potentials (E_{corr}) of all samples showed a marked ennoblement during the first day of immersion, with the initial E_{corr} values of 0.15 - 0.2 V_{SCE} quickly reaching 0.35 - 0.45 V_{SCE} after 1 day of immersion due to passivity reinforcement and kept these values till the end of the exposure period. The concomitant increase of R_p and E_{corr} values observed during the immersion period suggested that the superficial air-formed oxide films improved its protectiveness due to an increase in their thickness and/or a decrease in defect concentration.

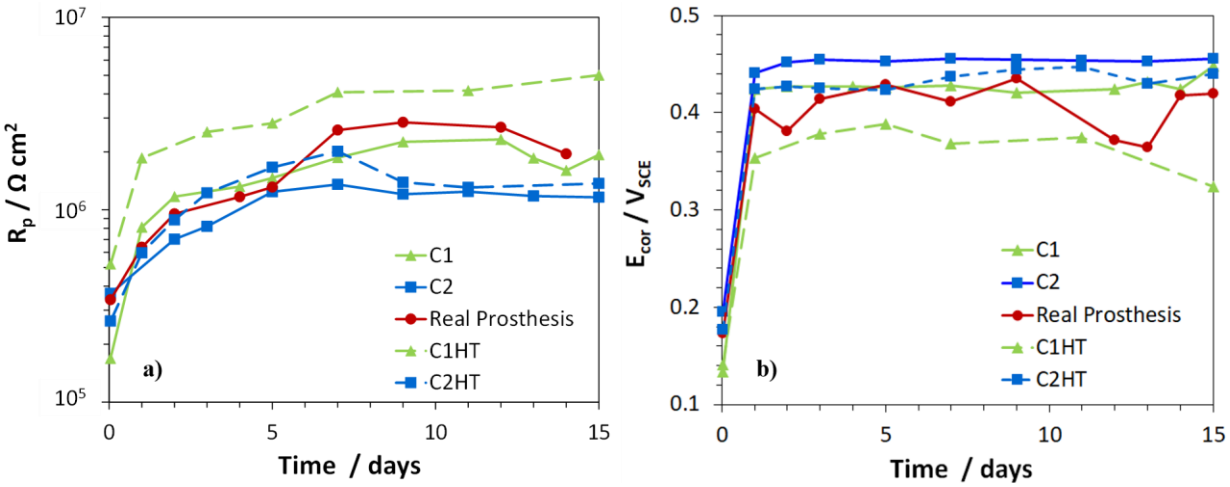

Figure 8.3. a) R_p, and b) E_{corr} values of SLM CoCrMo alloys as well as the real prosthesis samples, during 15 days of immersion in PBS pH 4+ 30 mM H_2O_2 solution.

8.2.2.2. Polarization curves

Figure 8.4 shows the cyclic polarization (CP) curves recorded on C1 and C2 samples both before and after heat treatment post-processing. After 1 hour of immersion, all specimens showed the same cathodic and anodic electrochemical behaviour, characterized by passive currents lower than 5×10^{-6} A cm^{-2} from the potential of zero current up to about 0.7 V_{SCE}, where formation of soluble cations, chromates, molybdates as reported in chapter 4 [19] and phosphomolybdates [20] is expected. The i_{corr} values evaluated by a Tafel fitting method resulted quite close to each other, in the range 0.13 - 0.20 µA cm^{-2}. The Mo silico-carbide precipitates formed during the heat treatment slightly protrude over the surface, indicating that they are electrochemically nobler than the surrounding matrix. These micrographs suggest that the higher currents of the backward scan are connected to the weakening of the alloy passive film during the polarization in the transpassive potential regime.

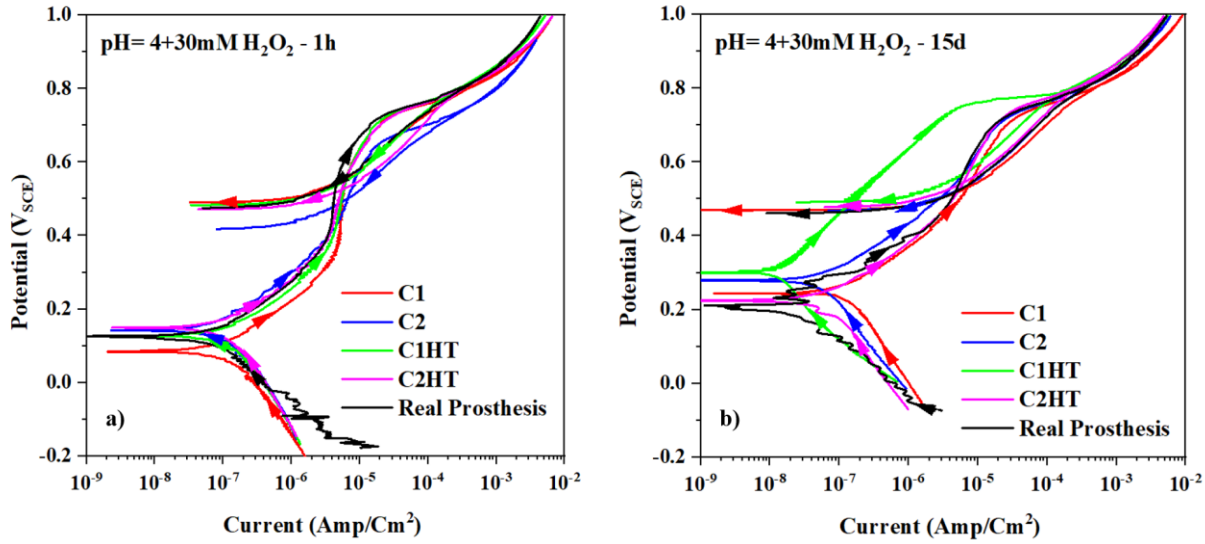

Figure 8.4. Cyclic polarization curves of the SLM CoCrMo alloys before (C1 and C2) and after heat treatment (C1HT and C2HT) at 850 °C for 180 minutes, after a) 1 hour and b) 15 days of immersion in PBS pH 4 + 30 mM H_2O_2 solution.

After 15 days of immersion, the cyclic polarization curves clearly showed an ennoblement of the potential of zero current and a decrease of the corrosion currents (i_{corr}). The i_{corr} values were in the range 0.10 - 0.18 µA cm^{-2} for C1, C2 and C2HT, but lower values were recorded on the real prosthesis alloy (0.016 µA cm^{-2}) and particularly on C1HT electrode (0.012 µA cm^{-2}). Particularly C1HT also showed one order of magnitude lower passive currents than the other samples, in agreements with EIS results. The polarization curves recorded in PBS + 30 mM H_2O_2 at pH 4 clearly showed that both as built, and heat treated SLM CoCrMo samples are passive during the whole 15 days of immersion. Passivity persisted up to 0.7 V, while at higher potentials transpassive dissolution occurred, but the SEM micrographs in Figure 8.5 show that after polarization only a uniform corrosion attack on the alloy matrix is evident. E_{corr}-time and R_p-time trends suggested that passive film stability increased with time as documented by a progressive ennoblement of E_{corr} and an increase in R_p values. C1 and C2 samples exhibited quite similar corrosion behaviour, with i_{corr} of respectively 0.178 and 0.154 µA cm^{-2} after 15 days of immersion. This suggests that the corrosion behaviour of SLM fabricated samples is comparable or superior (if adequate heat treatment is applied) with respect the conventional CoCrMo alloys, and they can be an alternative for conventional fabricated alloys to overcome their drawbacks.

The behaviour of C2HT was not very different from not heat-treated samples, with final R_p of 1.37×10^6 Ω cm^2 (almost overlapped to that of C2) and i_{corr} of 0.10 values μA cm^{-2}. Instead, C1HT showed a remarkably higher corrosion resistance, with a final R_p of 5×10^6 Ω cm^2 (2.6 times higher than that of not heat treated, C1), i_{corr} of 0.012 μA cm^{-2} and passive currents of about 1 order of magnitude lower than those of the other samples. It is likely that these results are attributed to the finer precipitates on C1HT than on C2HT, suggesting more uniform distribution of particles in C1 sample if compared to the C2 (see Figure 8.2).

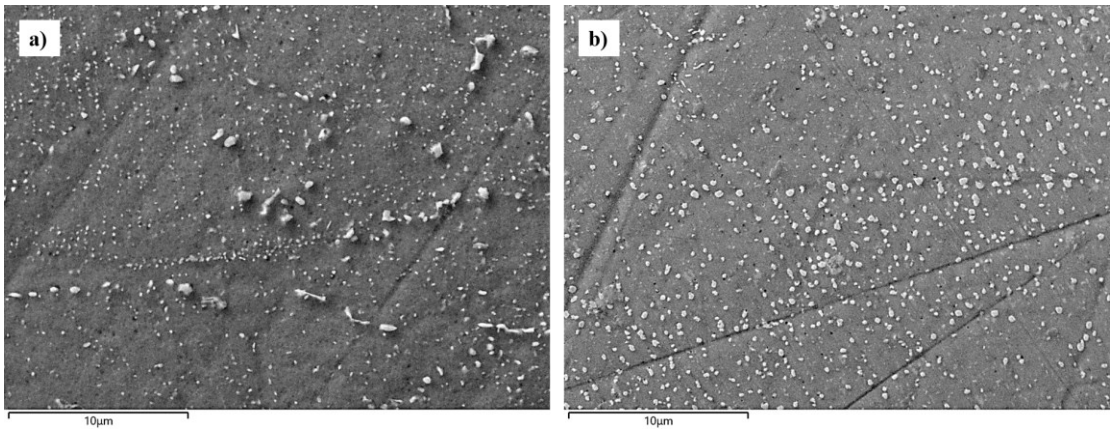

Figure 8.5. Post-polarization microscopy SEM/EDS analysis of the heat-treated SLM alloys after 15 days of immersion, a) C1HT sample, and b) C2HT specimen.

8.3. Conclusions

The present work focused on the heat treatment of the biomedical Co28Cr6Mo alloys produced by selective laser melting process. Once the microstructure of the SLM CoCrMo alloy characterized, the assessment of corrosion resistance of as-built and heat-treated alloys was carried out.

Results were also compared to the conventional wrought alloy that represent the current standard for the production of orthopaedic implants. Based on the outcomes, the following conclusions can be synthetized:

- SLM CoCrMo samples show the typical cellular or columnar structures, resulting from rapid solidification and non-equilibrium conditions during fabrication. A finer cellular structure was found in C1 sample.

- The heat treatments at 850°C for 180 min produced a progressive modification in the as-built cellular structure, that broke down into fine and homogeneously dispersed globular particles.
- Electrochemical and corrosion tests evidenced an overall good corrosion resistance of the as-built alloy, comparable with that of conventional wrought alloy. Optimized heat treatment (850 °C for 180 min) slightly improves corrosion behaviour of C2HT sample. However, C1HT showed a remarkably higher corrosion resistance, 2.6 times higher than that of not heat treated C1 sample and passive currents of about 1 order of magnitude lower than those of the other samples. It is likely that these results are attributed to the finer precipitates on C1HT than on C2HT, suggesting more uniform distribution of particles in C1 sample.

References

[1] S.M.J. Razavi, A. Avanzini, G. Cornacchia, L. Giorleo, F. Berto, Effect of heat treatment on fatigue behavior of as-built notched Co-Cr-Mo parts produced by Selective Laser Melting, Int. J. Fatigue. 142 (2021) 105926.

[2] S.L. Sing, S. Huang, W.Y. Yeong, Effect of solution heat treatment on microstructure and mechanical properties of laser powder bed fusion produced cobalt-28chromium-6molybdenum, Mater. Sci. Eng. A. 769 (2020) 138511.

[3] C. Song, M. Zhang, Y. Yang, D. Wang, Y. Jia-kuo, Morphology and properties of CoCrMo parts fabricated by selective laser melting, Mater. Sci. Eng. A. 713 (2018) 206–213.

[4] M. Béreš, C.C. Silva, P.W.C. Sarvezuk, L. Wu, L.H.M. Antunes, A.L. Jardini, A.L.M. Feitosa, J. Žilková, H.F.G. de Abreu, R.M. Filho, Mechanical and phase transformation behaviour of biomedical Co-Cr-Mo alloy fabricated by direct metal laser sintering, Mater. Sci. Eng. A. 714 (2018) 36–42.

[5] Y. Kajima, A. Takaichi, N. Kittikundecha, T. Nakamoto, T. Kimura, N. Nomura, A. Kawasaki, T. Hanawa, H. Takahashi, N. Wakabayashi, Effect of heat-treatment temperature on microstructures and mechanical properties of Co–Cr–Mo alloys fabricated by selective laser melting, Mater. Sci. Eng. A. 726 (2018) 21–31.

[6] A. Takaichi, Y. Kajima, N. Kittikundecha, H.L. Htat, H.H. Wai Cho, T. Hanawa, T. Yoneyama, N. Wakabayashi, Effect of heat treatment on the anisotropic microstructural and mechanical properties of Co–Cr–Mo alloys produced by selective laser melting, J. Mech. Behav. Biomed. Mater. 102 (2020) 103496.

[7] M. Zhang, Y. Yang, C. Song, Y. Bai, Z. Xiao, An investigation into the aging behavior of CoCrMo alloys fabricated by selective laser melting, J. Alloys Compd. 750 (2018) 878–886.

[8] L. Tonelli, A. Fortunato, L. Ceschini, CoCr alloy processed by selective laser melting (SLM): Effect of laser energy density on microstructure, surface morphology, and hardness, J. Manuf. Process. 52 (2020) 106–119.

[9] K. Darvish, Z.W. Chen, M.A.L. Phan, T. Pasang, Selective laser melting of Co-29Cr-6Mo alloy with laser power 180–360W: Cellular growth, intercellular spacing and the related thermal condition, Mater. Charact. 135 (2018) 183–191.

[10] K.-H. Shin, H. Natu, D. Dutta, J. Mazumder, A method for the design and fabrication of heterogeneous objects, Mater. Des. 24 (2003) 339–353.

[11] W. Kurz, D. Fisher, Fundamentals of Solidification: Fourth Revised Edition, Retrosp. Collect. (1998).

[12] Z.W. Chen, M.A.L. Phan, K. Darvish, Grain growth during selective laser melting of a Co–Cr–Mo alloy, J. Mater. Sci. 52 (2017) 7415–7427.

[13] B. Qian, K. Saeidi, L. Kvetková, F. Lofaj, C. Xiao, Z. Shen, Defects-tolerant Co-Cr-Mo dental alloys prepared by selective laser melting, Dent. Mater. 31 (2015) 1435–1444.

[14] M. Seyedi, F. Zanotto, C. Monticelli, A. Balbo, E. Liverani, A. Fortunato, Microstructural characterization and corrosion behaviour of SLM CoCrMo alloy in simulated body fluid, Metall. Ital. 110 (2018) 45–50.

[15] E. Liverani, A. Balbo, C. Monticelli, A. Leardini, C. Belvedere, A. Fortunato, Corrosion Resistance and Mechanical Characterization of Ankle Prostheses Fabricated via Selective Laser Melting, Procedia CIRP. 65 (2017) 25–31.

[16] Z. Guoqing, Y. Yongqiang, L. Hui, S. Changhui, Z. Zimian, Study on the quality and performance of CoCrMo alloy parts manufactured by selective laser melting, J. Mater. Eng. Perform. 26 (2017) 2869–2877.

[17] K.G. Prashanth, J. Eckert, Formation of metastable cellular microstructures in selective laser melted alloys, J. Alloys Compd. 707 (2017) 27–34.

[18] T. Narushima, S. Mineta, Y. Kurihara, K. Ueda, Precipitates in Biomedical Co-Cr Alloys, JOM. 65 (2013) 489–504.

[19] Marcel Pourbaix, Atlas of electrochemical equilibria in aqueous solutions - Marcel Pourbaix - Google Books, (1974) 644.

[20] E.A. Nagul, I.D. McKelvie, P. Worsfold, S.D. Kolev, The molybdenum blue reaction for the determination of orthophosphate revisited: opening the black box, Anal. Chim. Acta. 890 (2015) 60–82.


9

CHAPTER NINE

Conclusion remarks

In the present Ph.D. project, the corrosion behaviour of CoCrMo biomaterials fabricated by Selective Laser Melting (SLM) and conventional techniques in synthetic body fluids, simulating physiological both in presence and in absence of simulated inflammatory conditions is studied using electrochemical, mechanical and characterization techniques. This is performed to investigate the possibility of SLM technique as a promising method for fabrication of bio-implants to optimize the future implants and consequently, to improve the life quality of implanted patients.

The research activities provide a large amount of information; the key research findings are summarized in this chapter.

Based on this project, some general conclusions can be drawn: SLM exhibits significant benefits in producing customised implants for patients who may need a special implant. Replacing conventional implants with SLM-built ones is appropriate not only for hip implants but also other bone replacement applications due to tailored mechanical properties. In our general perspective, the bio implants fabricated with the SLM technologies are anticipated to be commercialised in the near future due to a significant improvement of AM technologies.

The specific findings of this thesis are collected and categorized based on the individual result chapters (4-8) and are listed as follows:

9.1. Microstructure characterization

The microstructures of CoCrMo biomedical alloy fabricated with conventional and selective laser melting techniques were investigated by Optical Microscopy (OM), Scanning Electron Microscopy (SEM) coupled with energy dispersive X-Ray spectroscopy (EDX), X-Ray Diffraction (XRD), Focused Ion Beam technique (FIB) associated to Scanning Transmission Electron Microscopy (STEM) and Scanning Kelvin Probe Force Microscopy (SKPFM);

- The selective laser melting process SLM parameters allow to obtain samples with different microstructural characteristics: the different process parameters lead to fabrication of materials with different residual porosity. Sample B1 obtained under high fluence has a relative density of 99.8% with few residual pores, while the B2 sample fabricated with lower fluence is characterized by a greater porosity percentage and larger pores with a relative density of 95%.

- The XRD analysis showed a higher amount of ε-phase and a smaller crystallite size in the γ-phase in the B2 samples compared to those measured on the B1 samples.
- The SLM technique induced a non-equilibrium microstructure characterized by a cellular structure in which micro and submicro cell growing in specific directions within grains that grow epitassially from n layer to n+1 layer.
- The different laser parameters adopted during the fabrication of the SLM samples induced a finer microstructure in the B2 samples characterized by a finer spacing between the primary dendrites with respect the B1 samples.
- The SLM particular morphlogy is charactrized by a non-unform distribution oa alloying elements, representing an enrichment in Mo, and to some extent also for Cr at the cell bundaries and depletion at the center of the cells. B2 sample with finer structure represents a lower segregation and more unifor distribution of alloying elements if compared to B1.
- CoCrMo alloy fabricated by conventional method already shows the typical twins of the FCC structure and a low volume fraction of precipitates randomly distributed throughout the matrix.
- This SKPFM result indicates that the melt pool boundary of SLM alloys may act as a preferential area for corrosion initiation, demonstrating a lower relative nobility in comparison to the adjacent matrix. However, no significant changes on Volta potential were detected in WRO alloys.
- The application of the FIB technique allowed the estimation of the oxide film thickness which varies between 100-50 nm after polarization at +0.9 $V_{SCE\ for}$ 30 minutes. However, the thickness of the surface layer in free corrosion condition after 15 days of immersion is much thinner than that of polarized condition and is around 4 nm.
- The EDS line scan long along the surface to bulk of thin lamella extracted by FIB evidenced that the protective oxide layer formed at +0.9 V_{SCE} mainly consisted of Cr-oxide with traces of Co-oxides. he elemental profiles of free corrosion condition suggests that in this case the protective layer is essentially constituted by Cr oxides which their percentages increase by passing from the oxide layer to the bulk.

9.2. Cyclic Voltammetry (CV) study

CV method has been demonstrated to be useful and sensitive tool for characterizing the influence of alloying elements on electrochemical behaviour of SLM CoCrMo alloy in simulated body fluids. To evaluate the dependence of the nature of the surface film on CoCrMo alloys with the potential and environment, cyclic voltammetry tests were conducted on both SLM and WRO alloys and on its main alloying elements, namely pure Co, Cr and Mo. Pourbaix diagrams of Co, Cr and Mo in water, at 37 °C, were also used to interpret CV tests. The voltagrammes have been conducted to understand the nature of the reduction peaks and therefore the nature of the compounds and ions formed during the scanning in anodic direction;

- In PBS at neutral pH, Co, undergoes spontaneous passivation because formation of cobalt hydroxide film, which, however, shows a limited protection if aggressive ions such as chlorides are present. The presence of phosphate ions may reinforce the passive film. At pH = 4 the formation of protective film is not allowed, and Co is oxidized to Co^{2+} at potential higher than those of thermodynamic equilibrium.
  No passive region was observed in the presence of H_2O_2, however the lower anode currents than those measured in the absence of hydrogen peroxide suggested the formation of an adsorption oxide layer.
- Chromium is the alloying element that mainly contributes to the high corrosion resistance of the CoCrMo alloy. In the tested environments Cr is spontaneously passive and the formation of a highly protective Cr_2O_3 film produced a large passivity region even in the presence of chlorides. In none of the tested environments is Cr subject to localized corrosion. In the presence of H_2O_2, the probable formation of CrOOH as well as Cr_2O_3 reduces the protection of the passive film.
- In PBS at pH=7.4 and pH=4 Mo showed a wide passive potential range with slightly increasing current on cycling. The passivity of molybdenum was ascribed to the formation of MoO_2. Transpassivity was observed at potentials nobler than -0.1 and -0 V_{SCE} at pH= 7.4 and pH=4 respectively, connected the formation of molybdate and/or heptamolybdate ion. The presence of H_2O_2 induced the formation of a defective oxide film, and a reduction of a passive range.

- The SLM and the WRO alloys showed similar behaviour at pH=7.4 and pH=4 suggesting comparable barrier properties of the passive film, mainly ascribed to the protective capability of Cr_2O_3, reinforced by the presence of MoO_2.
  The H_2O_2 addition scarcely affected the electrochemical behaviour of both SLM and wrought alloys that exhibited a quite similar electrochemical behaviour.

9.3. Electrochemical techniques

The corrosion and electrochemical stability of the SLM and WRO alloys were studied by determining the corrosion resistance. The study was performed using electrochemical impedance spectroscopy (EIS) and cyclic polarization during 15 days of immersion in simulated body fluids in presence and absence of inflammatory condition. The information about passive film dissolution and characteristics and corrosion resistance can be obtained from EIS tests, whereas by polarization curves we are able to study the corrosion behavior of the studied materials;

- Samples obtained with SLM techniques show low corrosion rates in the tested environments, which result comparable to those measured on WRO alloy in the case of B2 and slightly worse for B1.
- The SLM process parameters affect the corrosion behaviour of SLM alloys: in all tested conditions alloy B2 with its homogeneous fine microstructure exhibits lower corrosion rates than sample B1, characterized by a coarser microstructure and likely more important micro-segregation phenomena. The porosity present in B2 does not affect the alloy corrosion resistance.
- The lower corrosion resistance in the presence of simulated inflammation conditions is likely connected to the strong oxidative properties exhibited by H_2O_2 in the presence of metals or metal ions which are reported to contribute to the formation of aggressive species, such as hydroxyl radicals.

9.4. Mechanical properties

To determine whether the process parameters affect the mechanical behavior of the SLM fabricated CoCrMo alloys, multiple analysis were employed. Different approaches such as microhardness, tensile, and Slow Strain Rate Tests (SSRT) were conducted. Moreover, the scanning electron microscope was utilized in order to study the fracture surface after tensile and SSRT measurements;

- B1 samples have a relative density of 99.8%, while B2 samples show a lower relative density of 95%.
- The microhardness tests demonstrate that the SLM process can build parts with hardness only slightly lower that of WRO CoCrMo alloy. B1 exhibits relatively higher hardness values than B2. This can be correlated to their different density: higher hardness was afforded by the denser B1 alloy.
- The tensile tests revealed that the stiffness, yield strength, UTS, and strain percentage to fracture of B1 sample are higher than those obtained for B2. The reasons can be connected to the lower fluence adopted during the B2 alloy preparation, which caused higher porosity, higher fraction of the brittle ε phase and significant amount of unmelted powders, entrapped in the consolidated alloy.
- Interesting materials properties are achieved by adopting a double process parameters set in the fabrication of B1+B2 tensile samples. They are characterized by a B1 structure in the bulk and a B2 structure on the surface. The results of the tensile tests showed that B1+B2 mechanical properties are only slightly lower than those of B1. At the same time, the presence of B2 in the shell of the structure ensures better corrosion resistance (see chapter 6) and better matches with the surrounding porous bone. B2 is also expected to favour osseointegration. In the current study, B1+B2 sample represents the best trade-off between mechanical resistance, corrosion resistance and production time.
- In agreement with the results of the tensile tests, the slow strain rate test suggested that the B1 sample showed slightly better mechanical properties as well as higher ε_f % values, than B2. However, the large data scattering obtained with tests in air and in solution prevented a clear conclusion about the susceptibility of the two SLM alloys to SCC.

- From fractography analysis of SLM alloys after tensile and SSRT testing, in general, the failure type was recognized to be a quasi-cleavage fracture and dimple-like patterns as well as facet-like surface. Moreover, samples exhibited the presence of wedge-like cracks, while B2 samples showed un-melted particles which are sites prone to initiation and propagation of failure cracks.

9.5. Post-processing heat treatment

This part focused on the effect of post processing heat treatment on the microstructure and corrosion behaviour of the biomedical Co28Cr6Mo alloys produced by Laser-based Powder Bed Fusion (LPBF). Once the microstructure of the LPBF CoCrMo alloy identified, assessment of corrosion resistance of LPBF as-built and heat-treated alloys was carried out. Results were also compared to the conventional wrought alloy that represent the current standard for the production of orthopaedic implants;

- SLM CoCrMo samples show the typical cellular or columnar structures, resulting from rapid solidification and non-equilibrium conditions during fabrication. A finer cellular structure was found in C1 sample.
- The heat treatments at 850°C for 180 min produced a progressive modification in the as-built cellular structure, that broke down into fine and homogeneously dispersed globular particles.
- Electrochemical and corrosion tests evidenced an overall good corrosion resistance of the as-built alloy, comparable with that of conventional wrought alloy. Optimized heat treatment (850 °C for 180 min) slightly improves corrosion behaviour of C2HT sample. However, C1HT showed a remarkably higher corrosion resistance, 2.6 times higher than that of not heat treated C1 sample and passive currents of about 1 order of magnitude lower than those of the other samples. It is likely that these results are attributed to the finer precipitates on C1HT than on C2HT, suggesting more uniform distribution of particles in C1 sample.


10

CHAPTER TEN

Outlook and future perspective

More extensive experimental work may be carried out in the future to look at the potential factors that may influence the properties of the SLM fabricated CoCrMo alloys in simulated body fluids to ensure the effectiveness of these materials as promising bio implants.

- Study the passive composition of SLM alloys after exposure to SBFs, by using X-ray photoelectron spectroscopy (XPS)
- Measure the ion release from of SLM CoCrMo during the exposure to SBFs alloys by using inductively coupled plasma atomic emission spectroscopy (ICP-OES).
- Study the correlation between the process parameters and residual stresses of SLM fabricated samples, which is relevant for durability of SLM fabricated samples.
- Micro-abrasion corrosion tests can be conducted at different sliding distance and/or different applied load; scratching tests at different applied load and scratch cycles may also be conducted.
- The sub-surface of the worn samples can be examined by using FIB/TEM to provide better detail of the sub-surface microstructure.
- Systematical tribological testing with in-situ friction measurements (like scratching, pin-on-disc) need to be conducted under controlled conditions in order to find out the correlation between the test parameters (applied load, stress cycles) and the degree of phase transformation.
- Use of TEM technique for quantitative and qualitative analysis of the deformation substrate to look at the detailed sub-surface grain structure of the worn SLM CoCrMo alloys. The dislocation pattern, stacking faults, cell formation and grain reinforcement can be observed at a greater resolution.
- A corrosion current mapping which may indicate the difference in corrosion level at a specified location of wear damage can be established and therefore more insightful information regarding the change of surface corrosion properties due to micro-/nano-scale tribological processes can be obtained.
- A study the corrosion behaviour of SLM CoCrMo in a protein-rich synthetic body fluid (PBS with Bovine serum albumin (BSA))
- Study the effect of BSA on the corrosion behavior of SLM CoCrMo under a fretting conditions.


11

CHAPTER ELEVEN

Abbreviations and APPENDIX

11.1. List of abbreviations and symbols

Units

A	Ampere
Å	Ångström
at.%	Atomic percent
°C	Centigrade degree
d	Day
h (and hr)	Hour
Hz	Hertz
HV	Vickers hardness
K	Kelvin degree
M	Molarity
min	Minute
Pa	Pascal
rpm	Rotation per minute
s (and sec)	Second
V	Volt
wt.%	Weight percent

Variable parameters

$\mathbf{C_{dl}}$	Double Layer Capacitance (EIS)
d	Laser Focus diameter (SLM)
E	Laser Energy Density (SLM)
$\mathbf{E_{corr}}$	Corrosion Potential
E(t)	Potential at time t

G	Temperature gradient (SLM)
h	Hatch spacing (SLM)
$\mathbf{i_{corr}}$	Corrosion Current Density
No.	Number
P	Laser input power (SLM)
R	Rate of solidification (SLM)
$\mathbf{R_{ct}}$	Charge Transfer Resistance
ROS	Reactive Oxygen Species
$\mathbf{R_p}$	Polarization Resistance
t	Layer thickness (EIS)
t	Time
T	Temperature
ΔT	Undercooling gradient(SLM)
v	Laser scan speed (EIS)
ω	Radial frequency (EIS)
$\boldsymbol{\phi}$	Phase angle (EIS)
$\boldsymbol{\theta}$	Diffraction semi-angle (XRD)
$\boldsymbol{\lambda}$	Wavelength (XRD)
$\boldsymbol{\Delta\psi}$	Volta potental difference (SKPFM)

Abbreviations

2D	2-Dimensional
3D	3-Dimensional
AE	Auger Electron
AFM	Atomic Force Microscope/microscopy
AM	Additive manufacturing
ASTM	American Society for Testing and Materials
AT	Aging Treatment

BF	Bright Field
BSE	Back-Scattered Electron
BSA	Bovine Serum Albumin
CAD	Computer Aided Design
CCD	Charge-Coupled Device
CE	Counter Electrode
CNR	Consiglio Nazionale delle Ricerche
CoCr	Cobalt-Chromium
CoCrMo	Cobalt-Chromium-Molybdenum
CP-Ti	Commercially Pure Titanium
CV	Cyclic Voltammetry
DED	Directed Electron Deposition
DF	Dark Field
DLP	Direct Light Projection
EBF^3	Beam Freedorm Fabrication
EBM	Electron Beam Melting
EC	Equivalent Circuit
ECAFM	Electrochemical Atomic Force Microscope/microscopy
EDTA	Ethylenediaminetetraacetic Acid
EIS	Electrochemical Impedance Spectroscopy
EDS/EDX	Energy Dispersive X-ray Spectroscopy
FCC	Face-Centered Cubic
FDM	Fused Deposition Modeling
FEG	Field Emission Gun
FGM	Functionally Graded Materials
FIB	Focused Ion Beam
HAADF	High-Angle Annular Detector
HCP	Hexagonal Closed-Packed
HIP	Hot Isostatic Pressing
HT	Heat Treatment
ICP-AES	Inductively Coupled Plasma Atomic Emission Spectroscopy
ICP-MS	Inductively Coupled Plasma Mass Spectroscopy

ISO	International Organization for Standardization
KTH	Kungliga Tekniska Hogskolan
LED	Laser Energy Density
LENS	Laser Engineered Net Shaping
LC	Low Carbon
LOF	Lack of Fusion
LOM	Laminated Object Manufacturing
LPBF	Laser-based Powder Bed Fusion
MOM	Metal-on-Metal
MPB	Molten Pool Boundary
OCP	Open Circuit Potential
OM/LOM	Light Optical Microscope/microscopy
PBF	Powder Bed Fusion
PC	Polarization Curves
PBS	Phosphate Buffered Saline
PDM	Plasma Deposition Manufacturing
RE	Reference Electrode
ROS	Reactive Oxygen Species
RT	Reverse Treatment
SCC	Stress Corrosion Cracking
SCE	Saturated Calomel Electrode
SE	Secondary Electron
SEM	Scanning Electron Microscope/microscopy
SFE	Stacking Fault Energy
SHE	Standard Hydrogen Electrode
SIC	Simulate Inflammatory Conditions
SKPFM	Scanning Kelvin Force Microscope/microscopy
SLA	Stereo Lithography
SPBS	Saline Phosphate Buffer Solution
SPF	Simulated Physiological Fluid
SPM	Scanning Probe Microscope/microscopy
SPS	Simulated Physiological Solution (Hank's)
SSRT	Slow Strain Rate Test

ST	Solution Treatment
STEM	Scanning Transmission Electrocn Microscope/microscopy
STL	Standard Triangle Language
SLM	Selective Laser Melting
SLS	Selective Laser Sintering
TEM	Transmission Electron Microscope/microscopy
UCS	Ultimate Compressive Strength
UTS	Ultimate Tensile Strength
UNIBO	University of Bologna
UNIFE	University of Ferrara
UV	Ultraviolet
WE	Working Electrode
XPS	X-ray Photoelectron Spectrsoscopy
XRD	X-Ray Diffraction

11.2. Appendix

11.2.1. Appendix A

Table A. 1. Standard thermodynamic properties at 25°C and 1bar for Co-H_2O system, used E/pH diagram calculation.

Species	Selected data			
	ΔG°_f (kJ mol^{-1})	ΔH°_f (kJ mol^{-1})	S° (kJ mol^{-1} K^{-1})	C°_p (J mol^{-1} K^{-1})
H_2O	-237.141	-285.828	69.957	75.338
$H_{2(g)}$	0	0	130.679	28.977
H^+	0	0	0	0
$O_{2(g)}$	0	0	205.149	29.337
$Co_{(s)}$	0	0	30.04	25.394
Co^{2+}	-55.665	-58.125	-108.891	-32.848
Co^{3+}	133.626	92.048	-305.432	-102.018
Co_3O_4	-802.188	-918.799	109.300	123.270
$CoOH^+$	-240.1	-286.495	-42.178	100.904
$CoOH^{2+}$	-96.305	-151.042	-116.315	-22.305
$CoOOH_{(s)}$	-384.37	-	-	-
$Co(OH)_2^{\circ}$	-423.757	-523.598	30.999	-
$Co(OH)_{2(s)}$	-459.354	-539.736	79.496	90.00
$Co(OH)_{3(s)}$	-596.329	-730.526	83.68	-
Co_2OH^{3+}	-292.296	-371.00	-231.999	
$Co_4(OH)_4^{4+}$	-1000.549	-1224.000	-218.999	

Table A. 2. Standard thermodynamic properties at 25°C and 1bar for Cr-H_2O system, used E/pH diagram calculation.

Species	Selected data			
	ΔG°_f (kJ mol^{-1})	ΔH°_f (kJ mol^{-1})	S° (kJ mol^{-1} K^{-1})	C°_p (J mol^{-1} K^{-1})
H_2O	-237.141	-285.828	69.957	75.338
$H_{2(g)}$	0	0	130.679	28.977
H^+	0	0	0	0
$O_{2(g)}$	0	0	205.149	29.337
$Cr_{(s)}$	0	0	23.543	23.433
Cr^{2+}	-161.817	-143.500	-45.700	0
Cr^{3+}	-198.269	-242.900	-322.168	-94.517
Cr_2O_3	-1056.310	-1137.350	83.000	120.307
Cr_3O_4	-1324.590	-1417.465	169.420	143.059
$CrOH^{2+}$	-420.594	-496.222	-192.882	64.721
$Cr(OH)_4^-$	-1052.743	-1246.999	109.002	-212.999
CrO_4^{2-}	-724.224	-879.000	45.400	-248.461
$HCrO_4^-$	-757.355	-872.000	180.000	85.397

Table A. 3. Standard thermodynamic properties at 25°C and 1bar for Cr-H2O system, used E/pH diagram calculation.

Species	Selected data			
	ΔG°_f (kJ mol^{-1})	ΔH°_f (kJ mol^{-1})	S° (kJ mol^{-1} K^{-1})	C°_p (J mol^{-1} K^{-1})
H_2O	-237.141	-285.828	69.957	75.338
$H_{2(g)}$	0	0	130.679	28.977
H^+	0	0	0	-
$O_{2(g)}$	0	0	205.149	29.337
$Mo_{(s)}$	0	0	28,560	23,969
Mo^{3+} [1]	-45.843	-83.115	-292.499	-
MoO_2	-532,087	-587,900	46,510	55,910
MoO_3	-667.491	-744.600	77.660	73.503
MoO_2^{2+}	-411,236	-461,914	-66,944	-
MoO_4^{2-}	-837,916	-997,884	33,000	-196,835
H_2MoO_4	-912,27	-1046,00	121,00	-
$HMoO_4^-$	-868,62	-997,88	135,98	119,55

References

[1] P. Wan, L.L. Wilson, D.J. Wesolowski, J. Rosenqvist, A. Anderko, Solution chemistry of Mo(III) and Mo(IV): Thermodynamic foundation for modeling localized corrosion, Corr. Sci. 52 (2010) 1625–1634.

DE: Department of Engineering Ferrara